



HAL
open science

Advances in opto-electronic oscillator operation for sensing and component characterization

Toan Thang Pham

► **To cite this version:**

Toan Thang Pham. Advances in opto-electronic oscillator operation for sensing and component characterization. Electronics. École normale supérieure de Cachan - ENS Cachan, 2015. English. NNT : 2015DENS0013 . tel-01159548

HAL Id: tel-01159548

<https://theses.hal.science/tel-01159548>

Submitted on 3 Jun 2015

HAL is a multi-disciplinary open access archive for the deposit and dissemination of scientific research documents, whether they are published or not. The documents may come from teaching and research institutions in France or abroad, or from public or private research centers.

L'archive ouverte pluridisciplinaire **HAL**, est destinée au dépôt et à la diffusion de documents scientifiques de niveau recherche, publiés ou non, émanant des établissements d'enseignement et de recherche français ou étrangers, des laboratoires publics ou privés.

**THÈSE DE DOCTORAT
DE L'ÉCOLE NORMALE SUPÉRIEURE DE CACHAN**

présentée par

PHAM Toan Thang

pour obtenir le grade de

DOCTEUR de l'ÉCOLE NORMALE SUPÉRIEURE de CACHAN

domaine

Electronique, Electrotechnique, Automatique

Sujet de la thèse

**Advances in opto-electronic oscillator operation for
sensing and component characterization applications**

Soutenue à Cachan le 26 mars 2015 devant le jury composé de

Xavier CHECOURY	Université Paris Sud	Président
Gaële LISSORGUES	ESIEE	Rapporteur
Emmanuel BIGLER	ENSMM Besançon	Rapporteur
Isabelle LEDOUX-RAK	ENS Cachan	Examinatrice
Bernard JOURNET	ENS Cachan	Directeur

Acknowledgements

I would like to thank the following people for helping me to complete this thesis:

Firstly, I express my sincerest gratitude to my thesis supervisor, Mr. Bernard Journet, for accepting me in his research group with academic atmosphere, variety research facilities, for sharing his invaluable experience, immense knowledge and essential encouragement throughout my PhD thesis.

Prof. Joseph Zyss - former director of “Institut d’Alember”, Prof. Pascal Larzabal - director of SATIE laboratory, Prof. Isabelle Ledoux-Rak – director of LPQM laboratory and Marjolaine Vernier from Institut d’Alember for their excellent advice, discussions and support.

Mr. Du Kim Pha David, Mr. Christophe Salle (Département EEA, ENS Cachan) and Mr. Patrice Vallade (SATIE) for their enthusiasm and indispensable help in fabricating and providing many mechanical support and for making several electronic cards.

Asso. Prof. Vu Van Yem (HUST) for his valuable guidance and discussions and Asso. Prof. Bach Gia Duong (VNU-UET) for his collaboration and advice.

Asso. Prof. Lai Ngoc Diep (LPQM) and Nguyen Chi Thanh (LPQM) for their discussions and support.

All friends in the SATIE and LPQM laboratories and other Vietnamese friends for maintaining a creative and friendly studying atmosphere: B.D. Thanh, L.V.H. Nam, N.T. Minh, P.T. Thong, T.Q. Cong, P.V. Chi...

Vietnam International Education Development (VIED), Ministry of Education and Training, Vietnam for granting me a full scholarship for completing my PhD thesis in ENS Cachan.

Finally, no word can express my appreciation to my family: my parents, my beloved wife and my lovely son and daughter!

Table of contents

Acknowledgements	1
Table of contents	3
Abbreviations	7
List of tables	9
List of figures	11
Introduction	17
Chapter 1 Optoelectronic oscillator	21
1.1 Introduction.....	21
1.2 Optoelectronic oscillator.....	22
1.2.1 Oscillation loss phenomenon.....	24
1.2.2 Oscillation frequency drift.....	24
1.3 Electrooptic modulator.....	25
1.3.1 Optical modulation.....	25
1.3.1.1 Direct modulation.....	25
1.3.1.2 External modulation.....	25
1.3.1.3 Pockels effect.....	26
1.3.1.4 Intensity modulation.....	26
1.3.2 Mach-Zehnder Modulator (MZM).....	27
1.3.3 Drift phenomenon of EOM.....	27
1.4 Conclusions and motivations.....	29
Chapter 2 Optoelectronic oscillator simulation	31
2.1 Noise sources in OEO.....	31
2.1.1 Laser noise.....	31
2.1.2 Photodetector noise.....	32
2.1.2.1 Shot noise.....	32
2.1.2.1.2 Thermal noise.....	33
2.1.2.1.3 Flicker noise (1/f).....	33
2.1.2.1.4 Dark current noise.....	33
2.1.3 Amplifier noise.....	34

2.2	Phase noise	34
2.3	Experiment setup.....	35
2.4	Yao – Maleki model	38
2.5	Simulation with Matlab	40
2.5.1	Simulation models	40
2.5.1.1	Simulation analysis	41
2.5.1.2	Implementation of the Levy model.....	42
2.5.2	Simulation results.....	43
2.5.2.1	Case of 1000 m optical fiber length	43
2.5.2.2	Case of 500 m optical fiber length	45
2.5.2.3	Case of 1500 m optical fiber length	46
2.6	Other simulation software systems	48
2.7	Conclusions and discussions.....	49

Chapter 3 Impacts of temperature on behavior of the EOM and the OEO 51

3.1	Temperature measurement	51
3.1.1	Temperature sensors.....	51
3.1.1.1	Definition	51
3.1.1.2	Thermistor	52
3.1.2	Measurement circuit.....	53
3.2	Tuning temperature.....	56
3.2.1	Peltier module	56
3.2.2	Mounting Peltier to the EOM.....	57
3.2.3	Temperature tuning card	58
3.3	Controlling temperature.....	59
3.3.1	Digital signal processing	59
3.3.1.1	Spectrum Digital eZdsp F28335 card.....	61
3.3.1.2	Link Research LR-F28335DAQA daughtercard.....	62
3.3.1.2.1	Memory Address	63
3.3.1.2.2	ADC and DAC.....	64
3.3.2	PID controller	64
3.3.3	Software development	67
3.3.3.1	Matlab/Simulink.....	67
3.3.3.2	Code Composer Studio	68
3.3.3.3	Graphical user interface control on PC.....	69
3.3.4	Experimental results.....	69
3.4	Temperature impact on average optical output power of the EOM	72
3.5	EOM temperature and its transfer function	75
3.5.1	Transfer function determination.....	75
3.5.2	Transfer function drift.....	79
3.6	EOM temperature variation and OEO oscillation power.....	80
3.7	Fiber loop temperature and OEO oscillation frequency.....	81
3.7.1	Data acquisition program	82

3.7.2	Measuring temperature and oscillation frequency.....	84
3.8	Conclusions and discussions	86
Chapter 4 Controlling EOM by using DSP technique		89
4.1	Dither based bias control.....	89
4.1.1	Drift determination and control.....	89
4.1.1.1	EOM drift simulation.....	89
4.1.1.2	Drift determination principle.....	92
4.1.1.3	Drift control scheme in DSP	93
4.1.1.4	Designing model with Matlab/Simulink.....	94
4.1.1.5	Digital filter.....	95
4.1.2	EOM bias control by using external photodetector	96
4.1.2.1	Drift determination in terms of the Non-Linear Indicator.....	97
4.1.2.2	Bias control at EOM positive slope.....	97
4.1.2.3	Bias control at EOM negative slope.....	99
4.1.3	MZM bias control by using the internal photodiode.....	100
4.1.3.1	Designing interface card	100
4.1.3.1.1	Current to voltage circuit	100
4.1.3.1.2	AC amplifier circuit	102
4.1.3.2	Connection scheme and results.....	102
4.1.4	Integrating two controls: temperature and bias.....	105
4.2	Optical output power based bias control.....	107
4.2.1	DC amplifier circuit	107
4.2.2	Transfer function determination with the internal photodiode.....	108
4.2.3	Simulink model of optical power based control.....	111
4.3	Integrating both bias control techniques with other functions.....	112
4.3.1	Combining both bias control techniques.....	112
4.3.2	Integrating both bias control techniques with EOM temperature control and fiber temperature measuring.....	114
4.4	Conclusions and discussions	117
Chapter 5 OEO application to refractive index measurement		119
5.1	Measurement principle	119
5.2	Short-term refractive index measurement	122
5.2.1	Experimental setup.....	122
5.2.2	Calibration of the free spectral range.....	126
5.2.3	Individual measurement.....	127
5.2.3.1	Measurement with 500 m fiber and 2 mm cuvette.....	128
5.2.3.2	Measurement with 500 m fiber and 10 mm cuvette	129
5.2.3.3	Measurement with 4 m fiber and 2 mm cuvette.....	130
5.2.3.4	Measurement with 4 m fiber and 10 mm cuvette.....	130
5.2.4	Measuring with an RF generator	131
5.3	Real-time and long-term measurement by using an external frequency source	133

5.4	Conclusions	135
Chapter 6 Improving long-term refractive index measurement with a vector network analyzer 137		
6.1	Principle of measurement.....	137
6.2	Improving the phase measurement	141
6.3	Data acquisition program	144
6.4	Monitoring OEO frequency drift with a VNA	145
6.4.1	OEO oscillation frequency vs temperature.....	145
6.4.2	OEO oscillation frequency vs phase	147
6.5	Accuracy of this technique when applied for long-term measurement.....	149
6.6	Method for implementing the correction to the oscillation frequency drift.....	152
6.6.1	Principle	152
6.6.2	Determination of long-term refractive index variations.....	154
6.6.2.1	Refractive index of the liquid at time 0.....	154
6.6.2.2	Refractive index of the liquid at time t	154
6.6.2.2.1	Direct determination of the refractive index variation	154
6.6.2.2.2	Indirect determination of the refractive index variation	155
6.7	New software for long-term measurement.....	157
6.8	Conclusions	158
General conclusions and perspectives		161
Annex A Schematic diagrams of electronics cards		165
A.1	Schematic of temperature measuring card	165
A.2	Schematic of temperature tuning card.....	166
A.3	Schematic of bias input card	167
Annex B Descriptions of DSP kit		168
B.1	Spectrum Digital eZdsp F28335 card.....	168
B.2	Link Research F28335 daughter card.....	169
Annex C RF filters specifications		170
C.1	8 GHz RF filter.....	170
C.2	2.1 GHz RF filter	171
List of publications		173
Bibliography		175

Abbreviations

AC	Alternating Current
ADC	Analog-to-Digital Converter
ADS	Advanced Design System
ASIC	Application-Specific Integrated Circuit
LPF	Low Pass Filter
BNC	Bayonet Neill–Concelman
BPF	Band Pass Filter
CCS	Code Composer Studio
COMSIS	COMmunication System Interactive Software
DAC	Digital-to-Analog Converter
DC	Direct Current
DSP	Digital Signal Processing
EOM	Electro-Optic Modulator
FPGA	Field-Programmable Gate Array
FIR	Finite Impulse Response
FFT	Fast Fourier Transform
FRM	Forward Rectangular Method
GPIO	General Purpose Interface Bus
GUI	Graphical User Interface
HPF	High Pass Filter
IC	Integrated Circuit
IEEE	Institute of Electrical and Electronics Engineers
IIR	Infinite Impulse Response
ISR	Interrupt Service Routine
LIMO	Light-Induced Microwave Oscillator
LPF	Low Pass Filter
MZM	Mach-Zehnder Modulator
NLI	Non-Linear Indicator

RF	Radio Frequency
OEO	Opto-Electronic Oscillator
PI	Proportional-Integral
PID	Proportional-Integral-Derivative
PSoC	Programmable System-on-Chip
TF	Transfer function
VNA	Vector Network Analyzer

List of tables

Table 3.1	Some key features of eZdspF28335 card.....	62
Table 3.2	Memory address table of A/D and D/A channels of LR-F28335DAQA daughtercard.....	63
Table 3.3	Binary representation of LR-F28335DAQA daughtercard	64
Table 3.4	EOM photodetector output DC voltages at different triangle signal frequencies shown on the oscilloscope screen.....	75
Table 3.5	EOM photodetector output DC voltages at different temperatures shown on the oscilloscope screen.....	79
Table 5.1	Measurements of the FSR and equivalent loop length	126
Table 5.2	Measurement results with 500 m fiber and 2 mm cuvette.....	128
Table 5.3	Measurement results with 500 m fiber and 10 mm cuvette.....	129
Table 5.4	Measurement results with 4 m fiber and 2 mm cuvette	130
Table 5.5	Measurement results with 4 m fiber and 10 mm cuvette	130
Table 5.6	Measurement results with 4 m fiber, 10 mm cuvette and an external RF generator	132
Table 5.7	Reference refractive indexes.....	135
Table 6.1	Theoretical and experimental results of coefficient b	153

List of figures

Figure 1.1	Block diagram of a sinusoidal oscillator using an amplifier with a frequency-dependent feedback path [13].....	21
Figure 1.2	Basic structure of single loop OEO.....	23
Figure 1.3	Oscillation loss happens at 7445 s.....	24
Figure 1.4	Oscillation frequency drift during 7400 s.	24
Figure 1.5	Block diagram of direct modulation.....	25
Figure 1.6	Block diagram of external modulation.....	26
Figure 1.7	A structure of an electrooptic modulator (source: Photline).....	27
Figure 1.8	Classification of the different sources of the drift phenomenon of LiNbO_3 modulator.	29
Figure 2.1	Experimental setup for phase noise measurement.....	36
Figure 2.2	Spectrum and phase noise of 500 m OEO.....	37
Figure 2.3	Spectrum and phase noise of 1000 m OEO.....	37
Figure 2.4	Spectrum and phase noise of 1500 m OEO.....	37
Figure 2.5	Phase noise of the OEO in case of 1 km fiber loop, with simulation from Yao & Maleki theoretical model.....	40
Figure 2.6	Phase noise of the OEO in case of 1 km optical fiber length. Simulation results with different numbers N_{tot} of iterations ($N_{\text{it2}} = 10000$).	44
Figure 2.7	Phase noise of the OEO in case of 1 km optical fiber length. Simulation results with different values of GS parameter ($N_{\text{tot}} = 40000$).	44
Figure 2.8	Phase noise of the OEO in case of 500 m optical fiber length. Simulation results with different numbers N_{tot} of iterations ($N_{\text{it2}} = 10000$).	45
Figure 2.9	Phase noise of the OEO in case of 500 m optical fiber length. Simulation results with different values of GS parameter ($N_{\text{tot}} = 20000$).	46
Figure 2.10	Phase noise of the OEO in case of 1.5 km optical fiber length. Simulation results with different numbers N_{tot} of iterations ($N_{\text{it2}} = 10000$ for the curves (3), (4) and $N_{\text{it2}} = 30000$ for the curve (5)).	47
Figure 2.11	Phase noise of the OEO in case of 1.5 km optical fiber length. Simulation results with different values of G_S parameter ($N_{\text{tot}} = 150000$).	47
Figure 2.12	Open-loop OEO model with COMSIS software.	49

Figure 3.1	NTC thermistor and its resistance as a function of temperature. (source: Thermodisc).....	52
Figure 3.2	Scheme of Wheatstone bridge with a thermistor.....	53
Figure 3.3	Thermistor temperature as a function of Wheatstone bridge output voltage.....	54
Figure 3.4	Simplified drawing of AD620 and three op amp design.....	54
Figure 3.5	Schematic of temperature measurement circuit.....	55
Figure 3.6	Top view and bottom view of temperature measurement board	56
Figure 3.7	Structure of a Peltier module.....	57
Figure 3.8	Mounting MZM with Peltier modules and thermistor.....	58
Figure 3.9	Temperature tuning schematic with OPA541	58
Figure 3.10	Temperature tuning card built around OPA541	59
Figure 3.11	Block diagram of a digital signal processing system.....	60
Figure 3.12	Block diagram and top view of eZdspF28335 development system.	61
Figure 3.13	LR-F28335DAQA daughtercard plugged on the top of the F28335 eZdsp board	62
Figure 3.14	Block diagram of process with a feedback controller.....	65
Figure 3.15	Non-interacting and interacting form of the PID algorithm.....	65
Figure 3.16	Matlab/Simulink model for temperature control.....	68
Figure 3.17	Block diagram of Matlab/Simulink, CCS and DSP kit.	68
Figure 3.18	Software development and connections to DSP and other devices.....	69
Figure 3.19	MZM temperature control system around DSP kit.....	69
Figure 3.20	EOM temperature evolution with different currents applied to the Peltier modules.....	70
Figure 3.21	Compact view of temperature control software.....	71
Figure 3.22	Full view of temperature control software.....	71
Figure 3.23	Changing temperature from 20 °C to 25 °C.....	72
Figure 3.24	Structure for estimating the temperature impact on the average optical output power of the EOM	73
Figure 3.25	Evolutions of photodetector output DC voltage at different working conditions.....	73
Figure 3.26	Photodetector output DC voltage evolution under temperature changes	74
Figure 3.27	Photodetector DC voltage and 0.5 Hz triangle signal represented in Igor	77
Figure 3.28	Transfer function: oscilloscope data and fitting curve	78
Figure 3.29	OEO oscillation loss phenomenon due to EOM temperature change.....	81
Figure 3.30	OEO oscillation data acquisition program in Agilent VEE Pro 9.3.....	83
Figure 3.31	Drift of the oscillation frequency and temperature changes versus time.....	84
Figure 3.32	Drift of the oscillation frequency and opposite temperature changes versus time.....	85

Figure 3.33	Oscillation frequency as a function of the opposite temperature and the fitting curve determining a modeling of the frequency drift behavior	85
Figure 3.34	Fluctuations of the oscillation frequency compared to the modeling of Eq. (3.23) as a function of time.....	86
Figure 4.1	Simulation program for determining the MZM behavior $V_{b0} = 3 V$	90
Figure 4.2	Modulated signal and its spectral when $V_{b0} = 2 V$	90
Figure 4.3	Modulated signal and its spectral when $V_{b0} = 1 V$	91
Figure 4.4	Modulated signal and its spectral when $V_{b0} = 0 V$	91
Figure 4.5	Block diagram of Non-Linear Indicator evaluation	93
Figure 4.6	Bias control scheme in DSP	94
Figure 4.7	Matlab Simulink model for controlling the EOM bias point.	95
Figure 4.8	Frequency response of the band-pass filter	96
Figure 4.9	Block diagram of EOM bias control with DSP and an external photodetector	97
Figure 4.10	Long term evolution of the NLI caused by the EOM transfer function drift.....	97
Figure 4.11	EOM bias control with its external photodetector	98
Figure 4.12	Evolution of the NLI during the control process.....	99
Figure 4.13	Evolution of the EOM bias voltage during the control process.....	99
Figure 4.14	A Photline modulator MX-LN-10. The internal monitoring photodiode connected at pins 3 and 4.	100
Figure 4.15	Schematic of electronic circuit for converting Photline MX-LN-10 modulator's internal photodiode output current to a DC voltage signal.....	101
Figure 4.16	Schematic of electronics circuit for filtering the DC component and amplifying the AC component.....	102
Figure 4.17	EOM bias control by using internal photodetector	103
Figure 4.18	EOM bias control by using internal photodetector for a duration of 23.13 hours	103
Figure 4.19	A EOM bias control by using internal photodetector for a duration of 23.13 hours: a zoomed-in view.....	104
Figure 4.20	Simulink model for EOM bias and temperature control.....	105
Figure 4.21	GUI software operating on PC site for controlling MZM bias and temperature.....	106
Figure 4.22	Schematic of DC voltage amplifier circuit by using operational amplifier TL082. This circuit also filters the AC component of V_{1B}	107
Figure 4.23	EOM transfer function program interface.....	108
Figure 4.24	EOM transfer function with one scanning period view	109
Figure 4.25	EOM transfer function represented in Igor	110
Figure 4.26	EOM transfer functions at different laser power levels.	110
Figure 4.27	Simulink model for EOM bias control based on photodetector output DC	

	voltage. The control voltage is sent to EOM via DAC1_Output, and a copy sent to oscilloscope via DAC3_Output for testing purpose.....	111
Figure 4.28	The graphical user interface of EOM bias control based on average optical output power and temperature control.	111
Figure 4.29	Evolutions of voltage output with and without optical power based control.....	112
Figure 4.30	Schematic of bias input card with AC and DC outputs.	113
Figure 4.31	Photo of bias input card used with internal PD of EOM. It converts PD's current to AC and DC voltages	113
Figure 4.32	The bias input and temperature measurement cards are mounted with other connections on the same plate.....	114
Figure 4.33	AC/DC and temperature measurement cards mounted in the box with the EOM.....	115
Figure 4.34	DSP kit with all connections.....	115
Figure 4.35	Matlab/Simulink model of 4 functions: dither-based bias control, optical output power-based control, temperature control for the EOM and temperature measurement for optical fiber loop.	116
Figure 4.36	The integrated graphical user interface program for controlling EOM bias point (dither-based combined with optical output power-based), controlling EOM temperature and monitoring optical fiber temperature.	117
Figure 5.1	OEO with an optical fiber-to-fiber coupling system	121
Figure 5.2	Relation between the variation of the oscillation frequency and the optical length at 8.004 GHz [11]	121
Figure 5.3	Optical fiber-to-fiber coupling system	123
Figure 5.4	Refractive index measurement using an OEO with an optical fiber-to-fiber coupling system.....	123
Figure 5.5	2 mm and 10 mm quartz cuvettes used for measurements	124
Figure 5.6	Optical fiber-to-fiber coupler and the cuvette	124
Figure 5.7	FSR of 504 m fiber OEO with an empty cuvette placed in the fiber-to-fiber coupling system.....	127
Figure 5.8	2 mm cuvette and its supporting adapter placed the optical fiber-to-fiber coupling system.....	128
Figure 5.9	10 mm cuvette and its supporting adapter placed the optical fiber-to-fiber coupling system.....	129
Figure 5.10	Refractive index measurement with an OEO and a generator.....	131
Figure 5.11	Real-time and long-term refractive index measurement with two identical OEOs	133
Figure 5.12	Two-OEO-based configuration for real-time and long-term refractive index measurement	134
Figure 6.1	System for monitoring and modeling the frequency drift of the OEO. A VNA	

	loop is inserted in order to measure the phase of S_{21} parameter leading to the knowledge of the propagation time across the modulator and the fiber loop.	138
Figure 6.2	Experiment for monitoring and modeling the frequency drift of the OEO (PC, VNA, PSA, DSP and EOM).....	139
Figure 6.3	Experiment for monitoring and modeling the frequency drift of the OEO (VNA, PSA, DSP and OEO).....	139
Figure 6.4	Experiment for monitoring and modeling the frequency drift of the OEO (DSP kit, control cards and OEO elements).....	140
Figure 6.5	Behavior of the homemade filter associated to the amplifier. The bandwidth is equal to 108 MHz. The quality factor is approximately equal to 20.....	142
Figure 6.6	Modulus of S_{21} parameter in the VNA loop, showing the improvement in the quality of measurement thanks to the amplifiers placed in the loop.	143
Figure 6.7	S_{21} phase measurement improvement by increasing the amplification in the VNA loop. On top is the case of the filter alone, then with only the homemade amplifier, the Photline one and finally in the bottom with the two amplifiers.....	143
Figure 6.8	Data acquisition program with Agilent VEE Pro 9.3 for recording OEO oscillation frequency and VNA phase shift.....	145
Figure 6.9	Drift of the oscillation frequency and temperature changes versus time	146
Figure 6.10	Drift of the oscillation frequency and opposite temperature changes versus time	146
Figure 6.11	Oscillation frequency as a function of the opposite temperature and the fitting curve determining a modeling of the frequency drift behavior	147
Figure 6.12	Fluctuations of the oscillation frequency compared to the modeling expressed by Eq. (6.3), as a function of time	147
Figure 6.13	Drift of the OEO oscillation frequency and S_{21} phase parameter versus time.	148
Figure 6.14	Oscillation frequency of the OEO, as a function of the S_{21} phase.....	148
Figure 6.15	Fluctuations of the OEO oscillation frequency with respect to the modeled frequency, calculated from the measured S_{21} phase, as a function of time	149
Figure 6.16	Introduction of a sending part in the fiber loop for detecting a refractive index change (a). Another possibility is to detect a small distance modification obtained by moving the lens L2 (b).....	150
Figure 6.17	Refractive index variation determination without modeling frequency drift generated by fiber loop.	155
Figure 6.18	Refractive index variation determination with modeling frequency drift generated by fiber loop.	156
Figure 6.19	Interface of new software for all controls and long-term measurement	158

Introduction

The electronic systems are developed for all aspects of modern life and become essential things to human being. In these systems, oscillators are devices designed for generating signal at a specific frequency. The basic oscillators are electronic oscillators which generate signals with frequencies up to some tens of GHz by multiplying low frequency. Traditional electronic oscillator can satisfy the phase noise criteria for low frequency applications. However, when working with higher frequencies, because of basing on multiplication, the electronic oscillator creates more unwanted noise. In some applications such as Doppler radars, satellite communication, metrology or sensor which operate at ultra-high frequencies, high performance oscillators are really required. One potential candidate has ability to meet this requirement is the optoelectronic oscillator (OEO).

Chapter 1 briefly presents about the OEO which was first demonstrated by X. S. Yao and L. Maleki in 1994 [1], in 1995 [2] and in 1996 [3], [4]. The system was initially developed for next generation radar [5], [6] to replace microwave generator. Then new applications appear for time and frequency, telecommunication and navigation technology [7], [8]. This new microwave oscillator showed the ability to synthesize directly the signal with a very low phase noise. This advantage mostly comes from the use of a low loss optical fiber loop to make a very high Q factor cavity. Theoretically, the phase noise of the OEO does not depend on the frequency and it is only limited by the capability of available commercial RF and optical components when operating at high frequencies. Then we describe the Electrooptic Modulator (EOM), a key component in an OEO system. We analyze the drift phenomena of the Mach-Zehnder Modulator (MZM) which is caused by several factors.

Chapter 2 describes theoretical analysis of different noise sources in the OEO. Then we present simulation study for phase noise of a single loop OEO based on different models and compare with experimental results. OEO is a complex system in which the resonator quality factor is not the only parameter to optimize in order

to get a good phase noise performance. The OEO includes both optical and electronic elements by which many noise conversions occurred during the operation. These noises have contributions to the phase noise of the OEO and should be analyzed carefully. Yao-Maleki proposed the first model to analyze the time-averaged noise in relation with frequency offset from the carrier frequency, loop delay and oscillation power [4]. The limitation of this model is that it takes into account only white noise and it assumes the signal at any point in the OEO is in steady state. To generalize model of Yao-Maleki, Levy *et al.* proposed new method that takes into account all physical effects in Yao-Maleki model as well as other necessary physical effects [9]. There are several software packages which can be used to simulate an OEO system: ADS, COMSIS, Matlab. All these software packages can characterize individual components. However, only Matlab has full ability to simulate phase noise of a closed-loop OEO.

In Chapter 3, we analyze the impacts of temperature on the OEO behavior. The temperature affects not only the EOM transfer function but also the OEO oscillation frequency. To monitor at the same time several characteristics of the different elements of the OEO, we decided to work with Digital Signal Processing technique which has ability to handle multiple tasks with multiple inputs and outputs. Temperature belongs to extrinsic category and it should be the first factor to be monitored. We implemented two experiments to analyze the impact of temperature on the drift phenomena of the EOM. By changing the temperature of the EOM, we found that when the temperature changes, the average optical output power of the EOM also varies immediately. When the EOM is thermally stabilized, the drift of the EOM is significantly reduced. These results show that the EOM should be thermally stabilized during its operating duration. We also present method to determine the transfer function and demonstrate the drift effect under specific temperatures.

By designing temperature measurement and temperature tuning cards separately, we can monitor the temperature at different elements of the OEO and control element we want. We use both cards to control the temperature for the EOM and analyze its drift phenomena under different conditions. Both cards are connected to a DSP kit and control process is handled by a program developed and loaded into the DSP memory. The algorithm for temperature control is Proportional-Integral-Derivative (PID). Experimental results indicate logically that with thermal stabilization, the

EOM has less drift phenomena than in the case without thermal stabilization. The influence of EOM temperature variation on the OEO oscillation power is also studied and the experimental result shows that the OEO oscillation could be disappeared if the EOM temperature is varied big enough. In another experiment, by monitoring temperatures of EOM and fiber loop at the same time as measuring the oscillation frequency, we found that the oscillation frequency is also affected by the temperature of the fiber loop.

From the results in Chapter 3, we know that thermally controlling is not enough to totally avoid the EOM drift phenomena. Chapter 4 presents further studies in stabilizing the behavior of the EOM by using DSP technique. Firstly, we present the technique based on a dither signal at low frequency which is applied into DC electrode of the EOM. The second harmonic of this signal is detected by an appropriate digital filter. By evaluating this second harmonic, we can determine the drift level of the EOM transfer function. A digital PID controller one more time is used to control the EOM working at the best linear position on its transfer function.

In the first configuration, an optical coupler and an external photodetector is used to provide signal to the DSP kit. The EOM drift is well controlled not only at its negative slope but also at positive slope. In our case, the modulator from Photline has an internal photodiode and we take this advantage to reduce the size of the system. We design an electronic circuit to separate the internal photodiode output current into AC and DC components then amplify them to fit input voltage range of the DSP kit. With AC signal, we can apply the same technique used for the case of using external photodetector. With DC component, we develop another method to control the EOM by keeping its output power at an optimized value. Each bias control method has its own benefits and drawbacks. By combining both methods, we have a more powerful control method. Finally, we have successfully integrated both bias control methods, EOM temperature control and fiber loop temperature monitoring into one software suite.

With the control system built around DSP kit presented in Chapter 3 and Chapter 4, the OEO now can be operated stably for a long duration. Chapter 5 presents the applications of the OEO in refractive index measurement which is

basically based on the close relation between the global loop delay and the oscillation frequency. The long fiber loop length acts as a high Q cavity where the light energy is stored and delayed before being fed back to RF electrode of the modulator to create a closed loop. We insert into the optical fiber path a fiber-to-fiber coupling system with a transparent cuvette containing the liquid to be analyzed. By measuring the variation of the oscillation frequency before and after putting the liquid, we can determine the refractive index of the liquid. The results for individual measurements are suitable with values already published [10]. We also propose a configuration enabling to measure in long-term by using an external frequency source and a mixer.

In Chapter 6, we focus on how to improve the long-term refractive index measurement with a vector network analyzer (VNA). In individual measurements, the effect of environment change can be neglected. However, in long-term measurement, the surrounding variation creates bigger impact on sensitive elements of the OEO. To separate the impact of temperature change on the fiber loop from the variation created by sensing part, we have developed a technique to monitor the propagation time variation of the light inside the fiber loop. The principle of this technique relies on the relation between propagation time and the phase of the signal travels through this fiber loop. In addition to improving long-term measurement, this technique can also be applied to improve the individual measurement by means of calibrating the free spectral range parameter.

This work is a part of a general study of the optoelectronic oscillator and its applications initiated in 2006 by a first doctoral study following a master internship. The first work was conducted in the SATIE laboratory as projects of the d'Alembert Institute. The first thesis [11] has underlined many possible applications of the oscillator. The second thesis was concerning the electrooptic modulator and the compensation of the drift with PSoC microcontrollers [12]. Then the third thesis was initiated thoughts about the replacement of the fiber loop by a microresonator. In 2012, the group working on the OEO has joined the LPQM laboratory and belongs to the team "Components and technologies for the photonics". The aim of the work is now to develop applications in the field of sensing systems based on OEO.

Chapter 1

Optoelectronic oscillator

1.1 Introduction

RF and microwave oscillators are universally found in all modern radar and wireless communications systems to provide signal sources for frequency conversion and carrier generation [13]. At low frequencies, basic transistor oscillator is usually used with crystal resonators to enhance frequency stability and low noise characteristic. To create higher fundamental frequencies, diodes or transistors biased to a negative resistance operating point can be used with cavity, transmission line, or dielectric resonators. The main principle of an oscillator is converting a DC power to an AC signal by a nonlinear circuit. To minimize unwanted harmonics and noise sidebands, the outputs of RF oscillator are often sinusoidal signals.

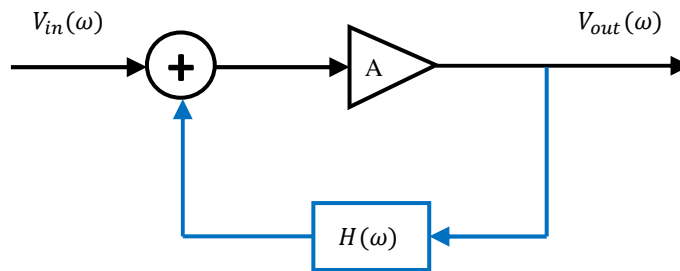


Figure 1.1 Block diagram of a sinusoidal oscillator using an amplifier with a frequency- dependent feedback path [13].

The basic conceptual operation of a sinusoidal oscillator can be described with the linear feedback circuit shown in Figure 1.1. An amplifier with voltage gain A has an output voltage V_{out} . This voltage passes through a feedback network with a frequency dependent transfer function $H(w)$, and is added to the input V_{in} of the circuit. Thus the output voltage can be expressed as

$$V_{out}(w) = AV_{in}(w) + H(w)AV_{out}(w) \quad (1.1)$$

From Eq. (1.1), it is easy to represent the output voltage as a function of the input voltage:

$$V_{out}(w) = \frac{A}{1 - AH(w)}V_{in}(w) \quad (1.2)$$

The oscillation will appear if the loop gain $AH(w)$ equal to unity in absolute magnitude or $1 - AH(w)$ becomes zero at a particular frequency, it is possible to achieve a non-zero output voltage for a zero input voltage [13]. The condition for an active feedback to produce self-sustained oscillations with sinusoidal output signal is known as the Barkhausen criterion and Nyquist stability criterion. It is important to note that the Barkhausen criterion is only necessary but not sufficient criterion for steady-state oscillation of an electronic circuit [14]. Oscillation startup condition is recently reinvestigated in several publications [15]–[19]. To our knowledge, the latest publication one more time reconfirms that the Barkhausen criterion is only necessary but not sufficient oscillation condition [20]. Furthermore, study [20] also pointed out that the Nyquist stability criterion, in its general form, only indicates instability but cannot provide any information if this instability will cause oscillations or not.

Moving to higher frequencies in microwave bands, it is more difficult to create fundamental frequency oscillators that can satisfy requirements in power, stability and noise. A popular approach is to use frequency multipliers that can be classified in three categories: reactive diode multipliers, resistive diode multipliers and transistor multipliers [13]. However, the biggest disadvantage of frequency multipliers is that noise levels are increased by the multiplication factor because the phase noise fluctuations is multiplied in the same way that frequency is multiplied. The increase in noise level is given by $20 \log n$, where n is the multiplication factor. From these difficulties and limitations, new types of microwave oscillator with better phase noise performance were expected and studied.

1.2 Optoelectronic oscillator

The first work related to the OEO was conducted by Neyer & Voges [21] when they studied the optoelectronic feedback circuits in 1982. Twelve years later, Yao and Maleki proposed the first optoelectronic oscillator (OEO) as an electro-optical oscillator capable of generating high stability optical signals at frequencies up to 70

GHz [1]. Then, in 1995, Yao – Maleki introduced this oscillator as light-induced microwave oscillator (LIMO) [2]. The two main descriptions were published in 1996 [3], [4]. The basic structure of an OEO is presented in Figure 1.2.

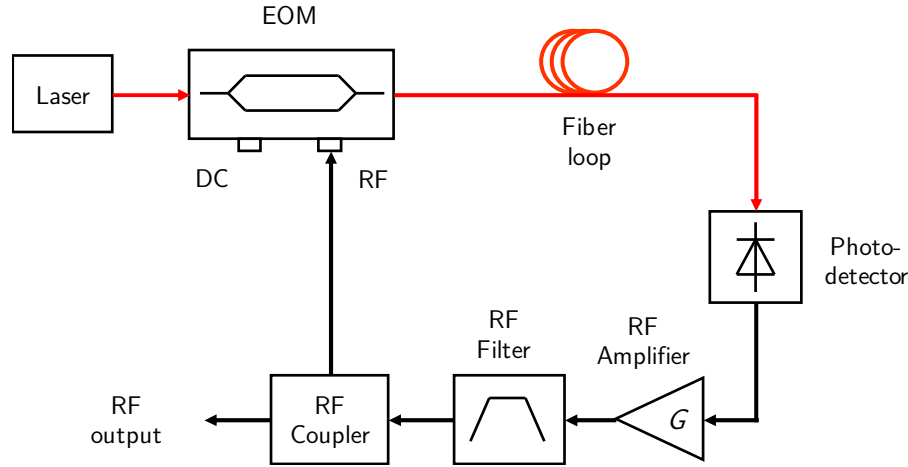


Figure 1.2 Basic structure of single loop OEO

As indicated in the Figure 1.2, the OEO consists of both optical and electronic components. The continuous light from a laser source is introduced into an electrooptic modulator (EOM). After travelling through the optical fiber loop, it is converted to radio frequency (RF) signal by a photodetector. This RF signal is then amplified, filtered and divided into two ways by a directional coupler: one way is fed back to RF electrode of the EOM to make a closed-loop oscillator and the other way is an RF output which can be used for a spectrum analyzer. The OEO can have an optical output which can be extracted by using an optical coupler before the photodetector.

The advantage of the OEO is that it has very low phase noise. The phase noise at 10 kHz offset frequency in Yao's single loop experiment was less than -130 dBc/Hz measured at a frequency of 800 MHz and a loop delay of $1.25 \mu s$ [4]. It was enhanced to -140 dBc/Hz by using a dual loop OEO working at 10 GHz [22]. This phase noise is 44 dB lower the phase noise -96 dBc/Hz of a high-performance HP frequency synthesizer HP 8617B. In the last two decades, several new structures of the OEO have been proposed with the target of improving the phase noise characteristics: -150 dBc/Hz by using a coupled OEO working at 9.4 GHz [23] and -160 dBc/Hz after optimization for an OEO working at 10 GHz [24].

1.2.1 Oscillation loss phenomenon

Although having a superior phase noise performance, the OEO still has some drawbacks that need to be improved. These downsides of a single loop OEO were observed in our laboratory. We found that, under specific circumstance, the OEO oscillation can be lost. Figure 1.3 illustrates the oscillation loss happened at the time of 7445 s.

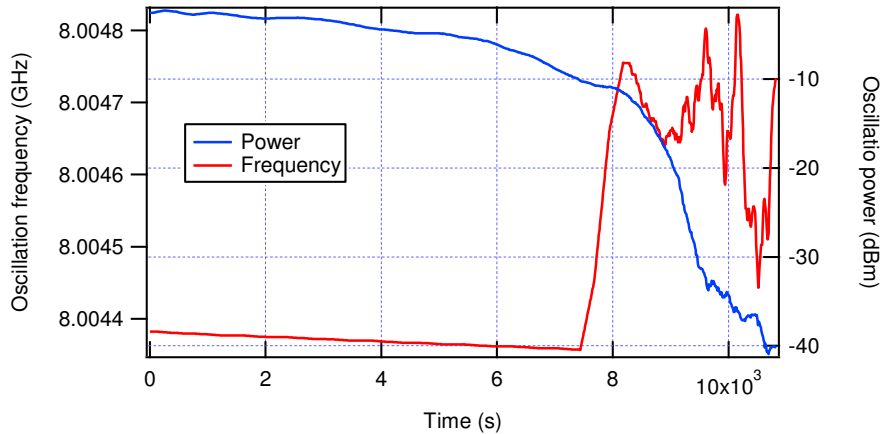


Figure 1.3 Oscillation loss happens at 7445 s.

1.2.2 Oscillation frequency drift

Another issue we faced during our observation was the oscillation frequency drift. The oscillation frequency does not remain unchanged at its original value, otherwise it drifts slowly. The data shown in Figure 1.4 is extracted from the data used in Figure 1.3 but is zoomed in for clearer visualization.

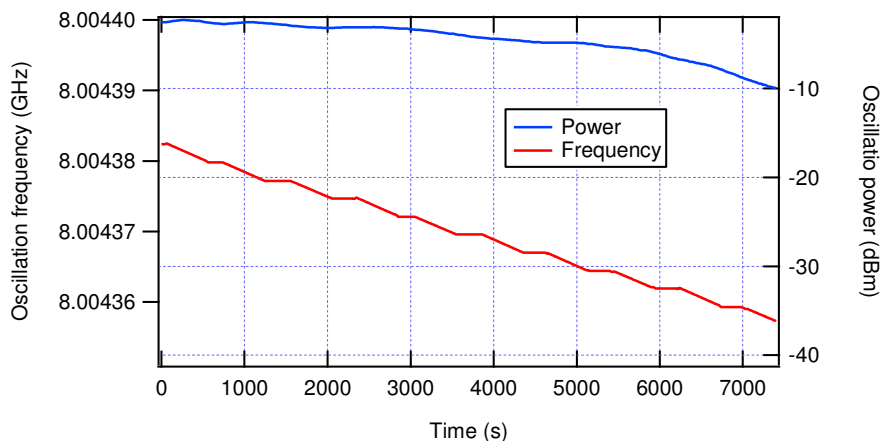


Figure 1.4 Oscillation frequency drift during 7400 s.

In order to apply this OEO to sensing application as our target, we need to find the

reason and the method to counteract these limitations. After analyzing all components of the OEO, we concentrate on the EOM and two high Q elements including the optical fiber and the RF filter.

Firstly, in the next section, we will analyze characteristics of the EOM.

1.3 Electrooptic modulator

1.3.1 Optical modulation

In signal transmission domain, a carrier signal is modulated by a modulating signal that contains information to be transmitted. The frequency of carrier signal is higher than that of modulating signal in order to have a high data carrying capability. There are many different modulation schemes: amplitude, frequency, phase and polarization. In optical telecommunication, there are two modulation methods:

1.3.1.1 Direct modulation

The information signal is used to modulate the current which will be supplied to a laser diode. The modulating signal is superposed on the polarization current and its frequency can reach several GHz [25]. This method is used to modulate the current supplied to the laser diode.

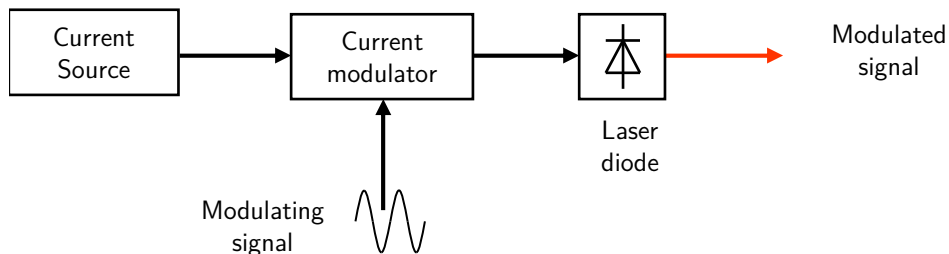


Figure 1.5 Block diagram of direct modulation

In cases of using high modulation frequencies, the direct modulation is rarely used because of disadvantages in following aspects: high Relative Intensity Noise (RIN), high signal distortions and large frequency chirp.

1.3.1.2 External modulation

When modulating frequency is higher than 5 GHz, an external modulation must be used [26]. The laser is biased at a constant current to provide continuous wave optical beam (CW) which is then modulated by an optical modulator. The scheme of external

modulation is illustrated in Figure 1.6

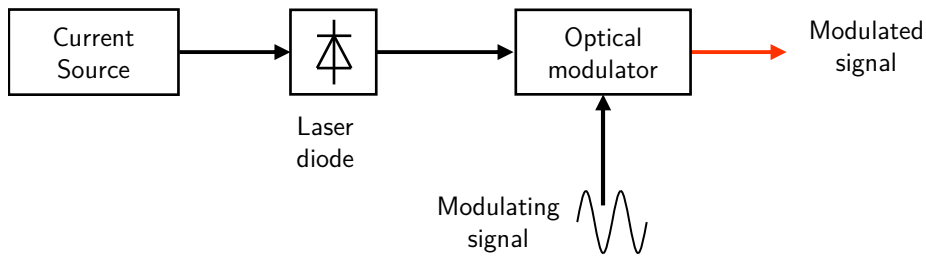


Figure 1.6 Block diagram of external modulation

1.3.1.3 Pockels effect

Electro-optic effect results from a change in the optical properties of a material in response to an electric field that varies slowly compared with the frequency of light. The term encompasses a number of distinct phenomena, which can be subdivided into:

Pockels effect (or linear electro-optic effect): change in the refractive index linearly proportional to the electric field. Only certain crystalline solids show the Pockels effect, as it requires lack of inversion symmetry.

Kerr effect (or quadratic electro-optic effect, QEO effect): change in the refractive index proportional to the square of the electric field. All materials display the Kerr effect, with varying magnitudes, but it is generally much weaker than the Pockels effect.

Electro-optic modulators are usually built with electro-optic crystals exhibiting the Pockels effect. The transmitted beam is phase modulated with the electric signal applied to the crystal. Amplitude modulators can be built by putting the electro-optic crystal between two linear polarizers or in one path of a Mach–Zehnder interferometer. Additionally, Amplitude modulators can be constructed by deflecting the beam into and out of a small aperture such as a fiber. This design can be low loss (<3 dB) and polarization independent depending on the crystal configuration.

1.3.1.4 Intensity modulation

In optical communication networks, the intensity modulation is the most widely used. Several types of external optical intensity modulators have been developed over the past several decades for optical fiber communication applications [27]. These include Lithium Niobate (LiNbO modulators, semiconductor electroabsorption modulators (EAMs), semiconductor Mach–Zehnder modulators (MZMs), and polymer

modulators. The most popular intensity modulator is MZM.

1.3.2 Mach-Zehnder Modulator (MZM)

The popular material used for fabricating the MZM is Lithium niobate (LiNbO_3). This is a ferroelectric material with excellent electro-optic, nonlinear, and piezoelectric properties. The basic structure of a MZM is depicted in the Figure 1.7:

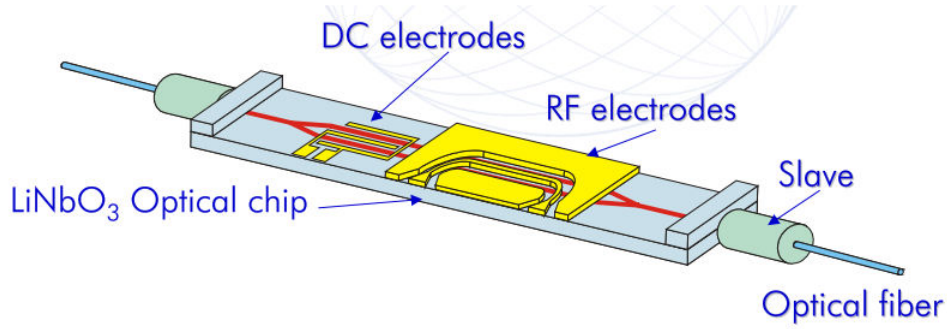


Figure 1.7 A structure of an electrooptic modulator (source: Photline)

The input light is separated equally into two arms and then these two signals are combined again at the output. In one arm, a voltage is applied in order to modify the refractive index of this arm that leads to change the phase of the light in this arm. Depending on the electronic field, the phase shift $\Delta\varphi$ between the two signals will make the intensity of the output signal to be increased or decreased.

$$I = \frac{I_0}{2} [1 + \cos(\Delta\varphi)] \quad (1.3)$$

where I_0 is the input light intensity

1.3.3 Drift phenomenon of EOM

In optical telecommunication, the modulator is electrooptic modulator (EOM). In typical application, the DC voltage is applied into one arm while the modulating RF signal is applied in the other arm (see Figure 1.7). In some cases there is only one electrode, DC and RF signals must be combined before to be applied to the device.

The transfer function of the EOM is a mathematical representation of the relation between the input and output power. It is expressed by the Eq. (1.4) :

$$P_{out}(t) = \frac{1}{2} \alpha P_{in} \left[1 + \eta \cos \left(\frac{\pi}{V_{\pi}} V_a(t) + \phi(t) \right) \right] \quad (1.4)$$

where P_{in} is the input power, P_{out} is the output power, α is the insertion loss of the modulator, η is the visibility factor [28] which leads to the extinction ratio $(1 + \eta)/(1 - \eta)$, $V_a(t)$ is the voltage applied to the modulator. This voltage contains the information that will be used to modulate the input light. In Eq. (1.4), $\phi(t)$ is a time dependent phase shift taking into account other physical effects than the modulating process. The quantity v_π is called half-wave voltage, corresponding to the applied voltage leading to a phase shift change equal to π .

A good transmission for analog or digital application is obtained in case of a modulator working in a symmetric way, leading to a good extinction ratio. The EOM should be biased at the optimum operating point to keep the MZM working at the best linear position on the transfer function curve. The best behavior of the modulator is obtained at its half-transparency bias points. In this case, the symmetry of the transfer function with respect to the average value is optimal. These points are called quadrature bias points.

However, the initial optimal state could not be kept for a long duration and it is called drift phenomena. The reason comes from the fact that electro-optic modulators are not perfectly stable with time and the optimum bias point changes during the operating time. In fact we consider now that the phase shift $\phi(t)$ in Eq. (1.4) is a function of time leading to the transfer function drift. When $\phi(t)$ changes, the transfer function of the EOM is shifted accordingly, to the right or to the left, during the operating time. The drift of the EOM transfer function can be explained by different effects such as changes of working temperature, optical coupling efficiency and photorefractive effects [29], [30]–[33]. In [29], Jean Paul Salvestrini *et al.* figured out that the drift of an lithium niobate (LN) Mach-Zehnder (MZ) modulator occurs due to different sources as indicated in Figure 1.8. The two main source categories are intrinsic and extrinsic origins.

Extrinsic sources of drift are due to changes of environmental conditions such as temperature, humidity or stress. Under some conditions, such as with optical sources of shorter wavelength and high power, photo-induced processes may also contribute to bias point drift.

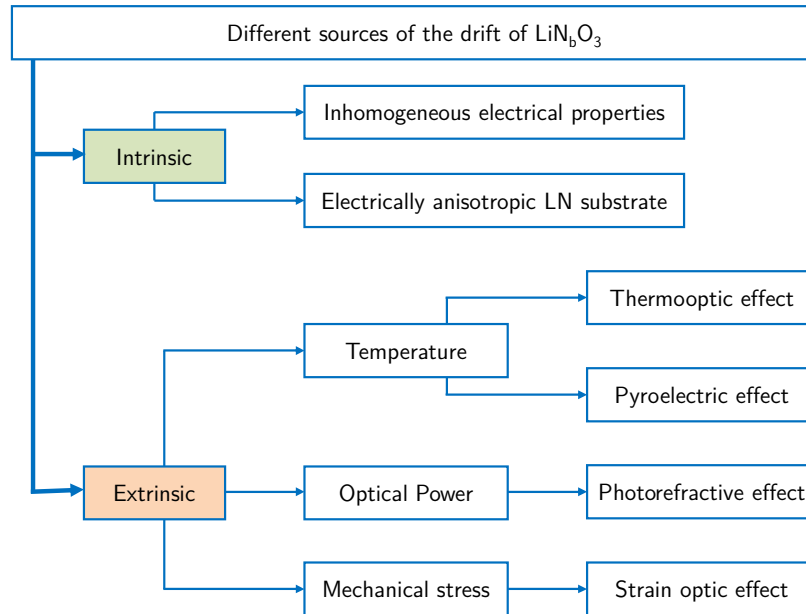


Figure 1.8 Classification of the different sources of the drift phenomenon of LiNb_3O_3 modulator.

If the bias voltage is constant and if the transfer function is horizontally shifted then the bias point is no more in the optimal quadrature position. Modulators made of lithium niobate material are much more stable than electro-optic polymer based devices [34], [35]. Nevertheless a drift can be observed even at a medium term time scale.

1.4 Conclusions and motivations

Our main motivation is to apply the OEO into the domain of sensing applications. In this thesis, we develop software and hardware to improve the accuracy of the refractive measurement of chemical solutions in short-term as well as in long-term duration. In order to apply the OEO for above motivation, the following tasks need to be first completed:

- Enhance the stability of the OEO in terms of operation time and oscillation power.
- Optimize the OEO by analyzing and simulating the phase noise of the OEO.
- Analyze the impacts of temperature on behavior of the OEO: Control temperature for the EOM and monitoring the temperature of fiber loop and RF filter.

- Controlling the transfer function drift of the EOM.
- Integrate all monitoring and controlling functions by using DSP technique.
- Short-term refractive index measurement with an OEO.
- Improve long-term refractive index measurement.

Chapter 2

Optoelectronic oscillator simulation

Since the time the OEO was first introduced as a low phase noise RF source in 1996 [4], many studies have been carried out to improve the phase noise of the OEO. In this chapter, we will present several noise sources in the OEO and phase noise simulation models.

2.1 Noise sources in OEO

There are two noise types: external noise and internal noise.

- External noise includes following sources: noise from transmission channels, coupling spurious signal close to the receiver, from power sources and noise from mechanical vibration.
- Internal noise includes following sources: shot noise, thermal noise and flicker noise $1/f$ noise.

2.1.1 Laser noise

The noise of laser exists in terms of the fluctuations in its optical power level and is often described by the Relative Intensity Noise intensity noise (RIN). For the case of Distributed Feedback Laser (DFB), fluctuations mainly stem from intrinsic optical phase and frequency fluctuations caused by spontaneous emission [36]. Low frequency laser RIN has only a minor influence on phase noise of the OEO [37].

Relative intensity noise can be generated from cavity vibration, fluctuations in the laser gain medium or simply from transferred intensity noise from a pump source. Since intensity noise typically is proportional to the intensity, the relative intensity noise is typically independent of laser power. Hence, when the signal to noise ratio (SNR) is limited by RIN, it does not depend on laser power. In contrast, when SNR is

limited by shot noise, it improves with increasing laser power. RIN typically peaks at the relaxation oscillation frequency of the laser then falls off at higher frequencies until it converges to the shot noise level. The roll off frequency sets what is specified as the RIN bandwidth. RIN is sometimes referred to as a kind of 1/f noise otherwise known as pink noise.

Relative intensity noise is measured by sampling the output current of a photodetector over time and transforming this data set into frequency with a fast Fourier transform. Alternatively, it can be measured by analyzing the spectrum of a photodetector signal using an electrical spectrum analyzer [38]. The photocurrent of a detector is proportional to the received optical power. Noise observed in the electrical domain is proportional to electrical current squared and hence to optical power squared. Therefore, RIN is usually presented as relative fluctuation in the square of the optical power in decibels per hertz over the RIN bandwidth and at one or several optical intensities. It may also be specified as a percentage, a value that represents the relative fluctuations per Hz multiplied by the RIN bandwidth.

RIN of laser is calculated by equation below [36], [39]:

$$RIN(f) = \frac{\langle \Delta P_{opt}^2 \rangle}{P_{opt}^2} \quad (2.1)$$

where the brackets $\langle \rangle$ denote time averaging.

Frequency noise of laser:

Laser frequency noise refers to random fluctuations of the instantaneous frequency of the laser. Laser frequency noise may be measured directly at the optical frequency, or by heterodyning to a reference laser [38], [40].

$$S_\varphi(f) = \frac{S_v(f)}{f^2} \quad (2.2)$$

where f is the noise frequency, $S_\varphi(f)$ is the phase noise of the laser and $S_v(f)$ is power spectral density of frequency noise.

2.1.2 Photodetector noise

Photodetector noise belong to the internal origin of noise, including shot noise, thermal noise, flicker noise (1/f) and dark current noise.

2.1.2.1.1 Shot noise

The normalized spectral density of the shot noise in terms of current is given by the equation below [39], [41]:

$$i_n^2(f) = 2q * I_{ph} \quad (2.3)$$

the unit is in A²/Hz, where I_{ph} is the photo current; $q = 1.6 \times 10^{-19}$ is the charge of an electron.

2.1.2.1.2 Thermal noise

When the Johnson noise is the result of random fluctuations, the current spectral density of thermal resistance noise of a photodetector can be expressed by equation below [39]:

$$i_{th}^2(f) = \frac{4kT}{R} \quad (2.4)$$

the unit is in A²/Hz. The voltage noise source is given by the Johnson – Nyquist formula [41]:

$$v_{N,R}(f) = \sqrt{4kTR} \quad (2.5)$$

the unit is in V/\sqrt{Hz} , where k is the Boltzmann constant: $k = 1.38 \cdot 10^{-23} \text{ J} \cdot \text{K}^{-1}$

T is the absolute temperature (in Kelvin);

R is the load resistance of the photodetector.

2.1.2.1.3 Flicker noise (1/f)

Because flicker noise is an elusive phenomenon and the analysis could not be based on an unified theory [42], [43]. While shot noise and thermal noise are white noise, flicker noise exists in another type of fundamental noise where the spectral density is not constant with frequency. Flicker noise dominates at low frequencies [39].

$$i_{1/f}^2(f) = K \frac{I_0^\beta}{f^\gamma} \quad (2.6)$$

where the unit is A²/Hz, $\gamma \approx 1$ and $\beta \approx 2$ depends on components and materials.

2.1.2.1.4 Dark current noise

Although in the case without illumination, the Photodetector has a current loss that derives from the presence of surface recombination and leakage paths in the material. This kind of current is unwanted and in fact, it is very small. The normalized spectral density of the dark current noise can be calculated by equation

below [39]:

$$i_{darkc}^2(f) = 2q \cdot I_{darkc} \quad (\text{in A}^2/\text{Hz}) \quad (2.7)$$

where I_{darkc} is the average value of the dark current.

2.1.3 Amplifier noise

Amplifier noise is also created by internal sources: thermal and shot noise. The amplifier is characterized by its noise factor F , as the ratio of the effective noise power in the load divided by the noise power in the load if the amplifier was noiseless. It can be expressed as:

$$F = \frac{SNR_{in}}{SNR_{out}} \quad (2.8)$$

F is usually expressed in dB and called noise figure [38]:

$$NF = 10 \times \log(F). \quad (2.9)$$

2.2 Phase noise

Phase noise presents the quality of a frequency source and it is the most important figure of merit of a microwave oscillator [44]. In a feedback oscillator, the phase fluctuations of the amplifier are directly converted into frequency fluctuations through the oscillator non-linearity. In a classical microwave oscillator, there are many factors leading to phase fluctuations. It includes the active element such as the RF amplifier, the flicker noise of the resonator. It also includes mechanical vibrations, the thermal fluctuation and electrical network contribution (50 Hz).

Let us consider a signal at the output of an oscillator, at frequency f_0 , with a constant amplitude and phase fluctuation $\varphi_n(t)$. It can be written as:

$$v(t) = V_0 \cdot \cos(2\pi f_0 t + \varphi_n(t)) \quad (2.10)$$

The quantity $S_\varphi(f)$ is introduced as the single side power spectrum density of phase fluctuations, $S_\varphi(f) = |\Phi_n(f)|^2$.

In 1978, P. Kartaschoff [45] defined phase noise is the ratio of the power in one sideband due to phase modulation by noise (for a 1 Hz bandwidth) to the total signal power (carrier plus sidebands):

$$\mathcal{L}(f) = \frac{\text{power density in one phase noise power modulation sideband, per Hz}}{\text{total signal power}} \quad (2.11)$$

In 1988, The IEEE standard 1139 [46] points out that the definition (2.11) breaks down when the mean squared phase deviation $\langle \varphi^2(t) \rangle = \int_f^\infty S_\varphi(f) df$ exceeds about 0.1 rad^2 or whenever there is a correlation between the power in the upper and lower sidebands. Phase noise is then designated as the standard measure of phase instability and is redefined as:

$$\mathcal{L}(f) = \frac{1}{2} S_\varphi(f) \quad (2.12)$$

The units of $\mathcal{L}(f)$ are dBc/Hz and it is practically calculated as $10 \log_{10} [\frac{1}{2} S_\varphi(f)]$ or it is equal to $10 \log_{10} [S_\varphi(f)] - 3 \text{ dB}$ [47]. The unit dBc/Hz stands for “dB below the carrier in a 1 Hz bandwidth”.

The 1999 revision of The IEEE standard 1139 [48] recommends phase noise as the standard measure for characterizing frequency and phase instabilities in the frequency domain and it was defined as one half of the double-sideband spectral density of phase fluctuations. Luckily, the equation was written the same as Eq. (2.12).

The new definition of IEEE reduces the difficulties in the use of phase noise $\mathcal{L}(f)$ when the small angle approximation is not valid. There are many factors affect to model the oscillator’s noise behavior. To simplify this model, D. B. Leeson has proposed a new model [49].

2.3 Experiment setup

According to the structure presented in Figure 1.2, we have set up a classical oscillator working at frequency of 8 GHz with following elements:

The laser source is a multiple quantum well laser diode FLD5F6CX from Fujitsu Company; its wavelength is 1535 nm and its FWHM is 0.1 nm. It is used in the OEO with an output power of 1.55 mW (or 1.9 dBm) in order to get the oscillation. The laser diode is stabilized for both its operating temperature at 25°C and its optical output power. The Mach-Zehnder intensity modulator is made of lithium-niobate with an RF bandwidth at -3 dB of 12 GHz and optical insertion losses of 3.5 dB (ref. MX-LN-10 from Photline Company [50]); the optical attenuation is about 4 dB.

It is associated at the input to a polarization controller FiberPro PC1100-15F/A

with 0.3 dB insertion loss. The fiber loop is made of SMF28 single mode fiber, all the connectors are FC/APC; in this experiment the fiber length is 1 km. The fiber loop is placed in a temperature controlled box. The detector is a 15 GHz PIN receiver associated to a preamplifier working up to 12.5 Gbps (ref. DAL-15-OI from DA-LightCom Company). We consider this system as the global photodetector.

The amplification section is composed by two amplifiers; the first one is a XKLA7585N2015-3MH from Seekon, with a bandwidth from 7.5 to 8.5 GHz, a measured gain of 22 dB at 8 GHz and a noise figure of 2 dB (it is a rather low noise amplifier); the second one is an AWB2018-23-22 from ALC Company with a bandwidth from 2 to 10 GHz a gain of 28 dB, and a noise figure of 5 dB. The cavity type RF filter BP8000-20/T-5TE01 from BL-Microwave with a center frequency of 8 GHz, a bandwidth of 20 MHz that correspond to a quality factor of 400. The datasheet of this filter is presented in Annex C.1. The filter is placed in the same thermal box as the fiber loop.

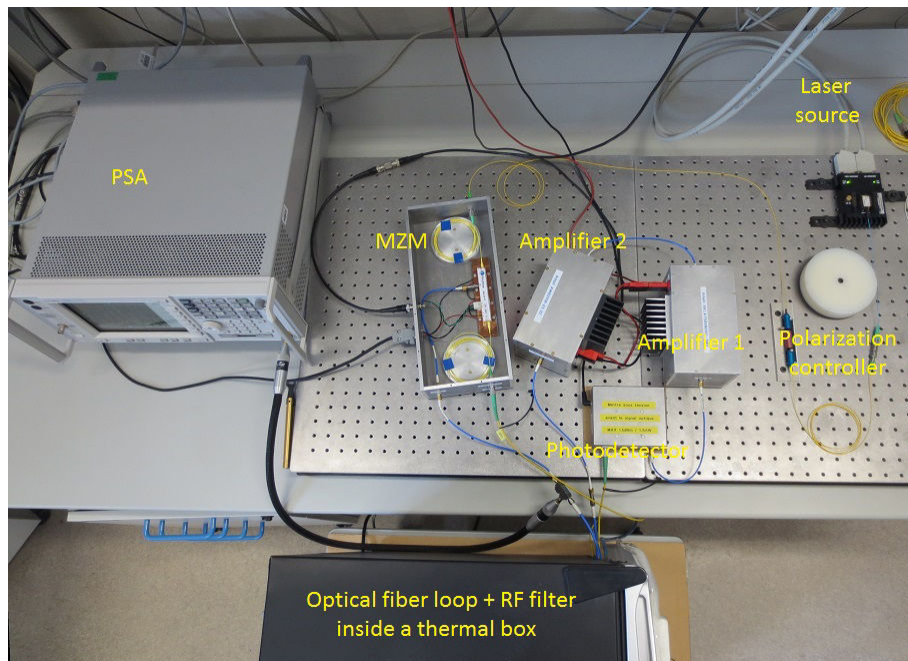


Figure 2.1 Experimental setup for phase noise measurement

To feedback the signal to the RF electrode of the MZM, we use a 10 dB coupler from ATM (C116-10, frequency range of 7.0 – 12.4 GHz) with the main output having an insertion loss of -3 dB. This coupler output has another output with insertion loss of -10 dB and is connected to a spectrum analyzer PSA-E4446A from Agilent Technologies. The Figure 2.1 presents photography of the experimental setup.

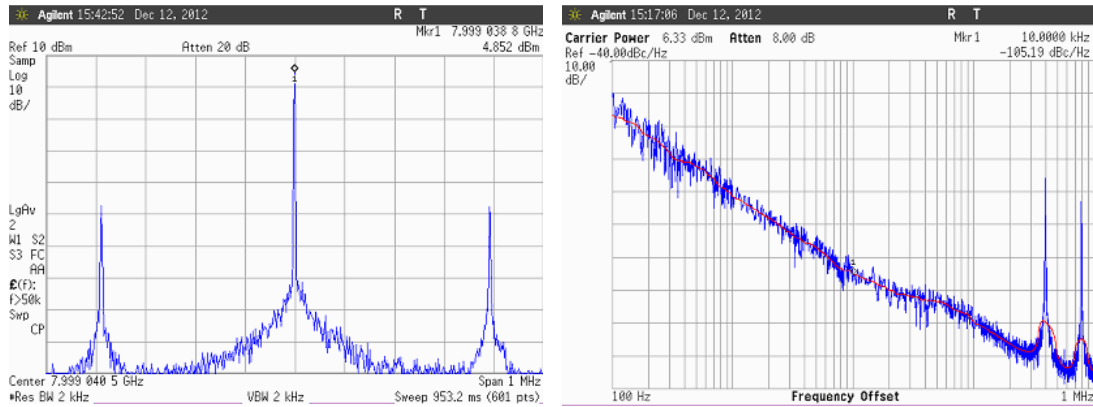


Figure 2.2 Spectrum and phase noise of 500 m OEO.

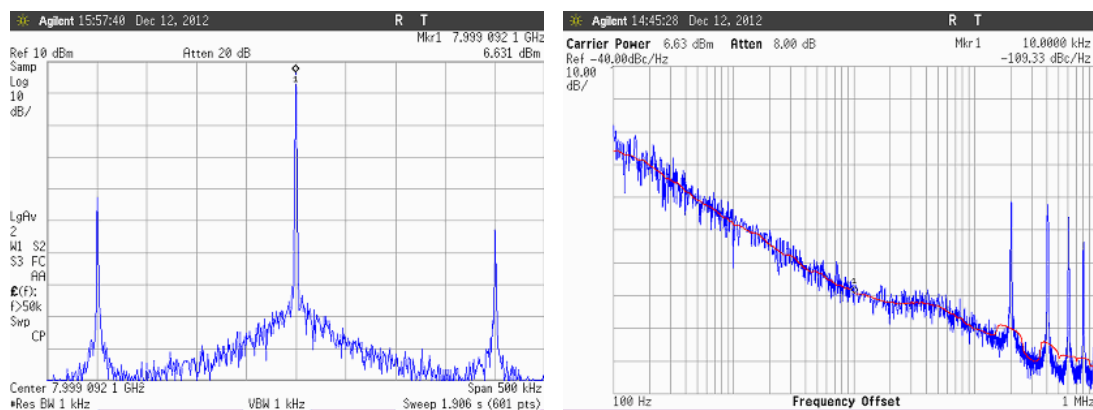


Figure 2.3 Spectrum and phase noise of 1000 m OEO

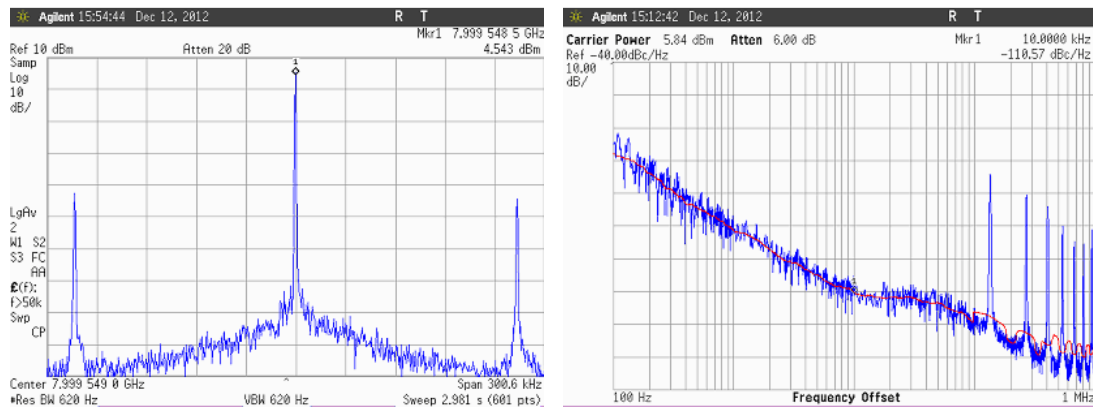


Figure 2.4 Spectrum and phase noise of 1500 m OEO

Both the fiber spools and the RF filter are sensitive to temperature, it is why we put them inside a thermal box with temperature stabilized around 22 – 23 °C . This thermal box is a thermoelectric wine cooler named “cave à vin thermoélectrique Climadiff CV48AD” which contains a small fan inside to evenly distribute the cool temperatures being created by the node throughout the interior of the box.

By using the spectrum analyzer PSA-E4446A, we measure spectrum and phase noise for three cases: 500 m, 1000 m and 1500 m. The results are presented as captured screens of the spectrum analyzer. The spectrum and phase noise measurements are presented in Figure 2.2, Figure 2.3 and Figure 2.4:

Free Spectral Range of the OEO is determined by:

$$FSR = \frac{c}{nL_g} \quad (2.13)$$

Optical fiber plays a role as an energy storage. An optical fiber length of $L = 1000$ m, popular refractive index $n = 1.5$ corresponds to a delay $T = 5 \mu\text{s}$ for keeping optical light stay inside the loop.

2.4 Yao – Maleki model

Theoretical analysis of the OEO has been made in Yao & Maleki's fundamental paper [4]. The output voltage of the amplifier is expressed as a function of the input voltage of the modulator (noted $v_{in}^{eom}(t)$):

$$v_{out}^{amp}(t) = V_A \left\{ 1 - \eta \sin \left[\pi \left(\frac{v_{in}^{eom}(t)}{V_\pi} + \frac{V_B}{V_\pi} \right) \right] \right\} \quad (2.14)$$

with:

$$V_A = G_A \times \frac{1}{2} \alpha P_0 \rho R_L \quad (2.15)$$

where α is the modulator insertion loss, P_0 is the input optical power, ρ is the photodetector responsivity, R_L is the photodetector output impedance, and G_A is the amplifier voltage gain; V_π is the modulator half-wave voltage, V_B is the DC bias voltage, and η is the visibility factor leading to the modulator extinction ratio $(1 + \eta)/(1 - \eta)$. The small-signal open-loop gain of the oscillator is:

$$G_S \equiv \left. \frac{dV_{out}}{dV_{in}} \right|_{V_{in}=0} = -\frac{\eta \pi V_A}{V_\pi} \cos \left(\frac{\pi V_B}{V_\pi} \right) \quad (2.16)$$

The input voltage of the modulator is considered as a sine function where ω_0 is the angular oscillation frequency:

$$v_{in}^{eom}(t) = V_0 \sin(\omega_0 t + \varphi) \quad (2.17)$$

The linearization of Eq. (2.14) is based on a development with Bessel functions. If the RF filter is able to eliminate all the harmonics of the oscillation frequency then we

get the linear expression based on the first order Bessel function J_1 of the first kind:

$$G(V_o) = G_s \frac{2V_\pi}{\pi V_0} J_1 \left(\frac{\pi V_0}{V_\pi} \right) \quad (2.18)$$

and so with the development in Taylor series of J_1 at order 2:

$$G(V_o) = G_s \left[1 - \frac{1}{2} \left(\frac{\pi V_0}{2V_\pi} \right)^2 + \frac{1}{12} \left(\frac{\pi V_0}{2V_\pi} \right)^4 \right] \quad (2.19)$$

The phase noise power density is given in [4] by:

$$S_{RF}(f') = \frac{\rho_N G_A^2 / P_{osc}}{1 + |H(f')G(V_0)|^2 - 2H(f')|G(V_0)|\cos(2\pi f' \tau_d)} \quad (2.20)$$

where f' is the offset frequency from the carrier, τ_f is the propagation time across the loop ($\tau_d = 5 \mu\text{s}$ for 1 km optical fiber length). $|H(f')|$ is the modulus of the filter transfer function considered here as a second order band-pass filter with a center frequency at 8 GHz, a quality factor of 400 and a bandwidth $\Delta f = 20$ MHz. G_A is the voltage gain in the loop ($G_A = 44$ dB), P_{osc} is the RF power at the modulator input ($P_{osc} = 13.6$ dBm) and ρ_N is the noise power spectral density at the output of the photodetector (the photodiode is associated to a first stage amplifier). $G(V_0) \approx 1$ and $|H(f')| \approx 1$ is a good approximation [4].

In order to compare the theoretical function and the experimental results we have decided here to align the theoretical model of Yao & Maleki and the experimental results at the 10 kHz offset frequency point. From the previous values and the experimental measurement of the phase noise -108.3 dBc/Hz at 10 kHz offset from the carrier, we obtain $\rho_N = 1.35 \cdot 10^{-18}$ or $\rho_N = -149$ dBm/Hz.

Figure 2.5 is a plot of the phase noise as a function of the frequency offset, with our experimental data and the theoretical curve from Yao & Maleki's model. The results obtained with Yao & Maleki's model agree actually very well with the results obtained from Rubiola's theoretical model [47].

In the offset frequency range 150 kHz – 1 MHz, two curves have similar shape and have exactly positions of the spurious peaks corresponding to k/τ_d with $k \in [1,5]$ and $\tau_d = 5 \mu\text{s}$. There is a disagreement in the range 20 kHz – 150 kHz of offset frequency, the experimental curve is higher than Yaho & Maleki curve. This irregular data from experimental data can be explained by the existence of not optimized RF components in the experiment.

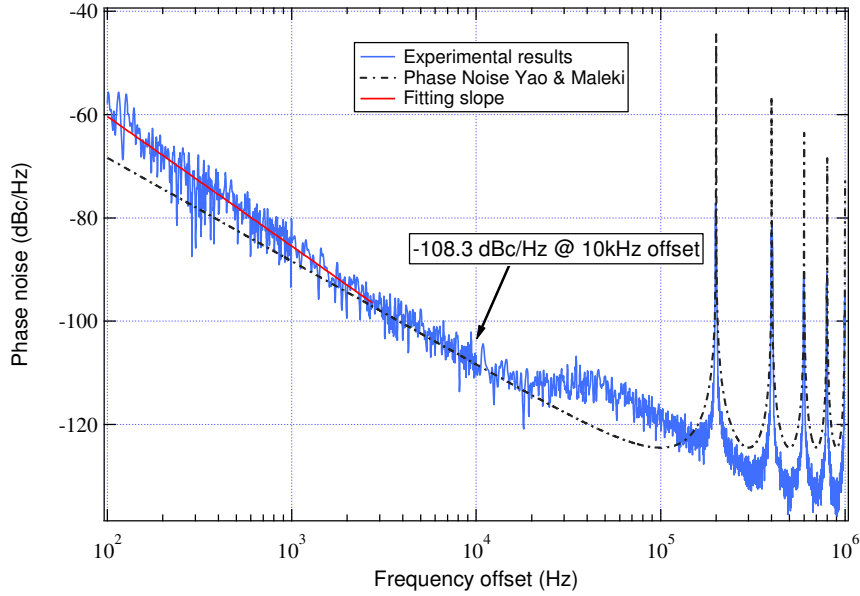


Figure 2.5 Phase noise of the OEO in case of 1 km fiber loop, with simulation from Yao & Maleki theoretical model

From the offset frequency 2 kHz to 20 kHz, the experimental slope is equal to the theoretical value of -20 dB/decade corresponding to a variation as f^{-2} .

Below 2 kHz the theoretical phase noise is diverging with respect to the experimental one. This can be explained by the existence of non-white noise sources in the real OEO, which was not taken into account in the Yao model. These non-white noise sources have been studied by other researchers, one important reference is Leeson model [49]. Flicker noise ($1/f$) component predominates at low offset frequencies compare to the feedback loop bandwidth and leads to a higher value of the slope. According to [47], [49], pure " $1/f$ " should lead to a variation of phase noise as f^{-3} . In our case, by fitting between 100 Hz and 2.7 kHz we get a variation as $f^{-2.51}$. There is flicker-noise effect but not pure " $1/f$ ".

2.5 Simulation with Matlab

2.5.1 Simulation models

Simulating the optoelectronic oscillator is fundamental in order to predict dynamical behavior, amplitude temporal changes, mode hoping and phase noise fluctuations. Yao and Maleki have analyzed the theoretical and experimental dependence of the time-averaged phase noise on the frequency offset from the carrier frequency, the optical filter length, and the oscillation power [4], but their model

concerns only the final steady state and does not take into account time dependent dynamical effects. These effects can degrade the performance of OEO in some operating regimes. First attempt to study the signal dynamics in OEO has been developed by Chembo *et al.* based upon delay-differential equation [51]. A new model of OEO was developed by Levy *et al.* [9], [52] implementing important dynamical effects. This model can deal with three different frequency scales, including the order of few gigahertz of the output RF signal frequency, the order of hundreds of kilohertz of the cavity mode spacing and the frequency offset of the phase noise in the order of several to thousands of hertz. Other frequency scale, of the order of 100 THz, corresponds to the carrier frequency of the light in the OEO's optical fiber. We use this simulation model, developed in the Matlab[®] programming environment [52] in this section.

2.5.1.1 Simulation analysis

In an OEO, the RF bandwidth of all the devices is considered as small compared to the oscillation frequency and the input signal of the electro-optic modulator is supposed to be a sine signal at the oscillation or carrier frequency with amplitude and phase depending slowly on time.

$$v_{in}^{eom}(t) = V_{in}^{eom}(T)\sin[\omega_0 t + \varphi(T)] \quad (2.21)$$

In Eq. (2.21), T is changing in a slow time scale of the round trip order of magnitude, some μs ; t is changing in a much more faster scale of the order of $2\pi/\omega_0$. From these hypotheses it is possible to find the expression of the amplitude of signal at the output of the amplifiers:

$$V_{out}^{amp}(T) = -2\eta\cos\left(\frac{\pi V_B}{V_\pi}\right) V_A J_1\left(\frac{\pi V_{in}^{eom}(T)}{V_\pi}\right) e^{j\varphi(T)} \quad (2.22)$$

The RF filter is supposed to be a linear system, the response in the time domain is the convolution product of the input signal, by the impulse response of the filter noted $h(T)$.

$$H(f') = \int_{-\infty}^{+\infty} h(t)e^{i2\pi f' T} dT \quad (2.23)$$

The Fourier transform of the signal at the output of the filter is hence equal to the transfer function of the filter by the Fourier transform of the signal at in output of the

amplifier:

$$\tilde{V}_{out}^{fil} = H(f_0 + f') \tilde{V}_{out}^{amp}(f') \quad (2.24)$$

Levy *et al.* have made the hypothesis [9] that the filter has a Lorentzian shape:

$$H(f) = \frac{\frac{i\Delta f}{2}}{f - f_c + \frac{i\Delta f}{2}} \quad (2.25)$$

where f_c is the center frequency of the filter and Δf is the bandwidth of the filter or its full width at half maximum. In the time domain the response of the filter can be written as:

$$h(t) = \pi \Delta f \exp \left[-i2\pi \left(f_c + \frac{i\Delta f}{2} \right) T \right] u(T) \quad (2.26)$$

where $u(T)$ is the Heaviside step function.

In their model [9], [52], Levy *et al.* calculate the complex amplitude of the signal at the output of the amplifier (or at the input of the filter) noted here $\tilde{V}_{out}^{amp}(f')$, on each round trip. In the time domain it becomes $V_{out}^{amp}(l, T)$ where l is the number of round trips after the OEO is switched on. The duration of one trip is equal to the propagation time t_d . The time response of the filter is supposed to be small compared to the propagation time and $V_{out}^{amp}(l = 0, T = 0)$.

In a first approximation the authors considered only white noise, thermal noise from the amplifiers, shot noise from the photodetector and intensity noise from the laser. Globally this noise is a white Gaussian noise $\tilde{w}_n(l, f)$ with a single side power spectral density ρ_N at the output of the photodetector: this noise is added at each round trip.

$$\tilde{V}_{out}^{amp}(l, f') = G_A [\tilde{V}_{in}^{amp}(l, f') + \tilde{w}_n(l, f)] \quad (2.27)$$

where $\tilde{V}_{in}^{amp}(l, f')$ and $\tilde{V}_{out}^{amp}(l, f')$ are Fourier coefficients of the complex amplitude at the input and output of the amplifier, at the round trip number l^{th} .

2.5.1.2 Implementation of the Levy model.

The calculation is performed on a computer with Intel Xeon CPU 3.1 GHz, 8 GB of RAM and is divided into two parts. For the first one there is no record of the calculated data. After N_{it1} iterations of round trip, the steady state is reached, then all the results are stored; there is N_{it2} more iterations in order to get the voltage

amplitude. All together there are $N_{tot} = N_{it1} + N_{it2}$ iterations. The phase noise is obtained by averaging N_{avg} cycles of the N_{tot} iterations leading to $N_{tot} \times N_{avg}$ runs. The simulation duration highly depends on the computer configuration and iterations number.

2.5.2 Simulation results

In this section we apply the Levy simulation with the value of ρ_N , the voltage gain G_A , the propagation time τ_d and the bandwidth Δf of the filter known from the experiment. Tunable parameters are the small-signal open-loop gain G_S and the numbers of iterations N_{it1} and N_{it2} . Levy *et al.* [9] have tested their model in case of a 56 m optical fiber length and obtained good results for simulation with $G_S = 1.5$, $N_{it1} = 2000$, $N_{it2} = 10000$, $N_{avg} = 350$. This value of G_S was already underlined in [4] as leading to the minimum of the noise-to-signal ratio, taking into account the non-linearity of the modulator.

2.5.2.1 Case of 1000 m optical fiber length

In Figure 2.7, simulations are conducted with $G_S = 1.05$ for different iterations number.

Only N_{it1} is concerned by this change, the second part is performed with $N_{it2} = 10000$. For low values of the iterations number, the simulation does not give good results by comparing with the experimental data. For $N_{tot} = 40000$ the simulation phase noise move closer to experimental curve especially around peak positions. When N_{tot} is increased to values greater than 40000, there is no significant improvement. At the offset frequency of 10 kHz, the phase noise from Levy's model is -110.6 dBc/Hz, which is 2.3 dB lower than the value of -108.3 dBc/Hz obtained by Yao & Maleki's formula after adjustment to the experimental data.

The Figure 2.7 presents, for the Levy's model, the effects of G_S for a given number $N_{tot} = 40000$ of iterations and 350 cycles. The simulation results, based on the experimental data used as input parameters for the Levy's model, are improved by decreasing the value of G_S down to 1.05.

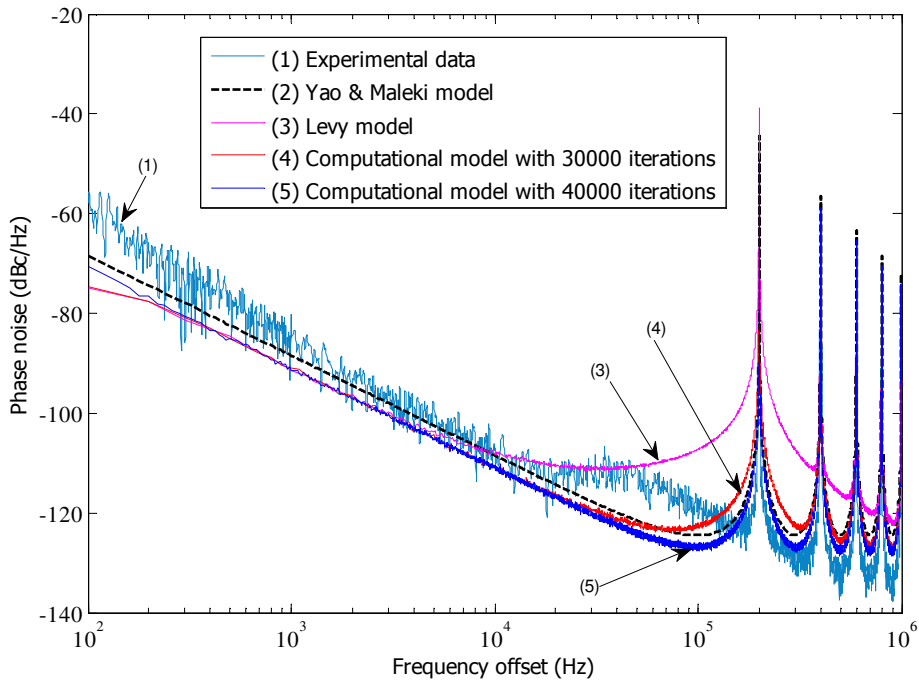


Figure 2.6 Phase noise of the OEO in case of 1 km optical fiber length. Simulation results with different numbers N_{tot} of iterations ($N_{it2} = 10000$).

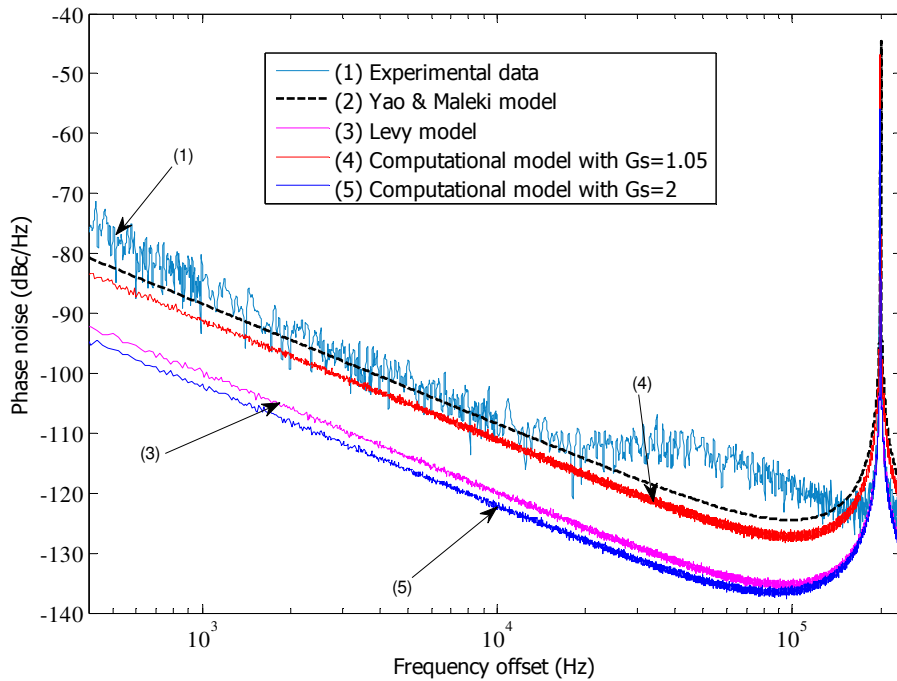


Figure 2.7 Phase noise of the OEO in case of 1 km optical fiber length. Simulation results with different values of GS parameter ($N_{tot} = 40000$).

The hypothesis of nonlinear distortions of the amplifier being lower than those of the modulator [9] is maybe not justified in our case. When working with a 20 m single loop OEO [53], by taking into account the non-linearity of microwave amplifier, it has been shown that the best choice of G_S should be 1.33 rather than 1.5 in [4].

2.5.2.2 Case of 500 m optical fiber length

The same study has been conducted with OEO in case of 500 m optical fiber length. We use the same value of the noise power density at the output of the photodetector as determined in case of 1 km optical fiber. Figure 2.8 and Figure 2.9 present the case of an OEO with 500 m optical fiber length, studying the effect of the iteration number and of G_S parameter.

For such a length, 20000 iterations are now necessary for a good simulation which means that the simulated phase noise is as close as possible to the experimental data. Even for a rather short optical fiber loop the necessary number of iterations is bigger than the 12000 ones used by Levy *et al.* for the case of 56 m length. As for 1 km length, $G_S = 1.05$ is a good value for the simulation.

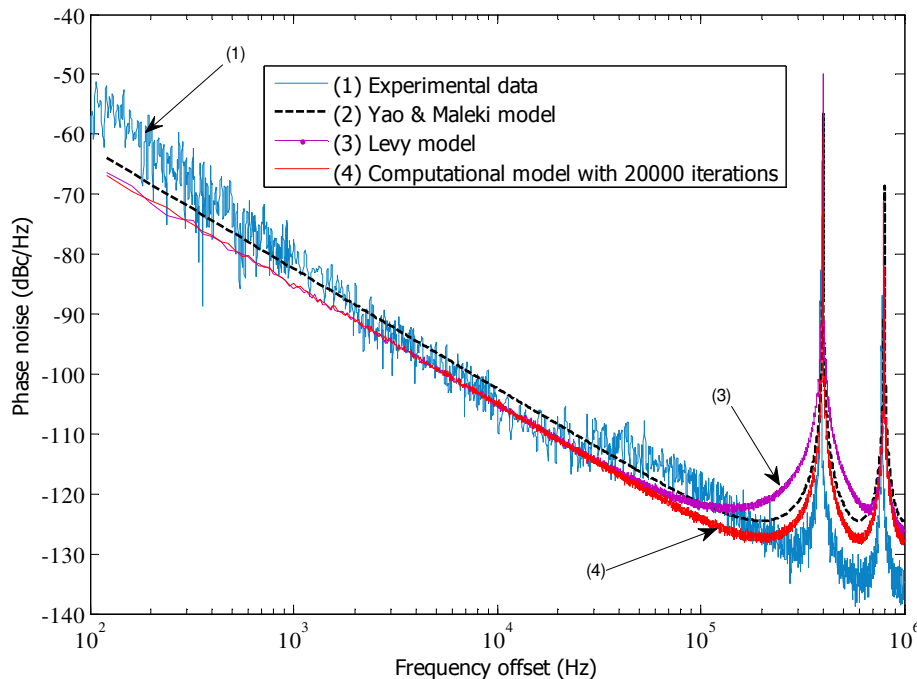


Figure 2.8 Phase noise of the OEO in case of 500 m optical fiber length. Simulation results with different numbers N_{tot} of iterations ($N_{it2} = 10000$).

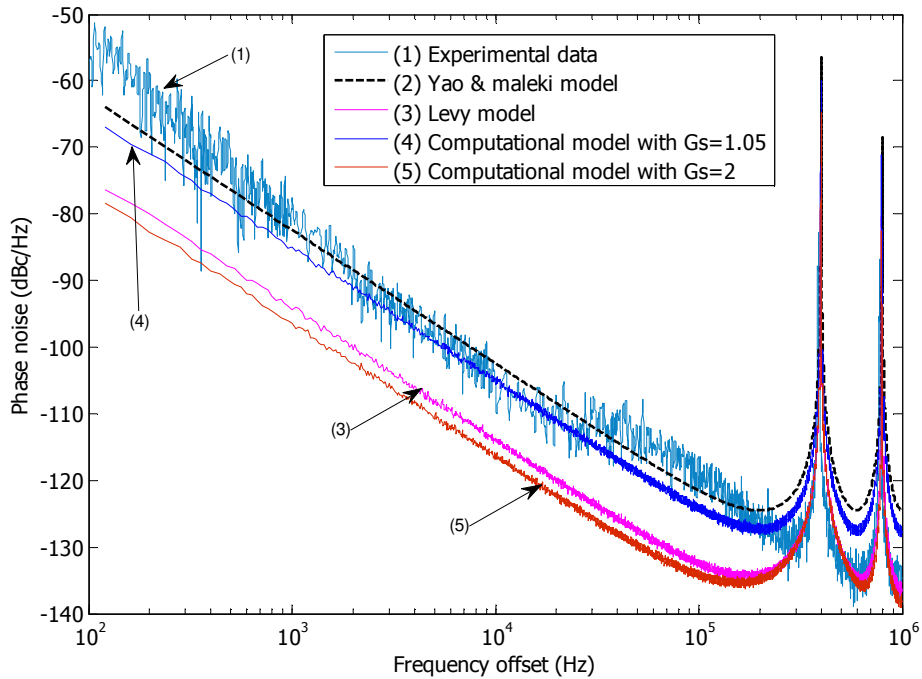


Figure 2.9 Phase noise of the OEO in case of 500 m optical fiber length. Simulation results with different values of G_S parameter ($N_{tot} = 20000$).

In both figures one can see a small difference between experimental and theoretical phase noise at 10 kHz offset from the carrier: as the experiment have not been conducted on the same day and not for the same temperature in the lab maybe the noise power spectral density was not exactly the same.

2.5.2.3 Case of 1500 m optical fiber length

Figure 2.10 and Figure 2.11 present the case of an OEO with 1.5 km optical fiber length. We found that the number of iterations need to be increased up to $N_{tot} = 150000$ with $N_{it1} = 120000$ and $N_{it2} = 30000$). But once again $G_S = 1.05$ is a good value for the quality of simulation. Logically the G_S parameter does not depend on the length of the optical fiber, but on the other parameters like the non-linear behavior of the modulator and amplifiers [53]. The number of iterations greatly depends on the length of the fiber.

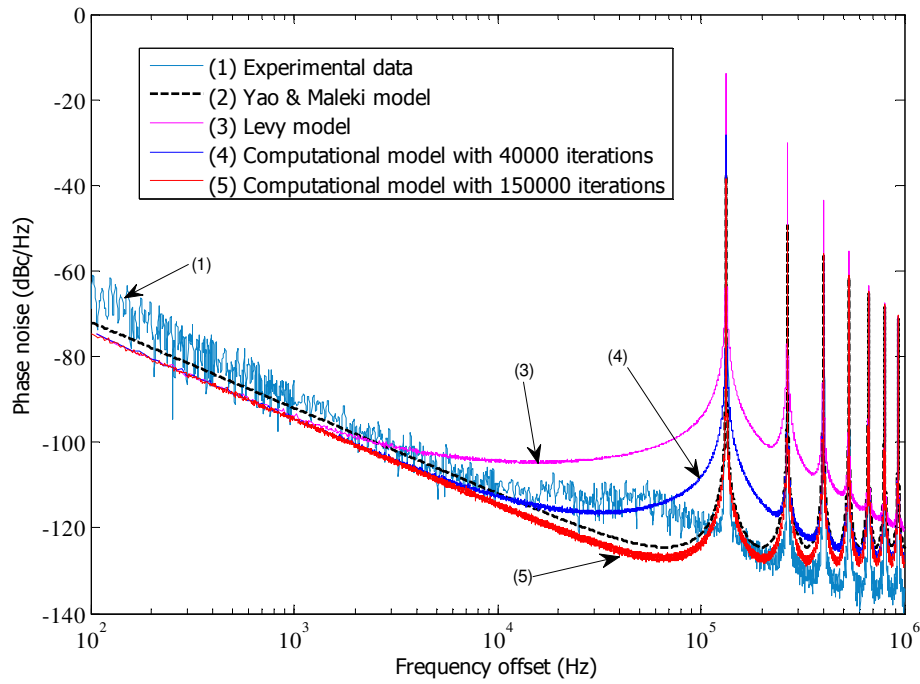


Figure 2.10 Phase noise of the OEO in case of 1.5 km optical fiber length.

Simulation results with different numbers N_{tot} of iterations

($N_{it2} = 10000$ for the curves (3), (4) and $N_{it2} = 30000$ for the curve (5)).

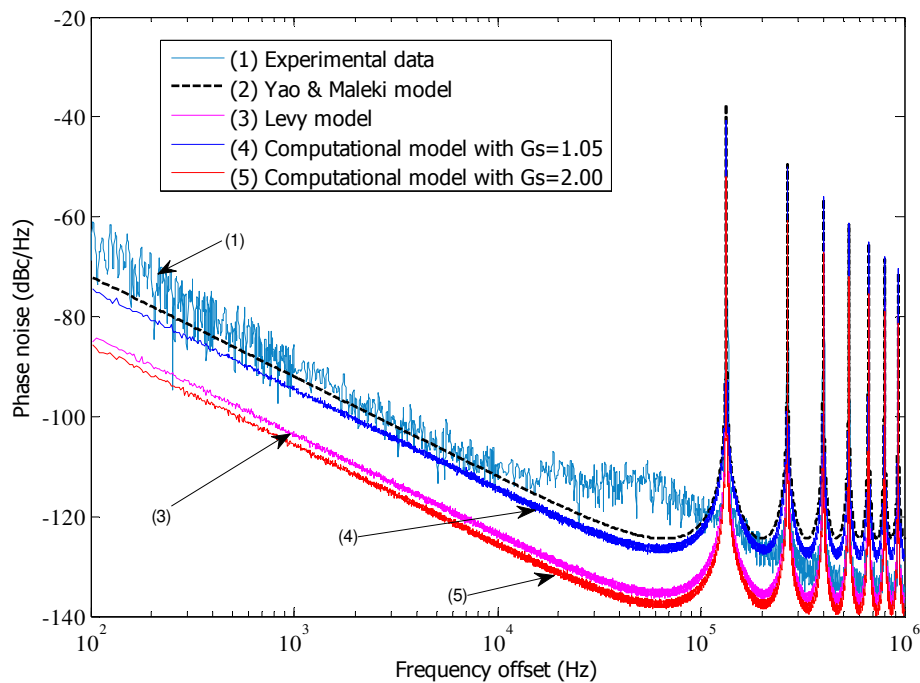


Figure 2.11 Phase noise of the OEO in case of 1.5 km optical fiber length. Simulation results with different values of G_S parameter ($N_{tot} = 150000$).

2.6 Other simulation software systems

Before working with Matlab, we have studied other simulation software systems. The first one is Advanced Design System (ADS) – an electronic design automation software system from Keysight Technologies (former name was Agilent Technologies). Because ADS is an electronic simulation software, it does not have model library for optical components. While OEO includes both electrical and optical components, so it must be to describe optical components by equivalent electrical circuits. ADS has been used to simulate microwave optical system for time and frequency applications [54], microwave optical system including phase noise [55]. To our knowledge, the most detailed study on OEO simulation using ADS is presented in [56] for a fiber ring resonator based OEO [56]. This OEO ADS model is well designed and can simulate all individual elements, OEO behavior for open-loop power and frequency part. However, when simulating OEO phase noise, this OEO ADS model shows some limitations. For open-loop configuration, the simulated phase noise seems to be very high regarding the quality factor of fiber ring resonator. For closed-loop configuration, phase noise simulations are more not realistic due to the fact that the oscillation is autonomously started from the noise amplified by the feedback loop. The difficulties come from original design of ADS with the use of “osc_port” for simulating classical RF oscillators. This “osc_port” simulation works when the system has only frequency. Unfortunately, in OEO system, there are two frequencies: laser frequency and OEO oscillation frequency. The author in [56] has tried several methods to overcome this obstacle. However, this OEO ADS noise modeling still needs further studies. For us, we also tried to work with ADS, but finally, we have not found any other solutions compared what author in [56] has already presented.

The second simulation software system is COMSYS (COMmunication System Interactive Software) which has been developed by a French company named IPSIS (Ingénierie Pour Signaux et Systèmes) [57]–[59] to simulate a communication system. The advantage of COMSIS comes from its electrical and optical component models library. The power and frequency of the open-loop OEO can be simulated with COMSIS as shown in Figure 2.12.

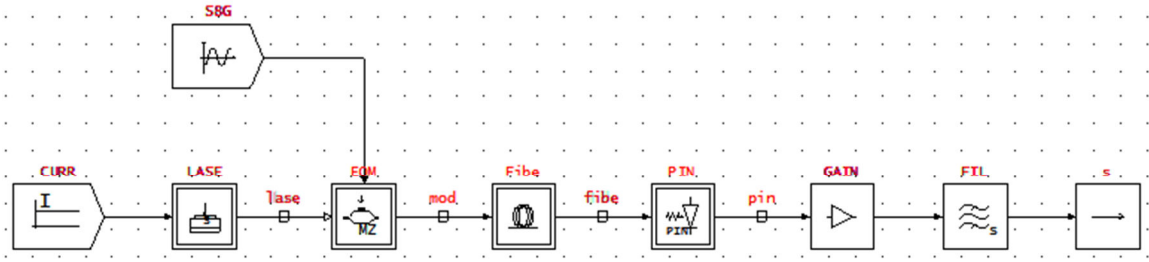


Figure 2.12 Open-loop OEO model with COMSIS software.

However, we found no way to simulate the OEO phase noise with COMSIS. Furthermore, the version used in our test is COMSIS v8.7.1, released in 2003 and COMSIS software seems not to be updated to newer version.

2.7 Conclusions and discussions

In this chapter, we have presented noise sources of main components inside an OEO such as laser noise, photodetector noise and amplifier noise. Then we concentrate on the phase noise simulation of the OEO based on models proposed by Yao – Maleki [4] and Levy *et al.* [9]. Some results concerning parameters to use in the Levy's computational model of OEO [9]. In this model, the signal is propagated in the loop a certain number of iterations and this process is repeated a certain number of cycles. An experimental OEO based on an optical fiber length of 1 km and working at an oscillation frequency of 8 GHz was the basis to calculate the values of noise, small-signal open loop gain and the optimum values of the iterations number. A comparison with the Yao & Maleki [4] theoretical formula with the phase noise of the OEO has also been introduced.

The experimental phase noise curves agree well with the theoretical formula in terms of peak position and slope close to the offset frequency of 10 kHz. The Yao & Maleki curve can be adjusted, at this offset frequency, to the experimental value of the phase noise -108.3 dBc/Hz, leading to an estimation of the noise power spectral density at the photodetector output of -149 dBm/Hz.

The Levy's model for simulating the OEO has then been performed with the data obtained previously. From different tests of the model it can be seen that the optimum small-signal open-loop gain is $G_S = 1.05$ and that the number of iterations necessary to get a good agreement with the experimental phase noise depends on the length of the optical fiber. In case of 1 km optical fiber length, the number of iterations is $N_{tot} = 40000$. Looking back to the phase noise, it can be seen that the Levy model

gives results lower by 2 to 3 dB than the experiment.

Chapter 3

Impacts of temperature on behavior of the EOM and the OEO

From the analysis in Chapter 1, the temperature is determined as one of the most important factors in the drift of the EOM. In this chapter, we will present in details the influences of temperature on the behavior of the EOM as well as of the OEO.

3.1 Temperature measurement

3.1.1 Temperature sensors

3.1.1.1 Definition

To measure the temperature, we need to use a temperature sensor which is a device with ability of detecting a small change in temperature and provides a corresponding output with good sensitivity and can be in the form of electrical or optical signal.

Temperature sensor can be classified into 2 categories [60]:

- + Contact temperature sensors: contact physically with the object or substance which can exist in solids, liquids or gases forms. The contact temperature sensors can be further classified into four categories: thermocouples, resistance temperature detectors (RTD), thermistors and temperature-transducer integrated circuits (ICs).

- + Non-contact temperature sensors: detect temperature by intercepting a portion of emitted infrared energy of the object or substance, and sensing its intensity. They can be used to measure temperature of only solids and liquids. It is not possible to use them on gases because of their transparent nature. The typical non-contact temperature sensor is infrared sensors.

3.1.1.2 Thermistor

Thermistor is a temperature sensitive resistor for which its resistance depends on its temperature. Generally, thermistors are made from ceramic material semiconductor, such as cobalt, manganese or nickel oxides coated in glass. It is formed into small pressed hermetically sealed discs that give relatively fast response to any temperature changes.

Due to the semiconductor material properties, thermistors have a negative temperature coefficient (NTC), i.e. the resistance decreases with the increase in temperature. However, there are also thermistors available with positive temperature coefficient (PTC), their resistance increases with the increase in temperature. Figure 3.1 shows photo of one NTC thermistor and its resistance-temperature relation curve.

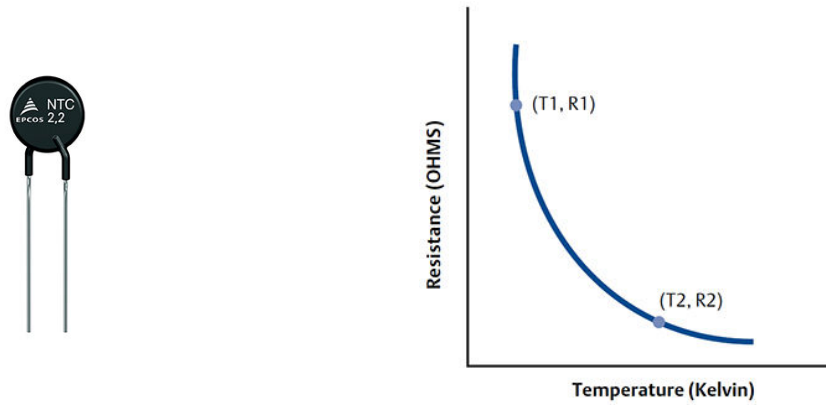


Figure 3.1 NTC thermistor and its resistance as a function of temperature.
(source: Thermodisc).

The resistance R of the thermistor at temperature T is determined by following equation [60]:

$$R_{Th} = R_0 e^{B\left(\frac{1}{T} - \frac{1}{T_0}\right)} \quad (3.1)$$

where:

- R_0 is the resistance at temperature T_0 in Kelvin.
- B is a constant of the thermistor.

Among several types of temperature sensor, thermistor was selected in our experiment because it has very high sensitivity (0.0001 °C) [61]. Thermistor also has disadvantages in non-linear relation curve which is determined by an exponential function and a limited working temperature range of $-100 \div 300$ °C.

3.1.2 Measurement circuit

The selected thermistor for our experiment is NTSA0XV103 from Murata. The resistance of this thermistor at 25 °C is 10 k Ω . The constant B of the thermistor can be selected within the range 3900-3949 with tolerance of 1%. The resistance of the thermistor can be converted into a voltage value by using the Wheatstone bridge diagram indicated in Figure 3.2.

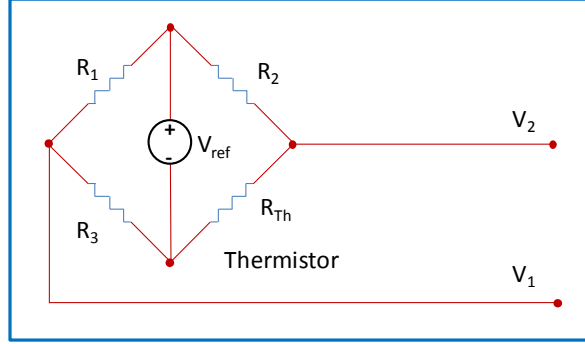


Figure 3.2 Scheme of Wheatstone bridge with a thermistor

The Wheatstone bridge is supplied by a constant voltage V_{ref} . The difference between V_1 and V_2 is determined by:

$$\Delta V = V_1 - V_2 = \frac{R_3}{R_1 + R_3} V_{ref} - \frac{R_{Th}}{R_2 + R_{Th}} V_{ref} \quad (3.2)$$

To simplify the calculation when using thermistor with Wheatstone bridge, we choose three identical resistors with resistance equal to resistance R_0 of thermistor at 25 °C: $R_1 = R_2 = R_3 = R_0 = 10 \text{ k}\Omega$.

By doing so, the Eq. (3.2) becomes:

$$\Delta V = V_1 - V_2 = V_{ref} \left(0.5 - \frac{R_{Th}}{R_2 + R_{Th}} \right) \quad (3.3)$$

or

$$R_{Th} = R_2 \frac{V_{ref} + 2\Delta V}{V_{ref} - 2\Delta V} \quad (3.4)$$

From Eq. (3.1), thermistor temperature can be expressed as a function of its resistance:

$$T = \frac{1}{\frac{1}{T_0} + \frac{1}{B} [\ln R_{Th} - \ln R_0]} \quad (3.5)$$

Replace R_{Th} determined in Equation (3.4) into Equation (3.5), we know the temperature of thermistor by ΔV :

$$T = \frac{1}{\frac{1}{T_0} + \frac{1}{B} \left[\ln \left(R_2 \frac{V_{ref} + 2\Delta V}{V_{ref} - 2\Delta V} \right) - \ln R_0 \right]} \quad (3.6)$$

From Eq. (3.6), we obtain the relation chart:

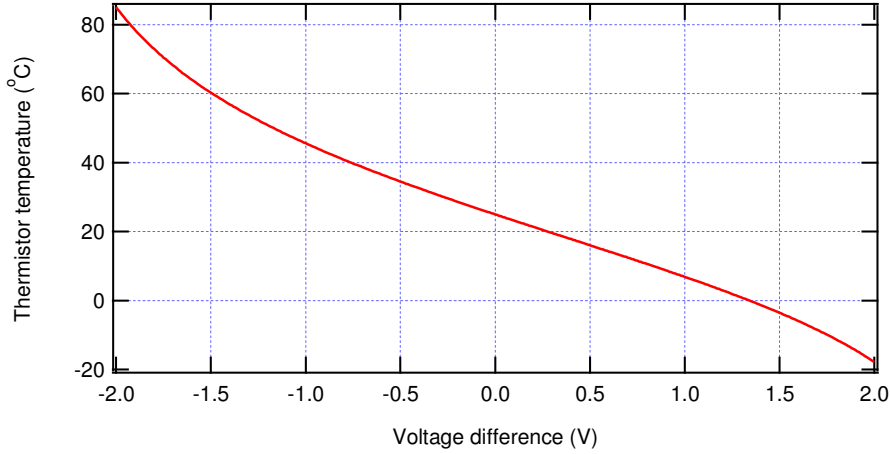


Figure 3.3 Thermistor temperature as a function of Wheatstone bridge output voltage.

As shown in Figure 3.3, the voltage output varies from -2 V to 2 V corresponding to a change in temperature from -17.9 °C to 85°C. This temperature range covers the working temperature range [0, +70 °C] of the modulator Photline MX-LN-10. Because the DSP input voltage is from -10 V to +10 V, so in order to take advantage of this wide input range, we amplify the Wheatstone bridge output voltage to a bigger range.

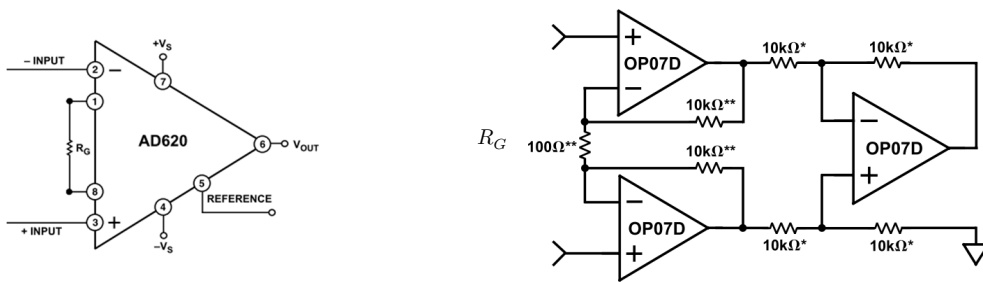


Figure 3.4 Simplified drawing of AD620 and three op amp design

Temperature measurement is made by connecting the Wheatstone bridge output to a low power instrumentation amplifier AD620. The AD620 is a monolithic instrumentation amplifier based on the classic three op amp scheme [62]. Absolute value trimming allows the user to program gain accurately (to 0.15% at $G = 100$) with

only one resistor.

The gain G is tunable thanks to external gain setting resistor R_G placed between Pin 1 and Pin 8. The relation between R_G and the gain G is given by:

$$G = \frac{49.4}{R_G} + 1 \quad (3.7)$$

where R_G is expressed in $k\Omega$.

The schematic drawing of the temperature measurement is shown in Figure 3.5. In Figure 3.5 (c), the ± 15 V voltage supply is regulated to ± 12 V by two three-terminal voltage regulators MC78M12 for positive voltage and MC79M12 for negative voltage.

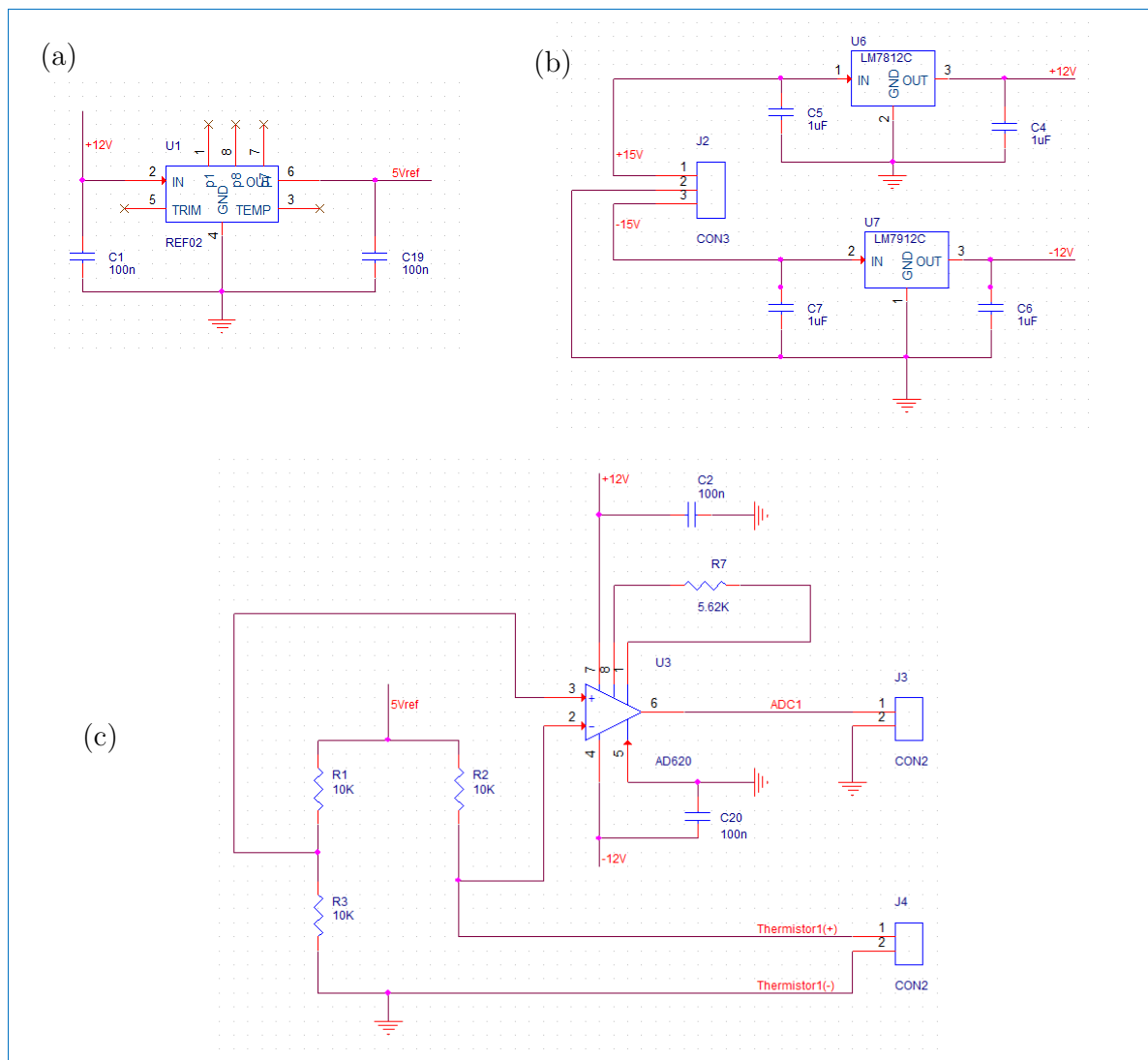


Figure 3.5 Schematic of temperature measurement circuit

The ± 12 V voltage source then is used as supply for the amplifier AD620 and for

+5 V precision voltage reference REF02. In Figure 3.5 (a), the REF02 creates an output voltage of +5 V with a good accuracy of ± 0.2 V which is used as reference voltage for the Wheatstone bridge. The thermistor is connected to resistors R1, R2, R3 to make a Wheatstone bridge via 2-pin connector J4. A resistor 5.62 k Ω is placed between pins 1 and 8 of the AD620. According to Eq. (3.7), the voltage difference between pins 2 and 3 is amplified 9.79 times and sent to pin 6.

Then, we convert the schematic drawing to printed circuit board (PCB) format by the software Cadence OrCAD which is used to make the real board by chemical technique. To reduce the size of the board, we use surface mount components. The top view and bottom view of the final board is shown in Figure 3.6.

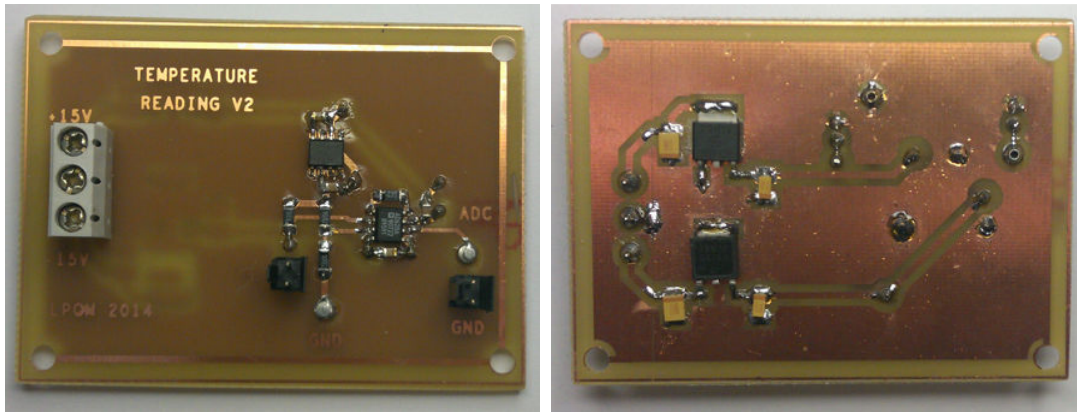


Figure 3.6 Top view and bottom view of temperature measurement board

The dimension of this card is 5 cm x 7 cm which is suitable to be mounted into our homemade MZM box.

In our experiment, we monitor temperature at two different positions: the temperature of MZM and the temperature of fiber loop. So, to bring the flexibility to our measurements, we created two different cards: one for temperature reading and one for temperature controlling.

3.2 Tuning temperature

3.2.1 Peltier module

Peltier module is a thermoelectric device that creates a different temperature on its two sides when there is a current applied to it and this phenomenon is called Peltier effect. A Peltier module comprises two conductors A and B, when a current I_{AB} flows through a junction between them, heat is generated or removed at the junction and is

determined by Eq. (3.8) [63], [64]:

$$\frac{dQ}{dt} = (\Pi_A - \Pi_B)I_{AB} \quad (3.8)$$

where:

+ dQ/dt is the heat generated at the junction

+ Π_A and Π_B is the Peltier coefficient of conductor A, B; and

+ I_{AB} is the current from A to B.

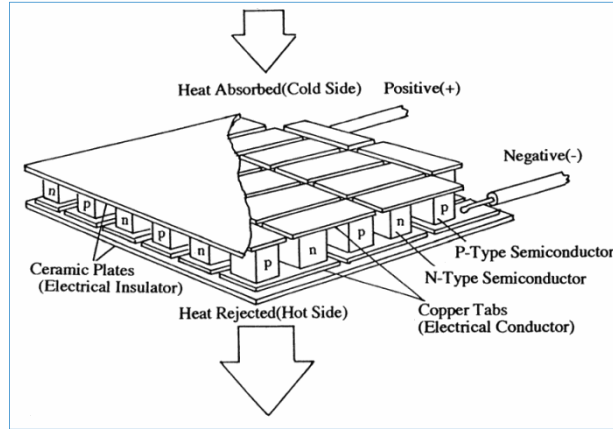


Figure 3.7 Structure of a Peltier module

The Peltier module has advantages in compact size, fast response time and simple control. In fact, a typical Peltier module has multiple junctions in series as shown in Figure 3.7.

3.2.2 Mounting Peltier to the EOM

To control the temperature for the MZM, we use the setup as indicated in the Figure 3.8 [12]. Two copper plates are connected together by two Peltier modules and are fixed by 4 plastic screws to avoid temperature leakage between these copper plates. The temperature is controlled by the current injected to Peltier 1 and Peltier 2 serially placed.

The MZM is attached on the top of the upper copper plate. In the upper copper plate, a groove has been etched to put a thermistor aligned with the middle of the modulator case. The distances of the thermistor to the two Peltier modules are the same to make sure that the temperature measured by the thermistor is the average temperature of the MZM.

The real time temperature is amplified and is sent to one input of DSP kit. This signal is used as input parameter for PID control process programmed by DSP script.

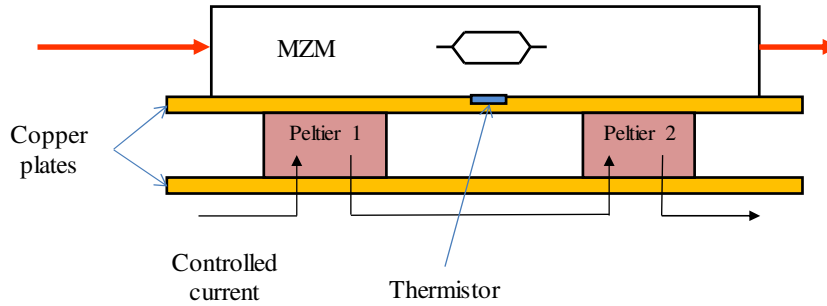


Figure 3.8 Mounting MZM with Peltier modules and thermistor

3.2.3 Temperature tuning card

The principle for controlling the temperature is to modify the current injected to Peltier modules to reach the desired temperature value or so called temperature setpoint. Normally, the current is modified by a voltage source via an operational amplifier.

In our experiment, we develop a temperature control circuit around a high power monolithic operational amplifier OPA541 [65] as shown in Figure 3.9. The packaging type of the OPA541 used in our design is plastic package.

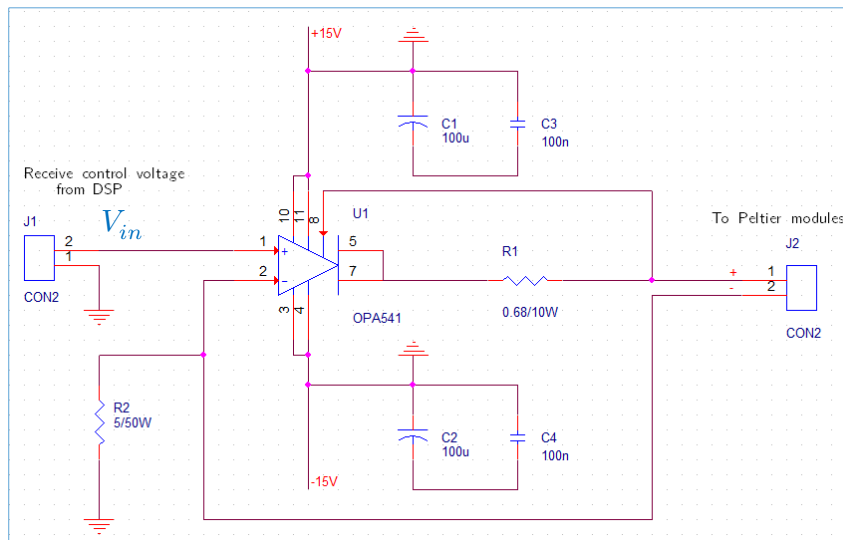


Figure 3.9 Temperature tuning schematic with OPA541

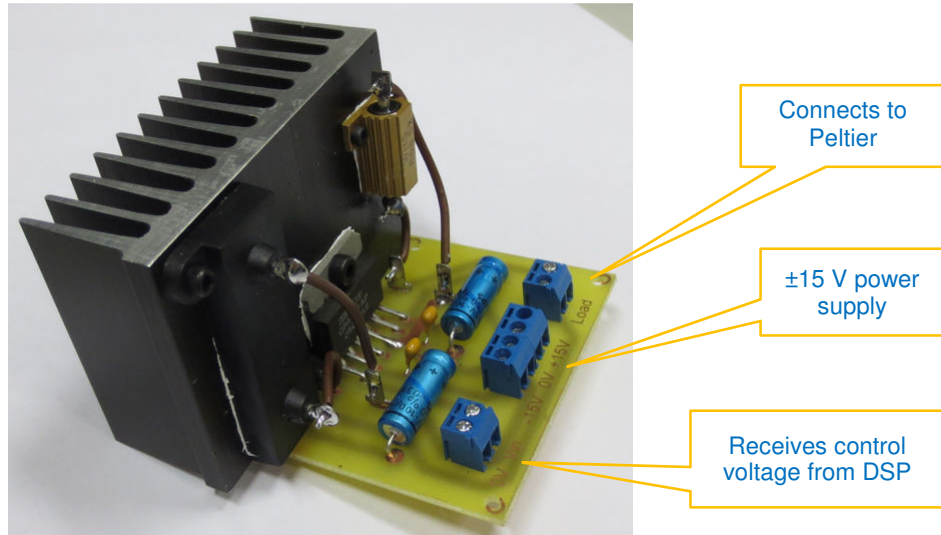


Figure 3.10 Temperature tuning card built around OPA541

The relation between the control voltage V_{in} and the current sent to the load made of Peltier modules $I_{peltier}$ is determined by:

$$I_{peltier} = \frac{V_{in}}{R_2} \quad (3.9)$$

The internal current limit circuitry is controlled by a single external resistor R_1 . Output load current flows through this external resistor. The current limit is activated when the voltage across this resistor is approximately a base-emitter turn-on voltage. The value of the current limit resistor is approximately:

$$R_1 = \frac{0.813}{|I_{lim}|} \quad (3.10)$$

We have chosen to limit the current at 1.2 A with a resistor R_1 equal to 0.68 Ω . Our final temperature tuning card is shown in the Figure 3.10 with the dimension is around 6.0 cm x 4.5 cm. Three blue connectors are connected to DSP kit, power supply and Peltier modules. A heat sink is used for dissipating heat generated by the OPA and two resistors during operation.

3.3 Controlling temperature

3.3.1 Digital signal processing

There are several methods to implement a temperature control system such as FPGA (Field-Programmable Gate Array), PSoC (Programmable System on Chip),

ASIC (Application-Specific Integrated Circuit), DSP (Digital Signal Processing)... Typically, the circuit design of ASIC is already set to a specific application. PSoC and FPGA are more powerful with programmable ability in its circuit configuration. DSP solution is often available in the form of a complete DSP kit providing the most flexible and performance to a control system.

In addition to temperature control, we also control and monitor other properties of the OEO. In our laboratory, the first solution for stabilizing the bias point of an polymer material-based EOM was implemented by using all analog components [66]. The implementation technique then has been further studied and improved to the use of a microcontroller PSoC CY8C29466 Cypress [12], [67]. A PSoC includes a core, tunable analog and digital blocks, programmable routing and interconnect. The advantage of PSoC comes from its low price and its programmable ability. However, due to the fact that this PSoC was originally designed to perform specific tasks and applications, so it has low operating frequency, limited resources such as Random Access Memory (RAM), Read-Only Memory (ROM). Some functions could not be implemented with this PSoC such as phase comparator, direct 500 Hz and 1 kHz signal generation and filters. These functions are then realized by using external analog elements and circuits connected to this PSoC. It is impossible to modify parameters of these analog elements and circuits after having been soldered on the card.

Due to these limitations, a DSP system has been studied for creating a new control system which has ability to handle multiple control processes with better performance and easier reconfiguration. The structure of a DSP system is illustrated in Figure 3.11. At the beginning, the analog input signal is converted to digital signal via an Analog-to-Digital Converter (ADC) then it is processed in the digital domain. Finally, processed digital signal is converted into analog by a Digital-to-Analog Converter before being sent to other analog systems.



Figure 3.11 Block diagram of a digital signal processing system

Compared to analog technique, DSP technique has following advantages:

+ Flexible programming: DSP enables creating digital signal processing programs

and these programs are easily modified to meet the change of requirement. It is not necessary to modify the hardware.

+ Implementing adaptive algorithms: It is possible to adjust a digital processing function in real time according to certain criteria of the signal changes (example: the adaptive filters). The signal processing functions are easy to implement digitally.

+ Stability: by using digital technique, DSP is stable under variations of temperature, supply voltage, aging, etc.

Nowadays, DSP technique is widely used in many aspects: signal processing, telecommunication, image analysis, monitor and control, robot, data security... After considering several solutions available on the market, we decided to work with a combination of two cards:

+ eZdspF28335 development system from Spectrum Digital Incorporated

+ Daughtercard from Link Research, which is designed to operate only with eZdspF28335 card.

We will present techniques to develop several monitoring and controlling functions based on this DSP kit to improve the behavior of EOM and OEO, and then integrate them all these function into a complete solution.

3.3.1.1 Spectrum Digital eZdsp F28335 card

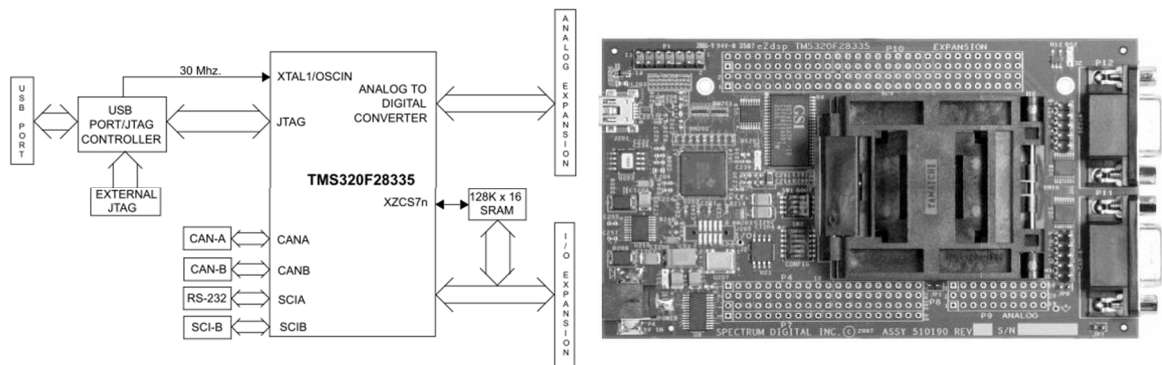


Figure 3.12 Block diagram and top view of eZdspF28335 development system.

The block diagram and top view of eZdspF28335 development system [68] are shown in figures. The heart of this card is its microprocessor - TMS320F28335 Digital Signal Controller – a product of Texas Instrument.

Some main features of eZdspF28335 are listed in the Table 3.1:

Table 3.1 Some key features of eZdspF28335 card

Hardware features	
TMS320F28335 Digital Signal Controller	256K bytes off-chip SRAM memory
150 MHz operating speed	On chip 32-bit floating point unit
68K bytes on-chip RAM	512K bytes on-chip Flash memory
On chip 12 bit Analog to Digital (A/D) converter with 16 input channels	
Software features	
Texas Instruments Code Composer Studio, Integrated Development Environment.	
Texas Instruments' Flash APIs to support the F28335.	

The TMS320F28335 supports +3.3V Input/Output levels which are NOT +5V tolerant. Connecting the eZdsp to a system with +5V Input/Output levels will damage the TMS320F28335.

3.3.1.2 Link Research LR-F28335DAQA daughtercard

To simplify the control process, we use the LR-F28335DAQA daughter card from Link Research which is designed to operate with eZdspF28335 card. This card is mounted on the top of the eZdsp F28335 as shown in figure below:

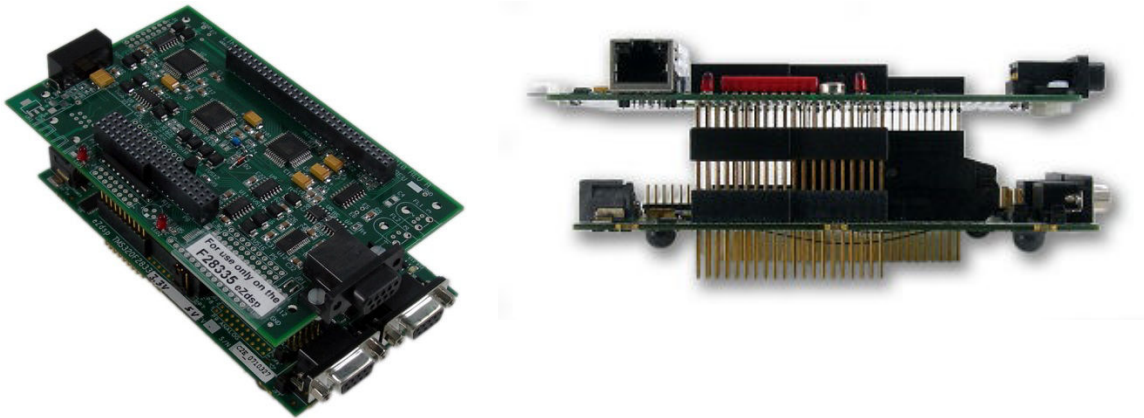


Figure 3.13 LR-F28335DAQA daughtercard plugged on the top of the F28335 eZdsp board

This daughtercard includes miscellaneous peripherals, like 8 user digital inputs, 2 user red LEDs and an RS-232 port with a maximum baud rate of 921.2 kbps. It also includes LR-DAQEXTSET4 height extenders, which are necessary to clear the tall DSP socket presents on the F28335 eZdsp board.

The LR-F28335DAQA daughtercard contains the following features:

- 4 A/D input channels (Optional support for up to 8 A/D channels), single ended, $\pm 10V$ range, simultaneous sampling.
- 8 D/A output channels, single ended, $\pm 10V$ range, simultaneous output update
- An RS232 asynchronous serial communications interface
- A software controllable output signal with a +15V to ground swing
- 08 general purpose digital logic inputs
- Optional support for a fiber optic asynchronous communications interface
- Optional support for a 10/100 802.3 Ethernet interface
- Support for up to 16 A/D and 16 D/A channels by using the optional model LR-28335DAQA8x8 daughtercard.

3.3.1.2.1 Memory Address

We can read data from A/D channels and write data to D/A channels via the addresses listed in the table below:

Table 3.2. Memory address table of A/D and D/A channels of LR-F28335DAQA daughtercard

Device / Channel	Hardware Address
A/D #1 (channels 1-4)	0x0108000
A/D #2 (channels 5-8)	0x0108004
D/A channel 1	0x0108008
D/A channel 2	0x0108028
D/A channel 3	0x0108048
D/A channel 4	0x0108068
D/A channel 5	0x0108088
D/A channel 6	0x01080A8
D/A channel 7	0x01080C8
D/A channel 8	0x01080E8

Each A/D IC has a single hardware address used to access the 4 channels of converted data. When the A/D signals the processor that it is done converting, the

processor can then make 4 consecutive reads of the A/D chip to obtain samples from channels 1, 2, 3 and 4, in that order. The D/A chip has 8 unique hardware addresses used to access each of its 8 channels.

3.3.1.2.2 ADC and DAC

The daughtercard contains 4 (optionally 8) A/D channels, and 8 D/A channels. All channels have a full +/- 10V range, and are protected against transient voltage spikes. All A/D channels have the capability of being simultaneously sampled, whereas all the D/A channels can be updated simultaneously [69].

All data processed by the DSP should be in Q13 format. This means that the lower 13 bits of a 16-bit word are the significant bits, and the 14th bit is the sign bit. Data read from the A/D within the interrupt service routine (ISR) will be sign-extended before being presented to the user. Data processed by the DSP and destined to be written to the D/A chip, not necessary to be sign-extended, since bits 14 and 15 are not used.

All ADC/DAC are 14 bits, the 14th bit is the sign bit and the binary representation is shown in table below:

Table 3.3. Binary representation of LR-F28335DAQA daughtercard

Voltage input	Hexadecimal value
+10V	0x1FFF
0	0x0000
-10V	0x2000

It should be noted that the D/A used on the daughtercard, the AD7841, has unipolar input values. That is, writing 0x0000 produces -10V output, writing 0x2000 produces 0V, and writing 0x3fff produces +10V output. This minor incompatibility is easily handled by software in the ISR.

3.3.2 PID controller

Proportional-Integral-Derivative (PID) controller is the most common control algorithm which has been widely used in industrial control [70]. Most feedback loops are controlled by this algorithm or minor variations. The principle of feedback can then be expressed as follows: increase the manipulated variable when the process variable is smaller than the setpoint and decrease the manipulated variable when the

process variable is bigger than the setpoint. The feedback principle is illustrated by the block diagram shown in Figure 3.14.

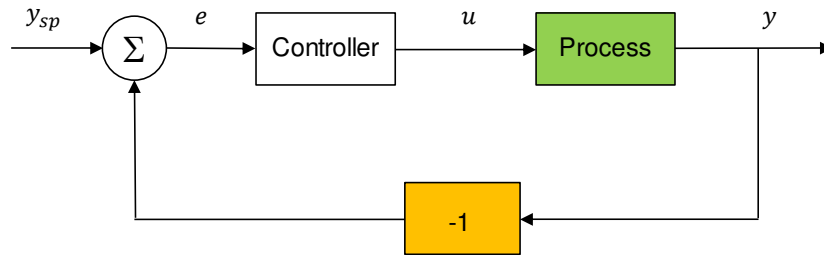


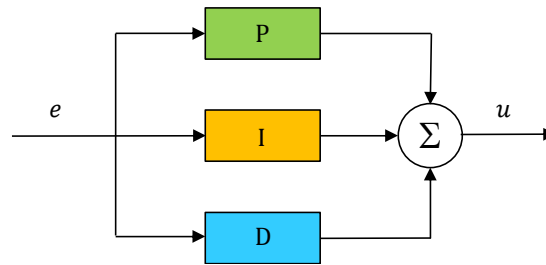
Figure 3.14 Block diagram of process with a feedback controller

The y_{sp} is the setpoint value, $e = y_{sp} - y$ is the control error, u is manipulated variable or also called control variable and y is the process output. The control variable is a sum of three terms: the P-term (which is proportional to the error), the I-term (which is proportional to the integral of the error), and the D-term (which is proportional to the derivative of the error).

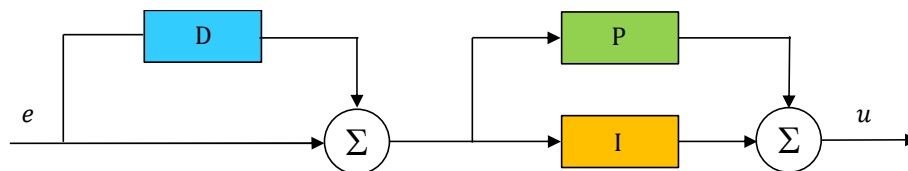
The textbook version of a continuous-time PID algorithm [70] is described as:

$$u(t) = K \left(e(t) + \frac{1}{T_i} \int_0^t e(\tau) d\tau + T_d \frac{de(t)}{dt} \right) \quad (3.11)$$

where K is proportional gain, T_i is integral time and T_d is derivative time.



Non-interacting form



Interacting form

Figure 3.15 Non-interacting and interacting form of the PID algorithm

Many studies to improve the performance of a PID controller have been carried out [71], [72]. The various structures can be classified into two main forms: non-interacting form and interacting form [70]. In the non-interacting form, the integral time T_i does not influence the derivative part, and the derivative time T_d does not influence the integral part. The non-interacting form of the PID algorithm is presented in Figure 3.15:

It should be noted that the Laplace transform [73] of a signal $x(t)$ is presented by:

$$X(s) = \int_0^{\infty} x(t)e^{-st} dt \quad (3.12)$$

where $s = \tau + iw$ is the complex number frequency and represents the Laplace transform operator. By using Laplace transform, it is possible to convert the Eq. (3.11) [74] into the form:

$$U(s) = K \left(1 + \frac{1}{sT_i} + sT_d \right) E(s) \quad (3.13)$$

From Eq. (3.13), the transfer function of the PID controller can be determined:

$$G(s) = \frac{U(s)}{E(s)} = K \left(1 + \frac{1}{sT_i} + sT_d \right) \quad (3.14)$$

PID controllers were originally implemented using analog techniques. Along with the development of digital signal processing, PID controllers are now popularly implemented by using microcontrollers, microprocessors or computers. All the issues applied in continuous-time PID controllers have been studied and presented by the way of digital implementations [73]–[75].

To present the continuous-time PID controller in the digital domain, the integral and derivative components of Eq. (3.11) must be discretized. When the sampling period T_0 is small and noise from the process output signal is effectively filtered out, the simplest algorithm is obtained by replacing the derivative with a difference of the first-order (two-point, backward difference) [74]

$$\frac{de}{dt} \approx \frac{e(k) - e(k-1)}{T_0} = \frac{\Delta e(k)}{T_0} \quad (3.15)$$

where $e(k)$ is the error value at the sampling number k , or at the time $t = kT_0$.

The integral part of Eq. (3.11) is approximated by using the forward rectangular method (FRM)

$$\int_0^t e(\tau) d\tau \approx T_0 \sum_{i=1}^k e(i-1) \quad (3.16)$$

The discrete-time PID controller version of the continuous-time PID controller demonstrated by Eq. (3.11) now becomes:

$$u(k) = K \left\{ e(k) + \frac{T_0}{T_i} \sum_{i=1}^k e(i-1) + \frac{T_d}{T_0} [e(k) - e(k-1)] \right\} \quad (3.17)$$

For a digital PID controller, the increment of the output $\Delta u(k) = u(k) - u(k-1)$ can be calculated by:

$$\begin{aligned} \Delta u(k) = K \left\{ e(k) - u(k-1) + \frac{T_0}{T_i} e(k) \right. \\ \left. + \frac{T_d}{T_0} [e(k) - 2e(k-1) + e(k-2)] \right\} \end{aligned} \quad (3.18)$$

Performing Z transform to the Eq. (3.17) in time domain, we achieve:

$$U(z) = K \left(1 + \frac{T_0}{T_i} \frac{1}{1-z^{-1}} + \frac{T_d}{T_0} (1-z^{-1}) \right) E(z) \quad (3.19)$$

The relation between input and output is:

$$G(z) = \frac{U(z)}{E(z)} = K \left(1 + \frac{T_0}{T_i} \frac{1}{1-z^{-1}} + \frac{T_d}{T_0} (1-z^{-1}) \right) \quad (3.20)$$

Replacing $K_p = K$, $K_i = K/T_i$ and $K_d = KT_d$, we achieve the transfer function of a digital PID controller in Z domain:

$$G(z) = \frac{U(z)}{E(z)} = K_p + K_i T_0 \frac{1}{1-z^{-1}} + \frac{K_d}{T_0} (1-z^{-1}) \quad (3.21)$$

3.3.3 Software development

3.3.3.1 Matlab/Simulink

We design the temperature control model in Simulink as denoted in Figure 3.16. The temperature information is sent from temperature measurement card and is converted in to digital values via ADC4_Input of the DSP. This value is data type converted and is put to a comparator with setpoint value. The error value is then forwarded to the PID block to control the temperature. The PID output is passed through a saturation block to limit the voltage will be converted to analog and sent to

temperature tuning card via DAC7_Output port of the DSP kit.

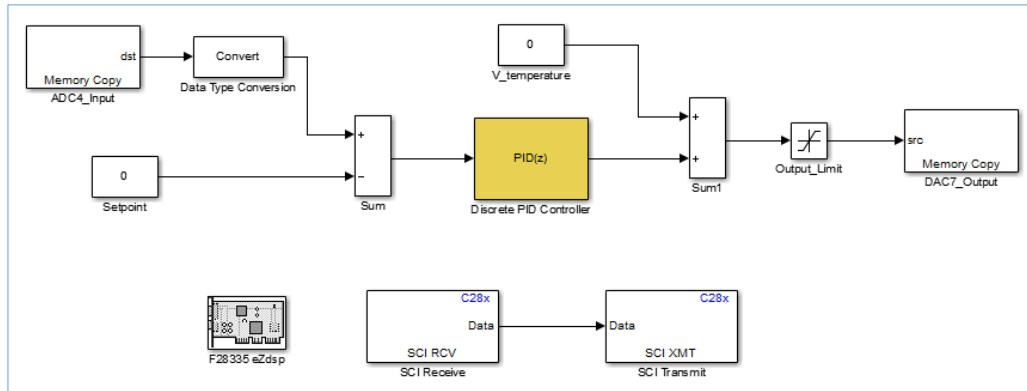


Figure 3.16 Matlab/Simulink model for temperature control.

3.3.3.2 Code Composer Studio

Code Composer Studio (CCS) is a powerful integrated development environment which is used for developing programs and applications for Texas Instruments embedded processors. In our works, we use CCS version 3.3 which was provided along with the purchase of eZdspF28335 development kit from Spectrum Digital.

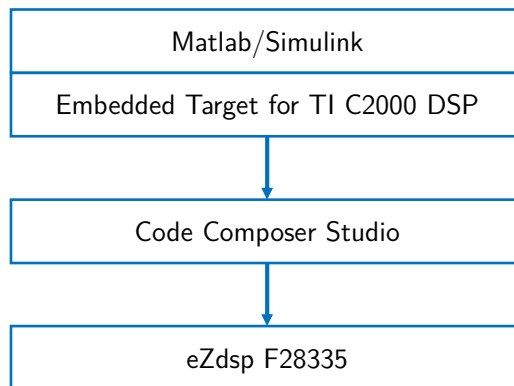


Figure 3.17 Block diagram of Matlab/Simulink, CCS and DSP kit.

The Real Time Workshop supported by Simulink in Matlab has Embedded Target for TI C2000 DSP blocks. Figure 3.17 shows how Simulink interacts with Code composer Studio. At the beginning, the model is created with Simulink. Then by using “Build model” inside Simulink, the Embedded Target for TI C2000 DSP platform generates frame to Code Composer Studio environment under the C code language. From this fundamental code, we need to develop addition code to meet our requirements such as temperature reading or temperature controlling... The final program is then compiled and loaded in to the memory of DSP board for executing.

3.3.3.3 Graphical user interface control on PC

In addition to the program developed for the DSP, to help users utilize the control program more easily, we have developed a Graphical User Interface (GUI) with Microsoft Visual Basic 6.0. This program communicates with the program developed in CCS and loaded into DSP via RS232 port as illustrated in Figure 3.18.

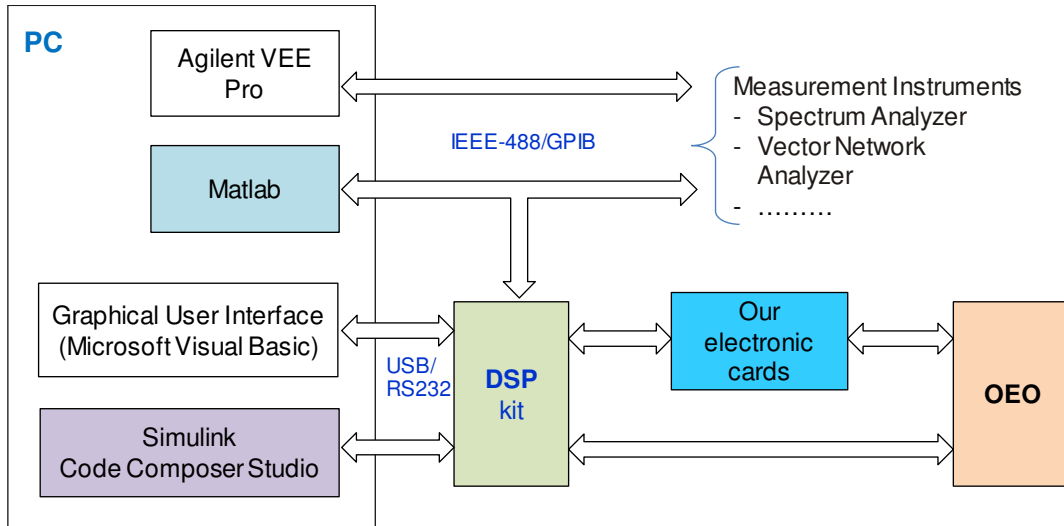


Figure 3.18 Software development and connections to DSP and other devices

3.3.4 Experimental results

Firstly, to test the effectiveness of the temperature tuning card, we set up an experiment as illustrated in Figure 3.19.

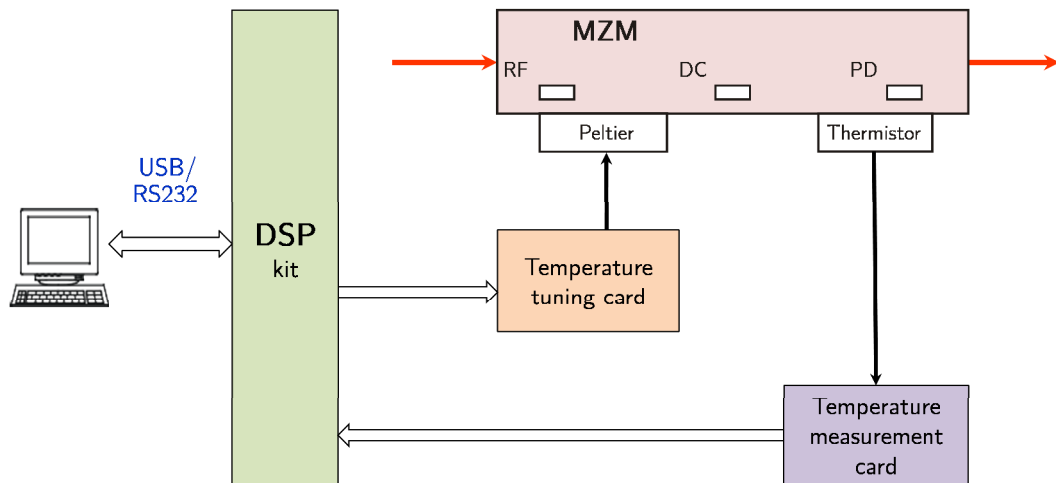


Figure 3.19 MZM temperature control system around DSP kit

The DSP kit is programmed to generate three voltages +1281 mV, 0 mV and -1770 mV to the control voltage port of the temperature card. As result, the output currents

are +255 mA, 0 mA and -351 mA respectively. These three currents are applied successively to the Peltier modules and we measure the temperature of the EOM by the temperature measurement card mentioned in previous section.

In Figure 3.20, at the beginning, we applied 0 mA current to the Peltier modules. With this current, there is no temperature modification happened between the top and bottom surfaces of the Peltier modules. The measured data is the room temperature with value started from 22.225 °C, slightly increased and reached 22.355 °C after 30 minutes and is plotted in blue color line. After that, the current is increased up to +255 mA, the temperature decreases from 22.355 °C to 18.748 °C within 30 minutes. Finally, the current is set to -351 mA, the EOM temperature is increased from 18.807 °C to 29.121 °C. All three measurements are realized in the same duration of 30 minutes or 1800 seconds.

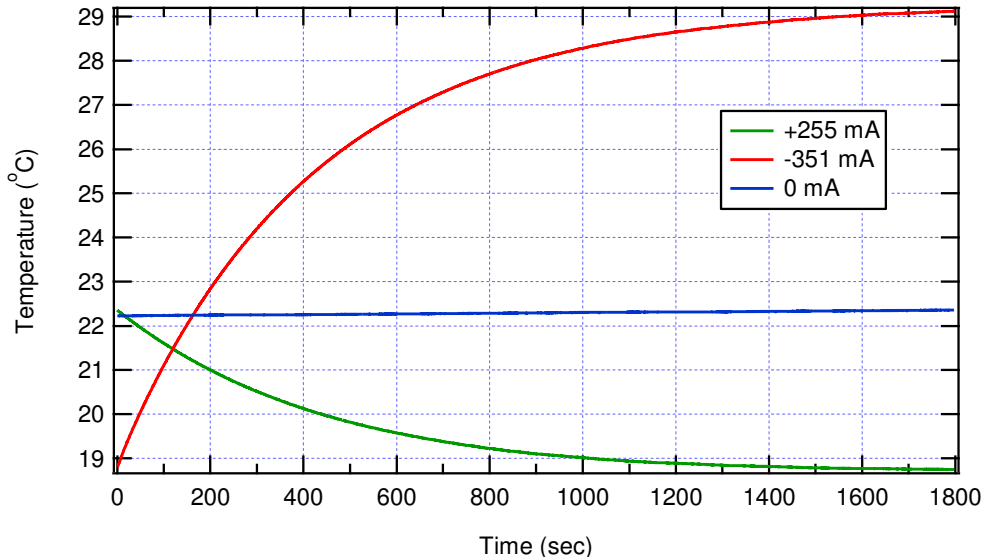


Figure 3.20 EOM temperature evolution with different currents applied to the Peltier modules

In fact, to increase the temperature changing speed, we can apply higher absolute value of current. However, our aim is to stabilize the EOM at normal room temperature (25 °C), so it is not necessary to do that. From these results, we can conclude that both the temperature measurement card and the Peltier mounting scheme to the EOM work fine. Now, we will create the temperature control circuit.

Then, we have developed a graphical user interface with Microsoft Visual Basic to monitor and control the temperature for the MZM. This program communicates with the DSP kit via RS232 Serial COM port with the Baud Rate is set to 57600. The

temperature data transmission from the DSP kit is tunable by software loaded to it.

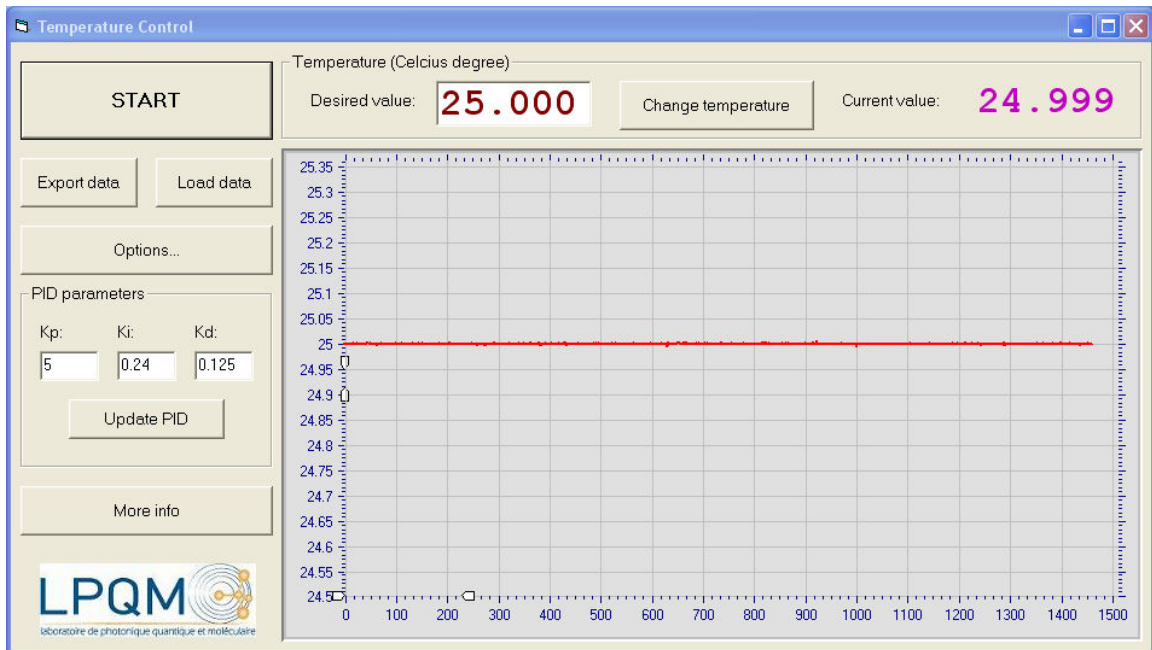


Figure 3.21 Compact view of temperature control software

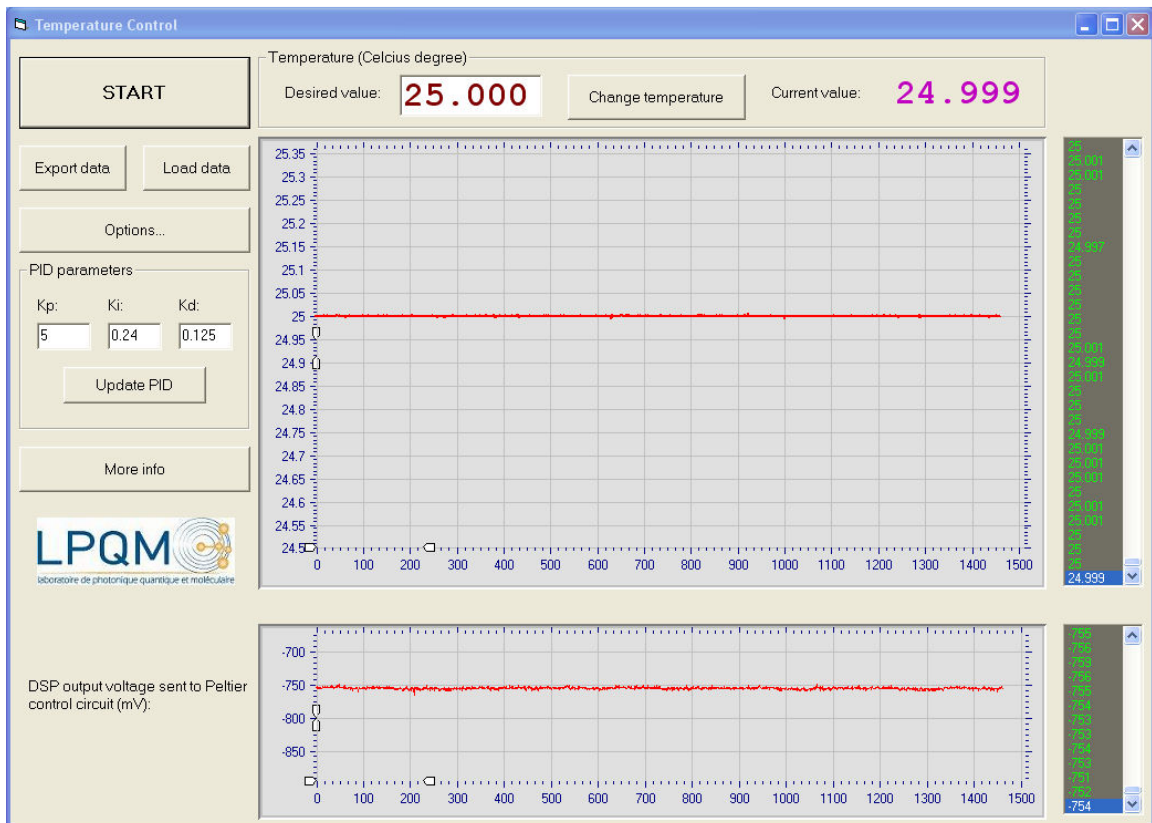


Figure 3.22 Full view of temperature control software

Figure 3.21 shows the controlled temperature at set point of 25 °C, for duration of

10 minutes at steady-state with 100 measured data sent per minute, the highest variation is 0.008 °C and the steady-state error is +0.0019 °C.

“More info” button shows the DSP output voltage sent to Peltier control circuit as shown in Figure 3.22 and two data lists which can be exported to Microsoft Excel by clicking on the button “Export data”. The PID parameters can be modified to meet specific demand and sent to DSP kit by clicking “Update PID” button.

Figure 3.23 shows the evolution of the temperature of the EOM when we change the temperature setpoint from 20 °C to 25 °C. The overshoot of the control is only 0.2 °C. The lower chart shows control voltage sent to temperature tuning card.

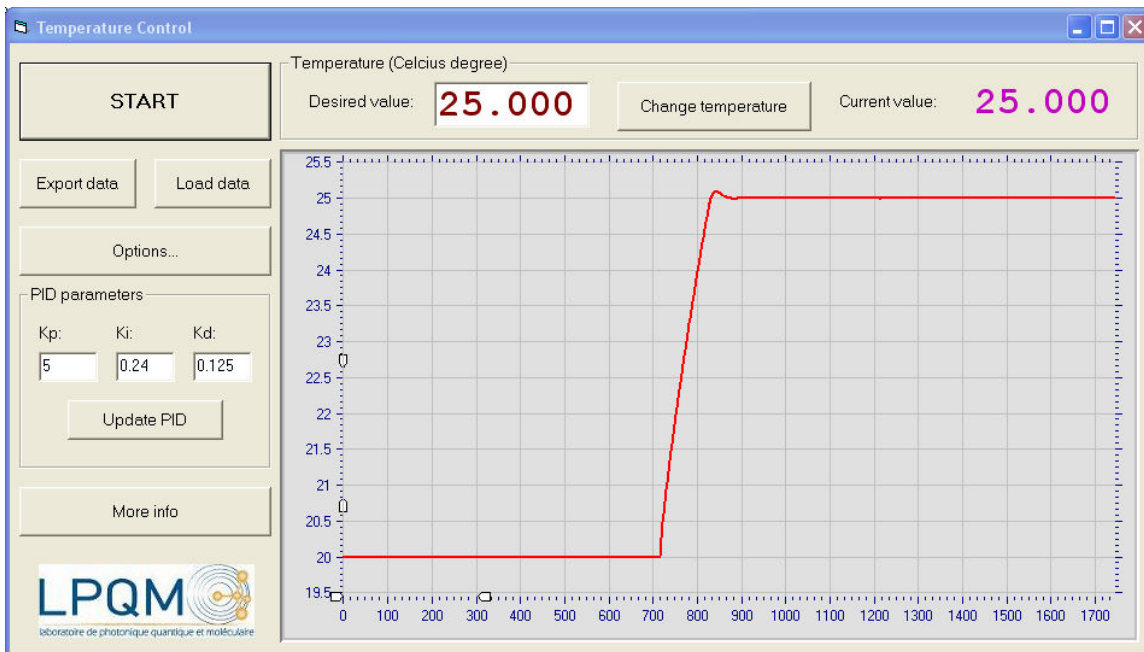


Figure 3.23 Changing temperature from 20 °C to 25 °C

3.4 Temperature impact on average optical output power of the EOM

The stability of the average optical output power of the EOM can be estimated by using the internal photodiode of the EOM. The electronic card to convert the internal photodiode current to DC voltage is presented in section 4.2.1.

We implemented two experiments to estimate the impact of temperature on the average optical output power of the EOM based on the configuration illustrated in Figure 3.24. The modulator is biased at its quadrature point of +5.5 V and at its optical input, a laser power of 1.50 mW is supplied.

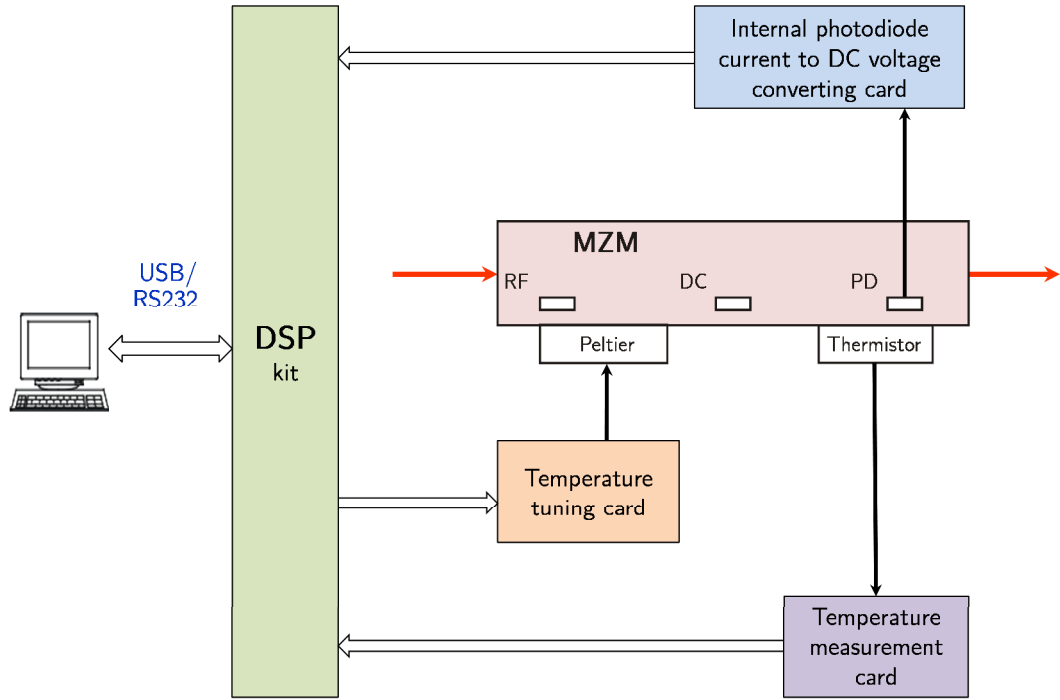


Figure 3.24 Structure for estimating the temperature impact on the average optical output power of the EOM

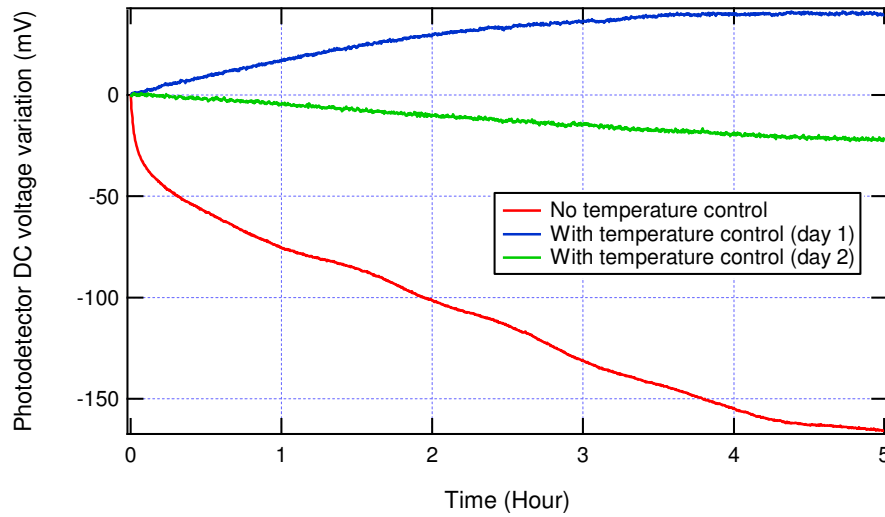


Figure 3.25 Evolutions of photodetector output DC voltage at different working conditions

In the first experiment as shown in Figure 3.25, the EOM is not thermally stabilized. We measure the change of the DC voltage which is converted from photodiode current, it is marked by the red curve. Then, we apply temperature control to the EOM to stabilize it at 25 °C and measure the changes of DC voltage for two different 5 hours duration on two different days. The first day is marked by the blue

curve and the second day is marked by the green curve. Because the starting DC voltages of three measurements are different, so in order to have a clearer comparison, each data stream is plotted relatively to its starting value.

Without temperature control, the change of photodetector output DC voltage is -165 mV, while with temperature control process it is reduced to $+39$ mV for the first day and -22 mV for the second day. Obviously, the optical average output power of the EOM is affected by the ambient temperature.

To present more clearly the changes of photodetector DC voltage caused by temperature variation, we implement the second experiment in which we tune the temperature of the EOM to different values. The results are illustrated in Figure 3.26.

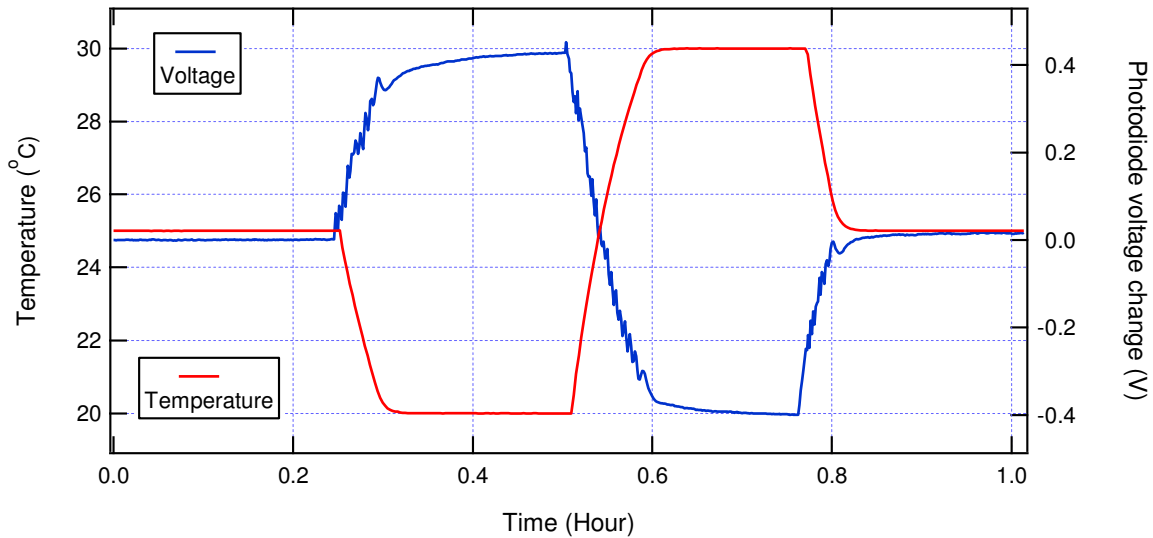


Figure 3.26 Photodetector output DC voltage evolution under temperature changes

At 25 °C, the photodetector voltage is unchanged. After 15 minutes, we decrease the temperature from 25 °C down to 20 °C, the photodetector DC voltage variation increases from 0 to $+0.4$ V. After 15 minutes more, we increase the temperature from 20 °C to 30 °C, the photodetector output DC voltage change decreases from $+0.4$ V to -0.4 V. Finally, we reduce the temperature from 30 °C to 25 °C and the photodetector output DC voltage comes back closely to 0.

From results of these two experimental, it is easy to recognize that the average optical output power of the EOM, presented in the form of photodetector output DC voltage, is clearly affected by the temperature.

3.5 EOM temperature and its transfer function

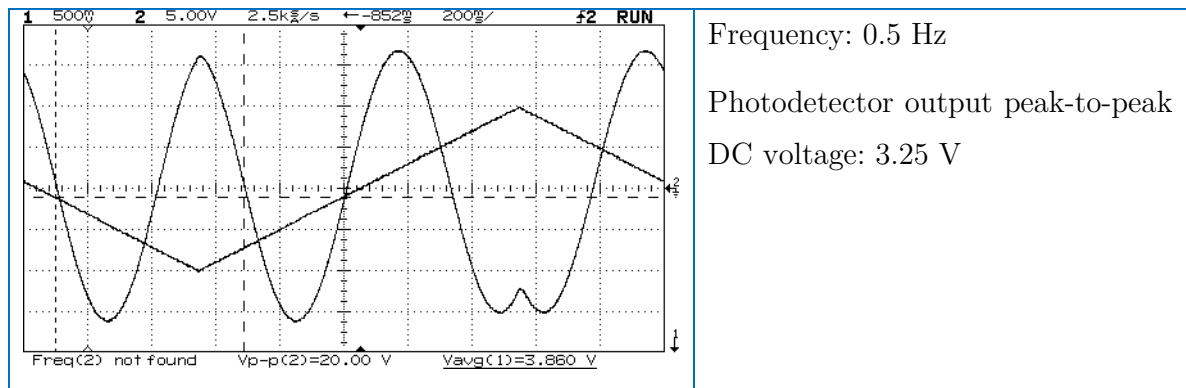
3.5.1 Transfer function determination

The EOM used for this study is a Mach-Zehnder (MZ) intensity modulator. It is a commercial device made of lithium niobate material (LiNbO_3) (ref. MX-LN-10 from Photline Company) with a 12 GHz modulation bandwidth. It has already been presented in a previous work [67]. The EOM has two electrodes, one for the bias signal (for DC or quasi DC signals) and one for the modulating signal corresponding to the data to be transmitted (AC high frequency signals). A laser diode at 1550 nm wavelength provides the constant laser beam intensity at the optical input of the EOM.

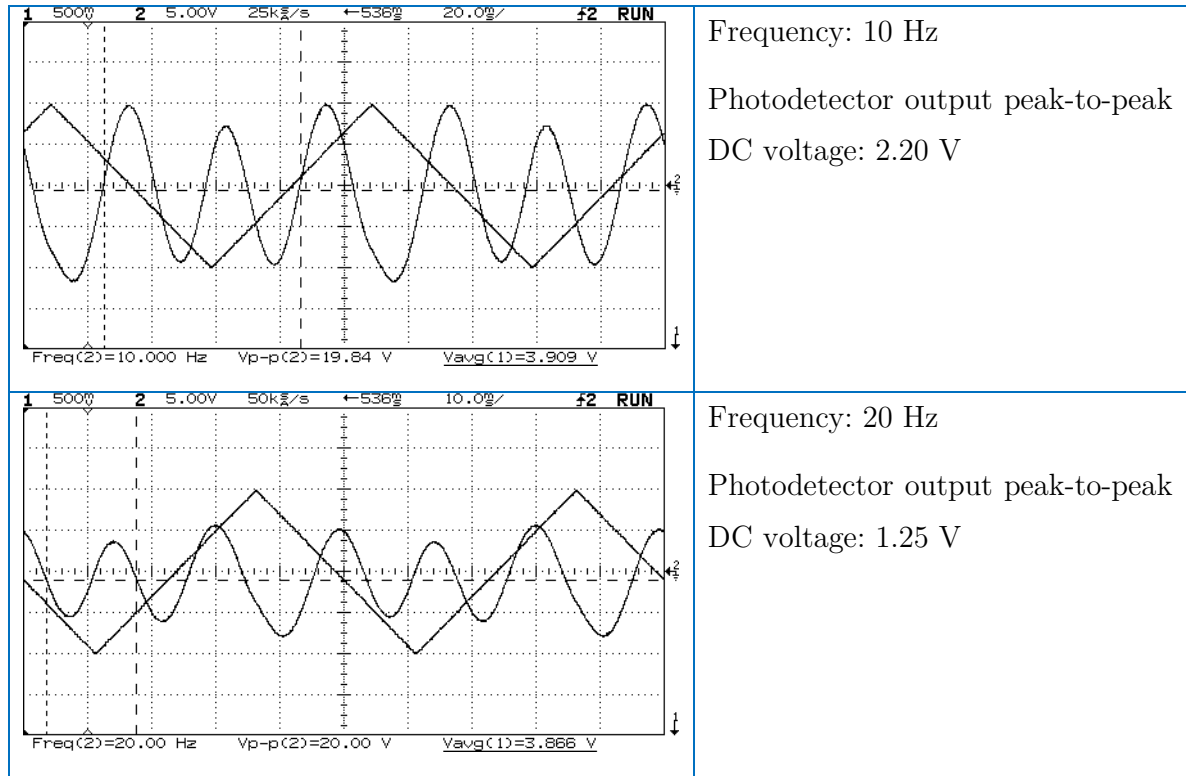
The principle to determine the transfer function of an EOM is to change slowly the bias voltage applied to the EOM and simultaneously register the optical output power. After getting the complete data, the transfer function can be achieved by drawing the optical output power as a function of bias voltage. In this part, we present the determination of the EOM transfer function by using laboratory instrumentations.

Because the EOM transfer function is “static” characteristic, the principle is to inject a low frequency triangle signal to the DC electrode of the EOM. We use an Agilent Arbitrary Waveform Generator HP 33120A to create a triangle signal at different frequencies as listed in Table 3.4, with a peak-to-peak amplitude of 20 V and an offset of 0 V. This triangle signal is fed into the DC electrode of the EOM. A laser power of 1.5 mW is injected into the input of the modulator.

Table 3.4 *EOM photodetector output DC voltages at different triangle signal frequencies shown on the oscilloscope screen.*



<p>1 500ns 2 5.00V 2.5k/s ←536g 200g/ f2 RUN Freq(2)=996.0MHz Vp-p(2)=19.84 V Vavg(1)=3.850 V</p>	<p>Frequency: 1 Hz Photodetector output peak-to-peak DC voltage: 3.25 V The shape is the same with the case of using 1 Hz frequency.</p>
<p>1 500ns 2 5.00V 10k/s ←536g 50.0g/ f2 RUN Freq(2) not found Vp-p(2)=19.84 V Vavg(1)=3.836 V</p>	<p>Frequency: 3 Hz Photodetector output peak-to-peak DC voltage: 3.00 V</p>
<p>1 500ns 2 5.00V 10k/s ←536g 50.0g/ f2 RUN Freq(2)=5.000 Hz Vp-p(2)=19.84 V Vavg(1)=3.839 V</p>	<p>Frequency: 5 Hz Photodetector output peak-to-peak DC voltage: 2.75 V</p>
<p>1 500ns 2 5.00V 25k/s ←536g 20.0g/ f2 RUN Freq(2) not found Vp-p(2)=20.00 V Vavg(1)=3.828 V</p>	<p>Frequency: 7 Hz Photodetector output peak-to-peak DC voltage: 2.50 V</p>



From the experimental results, we found that when the triangle signal frequency is increased, the photodetector output peak-to-peak DC voltage decreases. Especially, when 20 Hz frequency is used, the measured transfer function is severely distorted with the peak-to-peak voltage is reduced from 3.25 V in 0.5 Hz to only 1.25 V. Consequently, bias point determination will not be accurately determined. At frequencies of 0.5 Hz and 1 Hz, the transfer functions are similar and clear. It means that in order to achieve an accurate transfer function, a frequency lower than 0.5 Hz should be used.

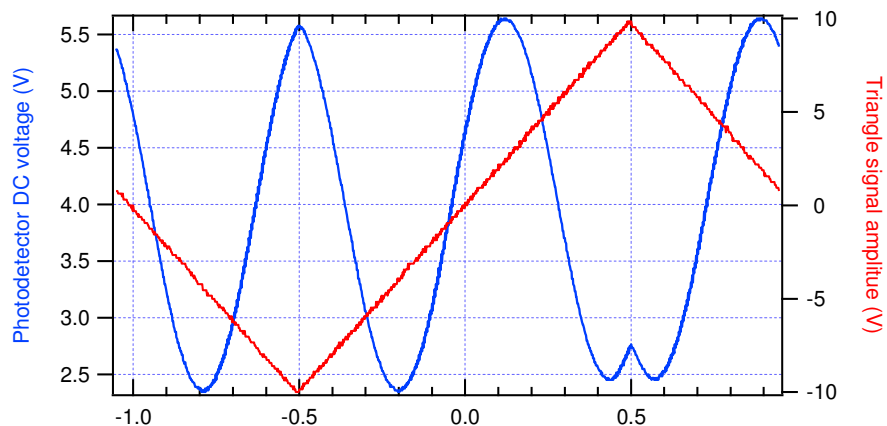


Figure 3.27 Photodetector DC voltage and 0.5 Hz triangle signal represented in Igor

To draw the transfer function, after capturing screen of the oscilloscope, we also

need to record the raw data. For example, from the raw data achieved in the case of using 0.5 Hz frequency, we can redraw the two curves of the EOM with Igor software as below.

The Figure 3.27 is the same with the captured screen shown in Table 3.4. Then, in order to visualize the transfer function, we need to present the photodetector output DC voltage as function of triangle signal amplitude.

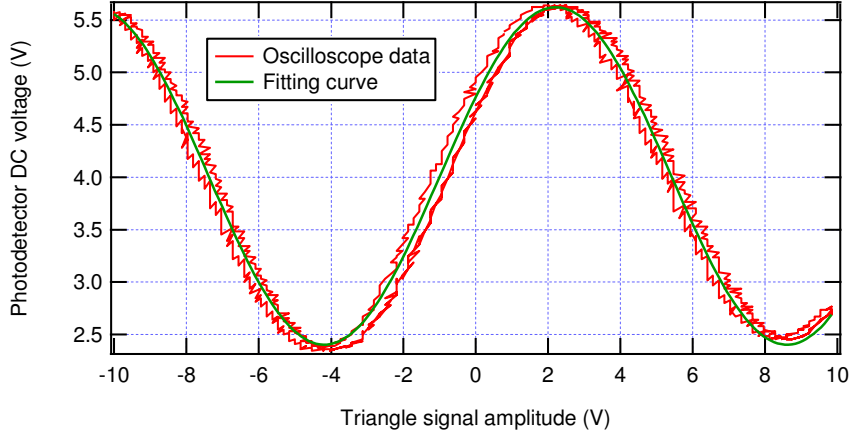


Figure 3.28 Transfer function: oscilloscope data and fitting curve

The resulting curve shown in Figure 3.28 presents the output voltage of a photodetector placed at the output of the modulator, as a function of the slowly varying voltage applied to the DC electrode. The transfer function displays a sinusoidal behavior and the equation corresponding to the experimental results is given by:

$$V_{out}(V_b) = V_0 + V_{oM} \sin(K \cdot V_b + \phi_0) \quad (3.22)$$

Where:

$$V_{oM} = (1.6107 \pm 0.0057) \text{ V}$$

$$V_0 = (4.0132 \pm 0.0042) \text{ V}$$

$$K = (0.4910 \pm 0.0006) \text{ V}^{-1}$$

$$\phi_0 = (0.4849 \pm 0.0037) \text{ rd}$$

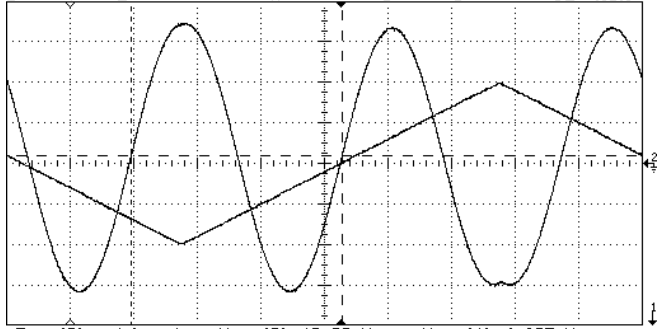
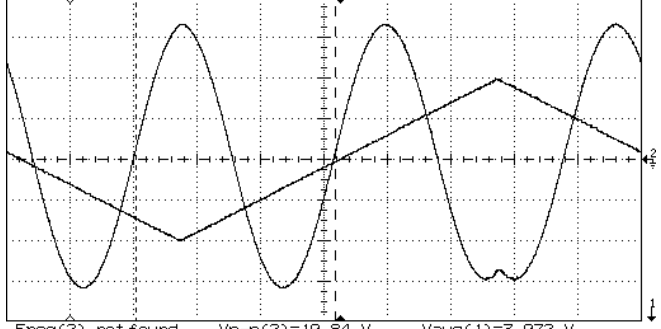
From this equation, the half-wave voltage can be determined by $V_\pi = \pi/K$ and we found the half-wave voltage of this EOM is $V_\pi = (6.3980 \pm 0.0085) \text{ V}$.

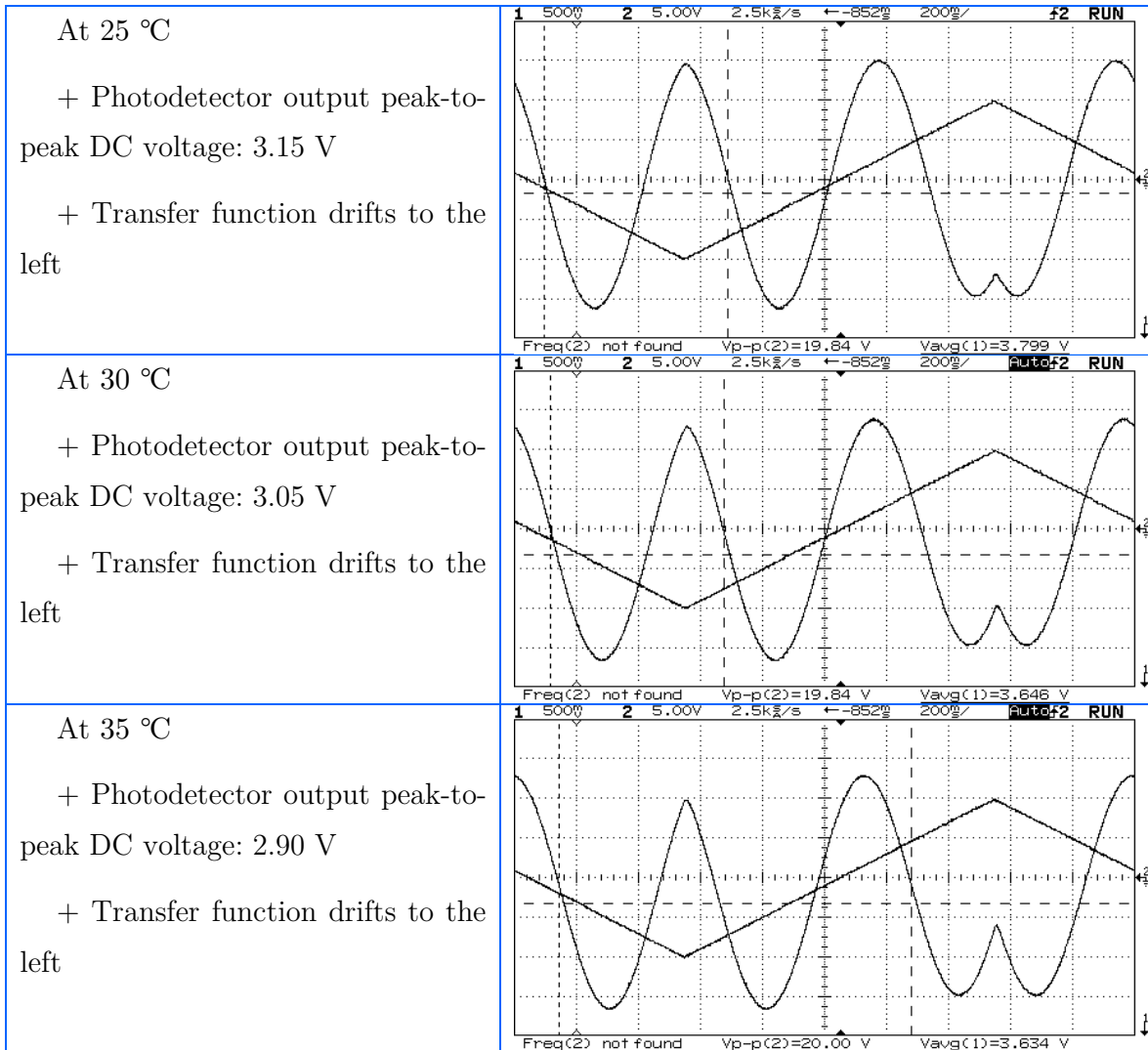
3.5.2 Transfer function drift

To visualize the impact of temperature on EOM transfer function, the frequency of triangle signal is set to 0.5 Hz, then we change the temperature of the EOM at different values and capture 2 data streams of photodetector output DC voltage and the amplitude of triangle signal from the oscilloscope. The results are listed in Table 3.5.

In order to see the “real” transfer function of the EOM, we need to perform procedures similar to those presented in previous section (3.5.1). However, due to the fact that, two data streams on the oscilloscope are presented in the time domain, so by keeping the same setting for the oscilloscope and observing captured screens, we can have a quite clear view about the drift of the transfer function.

Table 3.5 EOM photodetector output DC voltages at different temperatures shown on the oscilloscope screen

<p>At 15 °C</p> <p>+ Photodetector output peak-to-peak DC voltage: 3.25 V</p>	 <p>1 500ns 2 5.00V 2.5kHz/s ← 852ps 200ps/div #2 RUN</p> <p>Freq(2) not found Vp-p(2)=19.69 V Vavg(1)=4.063 V</p>
<p>At 20 °C</p> <p>+ Photodetector output peak-to-peak DC voltage: 3.25 V</p> <p>+ Transfer function drifts to the left</p>	 <p>1 500ns 2 5.00V 2.5kHz/s ← 852ps 200ps/div Auto#2 RUN</p> <p>Freq(2) not found Vp-p(2)=19.84 V Vavg(1)=3.972 V</p>



It is easy to figure out that the temperature variation does not only make the EOM transfer function drift phenomenon more clearly but also make the transfer function deformed. To simplify the transfer function determination, another method will be presented in Chapter 4, section 4.2.2.

3.6 EOM temperature variation and OEO oscillation power

From above results, we know that the EOM is significantly affected by the temperature. In the OEO structure, EOM plays an important role. In this section, we study how EOM behavior under temperature changes can influence the OEO oscillation characteristic.

We use the OEO structure as presented in Chapter 2. The EOM is thermally stabilized at 15 °C, the OEO is started with oscillation power is 7.35 dBm. Then the

temperature is increased to 35 °C, the oscillation power reduces gradually. At the time of 583 s, the oscillation power drops from 0 dBm to -57 dBm, and consequently the oscillation is lost.

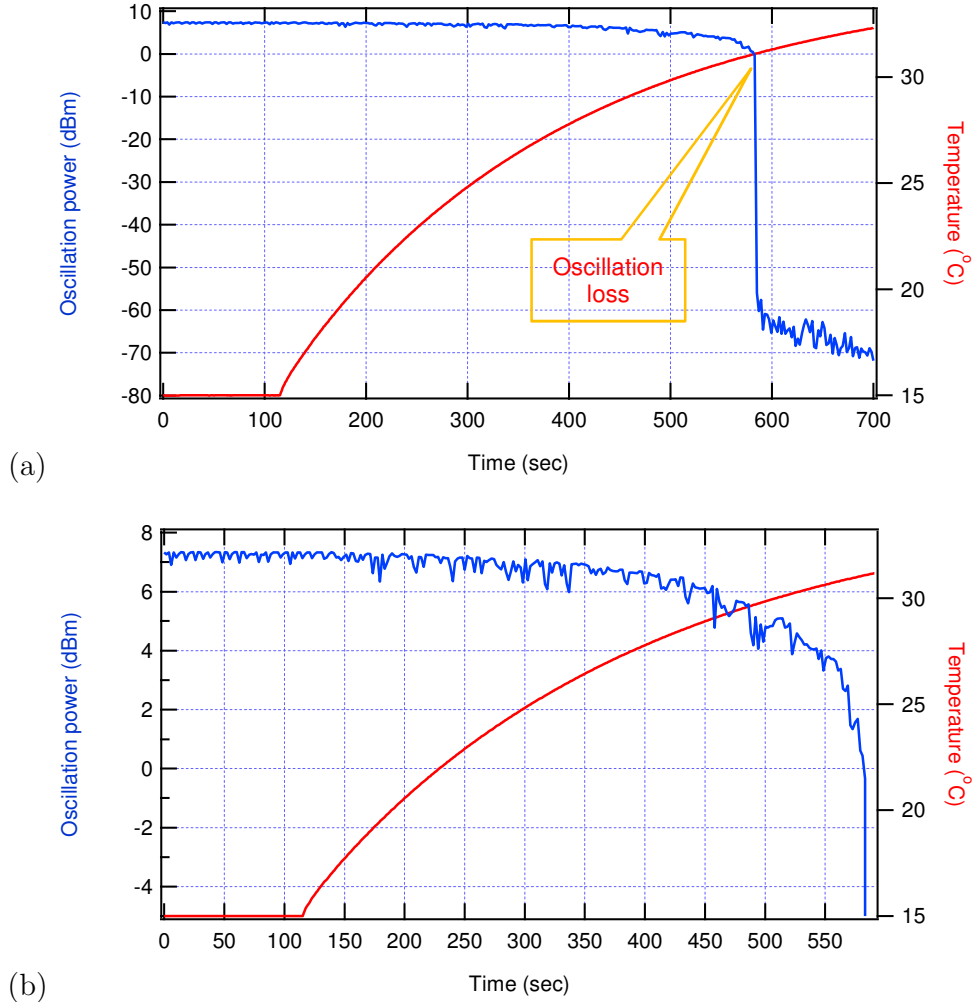


Figure 3.29 OEO oscillation loss phenomenon due to EOM temperature change

Figure 3.29 (a) shows the relation between the EOM temperature evolution and the OEO oscillation power during 700 s. Figure 3.29 (b) shows a closer view of (a) which is equivalent to 590 s.

3.7 Fiber loop temperature and OEO oscillation frequency

The long-term stability is usually estimated by the oscillation frequency drift in a long duration. In 2003, D. Eliyahu *et al.* made an experiment to figure out the relation of the oscillation frequency versus the temperature during 52 days [76]. There are two

high Q elements in the OEO: the optical fiber loop and the RF filter. Both are sensitive to the surrounding temperature variations, leading to a change of the phase shift and so creating a drift of the oscillation frequency. The fiber delay change due to temperature has the strongest contribution to the oscillation frequency drift with a slope of about -8 ppm/ $^{\circ}\text{C}$ [77]. The negative sign indicates that the change of frequency has opposite direction with the change of temperature. Comparing with the case of fiber, the temperature has less impact on the RF filter with a phase drift of -0.3 ppm/ $^{\circ}\text{C}$.

The result mentioned above was carried out in very good laboratory conditions with thermal stability kept as low as 0.001 $^{\circ}\text{C}$ and 0.003 $^{\circ}\text{C}$ over 1 hour and 24 hours respectively. In the real implementation, this condition is sometimes difficult to be satisfied. In this real case, in order to use the OEO for any application, it is substantial to analyze the behavior of the OEO under the real condition.

To estimate the relation between the fiber temperature and the OEO oscillation frequency, we need to record the temperature and the oscillation frequency data at the same time for a long duration.

3.7.1 Data acquisition program

The oscillation frequency and power are measured with our Agilent spectrum analyzer PSA E4446A connected to a personal computer (PC) by an IEEE-488 (Institute of Electrical and Electronics Engineers) interface with following parameters:

- Center frequency determined by peak search function and the returned value is the oscillation frequency of the OEO.
- Span: 50 kHz.
- Resolution bandwidth: 470 Hz
- Sweep points: 600 points.

Another software was used in our experiment is Agilent VEE Pro – a graphical dataflow programming development environment. It is optimized for building automated test and measurement applications [78]. VEE is originally developed by Hewlett-Packard in 1991, it stood for Visual Engineering Environment then it has been renamed to Agilent VEE.

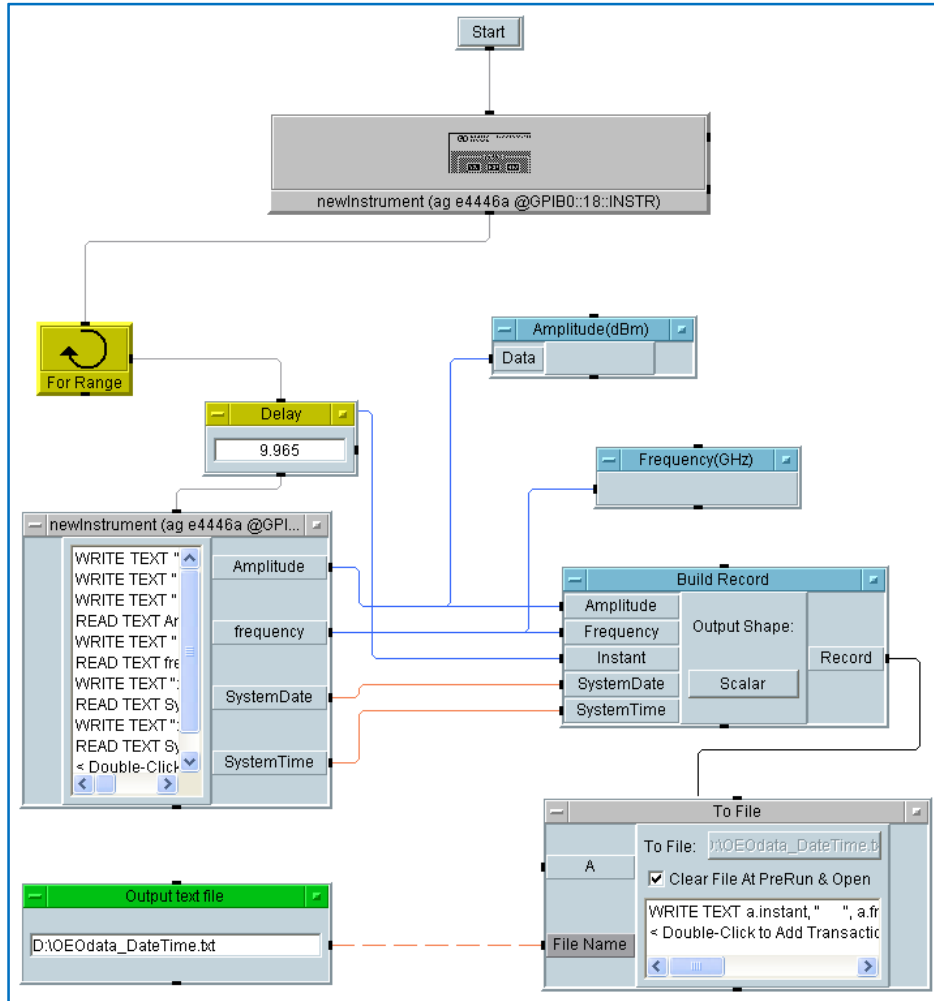


Figure 3.30 OEO oscillation data acquisition program in Agilent VEE Pro 9.3

To record the measurement data, we created an acquisition program with Agilent VEE Pro 9.3. The block diagram of this program is shown in Figure 3.30.

Fourth parameters are recorded includes:

- Oscillation frequency (Hz)
- Oscillation power (dBm)
- System date information of the PSA E4446A
- System time information of the PSA E4446A

The date and time information is used for post tracking and for synchronizing with temperature data measured DSP mentioned in 3.1. All these information is saved to a text file (.txt) and then this text file is converted to Microsoft Excel and imported into Igor software for analysis and creating comparison charts.

The interval between two recordings is 10 s. This interval is defined by the “Delay” block. However, if we set Delay = 10 s, the experimental results saved in the text file showing that the real interval is greater than 10 s but very close. The tolerance can be explained by the time used for sending commands to PSA, receiving result and writing to the text file. This tolerance depends on the measurement instrument and the configuration of the PC. With our system, after doing some tests and calibrations, we found the real interval of 10 s can be guaranteed by setting Delay = 9.965 s.

“For Range” block allows us to specify “From”, “Thru” and “Step” parameters. The program’s counter starts from “From” value to “Thru” value with an increment of “Step” value.

3.7.2 Measuring temperature and oscillation frequency

In our experiment, we used a commercial fiber loop with a plastic protective box. This plastic box was then put into a thermal box which operates based on Peltier effect with stability of ± 1 °C. This thermal box and other system were arranged inside a room without any air conditioner.

We use the temperature measurement card mentioned in 3.1 to monitor the temperature of the fiber loop during 13 hours. The temperature information is amplified and transmitted to our Digital Signal Processing (DSP) kit. This DSP then sends temperature information to a Personal Computer via RS232 port. At the same time, the oscillation frequency is recorded every 10 s by a program created and executed within Agilent VEE environment. Two data streams then are processed, synchronized, plotted by Igor software and the result is presented in Figure 3.31.

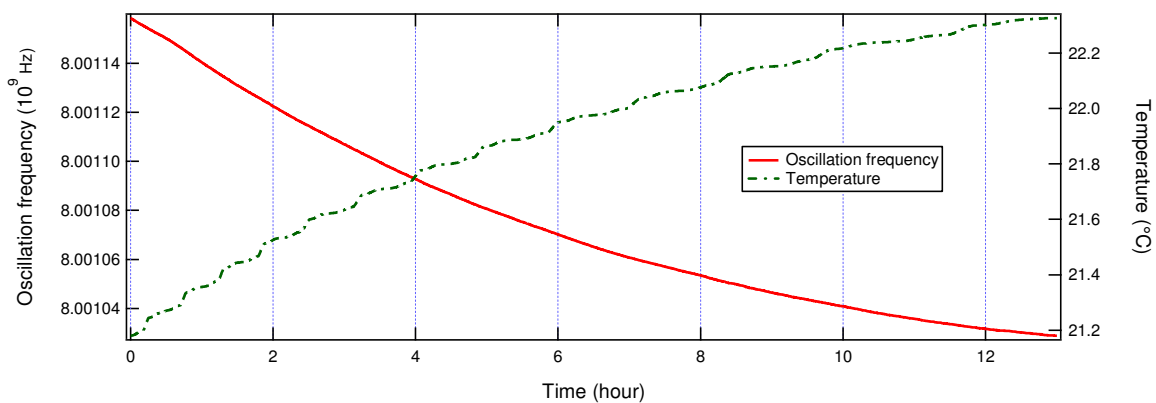


Figure 3.31 Drift of the oscillation frequency and temperature changes versus time

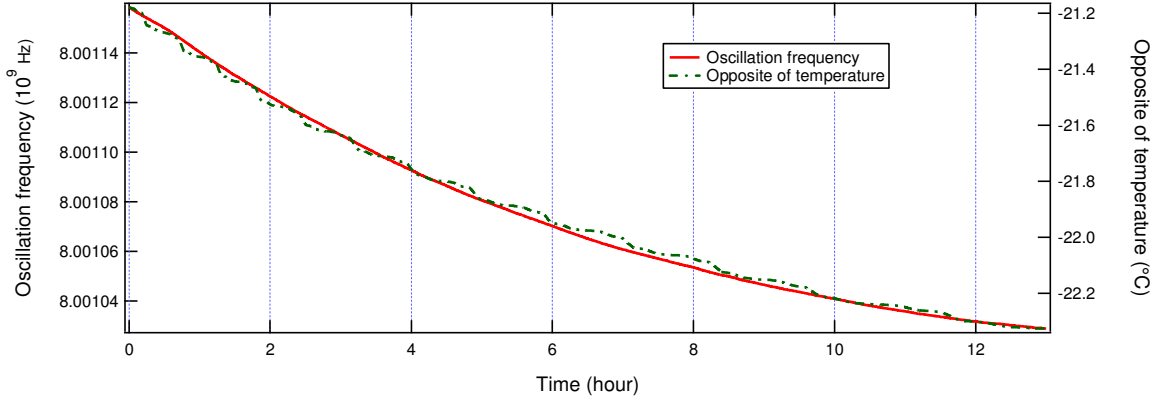


Figure 3.32 Drift of the oscillation frequency and opposite temperature changes versus time

The oscillation frequency is presented simultaneously with the opposite temperature to show more clearly their correlation as shown in Figure 3.32. The drift of the OEO oscillation frequency appears clearly and there is a good correlation between the two curves. In Figure 3.33, the oscillation frequency is presented as a function of the opposite temperature showing a linear relation between them, and a fitting line from Igor software leads to the modeling expression in Eq. (3.23).

$$f_{osc} = 8.003619 \times 10^9 + 1.161 \times 10^5 \times (-\theta) \quad (3.23)$$

where θ is optical fiber temperature. So we can introduce the oscillation frequency fluctuations as the difference between the measured frequency and the value obtained by (3.23); these fluctuations are presented in Figure 3.34 as a function of time.

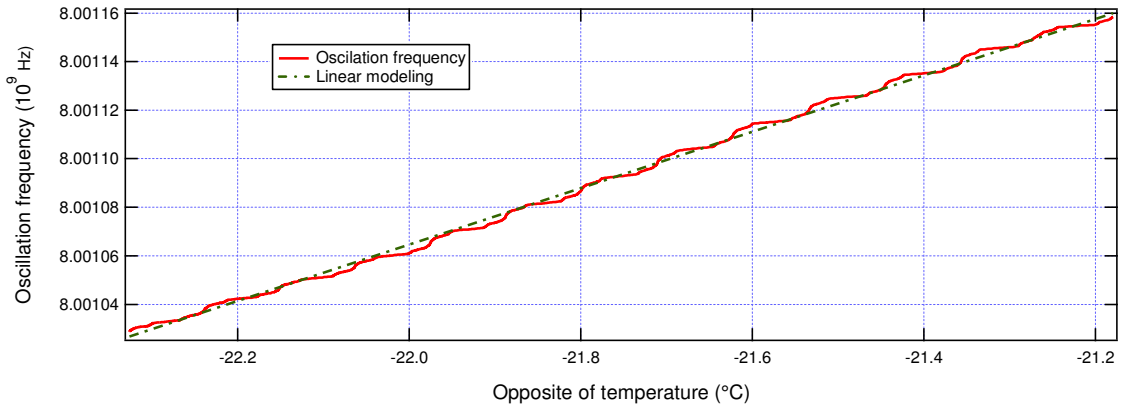


Figure 3.33 Oscillation frequency as a function of the opposite temperature and the fitting curve determining a modeling of the frequency drift behavior

The relevance of the modeling introduced here, can be checked by comparing the evolutions of the oscillation frequency in Figure 3.32 and Figure 3.34. In Figure 3.32 the peak-to-peak variation of the oscillation frequency is equal to 130 kHz, its

standard deviation is 37.53 kHz. For the fluctuations of the OEO frequency with respect to the modeling of Eq. (3.23), in Figure 3.34, the peak-to-peak variation is 7.02 kHz, and the standard deviation is 1.65 kHz. Taking into account the standard deviation, the improvement corresponds to a factor 23, and for a less flattering comparison, with the peak-to-peak variations, the improvement factor is equal to 18.5.

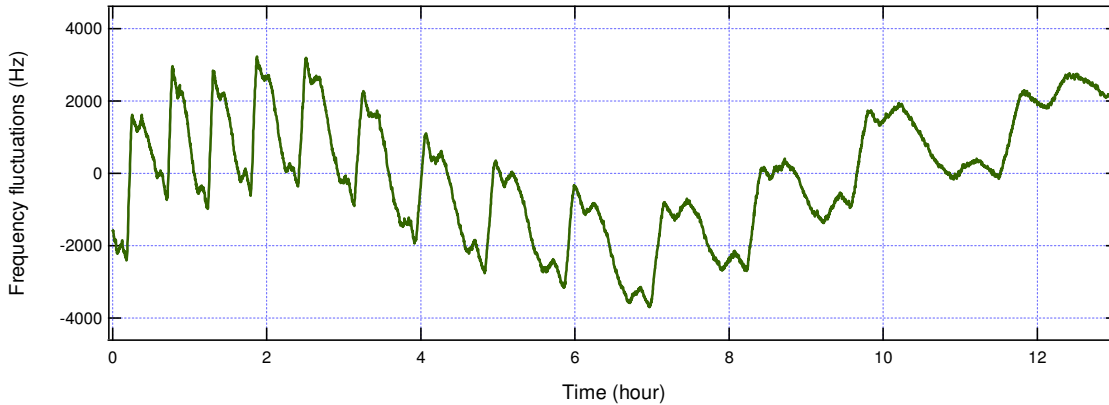


Figure 3.34 Fluctuations of the oscillation frequency compared to the modeling of Eq. (3.23) as a function of time

In Figure 3.34, we can clearly see a periodic behavior of the frequency fluctuations. It cannot be a "random" effect but seems to be a "periodic" one. It could be explained by the way of the thermal box containing the fiber loop is working: it is based on thermoelectric effect cooler, with a fan for circulating the air inside the box. The working time of the cooler and fan depends on the gap between the real temperature inside the box and the set-point but also on the difference between the room temperature and the internal temperature. The fluctuation repetition rate in the first four hour is faster than that in the last five hours. This can be explained by the fact that the room temperature in the morning is quickly increased by the direct sunlight. It makes the thermoelectric-based thermal box need to control its internal temperature more frequently than that in that last 5 hours, when the room temperature is more stable.

The results mentioned above improve the fact that the OEO oscillation frequency has close relation with temperature of the fiber loop. In Chapter 5, we will analyze this issue in comparison with the delay time across the fiber loop.

3.8 Conclusions and discussions

In this chapter, we presented analysis of several influences of temperature on

behavior of the EOM and the OEO. Firstly, we designed a temperature measurement schematic with Cadence OrCAD and fabricated the PCB card. Then we developed the temperature tuning card with the same technique with temperature measurement card. The system is designed around the DSP kit. The DSP kit interacts with PC via a RS 232 interface. A Graphical User Interface (GUI) software is developed with Microsoft Visual Studio to control, monitor and acquire data. The temperature control process is handled by a PID algorithm. With this system, we stabilized the temperature of the EOM at a desired value. Here, in our case, it is set to a temperature of 25 °C.

Secondly, we estimated the effect of temperature on average optical output power of the EOM with two experiments. The first experiment is conducted with and without temperature controls. The second one is conducted by controlling the EOM at different temperatures.

Thirdly, we demonstrated method to determine the transfer function of an EOM. Then we analyze the influences of temperature on the transfer function of the EOM. In the next chapter, we will introduce other techniques for stabilizing the EOM transfer function.

In the fourth experiment, we showed the influence of EOM temperature change on the stability of the OEO oscillation.

Finally, we carried out experiments to analyze the impact of fiber loop temperature on the OEO. This result shows the high correlation level between oscillation frequency and temperature variation that will be studied in more detail in Chapter 6.

Chapter 4

Controlling EOM by using DSP technique

As shown in Chapter 3, the drift of the EOM can be reduced by applying a thermal control to this EOM. However, there is still a small drift during operating time. This chapter presents other techniques to eliminate the transfer function drift. The evolution of the modulator characteristics can be followed through its non-linear behavior by detecting the second harmonic of a low frequency modulating signal injected to DC electrode of the modulator. Using DSP technique is a great improvement because of all the available possibilities.

4.1 Dither based bias control

4.1.1 Drift determination and control

4.1.1.1 EOM drift simulation

In order to visualize the drift behavior of the EOM, we have developed a simulation focusing on its transfer function. In Figure 4.1, the EOM transfer function is shown by blue curve in the upper left chart. This transfer function is simulated with bias voltage in the range of [-10 V, +10 V] which is similar to the output working range of the DSP. Under the EOM transfer function is a slider to change the real bias voltage applied to the DC electrode of the EOM. The current value of bias voltage is indicated by a magenta line in the EOM transfer function chart.

Under the bias voltage slider is the modulating signal graph with frequency of 500 Hz, the time duration for presenting here is $8 \cdot 10^{-3}$ seconds, which is equivalent to 4 cycles. This modulating signal then is fed to the DC electrode.

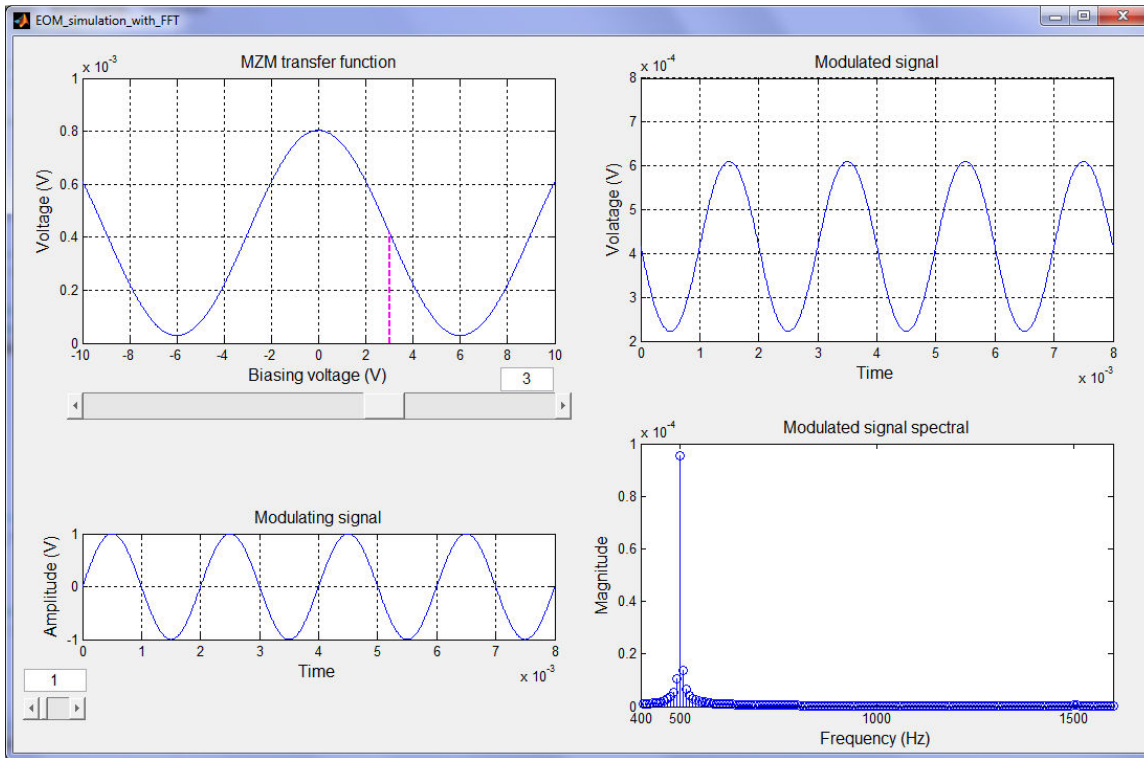


Figure 4.1 Simulation program for determining the MZM behavior ($V_{b0} = 3\text{ V}$)

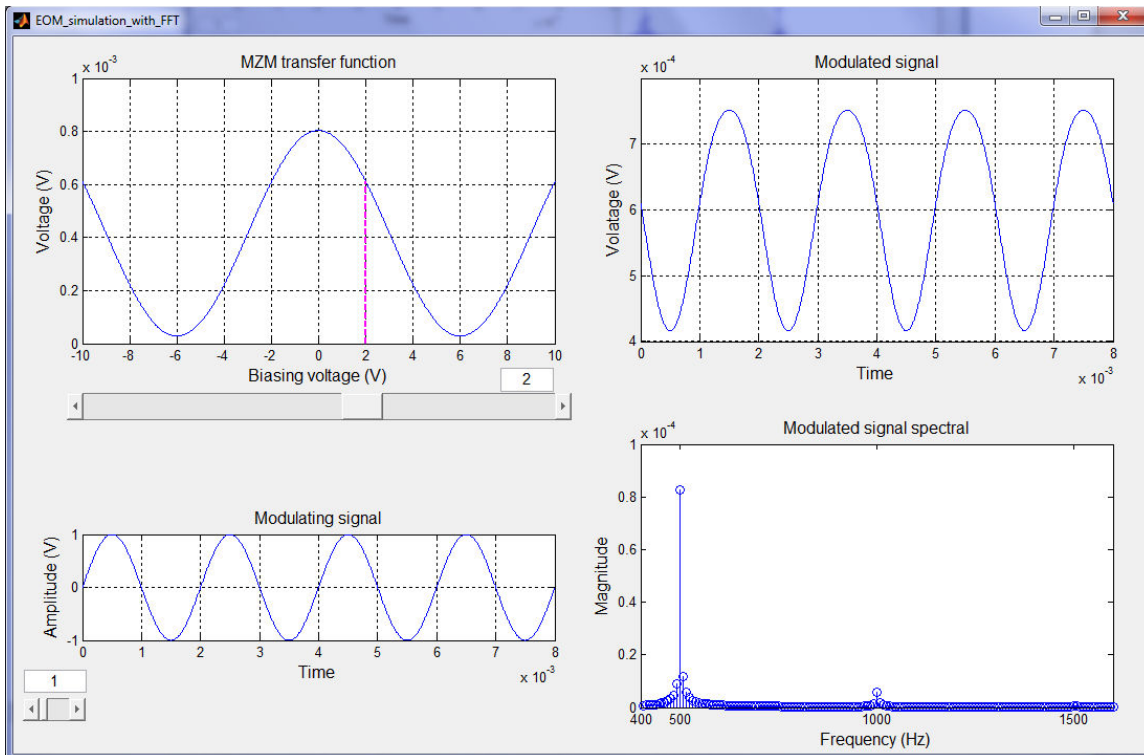


Figure 4.2 Modulated signal and its spectral when $V_{b0} = 2\text{ V}$

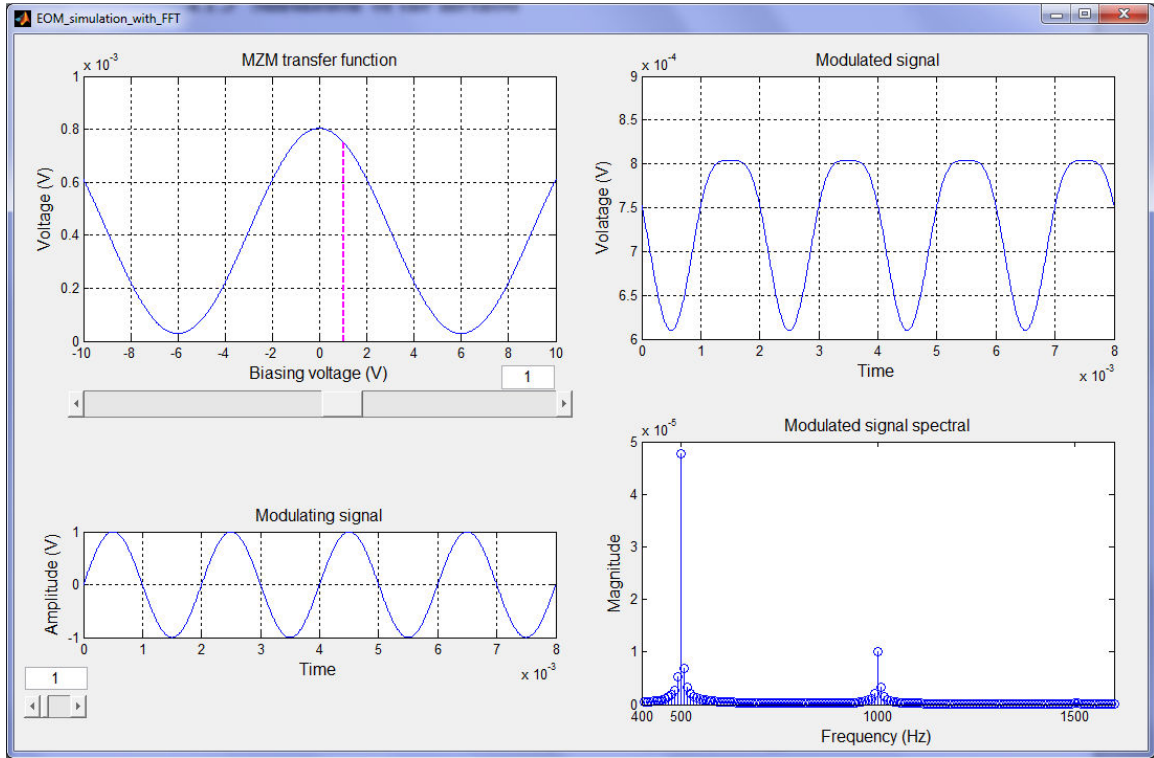


Figure 4.3 Modulated signal and its spectral when $V_{b0} = 1$ V

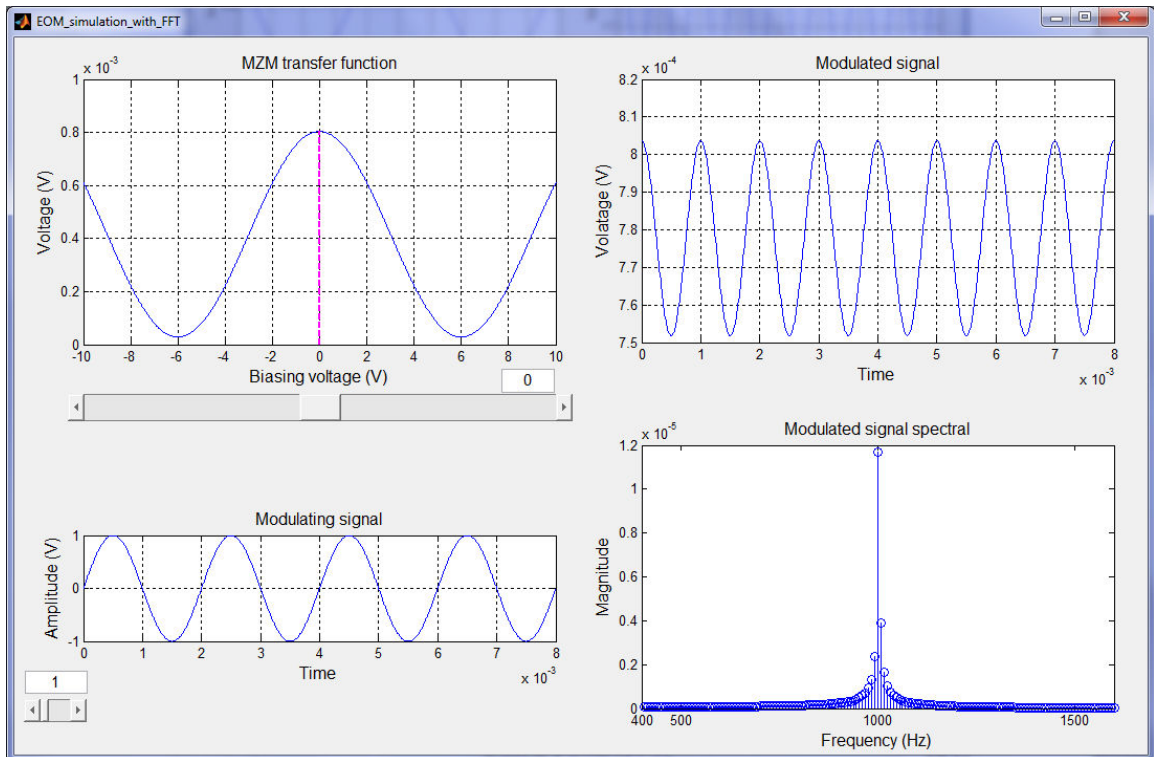


Figure 4.4 Modulated signal and its spectral when $V_{b0} = 0$ V.

The modulated signal is presented in the upper right chart corresponding to bias voltage of 3 V corresponding to the quadrature point. Because the EOM is working at the best linear point, so theoretically there are only 500 Hz component and other odd order harmonics components. There is no even order harmonics at this operating condition.

Under the modulated signal presented in the time domain is the spectral representation of modulated signal in the frequency domain.

In Figure 4.2, when the bias voltage is set to 2 V, the modulated signal is no more symmetric and contains both odd and even harmonics. It is clear to see both 500 Hz and 1 kHz signals in the modulated signal spectral chart at the bottom right. The 1000 Hz component becomes bigger when the bias voltage is set to 1 V as shown in Figure 4.3.

In Figure 4.4, the bias voltage is set to the peak point of transfer function. At this operating point, the output of MZM is the modulated signal with only the even order harmonics.

4.1.1.2 Drift determination principle

From the drift simulation results presented in previous section, a technique which has been developed to determine the drift level which based on a synchronous detection scheme is now introduced. The method for estimating the drift of the transfer function is based on an evaluation of the non-linear behavior of the modulator [35]. Testing the linearity of the modulator is performed by the way of a dither signal which is a sine wave, applied to the bias DC electrode for modulating the optical beam.

$$v_d(t) = V_D \sin(2\pi f_d t) \quad (4.1)$$

Because the dither signal $v_d(t)$ should not perturb the high modulated frequency dedicated to the transmitted data, we have chosen a rather low frequency $f_d = 500$ Hz. For detecting a non-linear effect with a good sensitivity the dither signal is a large signal with an amplitude $V_D = 850$ mV.

Taking into account a DC bias voltage V_{b0} and the modulating signal $v_d(t)$ applied simultaneously to the DC electrode.

$$v_m(t) = V_{b0} + v_d(t) \quad (4.2)$$

Then the transfer function in the time domain of the EOM is obtained from Eq. (1.4):

$$h_{op}(t) = \frac{P_{out}(t)}{P_{in}(t)} = \frac{\alpha}{2} \left\{ 1 + \eta \cos \left[\frac{\pi}{V_{\pi}} (V_{bo} + v_d(t)) + \phi(t) \right] \right\} \quad (4.3)$$

If the EOM is biased at the quadrature position then the transfer function is symmetric around this bias point, and $h_{op}(t)$ contains only odd harmonics. In case of a drift of the transfer function, the bias point is no more at the quadrature position and the curve is no more symmetric, even harmonics will appear in $h_{op}(t)$. The synchronous detection process is built in order to detect the amplitude of the second harmonic of the modulating signal $v_d(t)$. The optical signal at the output of the EOM is detected by a photodetector, then filtered around $2f_d$; then there is the multiplication process by a reference signal at $2f_d$ and a low pass filtering (see Figure 4.5).

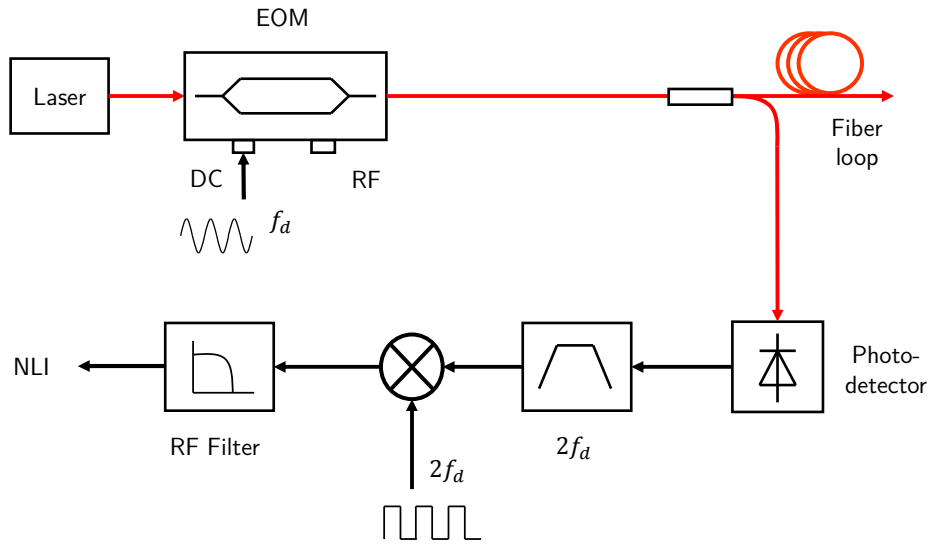


Figure 4.5 Block diagram of Non-Linear Indicator evaluation

The output of detection scheme indicates level of the second harmonic component in the modulated signal and it is an indication of drift level of current bias point on the transfer function. This quantity has been called the Non-Linear Indicator during our development steps and is denoted with the acronym *NLI*. *NLI* equals to 0 when the EOM is biased at quadrature point and it increases when the bias point is drifted.

4.1.1.3 Drift control scheme in DSP

From above analysis, drift control is a process to keep *NLI* close to 0 as much as possible. There are different techniques have been developed to control the EOM and

can be classified into two categories: dither-less category and dither-based category. In dither-less category, the operating parameters of modulated signal are directly analyzed [32], [79], [80]. In the second category, a dither signal is injected into the EOM then the modulating signal is observed [31], [81] or the second harmonic of dither signal is estimated [67], [82].

From Figure 4.5, we propose a control scheme in DSP as shown in Figure 4.6 with input is photodetector output voltage and the output is bias voltage will be sent to DC electrode of the EOM.

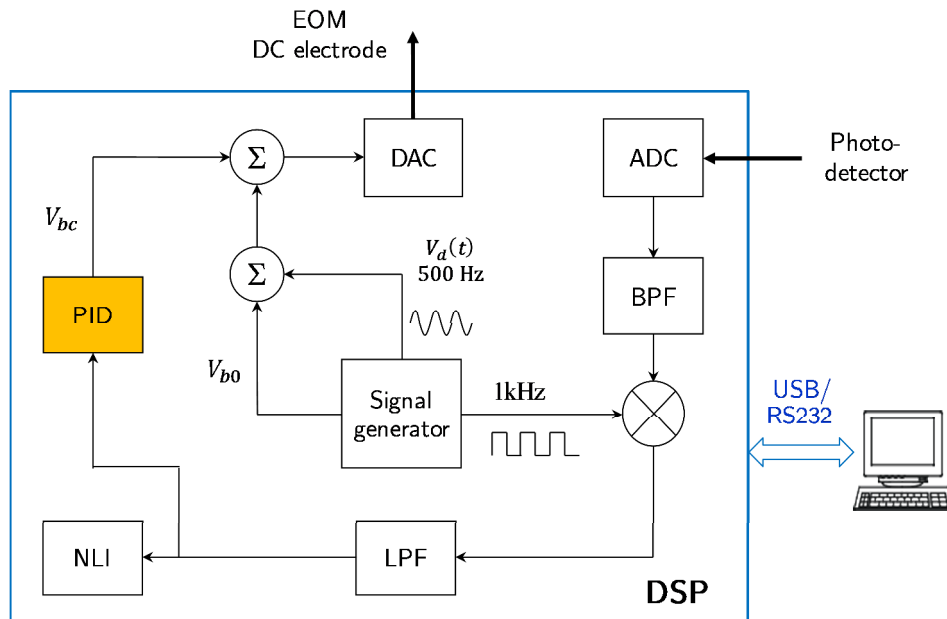


Figure 4.6 Bias control scheme in DSP

The modulating signal $v_d(t)$ is obtained by a VCO block in Matlab/Simulink with a sampling frequency $f_s = 40$ kHz leading to 80 points in one period. The signal at $f_{2d} = 2f_d = 1$ kHz is built with the same method, but it is a square signal. The photodetector output signal is directly acquired by the Link-Research board also with sampling rate of 40 kHz.

Similar to temperature control described in section 3.3, a PID controller is used again. However, in this case, the input of PID controller is not the different between setpoint and current value but only the NLI .

4.1.1.4 Designing model with Matlab/Simulink

From the knowledge of NLI it is possible to build a control system for compensating the changes of $\phi(t)$ by adding a control signal to the bias voltage V_{b0} in

order to keep $NLI \approx 0$: the bias point is controlled at the quadrature position. The control loop is designed with a PID controller [75], [83]. The experimental system for controlling the bias point of the EOM at a quadrature position is presented as it has been developed with Matlab Simulink in Figure 4.7.

The signal $v_m(t)$ applied to the DC electrode has three components, tuned from the eZdsp-DSP-F28335 board: the DC bias voltage V_{b0} , the dither signal $v_d(t)$ at $f_d = 500$ Hz and the control signal V_{bc} obtained from the digital PID.

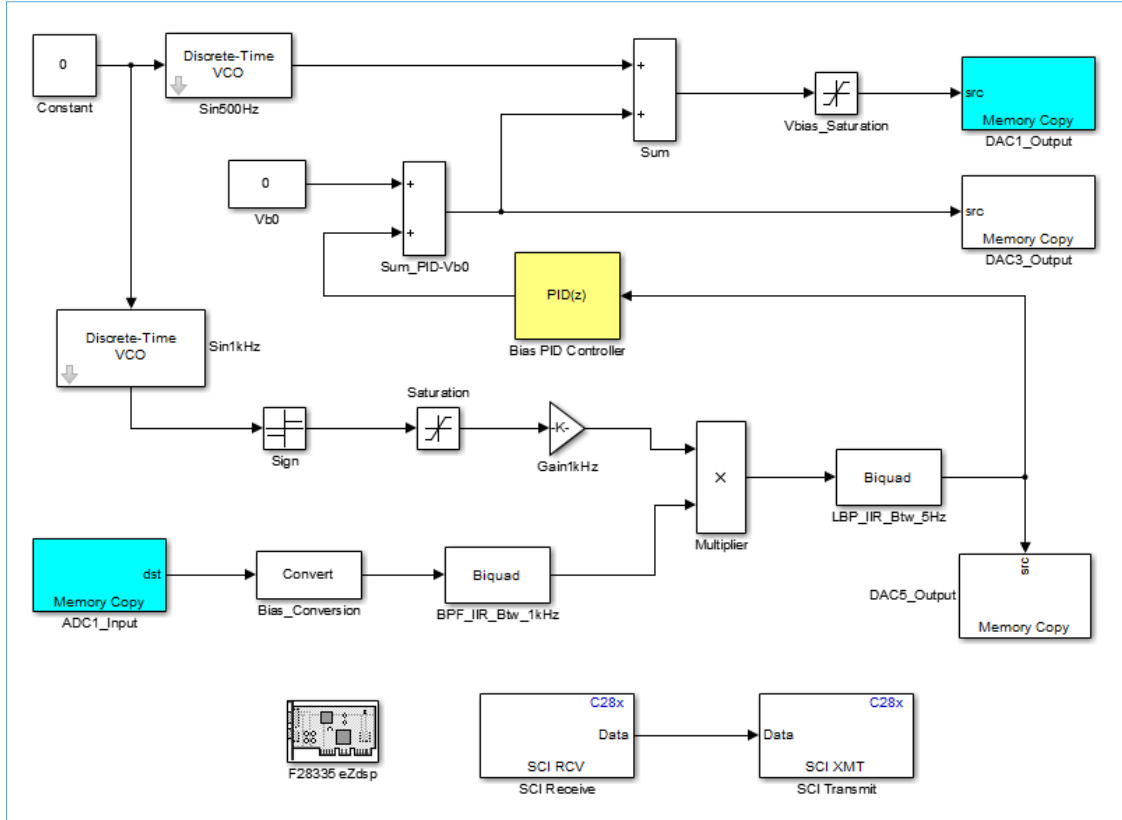


Figure 4.7 Matlab Simulink model for controlling the EOM bias point.

The generation of dither signal and of reference signal at 1 kHz is achieved by two VCO blocks. The input signal at ADC1 comes from the photodetector and the output signal $v_m(t)$ is placed at DAC1 for applying to the EOM electrode. The other outputs are $V_{bias} = V_{b0} + V_{bc}$ at DAC3 and NLI at DAC5.

$$v_m(t) = V_{b0} + V_{bc} + v_d(t) \quad (4.4)$$

4.1.1.5 Digital filter

The band-pass filter is an important part of the system. It has been designed with the Filter Design & Analysis toolbox of Matlab [84]. There are two major digital filter

types: finite impulse response (FIR) and infinite impulse response (IIR) [85]. In this study, a second order Butterworth IIR filter has been chosen because its advantage in requiring lower filter order than FIR filter to achieve the same performance level. For designing the filter, the center frequency is 1 kHz, the sampling frequency 40 kHz and the two cut-off frequency are 998 Hz and 1002 Hz. The frequency response of the filter (shown in Figure 4.8) has been obtained from a function generator and an oscilloscope.

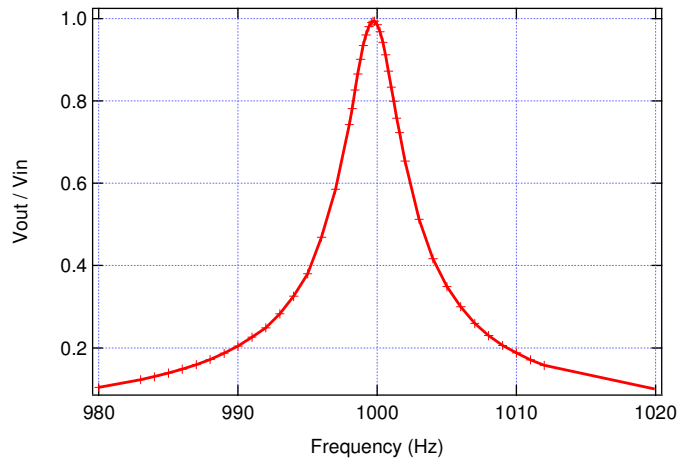


Figure 4.8 Frequency response of the band-pass filter

Experimentally the bandwidth of the filter centered at $f_{2d} = 2f_d = 1$ kHz is found to be $\Delta f = 4.2$ Hz, the corresponding quality factor of this digital filter being therefore $Q = f_{2d} / \Delta f = 238$. Such a Q factor would have been impossible to obtain with analog technique.

4.1.2 EOM bias control by using external photodetector

In order to measure the optical power at the output of the MZM, we use an optical coupler to extract one part of EOM output light energy and feeding a low frequency photodetector.

In our experiment, a homemade photodetector is used to convert the EOM output light signal to RF signal. This signal is then connected directly to the ADC input of Link Research Daughter card. The controlled voltage output of the DSP is connected to the DC electrode of the MZM as shown in Figure 4.9.

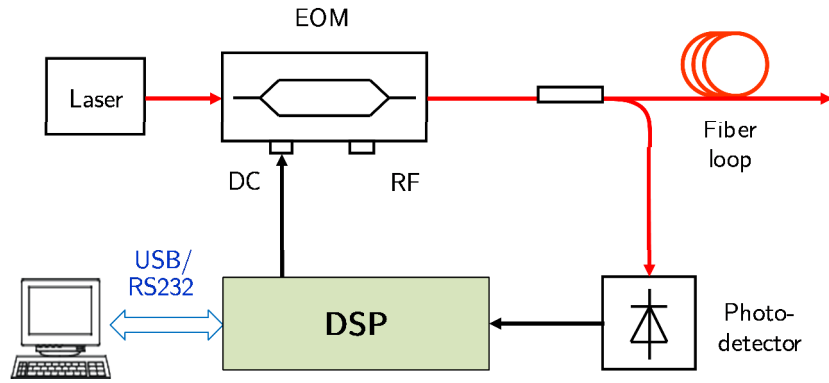


Figure 4.9 Block diagram of EOM bias control with DSP and an external photodetector

The only disadvantage of this method is that it requires more space to arrange one optical coupler and a photodetector.

4.1.2.1 Drift determination in terms of the Non-Linear Indicator

To determine the drift in working condition without any control, the dither signal with DC component of +5.5 V, AC amplitude of 0.85 V and frequency of 500 Hz is injected to DC electrode of the EOM. The evolution of the *NLI* parameter as a function of time has been recorded and the corresponding result for an experimental time of 7.45 hours is shown in Figure 4.10.

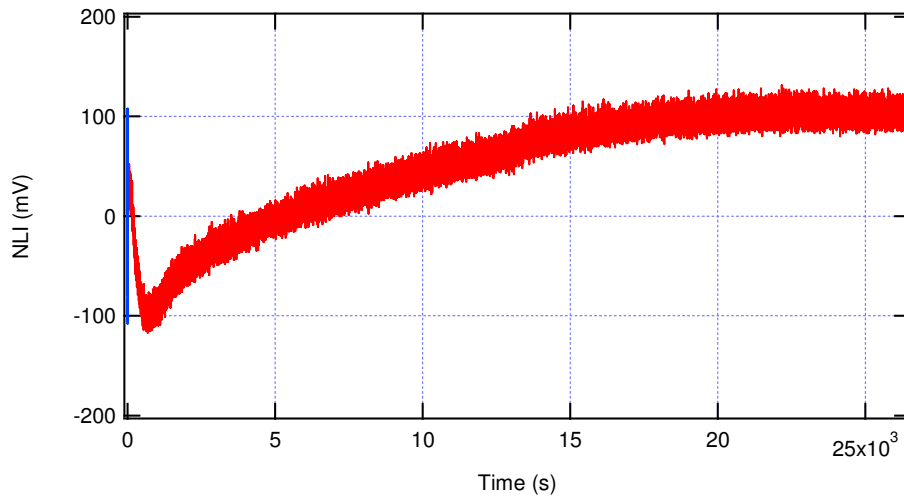


Figure 4.10 Long term evolution of the *NLI* caused by the EOM transfer function drift.

The peak-to-peak variation of *NLI* is 248 mV and the standard deviation is 56 mV.

4.1.2.2 Bias control at EOM positive slope

We developed a GUI software with Microsoft Visual Basic to control the bias point

as illustrated in Figure 4.11. Two real-time values are shown in the “Parameters” panel including bias voltage sent to DC electrode of the EOM, the non-linear indicator. For short-term observation, we can decrease the sampling interval (increase sampling rate) to several samples per second. For long-term monitoring, this interval is increased and usually we set it to 10 s.

The bias control software has two options: positive slope and negative slope. These two values indicate which slope of the transfer function that the bias point is being controlled. If the bias point is on positive slope, the modulating signal and the modulated signal are in phase. And if the bias point is on the negative slope, they will be 180 degrees out of phase. By default, the positive slope is selected.

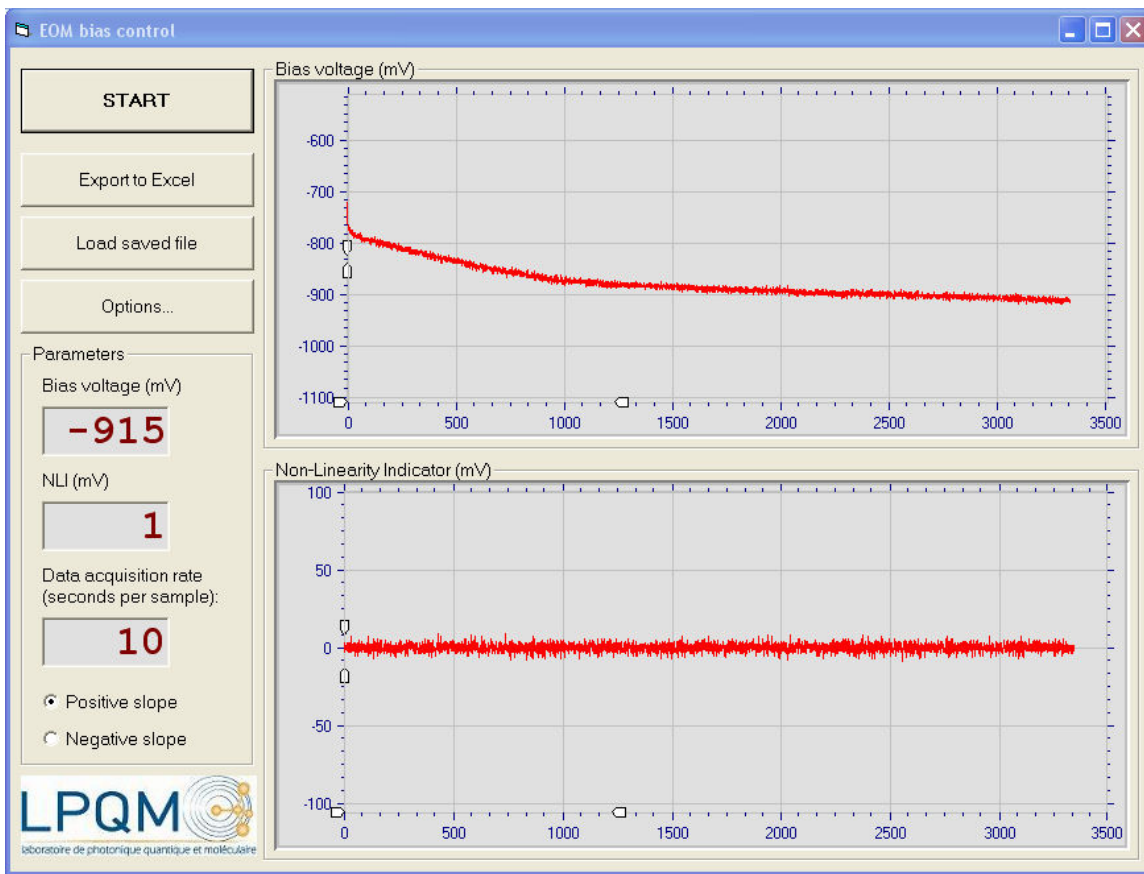


Figure 4.11 EOM bias control with its external photodetector

In this experiment, the bias control is applied to EOM positive slope. After a duration of 33.450 s (or 9.29 hours), *NLI* is kept closed to 0 with the minimum and maximum are -9 mV and $+9$ mV respectively. The controlled bias voltage is reduced from -718 mV down to -915 mV.

4.1.2.3 Bias control at EOM negative slope

In this experiment, the bias control is set to work at negative slope of the EOM for a duration of 30000 s or 8.3 hours. The result is presented in Figure 4.12.

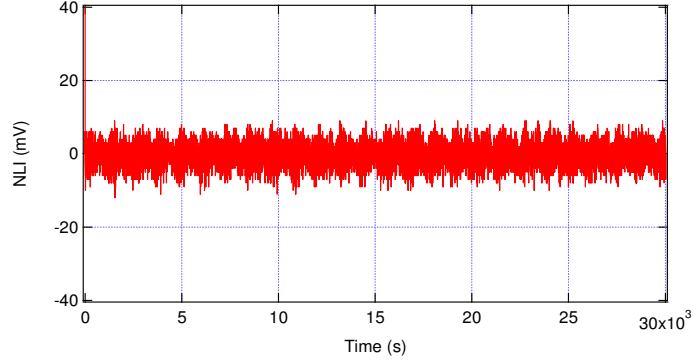


Figure 4.12 Evolution of the NLI during the control process.

The average value of NLI is $-1.314 \mu\text{V}$, the standard deviation is 3.074 mV and the peak-to-peak variation is 21 mV . Comparing the peak to peak variations with the case without control (Figure 4.10) there is a reduction by a coefficient 11.8 for the NLI variations; comparing the standard deviation the reduction of the variations corresponds to a factor 18.2 thanks to the bias point control.

For compensating the drift, the bias voltage is automatically modified by the DSP software as shown in Figure 4.13 with the variations of $V_{bias} = V_{bo} + V_{bc}$ as a function of time.

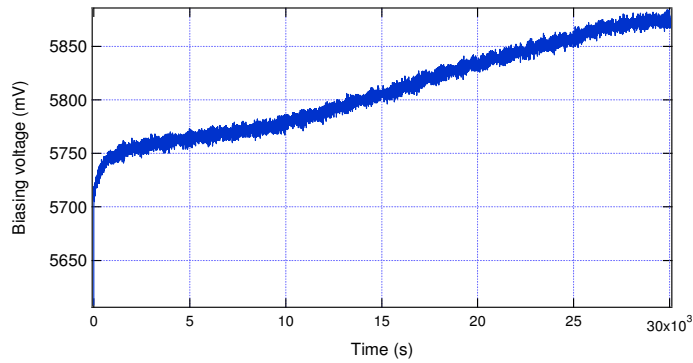


Figure 4.13 Evolution of the EOM bias voltage during the control process.

These two experimental results indicate that the bias control operates well on positive slope as well as negative slope of the EOM and the EOM is stabilized at its quadrature point for long duration.

4.1.3 MZM bias control by using the internal photodiode

In our laboratory, we work with several modulators with type of MX-LN-10 from Photline and one of these modulators is illustrated in Figure 4.14. One advantage of this modulator is that it has an internal monitoring photodiode connected at pins 3 and 4.

The output of this internal photodiode is a current while the DSP working with a voltage signal input. So to use this internal photodetector with DSP kit, we need to convert this current to voltage.

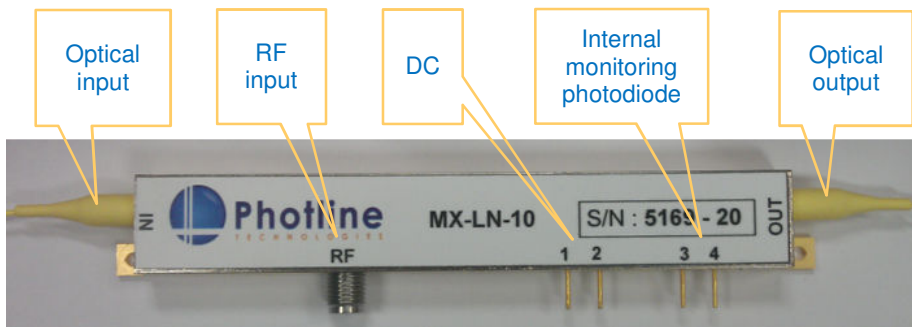


Figure 4.14 A Photline modulator MX-LN-10. The internal monitoring photodiode connected at pins 3 and 4.

The advantages of using internal PD for controlling MZM are:

- It is not necessary to use an optical coupler to extract laser power for the photodetector. The optical output power is 100% provided to the OEO system,
- The system structure is simpler and the size of the system is reduced.

4.1.3.1 Designing interface card

4.1.3.1.1 Current to voltage circuit

Because the internal photodiode output signal in our case is a current signal, so we need to design an electronic circuit to convert current signal to a voltage signal which is used as the input for the DSP kit. This circuit is called current-to-voltage converter circuit or a trans-impedance amplifier and is presented in Figure 4.15.

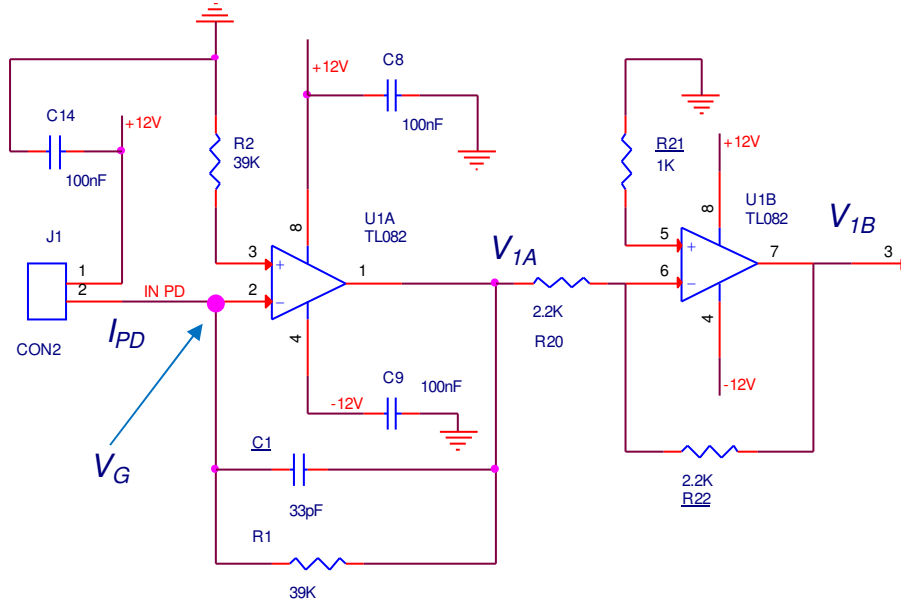


Figure 4.15 Schematic of electronic circuit for converting Photline MX-LN-10 modulator's internal photodiode output current to a DC voltage signal.

In Figure 4.15, the two output pins of the internal photodiode of the Photline MX-LN-10 are connected to 2-pin connector J1. The internal photodiode cathode is connected to a +12 V voltage source and its anode is connected to pin 2 of the first TL082 (named U1A in the schematic). The feedback resistor R_1 is placed in parallel with a capacitor C_1 which is placed for the stability of the amplifying circuit. The output voltage correlated with the photodiode current I_{PD} is:

$$V_{1A} = \frac{-I_{PD}R_1}{1 + j2\pi fR_1C_1} \quad (4.5)$$

Because the current output of the internal photodiode I_{PD} is very small (order of μA), the feedback resistor R_1 is chosen high enough to achieve a reasonable value for the output voltage. At low frequencies, the value of $2\pi fR_1C_1$ are small and can be negligible. In this case, the Equation (4.5) becomes:

$$V_{1A} = -I_{PD}R_1 \quad (4.6)$$

Now, the current output of the internal photodiode has been converted to voltage. However, their changes are in opposite directions as indicated by the sign minus in the Equation (4.6). To make voltage output is proportional to I_{PD} , as shown in Figure 4.15, the voltage output V_{1A} is connected to an inverting amplifier circuit [86] implemented by the OPA U1B. The voltage output V_{1B} is determined by:

$$V_{1B} = -\frac{R_{22}}{R_{20}} V_{1A} = \frac{R_{22}}{R_{20}} I_{PD} R_1 \quad (4.7)$$

The role of resistors R_2 and R_{21} is to reduce the offset at the output of the amplifiers.

4.1.3.1.2 AC amplifier circuit

The signal V_{1B} contains both DC and AC components. When using dither based technique, we are only interested in AC components and do not need DC component. We added a circuit to filter the DC component and amplify the AC component as presented in Figure 4.16:

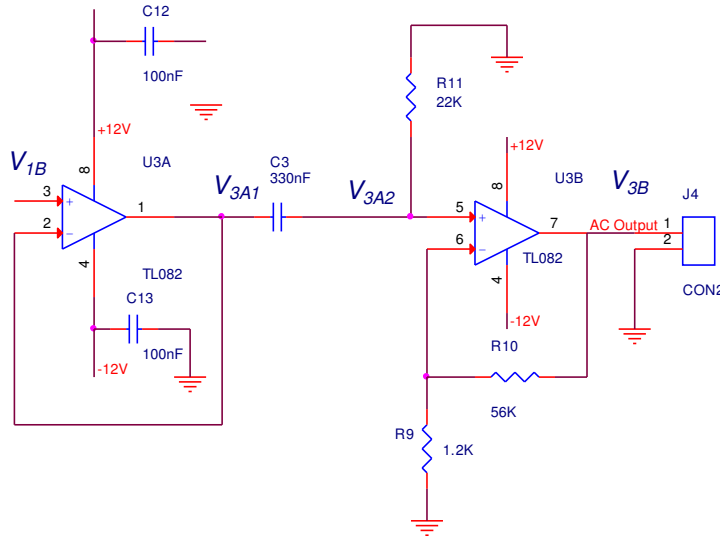


Figure 4.16 Schematic of electronics circuit for filtering the DC component and amplifying the AC component.

Firstly, the signal V_{1B} is passed through the amplifier circuit with unity gain, the output signal is $V_{3A1} = V_B$. Then the DC component of the signal V_{3A1} is filtered out by capacitor C3.

After passing one more non-inverting amplifier circuit, the final output is:

$$V_{3B} = \frac{jR_{11}C_3\omega}{1 + jR_{11}C_3\omega} \left(1 + \frac{R_{10}}{R_9}\right) V_{1B} \simeq \left(1 + \frac{R_{10}}{R_9}\right) V_{1B} \quad (4.8)$$

4.1.3.2 Connection scheme and results

To control the bias point of the EOM, we setup a configuration as shown in Figure 4.17. Obviously, this configuration is simpler and more compact than that of the case using the external photodetector. The signal V_{3B} is injected to the ADC1_Input of the

DSP kit, the DSP kit execute the program developed in section 4.1.1. The control voltage is sent to DC electrode of the EOM via DAC1_Output.

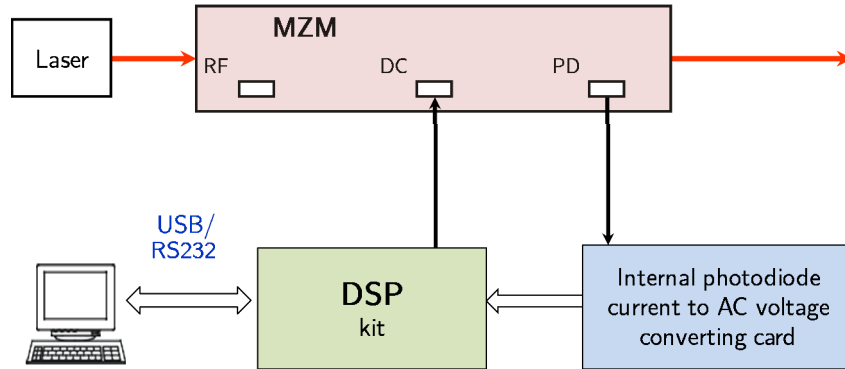


Figure 4.17 EOM bias control by using internal photodetector

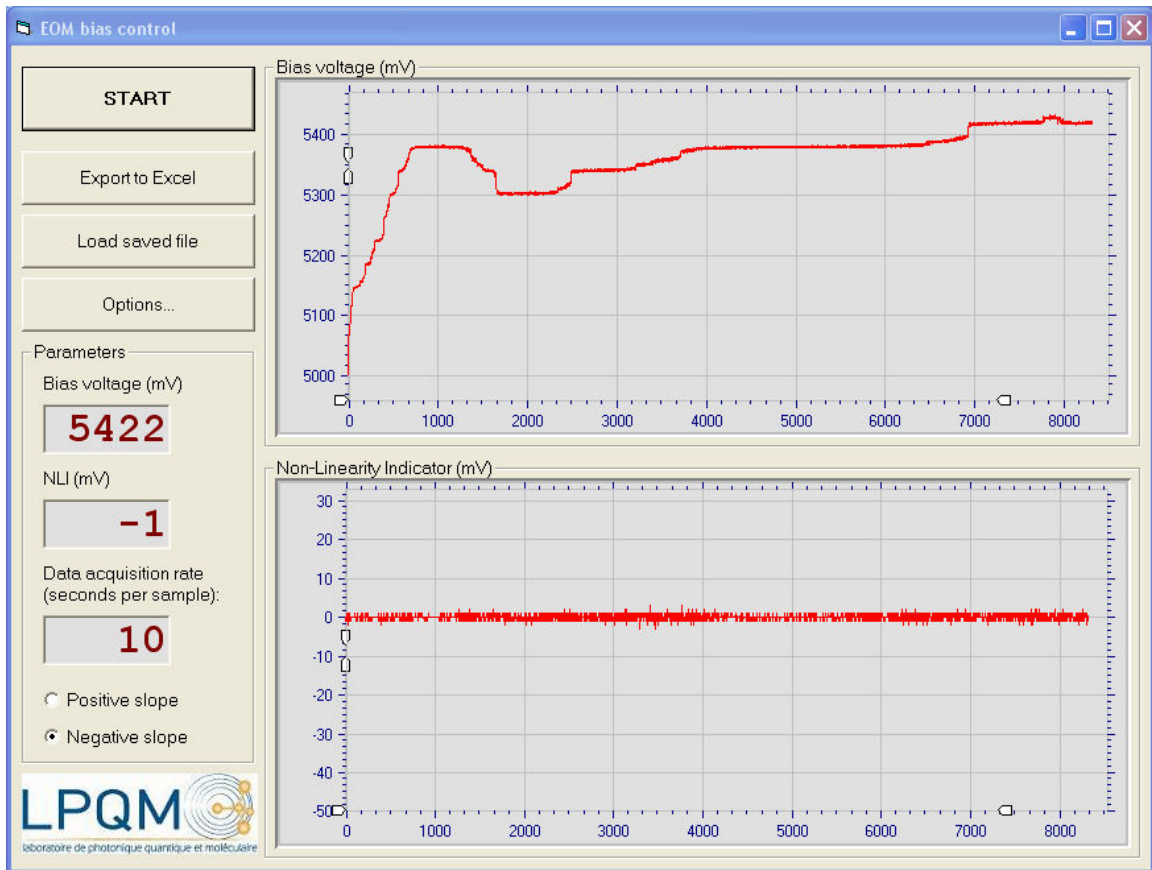


Figure 4.18 EOM bias control by using internal photodetector for a duration of 23.13 hours

From Eq. (4.8) and schematic in Figure 4.16, it is easy to calculate the AC amplification gain of this circuit and the result is 47.67. The dither signal amplitude is reduced from 850 mV down to 250 mV. With high amplification gain, the AC voltage arrived to the ADC port of the DSP kit will be bigger and it helps the DSP to analyze

more accurately.

This experiment is conducted for a longer duration. After 83.270 s or 23.13 hours, the result is achieved and displayed in Figure 4.18. The controlled bias voltage varied from +5000 mV to +5422 mV to keep NLI around to 0. The average value of NLI is $-2.64 \mu\text{V}$, the standard deviation is 0.473 mV and the peak-to-peak variation is only 6 mV.

To show it more clearly, we used horizontal zooming handles to view a portion of this control process, starting from time around 16000 s to 26000 s. The result is shown in Figure 4.19. Obviously, the controlled bias voltage in this experiment is much more stable than that shown in Figure 4.13.

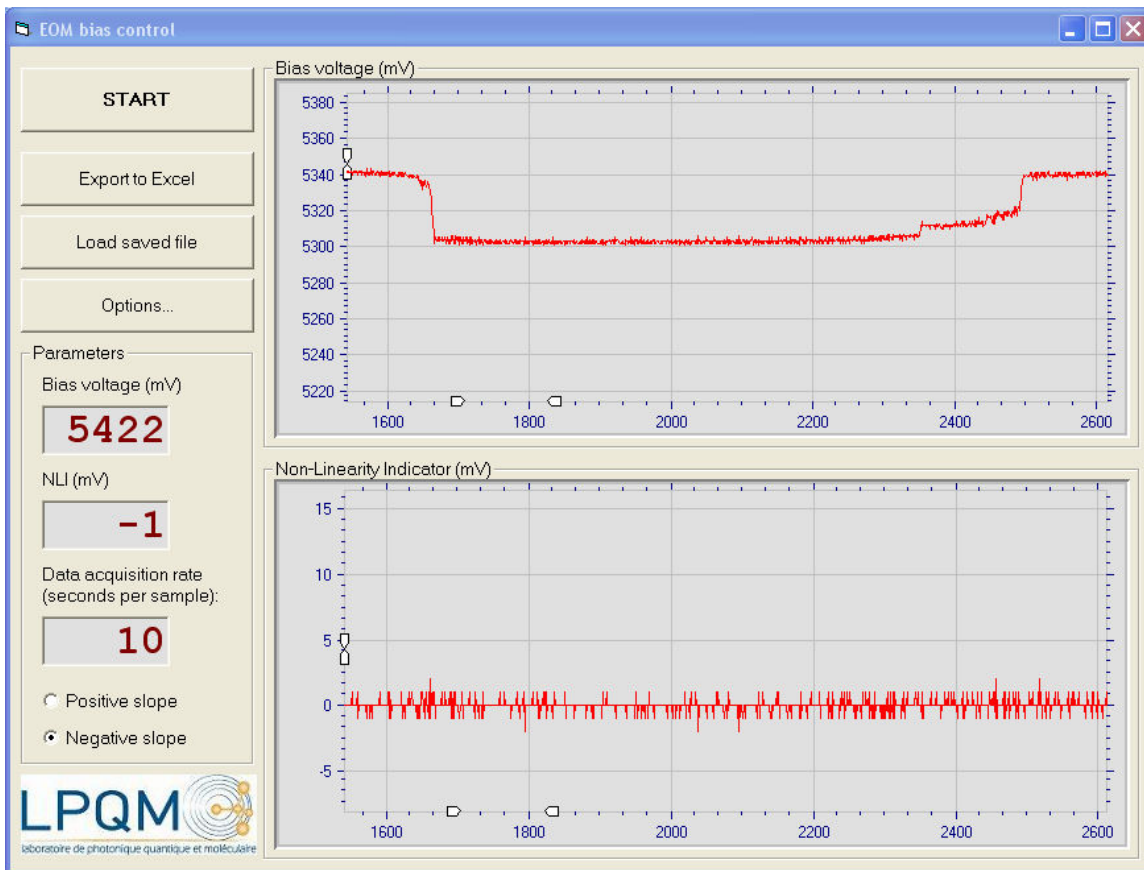


Figure 4.19 A EOM bias control by using internal photodetector for a duration of 23.13 hours: a zoomed-in view.

This experimental result improves a significant enhancement in NLI and controlled bias voltage in compare with that in the case of using the external photodetector. The advance does not depend on the use of external photodetector or internal photodiode but it is result of using the AC amplification card.

4.1.4 Integrating two controls: temperature and bias

Up to now we have two separate control processes for the EOM: temperature control and bias control. Because the DSP kit has ability to handle greater amount of processes so we will present the way to integrate these two programs into one.

The first step is to design new model with Matlab/Simulink with both controls, the result is presented in Figure 4.20. At the input, the voltage signal from photodetector is connected to ADC1_Input and the temperature information is connected to ADC4_Input. Among 8 outputs supported by Link Research daughter card, two outputs DAC1_Output and DAC7_Output are used for bias voltage and temperature control voltage. Other ports are used to test the values at different points of the scheme such. For example, DAC4_Output allows us to know the output of the band pass filter at 1 kHz, DAC5_Output gives us the NLI value...

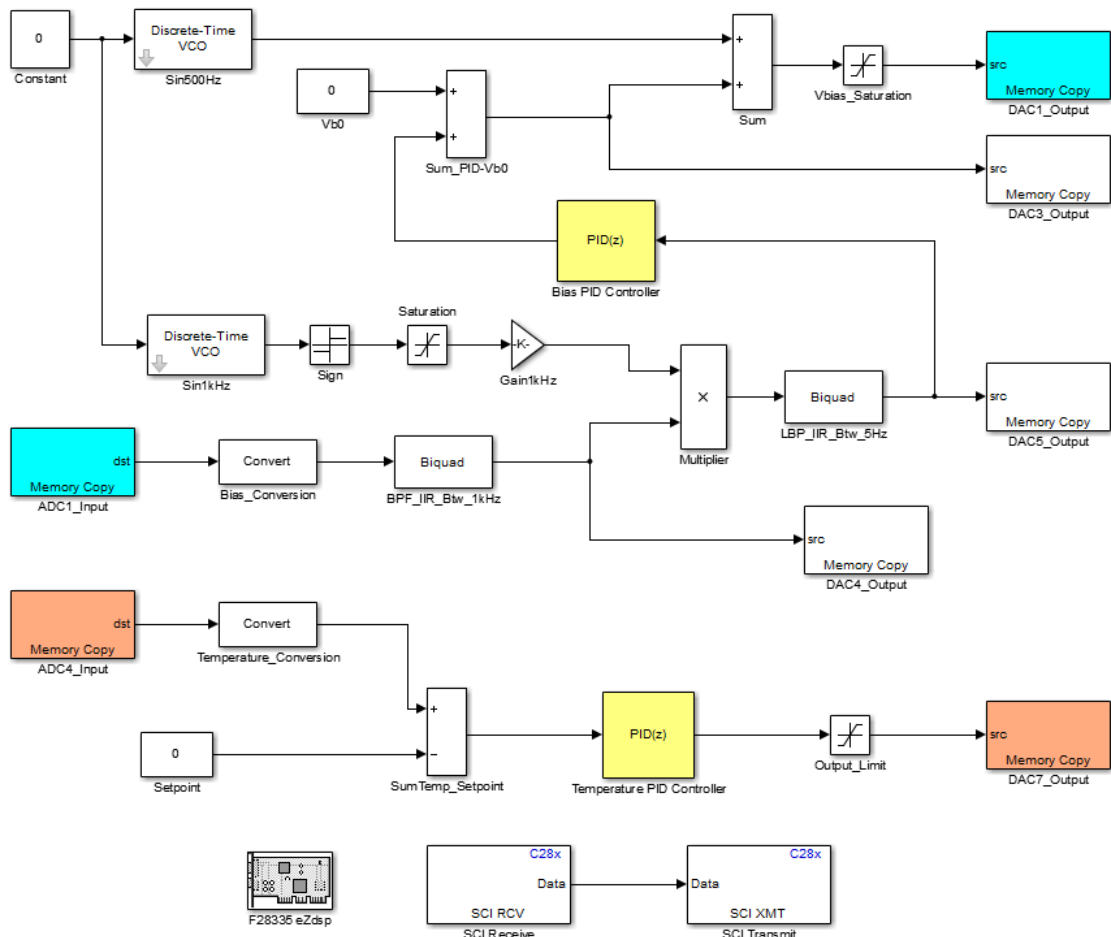


Figure 4.20 Simulink model for EOM bias and temperature control.

After completing the first work, we continue to create the new GUI software for

both controls. The reason comes from the fact that, the DSP kit communicates with PC via a serial connection port RS232, when this port is opened and locked by one application it is impossible to open this port for another application. The new program must contain all functionalities from both individual ones.

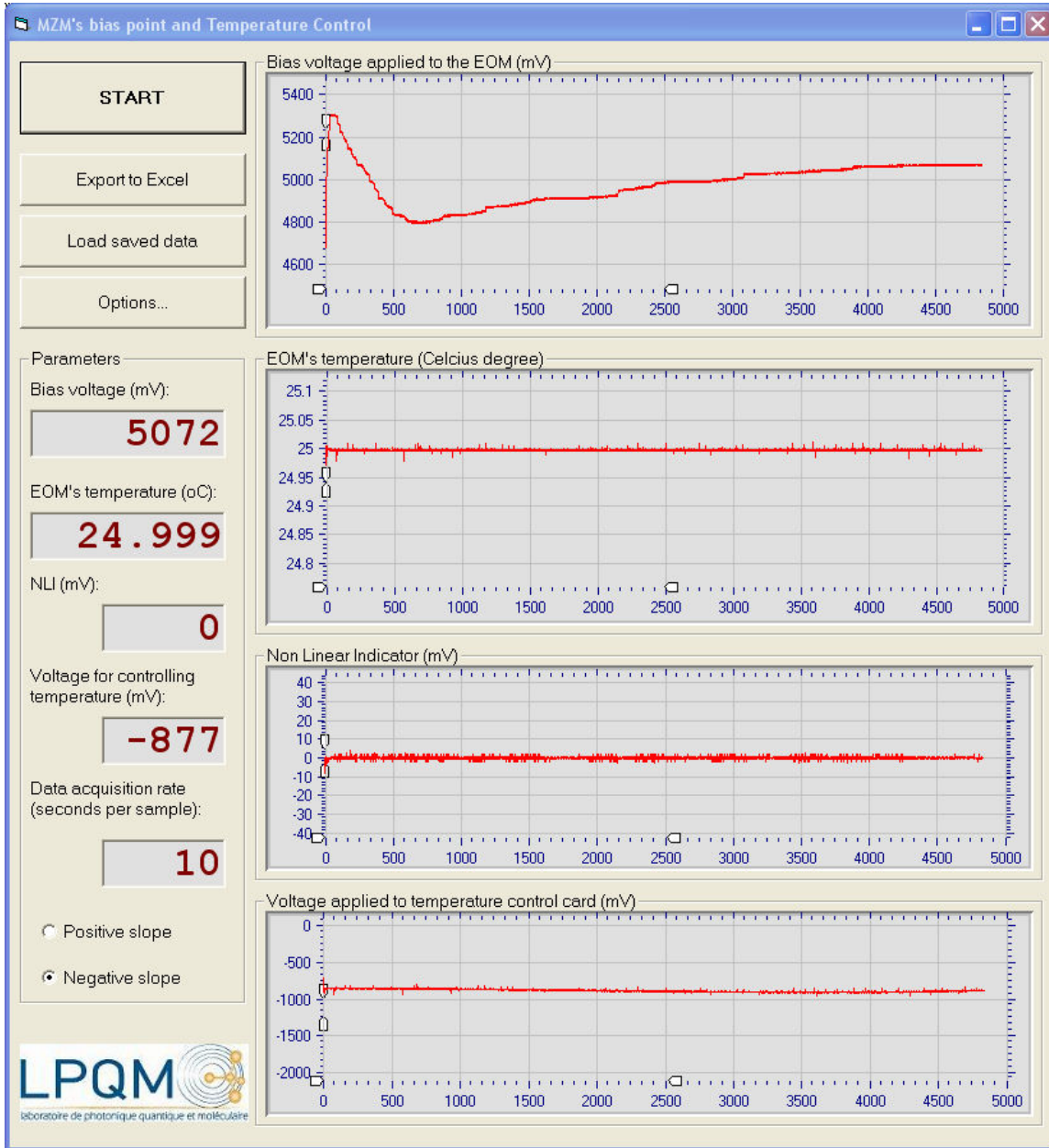


Figure 4.21 GUI software operating on PC site for controlling MZM bias and temperature.

This GUI software is created with Microsoft Visual Basic and the result is presented in Figure 4.21. Four real-time values are shown on the “Parameters” panel including bias voltage sent to DC electrode of the EOM, the EOM temperature, the non-linear indicator and the control voltage used for temperature controlling. Another

information is also listed in the “Parameters” panel is data acquisition rate, in this case, it is sampling interval indicated in second.

On the right side, there are four charts which allow us to know history of the whole control process. Each chart has horizontal and vertical handles for zooming and panning. With these functions, we can view in more detail a specific duration of control process. All these values can be saved to Microsoft Excel file by clicking on the “Export to Excel” button. In the inverse direction, the saved file can be opened by one click on the “Load saved data” to review the control process in the past.

4.2 Optical output power based bias control

The dither based bias control technique described in 4.1 can control the EOM to operate in its quadrature point in a long duration. The fact shows that, the drift of EOM is a slow process, so the dither signal is not necessary to be used continuously. Furthermore, dither signal can create a detrimental effect on modulation link’s dynamic range [87].

In this section, we present another way to control the drift of the EOM. Instead of using a dither signal, we use directly the output power of the EOM, which is done here by using the internal photodiode.

4.2.1 DC amplifier circuit

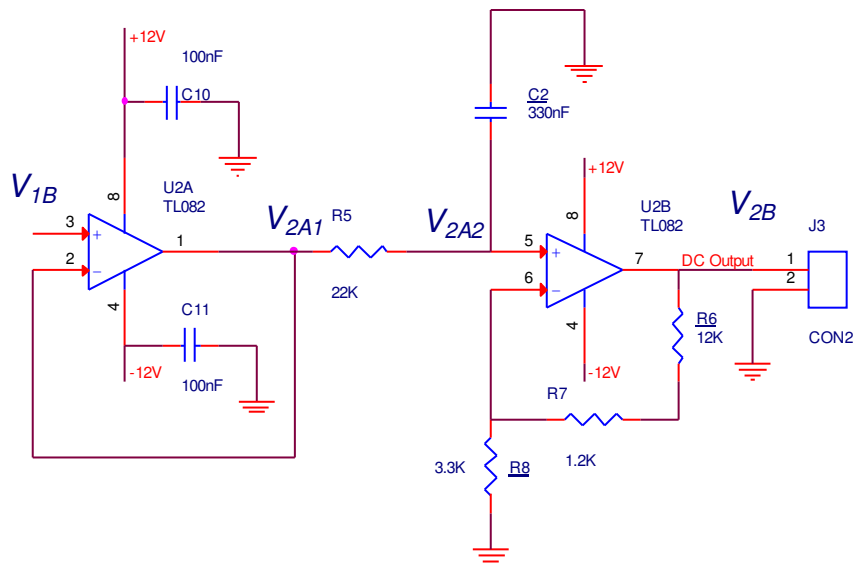


Figure 4.22 Schematic of DC voltage amplifier circuit by using operational amplifier TL082. This circuit also filters the AC component of V_{1B} .

With the circuit presented in Figure 4.15, we achieved the voltage V_{1B} which reflects the optical power arrived to the internal photodiode. In order to take advantages of +10 V input range of the DSP, we amplifier this DC signal by the amplifier circuit:

The relation between V_{1B} and V_{2A1} is:

$$V_{2A1} = V_{1B} \quad (4.9)$$

Then the AC component V_{2A2} of the signal is routed to ground by capacitor C2, only the DC component continues travelling to pin 5 of U2B with $V_{2A2} = V_{2A1}$. After passing one more non-inverting amplifier circuit, the final output is:

$$V_{2B} = \left(1 + \frac{R7 + R6}{R8}\right)V_{2A2} \quad (4.10)$$

4.2.2 Transfer function determination with the internal photodiode

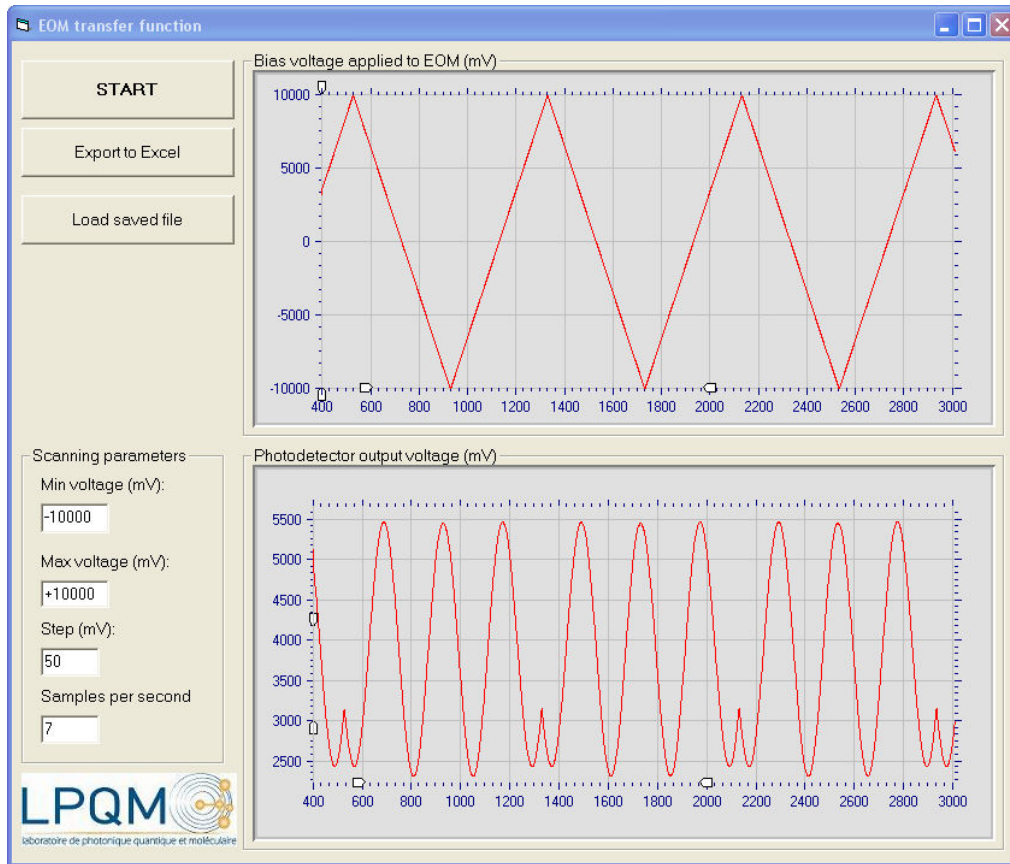


Figure 4.23 EOM transfer function program interface

To simplify the determination of the transfer function of the EOM, we have developed a program with CCS and loaded it to DSP kit. On the PC side, we developed a program with Microsoft Visual Studio which allows us to obtain easily the EOM transfer function.

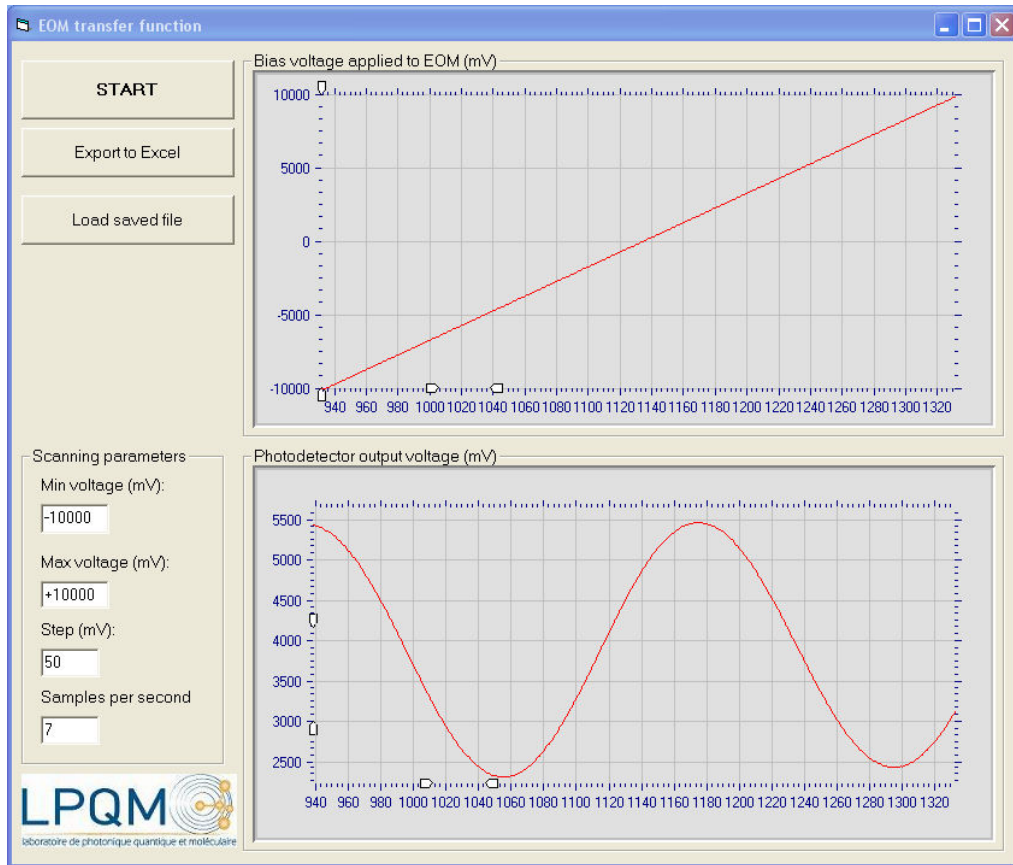


Figure 4.24 EOM transfer function with one scanning period view

The GUI program generates a bias voltage which is applied to the DC electrode of the EOM. This voltage starts from a minimum value of -10 V, and then it is increased gradually to the maximum voltage of $+10$ V by step of 50 mV. So, totally we have 401 points for one full scan and it is big enough to draw a smooth chart of transfer function. After reaching the maximum value, the bias voltage then is decreased to the min value and so on. To show only one scan period, the user can use the horizontal zooming handles in the two strip charts to zoom in only one full scan of bias voltage from -10 V to $+10$ V. The result looks like in Figure 4.24.

The bias voltage is controlled by the DSP kit and a program written with MS Visual Studio. Firstly, the bias voltage is set to -10 V and then it is increased to $+10$ V with a step of 25 mV at every 150 milliseconds. At the same time, we measure

the voltage V_{2B} as shown in Figure 4.22.

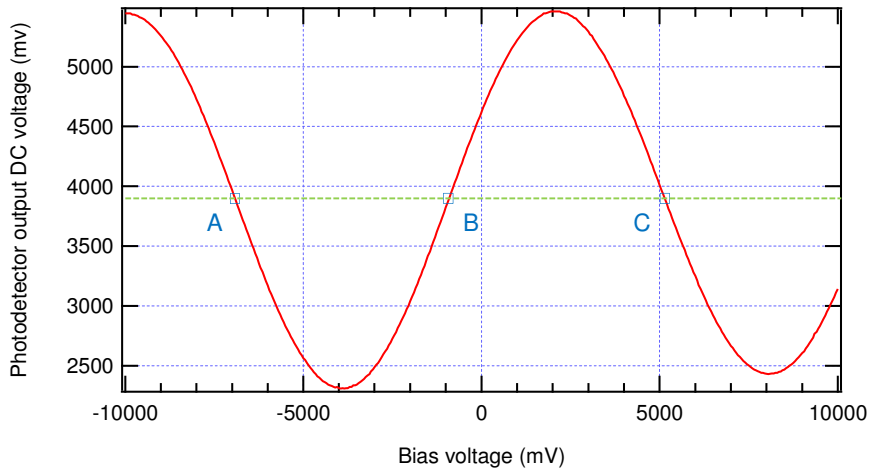


Figure 4.25 EOM transfer function represented in Igor

From the data achieved in Figure 4.24, we export to MS Excel, then imported into Igor. The transfer function presented in Igor is illustrated in Figure 4.25. It is identical with result plotted in Figure 4.24. Three possible quadrature points are A, B and C. The null point on the left side is at -3.9 V corresponding to a DC voltage output of 2309 mV and the peak point is at $+2.3$ V corresponding to a DC voltage output of 5463 mV. The average line, indicated by a green line, is around 3886 mV.

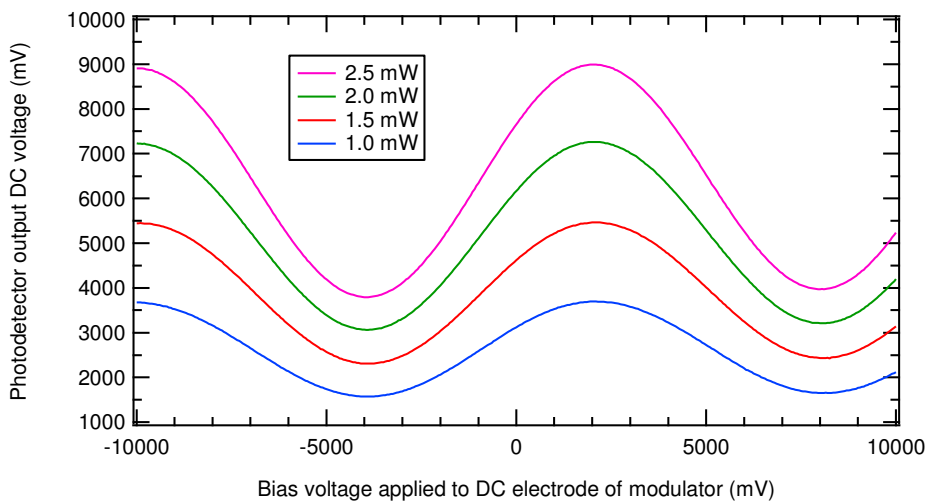


Figure 4.26 EOM transfer functions at different laser power levels.

With this program, we can draw the transfer function of the EOM at different laser power levels as shown in Figure 4.26.

4.2.3 Simulink model of optical power based control

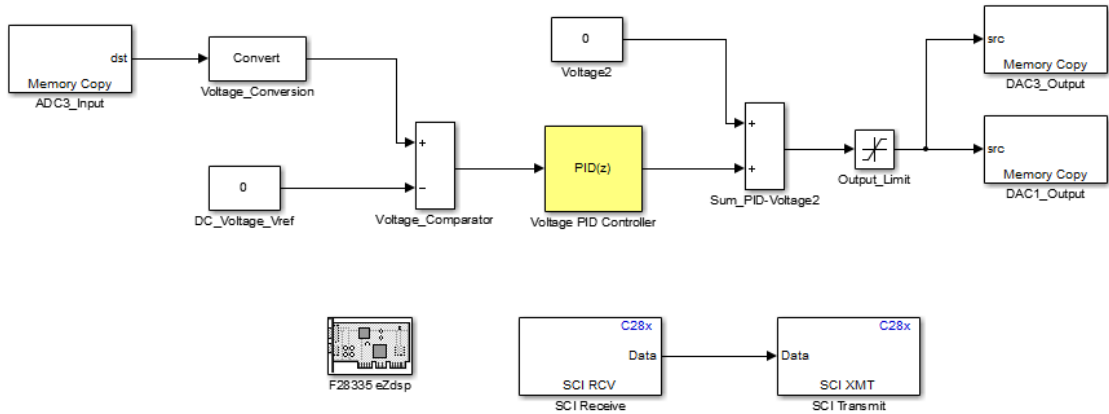


Figure 4.27 Simulink model for EOM bias control based on photodetector output DC voltage. The control voltage is sent to EOM via DAC1_Output, and a copy sent to oscilloscope via DAC3_Output for testing purpose.

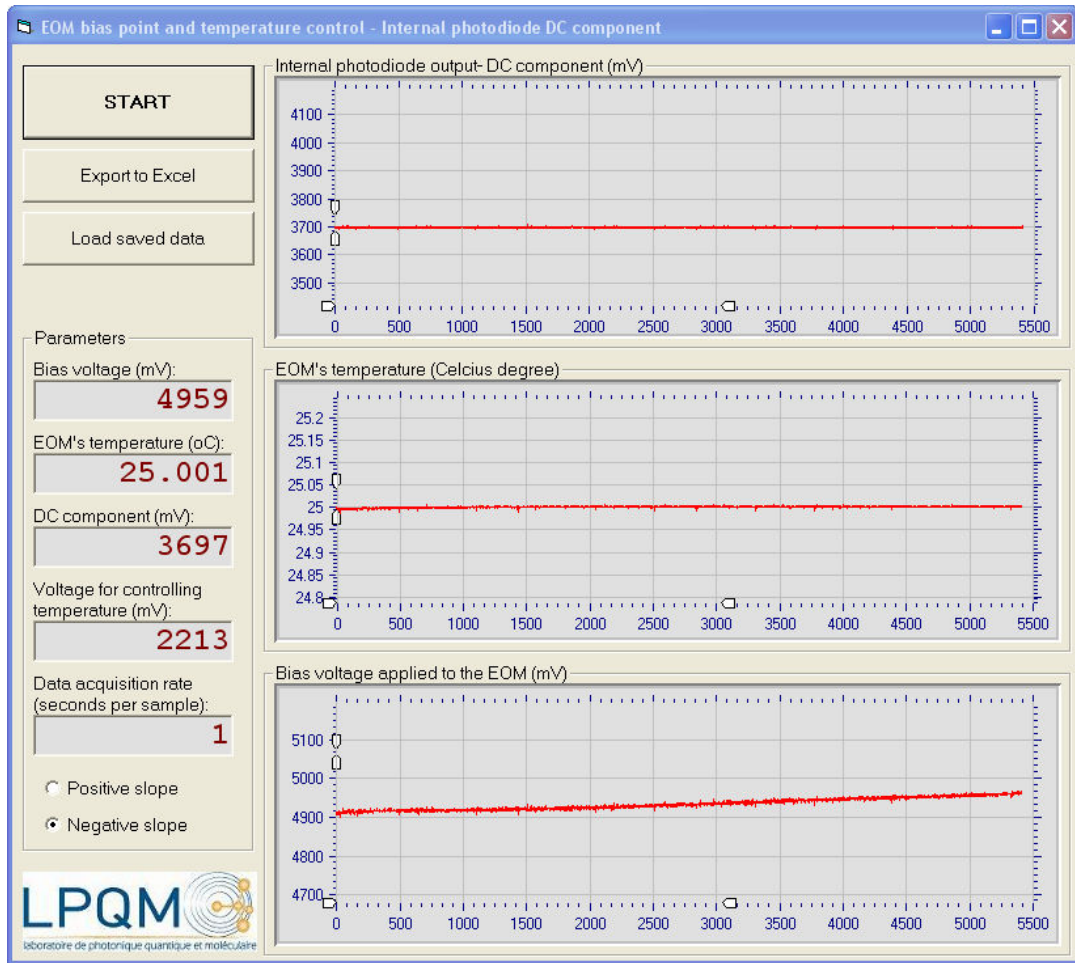


Figure 4.28 The graphical user interface of EOM bias control based on average optical output power and temperature control.

We use Simulink to build the model for generating code to Code Composer Studio v3.3 for handling the DSP F28335. The DC voltage is from the electronic circuit in Figure 4.22 is connected to ADC1_Input then it is put into a comparator. The output of this comparator is the error value to put into the PID controller.

Base on the generated frame code, we complete the control program with CCS. .

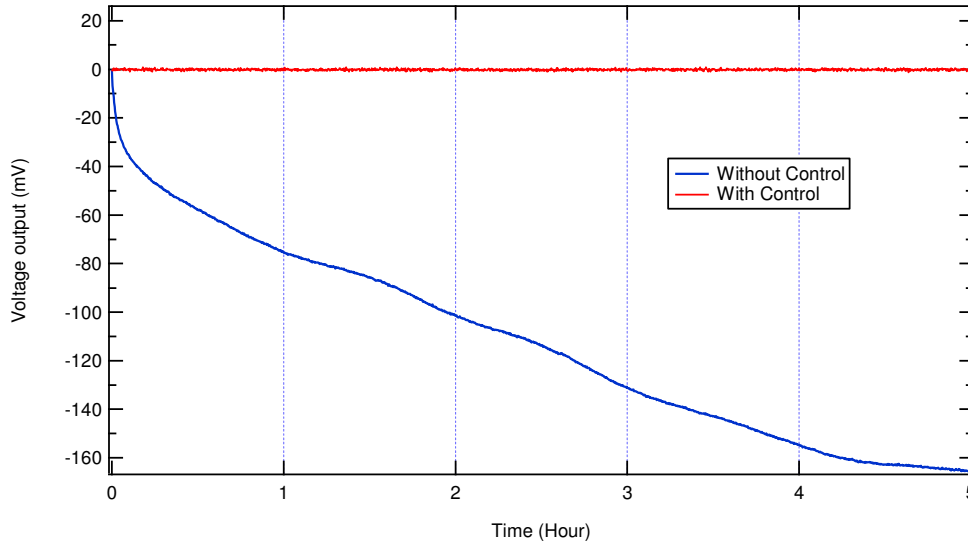


Figure 4.29 Evolutions of voltage output with and without optical power based control.

Without control, the photodetector output DC voltage decreases quickly during the first 10 minutes then it decreases more gradually down to -165.396 mV. The peak-to-peak variation is 165.396 mV and the standard deviation is 39.256 mV. While with the control process, the amplified voltage output is stabilized around set point with the min of -1.204 mV and the max of 0.903 mV leading to a peak-to-peak variation of 2.107 mV, a mean value of -0.128 mV and a standard deviation of 0.326 mV. The improvement for the standard deviation is 120.4 times and for the peak-to-peak variation it is 78.2 times.

4.3 Integrating both bias control techniques with other functions

4.3.1 Combining both bias control techniques

Why do we need to combine both techniques together? The answer is to achieve the advantages of both ones and eliminate those disadvantages.

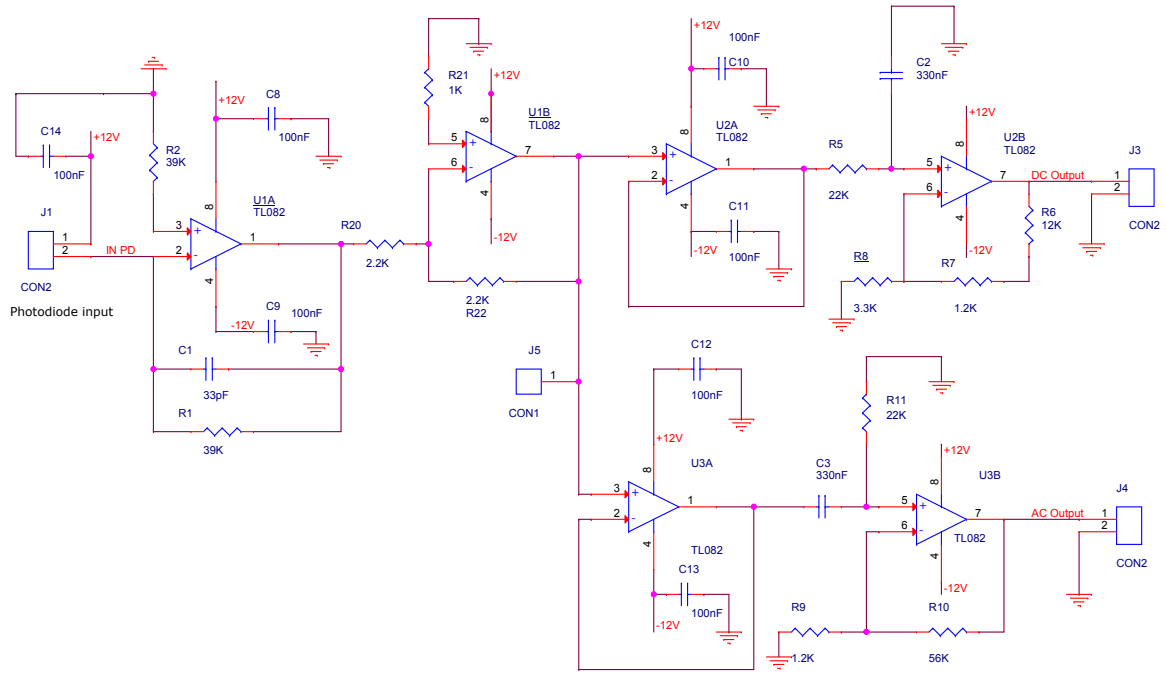


Figure 4.30 Schematic of bias input card with AC and DC outputs.

From the electronic circuits presented in Figure 4.15, Figure 4.16 and Figure 4.22, we combined them into one common circuit as described in Figure 4.30. The completed schematic is presented in the Annex A.3. The internal photodiode output current is converted to voltage and then is divided into AC and DC voltages. These two signals are amplified and sent to appropriate AC and DC output ports.

From this common schematic, we create the printed circuit board (PCB), choosing surface mount components to reduce the size of the board. The final board has a dimension of 7 x 5 cm with double sides as shown in Figure 4.31. The voltage source ± 15 V is down converted to ± 12 V by regulators are placed at the bottom side for an even more compact board.

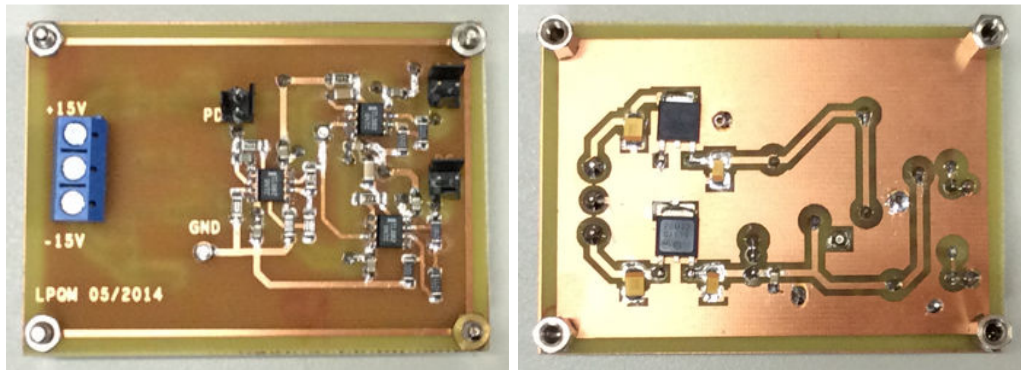


Figure 4.31 Photo of bias input card used with internal PD of EOM. It converts PD's current to AC and DC voltages

Finally, the board is attached to the box containing the EOM. The AC and DC output ports of this card then are connected to two ADC input ports of the DSP kit via two Bayonet Neill–Concelman (BNC) cables. These two signals will be used by dither-based bias control technique and optical output power-based technique.

Now, the hardware for combining both bias control techniques is ready. It will be integrated with other functions.

4.3.2 Integrating both bias control techniques with EOM temperature control and fiber temperature measuring

With the bias input card mention in previous part and based on the successful integration of bias control with temperature control in section 4.1.4, we will present the way to integrate dither-based bias control, optical power-based control with temperature control and temperature measuring.

At the beginning, the bias input card and temperature measurement card are mounted on one aluminum plate of our homemade EOM box as shown in Figure 4.32. These two cards are supplied with the same power source. One reverse-voltage protection card has also been made to avoid any damages could be happened by an improper connection to external power supply.

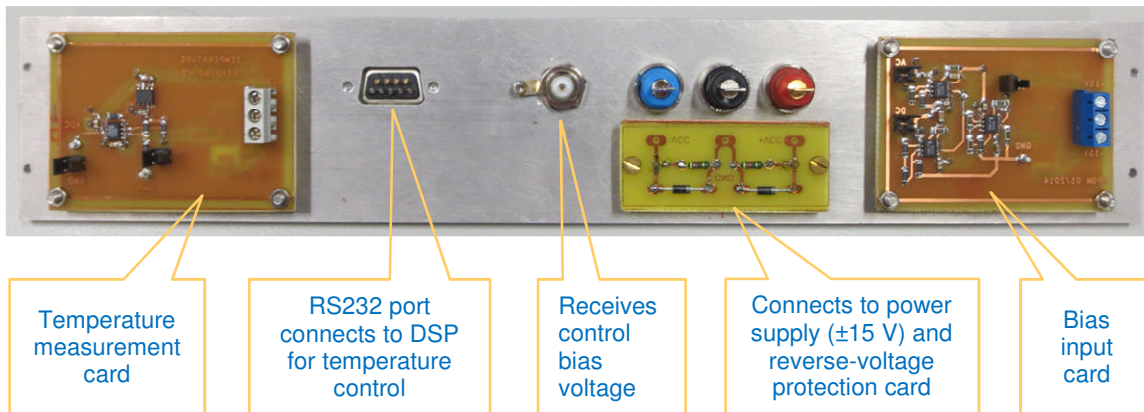


Figure 4.32 The bias input and temperature measurement cards are mounted with other connections on the same plate.

This plate then is mounted to EOM box as illustrated in Figure 4.33. Other connections are also firmly plugged or soldered.

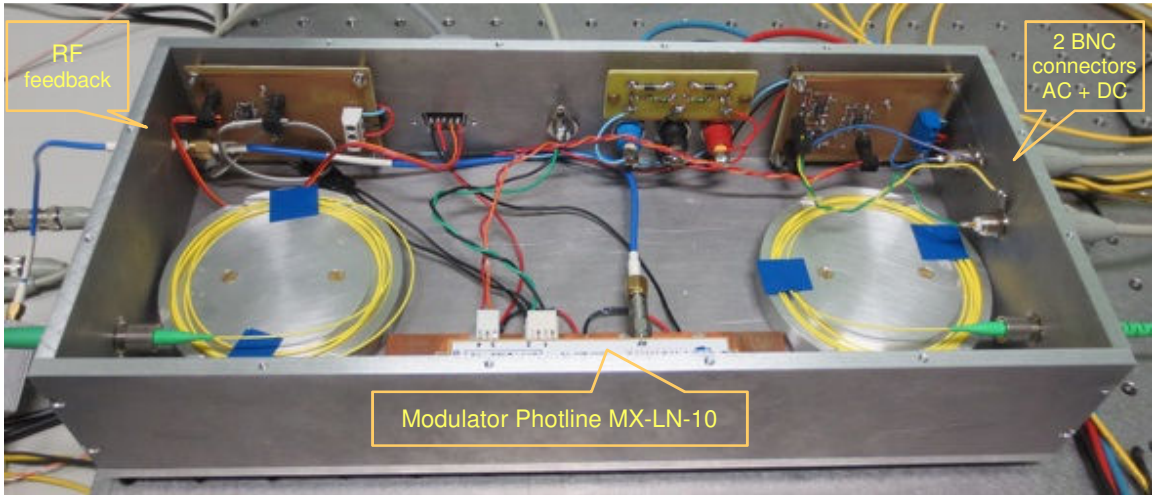


Figure 4.33 AC/DC and temperature measurement cards mounted in the box with the EOM

The DSP kit with all connections is presented in Figure 4.34.

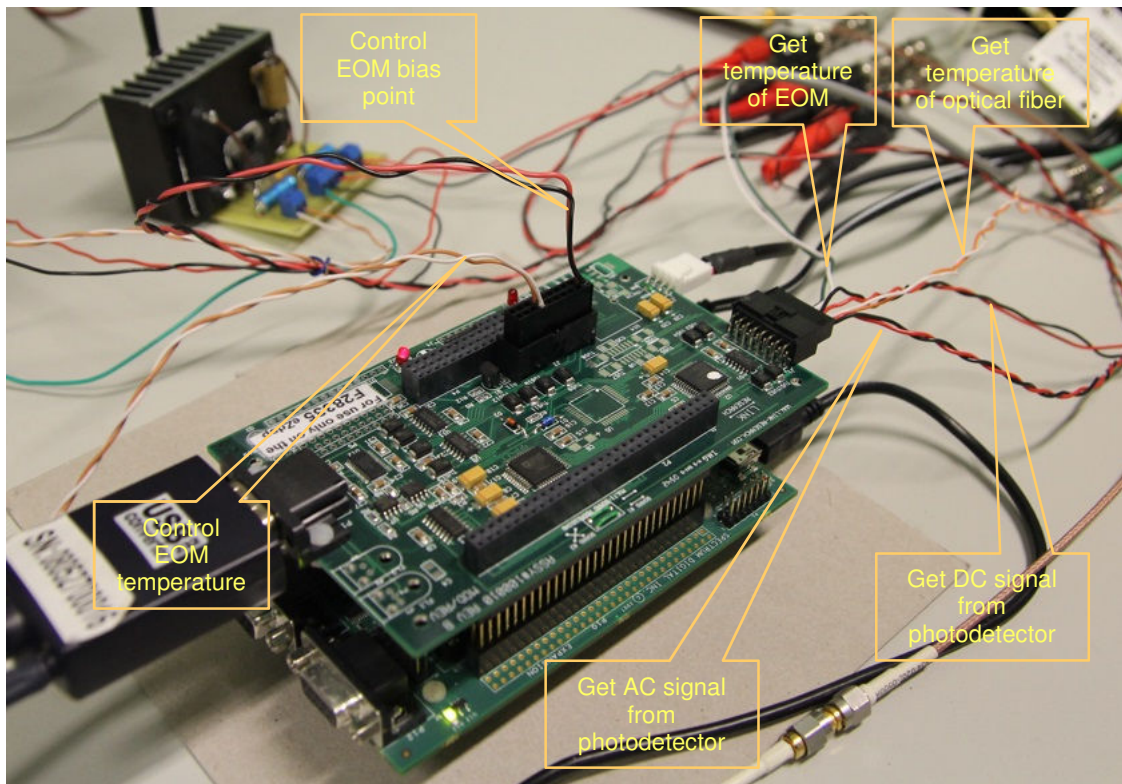


Figure 4.34 DSP kit with all connections.

Now, all the necessary cards are ready. It should be noted that another temperature measurement card is separately mounted close to the thermal box where the fiber loop temperature sensor is situated. We develop new software to control all these functions: one program with Simulink, CCS and one graphic user interface

(GUI) with Visual Basic.

The Simulink model is illustrated in Figure 4.35.

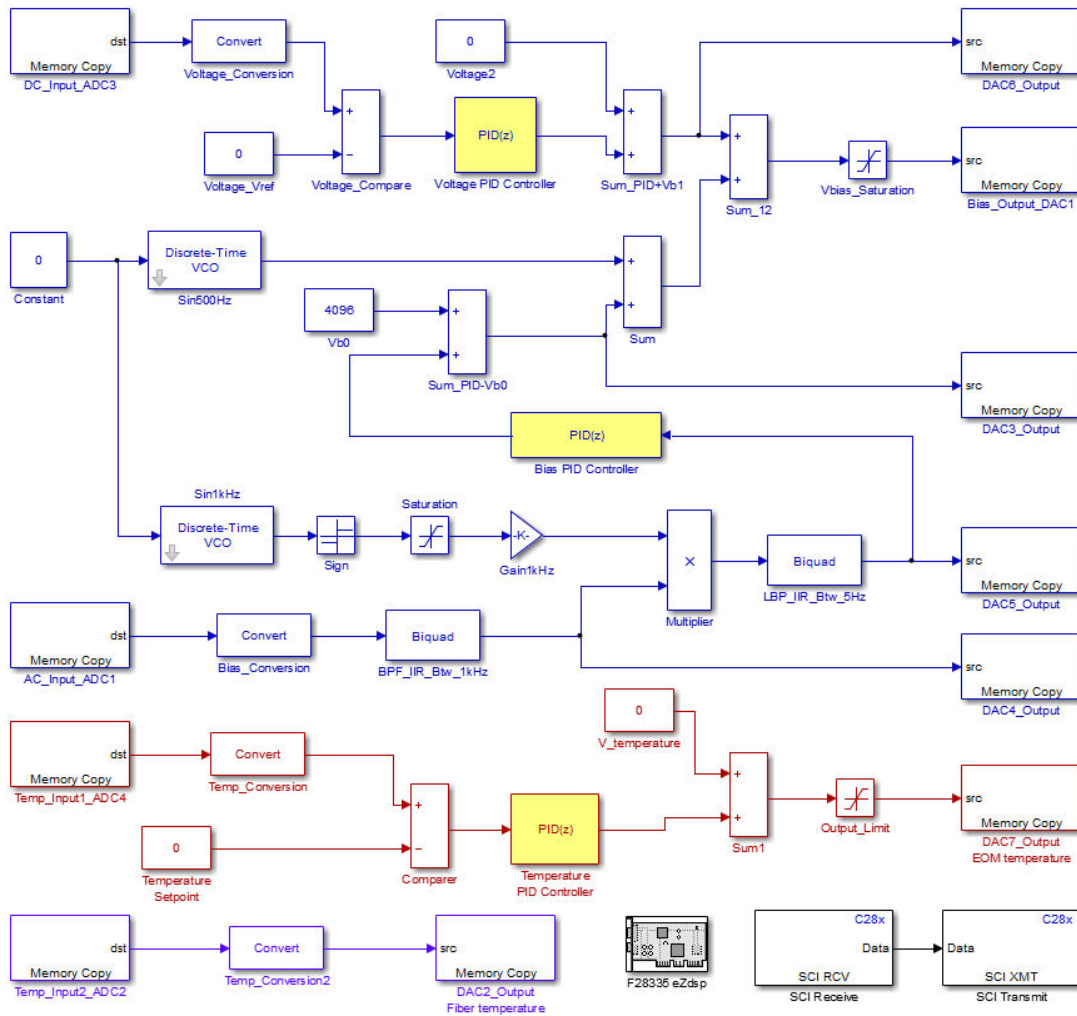


Figure 4.35 Matlab/Simulink model of 4 functions: dither-based bias control, optical output power-based control, temperature control for the EOM and temperature measurement for optical fiber loop.

The GUI software is shown in Figure 4.36 with experimental result for a duration of 94970 s, equivalent to 26.38 hours.

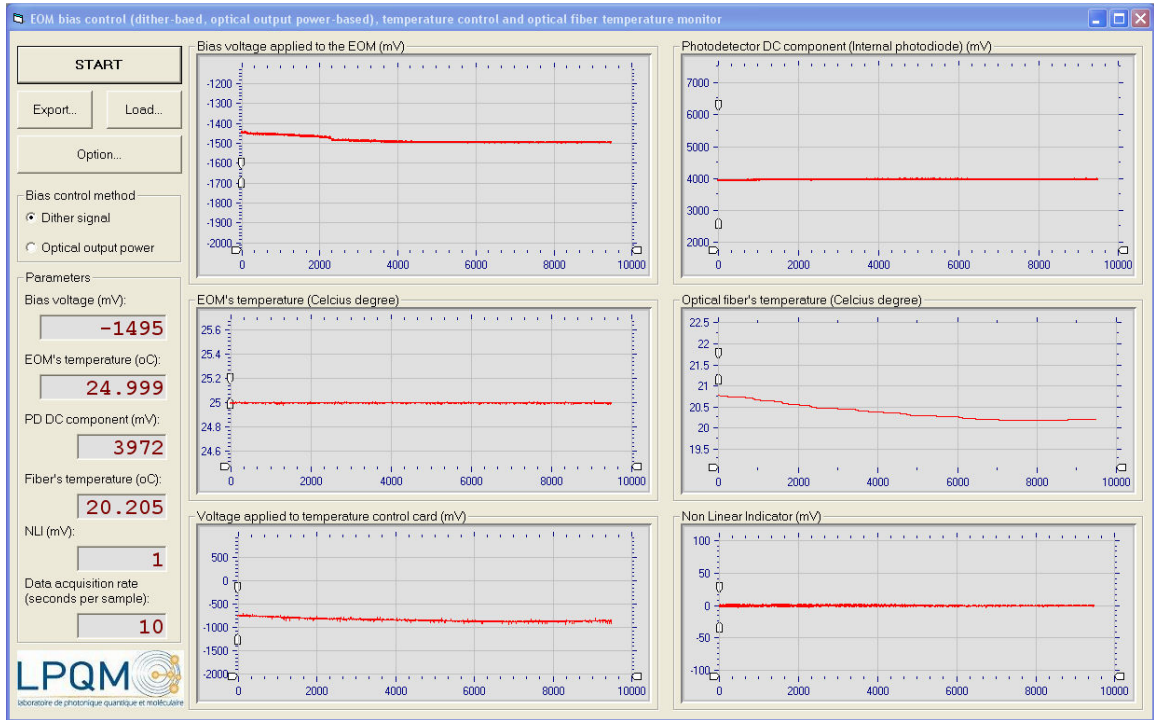


Figure 4.36 The integrated graphical user interface program for controlling EOM bias point (dither-based combined with optical output power-based), controlling EOM temperature and monitoring optical fiber temperature.

4.4 Conclusions and discussions

In this chapter, we introduced two techniques for controlling bias point of the EOM. The dither based bias control was implemented by using a tone signal injected into the DC electrode of the EOM. To understand the behavior of the EOM due to different input conditions, we have built a visual simulation with Matlab. The non-linear behavior of the EOM is evaluated by its second harmonic signal generated in case of a non-symmetric position of the bias point on the transfer function. This quantity is kept at 0 thanks to a digital PID and the bias point is kept at quadrature point. In the case of using the external photodiode, with process control, we obtain an improvement of 18 for the standard deviation when working at EOM negative slope. In another experiment, the bias control process works well with the positive slope.

To take advantage of the MZM in our laboratory which has an internal photodiode, we created an electronic circuit to convert the internal photodiode output current to AC voltage and to amplify it with an amplification gain of 47.67. Thanks to this gain, *NLI* and the control voltage become more stable. In the next experiment, we present the way to integrate bias control with temperature control.

The second technique to control the EOM is based on optical average output power. An electronic circuit has been made to convert internal photodiode output current to DC voltage. This technique is simpler than the dither-based technique. By implementing two 5-hour experiments, we obtain an improvement of 120 for the standard deviation.

Each technique has its own advantages and disadvantages. These two techniques are then combined and integrated with EOM temperature control and fiber temperature monitor. The temperature measurement and bias input cards are then attached to the EOM box.

Chapter 5

OEO application to refractive index measurement

Traditional method to measure refractive index is to use a refractometer which operates based on Snell's law. Among several types of refractometers, the Abbe refractometer is the benchtop one with the highest precision. The standard refractometer uses the wavelength 589 nm and measures at 20 °C. Laboratory refractometers can provide resolutions between 0.0001 and 0.00001, while the handheld models have resolutions between 0.1 and 0.01 [88]. Ellipsometry is another technique that can be used for determining the refractive index of a thin film by studying the change in the polarization state of a light beam reflected on the sample that has been prepared and installed into the instrument.

With the system developed in Chapter 3 and Chapter 4, the EOM is stabilized at quadrature point with a controlled bias voltage and the OEO can operate in a long duration. In this chapter, we focus on how to apply this OEO into sensing application, especially to measure the refractive index of chemical solutions. The reason to work with refractive index is that refractive index is fundamental physical property of substance and it is often used to determine the purity or the concentration of a particular substance [89]. By definition, the refractive index of a medium is a measure of how much the speed of light is reduced inside the medium. It is a fundamental optical property of polymers that is directly related to other optical, electrical, and magnetic properties. For example, electron-rich organic dopants, dissolved in polymers, cause a pronounced increase in the refractive index.

5.1 Measurement principle

Global loop delay τ_g of the OEO is composed of optical delay τ_{op} and electrical

delay τ_{el} . The optical delay is the time for the optical signal to travel through the optical fiber in one single loop. This delay depends on the velocity of the light inside the fiber loop which is affected by the refractive index of the fiber. The electrical delay is the time for the electrical signal to travel from the photodetector output to the RF electrode of the MZM in one single loop. This electronics part includes RF amplifiers, RF filter, RF coupler and some connecting cables. We also present the way to estimate the equivalent electrical delay in the OEO based on the theoretical calculation and experimental measurements.

It should be reminded that, the oscillation frequency has a relation with global delay by:

$$f_{0k} = \frac{k}{\tau_g} = \frac{k}{\tau_{op} + \tau_{el}} \quad (5.1)$$

According to the Eq. (5.1), with the same mode number k , by changing the global delay, we can change the oscillation frequency. Considering a very small change of the global delay due to a variation of τ_{op} , we obtain at the first order the change of the oscillation frequency:

$$\frac{\Delta f_{osc}}{f_{osc}} \cong -\frac{\Delta \tau_g}{\tau_g} = -\frac{\Delta \tau_{op}}{\tau_g} \quad (5.2)$$

To visualize this relation for the frequency of 8 GHz, as indicated in Figure 5.1, two collimated lenses are inserted into one end of the fiber loop.

The two lenses are tuned and aligned to have maximum transmitted light through it. This setup allows the light can be transmitted through the free space between two lenses and by that it can maintains a closed loop. Lens 1 is mounted at a fixed position while lens 2 is mounted on an accurate tunable mechanic tool which can keep these two lenses on the same concentric axis.

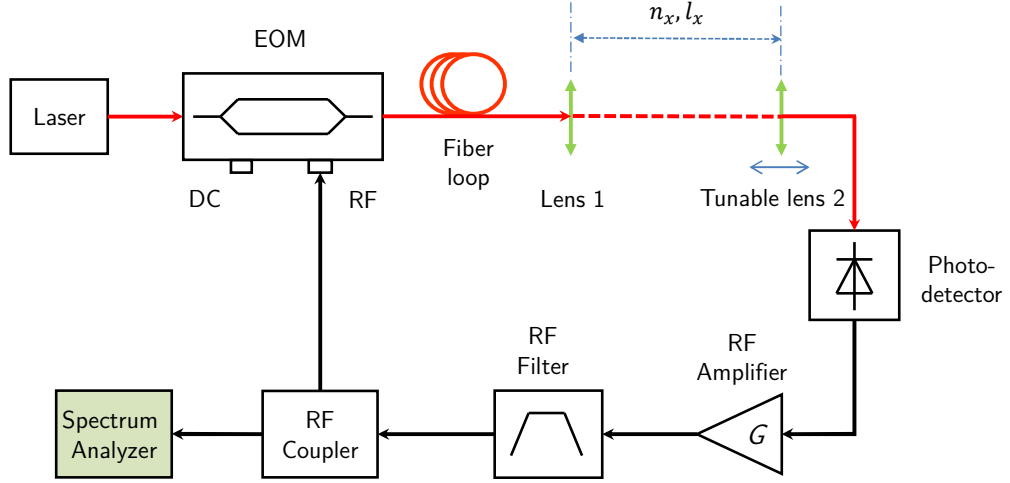


Figure 5.1 OEO with an optical fiber-to-fiber coupling system

By tuning the position of lens 2, we can tune the distance between lens 1 and lens 2. By that, the optical length τ_{op} of the OEO is varied and as result the oscillation frequency of the OEO is changed as shown in Figure 5.2 [11]. It is logically conformed to Eq. (5.1) that when we increase the optical length, the oscillation frequency decreases.

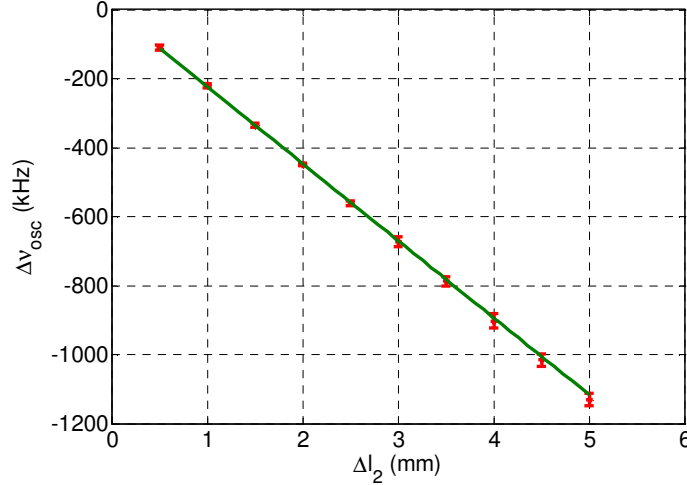


Figure 5.2 Relation between the variation of the oscillation frequency and the optical length at 8.004 GHz [11]

To measure a distance variation, we should mount two lenses on two ends of the structure or object to be monitored. The way of mounting is required to keep two lenses are always in line of sight and well aligned. From Eq. (5.2) and as on one hand $\Delta\tau_{op} = \Delta l_x \frac{n_{op}}{c_0}$ and on the other hand $\tau_g \cong \tau_{op} = \frac{n_{op} l_{op}}{c_0}$ the distance variation is given

by:

$$\Delta l_x = -\frac{\Delta f_{osc} n_{op} l_{op}}{f_{osc} n_x} \quad (5.3)$$

where:

n_x : refractive index of the environment between two lenses. Our experiment is carried out in the room condition, so we can consider that $n_x = n_{air} \approx 1$.

l_x : length of the free space part included in the optical loop.

n_{op} : refractive index of the optical fiber.

l_{op} : optical fiber length.

At the beginning, we measure the first oscillation frequency f_{osc1} . To detect a distance variation, we measure the new oscillation frequency f_{osc2} . From these two values, we can get the frequency difference $\Delta f_{osc} = f_{osc2} - f_{osc1}$. Replace this value to Eq. (5.3), we can obtain the distance variation between two lenses.

5.2 Short-term refractive index measurement

5.2.1 Experimental setup

Based on the principle of oscillation frequency versus optical delay, the OEO can be used to measure the refractive index of a liquid. For the refractive index measurement, when the light travels through the liquid, its intensity is reduced due to the absorption caused by the liquid. To compensate this reduction, we need to use a greater laser power.

In the experiment in Chapter 2, a laser diode FLD5F6CX from Fujitsu Company is used, the maximum optical output power is less than 4 mW. In this experiment, we use a tunable laser 81940A inserted in a lightwave multimeter 8163B from Agilent Technologies. Its wavelength is tunable in the range of 1520 nm – 1630 nm, the optical power is from 4 mW to 20 mW (13 dBm). The wavelength has been tuned at 1550 nm.

Then, we open the fiber loop and insert another optical fiber-to-fiber coupling system as shown in Figure 5.3.

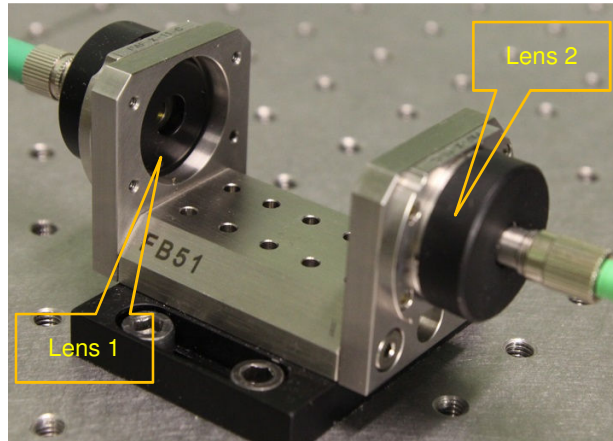


Figure 5.3 Optical fiber-to-fiber coupling system

Unlike the configuration shown in Figure 5.1, both lenses in this experiment are firmly fixed. To increase the stability and the accuracy of the measurement, we use an optical fiber-to-fiber coupling system from Thorlabs which includes two Fiber-Port collimators (PAF-X-11-C), a single axis fiber bench with wall plates (FB-51W). Furthermore, in order to keep the quartz cuvette in the perpendicular position with the optical path between two collimated lenses, we use a universal component base (UCB) from Thorlabs and design several adapter structures by ourselves.

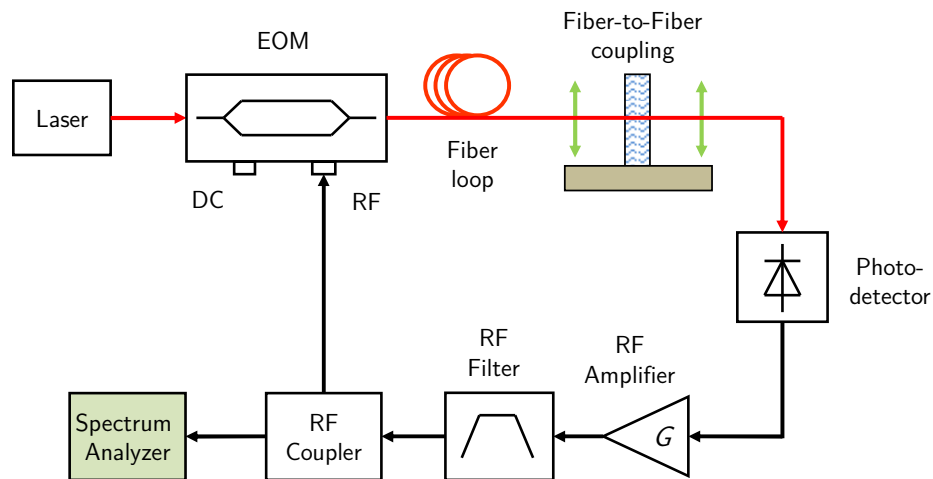


Figure 5.4 Refractive index measurement using an OEO with an optical fiber-to-fiber coupling system

Figure 5.4 shows the structure of our system when the cuvette is inserted into the OEO. A cuvette made of quartz has been chosen in order to meet high transmission requirement.

In the middle of two lenses, we will place a transparent cuvette containing the

liquid to be analyzed. To ensure the laser is highly transmitted from lens 1 to lens 2, the cuvette should be made of a high quality glass. Here, we used a 2 mm quartz cuvette (ref: 441/2mm) from Thuet (France) [90] and a 10 mm quartz cuvette (ref: 111-QS) from Hellma (Germany) [91].

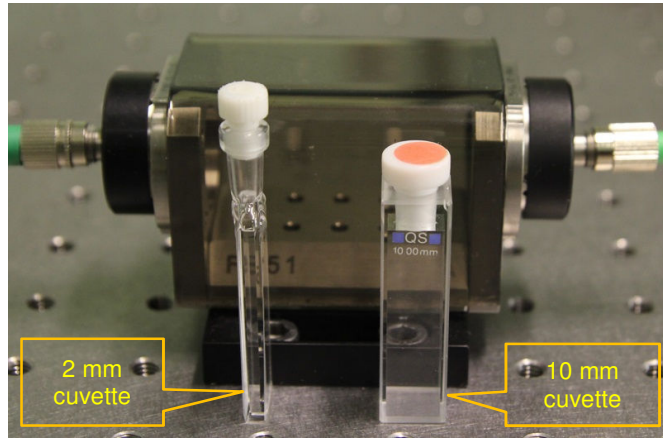


Figure 5.5 2 mm and 10 mm quartz cuvettes used for measurements

To reduce the light refraction and reflection effect, the cuvette is placed perpendicularly to the laser beam, by that the laser is transmitted through two opposite sides of the cuvettes. Filling the cuvette with a liquid creates minor changes to the optical path and also to the global delay of the loop. By the way the oscillation frequency is slightly shifted, and by measuring this change, for example with a spectrum analyzer, it is possible to determine the variation of the refractive index which occurred inside the cuvette.

The sensing part can be illustrated by Figure 5.6:

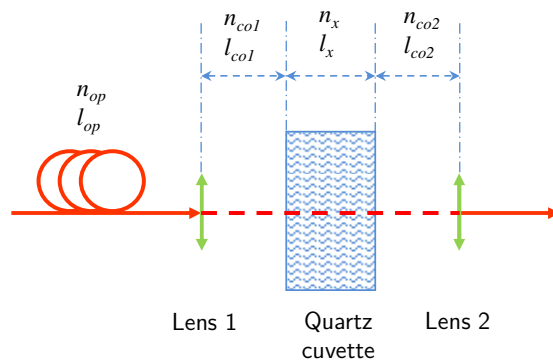


Figure 5.6 Optical fiber-to-fiber coupler and the cuvette

where

n_{op}, l_{op}	refractive index and length of the fiber.
n_{co1}, l_{co1}	refractive index and length of the air between lens 1 and cuvette
n_{co2}, l_{co2}	refractive index and length of the air between lens 2 and cuvette
n_x	refractive index of the liquid to be measured
$l_x = d_c$	width of the cuvette

In case of an empty cuvette, we can write at a fixed order k :

$$k = f_{osc}(\tau_{op} + \tau_e + \tau_{co} + \tau_{ac}) \quad (5.4)$$

where:

τ_{op}	the optical delay of the fiber loop $\tau_{op} = n_{op}l_{op}/c_0$.
τ_e	the delay in the electronic part of the oscillator.
τ_{co}	the delay due to the air within the space of fiber-to-fiber coupling system but outside the cuvette.
τ_{ac}	the delay due to the air in the test cuvette.

When the cuvette is empty, the air inside the cuvette has a refractive index n_{air} approximately equal to 1. Then, the liquid is filled into the cuvette. The variation Δn_x between the refractive index of the air before filling and the filled liquid creates a change in the oscillation frequency. The corresponding refractive index of the liquid is determined by:

$$n_x = n_{air} + \Delta n_x \quad (5.5)$$

Eq. (5.4) can be written as:

$$k = f_{osc}(\tau_{op} + \tau_e + \tau_{co} + \tau_x) \quad (5.6)$$

where τ_x is the optical delay in the liquid to be studied depending on the refractive index n_x to be determined.

$$\tau_x = \frac{n_x d_c}{c_0} \quad (5.7)$$

where d_c is the inner width of the cuvette.

From Eq. (5.2), (5.4), (5.6) and (5.7), we can obtain the difference of the refractive indexes of the liquid and of the air:

$$\Delta n_x = -\frac{\Delta f_{osc} \cdot c_0}{f_{osc} \cdot FSR \cdot d_c} \quad (5.8)$$

So the refractive index of the liquid can be calculated from Eq. (5.5). From Eq. (5.8), with a given variation of refractive index, it is easy to calculate the change of oscillation frequency:

$$\Delta f_{osc} = -\Delta n_x \frac{f_{osc} \cdot FSR \cdot d_c}{c_0} \quad (5.9)$$

Considering this formula, it appears necessary to increase as much as possible the oscillation frequency, the free spectral range and the width of the cuvette for improving the sensitivity of the system. By this way it should be possible to improve the detection limit in term of RIU (Refractive Index Unit).

5.2.2 Calibration of the free spectral range

It should be reminded that from Eq. (2.13) $FSR = c/nL_g$, it is easy to figure out that the FSR is an important factor in accuracy of the measurements using the single loop OEO. The FSR of the OEO has a close relation with the equivalent loop length.

A calibration of the FSR has been conducted using an OEO starting from the basic fiber loop length of 4 m. Then, the loop length has been increased with a step of 500 m by using Corning SMF-28 fiber loops which have an effective refractive index of 1.4682 at the wavelength of 1550 nm. The 4 m fiber corresponds to two connecting fibers attached to the fiber-to-fiber coupling system. Other sections of short optical fibers are mounted with the modulator and at the input of the photodetector. These unknown quantities of fiber loop and the electrical delay can be globally determined from the different FSR measurements. In this calibration, the fiber-to-fiber coupling system with empty cuvette is placed in the oscillator loop.

Table 5.1. *Measurements of the FSR and equivalent loop length*

Fiber loop length (m)	4	504	1,004	1,504
Measured FSR (kHz)	8,997.0	388.3	199.4	133.5
Equivalent length (m)	23	526	1,025	1,531

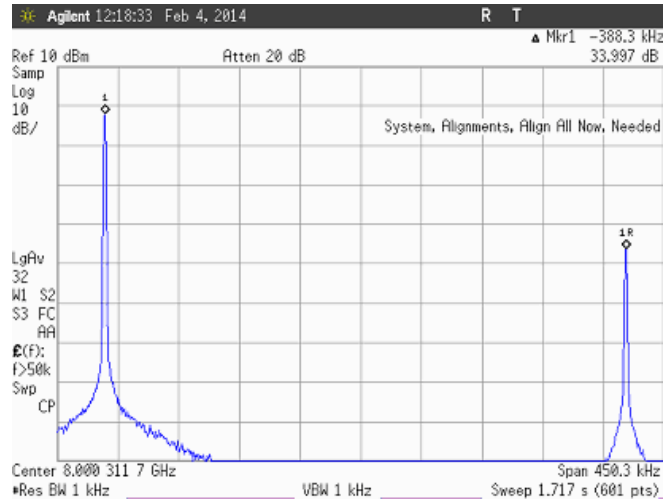


Figure 5.7 FSR of 504 m fiber OEO with an empty cuvette placed in the fiber-to-fiber coupling system

From Table 5.1, we can see that the equivalent global length of the oscillator delay line is systematically longer than the real length of the fiber loop. These differences are approximately in the range of 19 m to 27 m corresponding to the short fibers, fiber-to-fiber coupling with empty cuvette and the electrical delay.

Figure 5.7 shows the FSR measurement in the case of a fiber loop length of 4 m + 500 m with the empty cuvette inserted in the fiber-to-fiber coupling. The center frequency is 8.0003117 GHz, span is 450.3 kHz and the number of points is 601. To increase the accuracy, we used the averaging function of the spectrum analyzer with a factor of 32. Another way to improve the accuracy of FSR measurement is to increase the number of points or improving the resolution bandwidth in the setting of the spectrum analyzer.

5.2.3 Individual measurement

In this type of measurement, the laser will be transmitted through the liquid, so the liquid to be measured must be transparent enough and has low absorption at the wavelength 1550 nm. We select 4 solutions matching these criteria: acetone, acetonitrile, dioxane and dioxolane.

Steps of individual measurement:

- a) Clean inside and outside of the cuvette with acetone and tissue. Let it be dried.
- b) Put the empty cuvette in the middle of the fiber-to-fiber coupling system.

- c) Measure the first oscillation frequency.
- d) Fill the solution into the cuvette.
- e) Measure the second oscillation frequency.
- f) Calculate the refractive index from measured variation of frequency.

The oscillation frequency is measured by our Agilent spectrum analyzer PSA E4446A which is configured with a span of 5 kHz and a resolution bandwidth (RBW) of 47 Hz.

In this work, we keep f_{osc} at 8 GHz, and we set up four different combinations of optical fiber lengths and quartz cuvette types. The measurements are repeated 10 times for each solution.

5.2.3.1 Measurement with 500 m fiber and 2 mm cuvette

In the first configuration, we use a fiber loop of 500 m long and a cuvette of 2 mm width. The 2 mm cuvette is placed in the middle of the fiber-to-fiber coupling system with a homemade supporting adapter as shown in Figure 5.8.

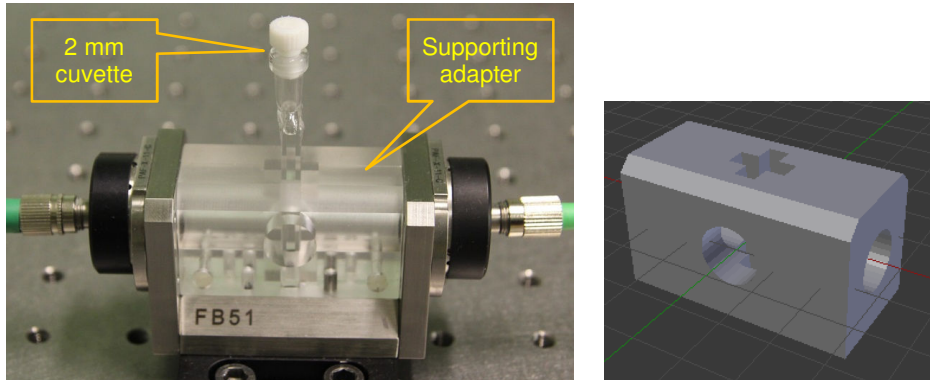


Figure 5.8 2 mm cuvette and its supporting adapter placed the optical fiber-to-fiber coupling system.

Table 5.2. Measurement results with 500 m fiber and 2 mm cuvette

Measured solution	Δf_{osc} (kHz)	Refractive index	Standard deviation
Acetone	6.950	1.3356	0.0097
Acetonitrile	6.784	1.3276	0.0073
1,4 – Dioxane	8.167	1.3943	0.0045
1,3 – Dioxolane	7.869	1.3800	0.0058

After measuring for four chemical solutions, the results are listed in Table 5.2. The results obtained in Table 5.2 have lower standard deviation than our previous experiment [92] thanks to the mechanical precise improvement of the quartz cuvette mount in the fiber-to-fiber coupling structure.

5.2.3.2 Measurement with 500 m fiber and 10 mm cuvette

From Eq. (5.8), we found that, in order to increase the measurement resolution, we can increase the oscillation frequency f_{osc} , the FSR , or the width of the cuvette d_c . In the second configuration, we keep the fiber loop of 500 m long but replace 2 mm cuvette by 10 mm one. Another supporting adapter suitable with 10 mm is used as in Figure 5.9

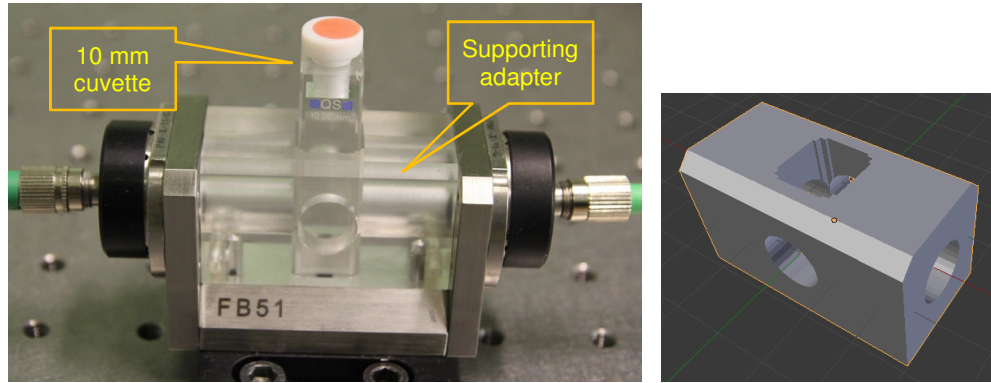


Figure 5.9 10 mm cuvette and its supporting adapter placed the optical fiber-to-fiber coupling system.

Repeating the refractive index measurements for four liquids, we achieve the results in the Table 5.3.

Table 5.3. Measurement results with 500 m fiber and 10 mm cuvette

Measured solution	Δf_{osc} (kHz)	Refractive index	Standard deviation
Acetone	36.872	1.3561	0.0031
Acetonitrile	35.105	1.3390	0.0029
1,4 – Dioxane	43.252	1.4177	0.0008
1,3 – Dioxolane	41.090	1.3968	0.0022

The results show that by using a 5 times bigger cuvette, the Δf_{osc} values in this experiment are approximately 5 times greater than those acquired in Table 5.2. It is theoretically conform to Eq. (5.8) and Eq. (5.9).

5.2.3.3 Measurement with 4 m fiber and 2 mm cuvette

In this experiment, we try to increase the resolution more by using a shorter fiber loop. The 500 m fiber used in the first two configurations is replaced by a 4 m fiber.

All necessary steps are taken to achieve the results listed in Table 5.4.

According to Table 5.1, the equivalent length of 4 m and 500 m configurations are 23 m and 526 m respectively, corresponding to a ratio of 22.87. We will verify this ratio by considering Δf_{osc} of acetone of the first configuration and this experiment.

In the first configuration, Δf_{osc} is 6.950 kHz while in Table 5.4 it is 162.029 kHz which corresponding to a ratio of 23.31. Comparing with the fiber length ratio of 22.87, this value is reasonable.

Table 5.4. Measurement results with 4 m fiber and 2 mm cuvette

Measured solution	Δf_{osc} (kHz)	Refractive index	Standard deviation
Acetone	162.029	1.3414	0.0079
Acetonitrile	159.835	1.3368	0.0061
1,4 – Dioxane	197.251	1.4156	0.0058
1,3 – Dioxolane	185.231	1.3903	0.0065

5.2.3.4 Measurement with 4 m fiber and 10 mm cuvette

In the fourth experiment, one more time, we keep 4 m fiber and replace 2 mm cuvette by 10 mm cuvette. Similar to thee configurations mentioned above, we display our result in Table 5.5.

Table 5.5. Measurement results with 4 m fiber and 10 mm cuvette

Measured solution	Δf_{osc} (kHz)	Refractive index	Standard deviation
Acetone	900.525	1.3753	0.0051
Acetonitrile	845.063	1.3522	0.0031
1,4 – Dioxane	1,061.971	1.4426	0.0016
1,3 – Dioxolane	1,007.755	1.4200	0.0041

Taking one value of Δf_{osc} of 1,4-Dioxane for comparing with the third configuration: 1,061.971 kHz vs 197.251 kHz leading to a ratio of 5.38. It is a little bit

greater than the cuvette length ratio of 5.

5.2.4 Measuring with an RF generator

For each individual measurement mentioned in 5.2.2, it is necessary to measure twice the oscillation frequency: when the cuvette is empty and when the cuvette is filled with the chemical solution. In order to get directly the frequency shift due to the change in liquid's refractive index, we propose a new configuration as shown in Figure 5.10.

In Figure 5.10, the first oscillator is used with a fiber-to-fiber coupling and is called measurement oscillator. Its oscillation frequency is called as f_0 . The RF generator plays a role as a reference source, its oscillation frequency is f_{ref} . In our laboratory, the RF generator is Agilent 8257D.

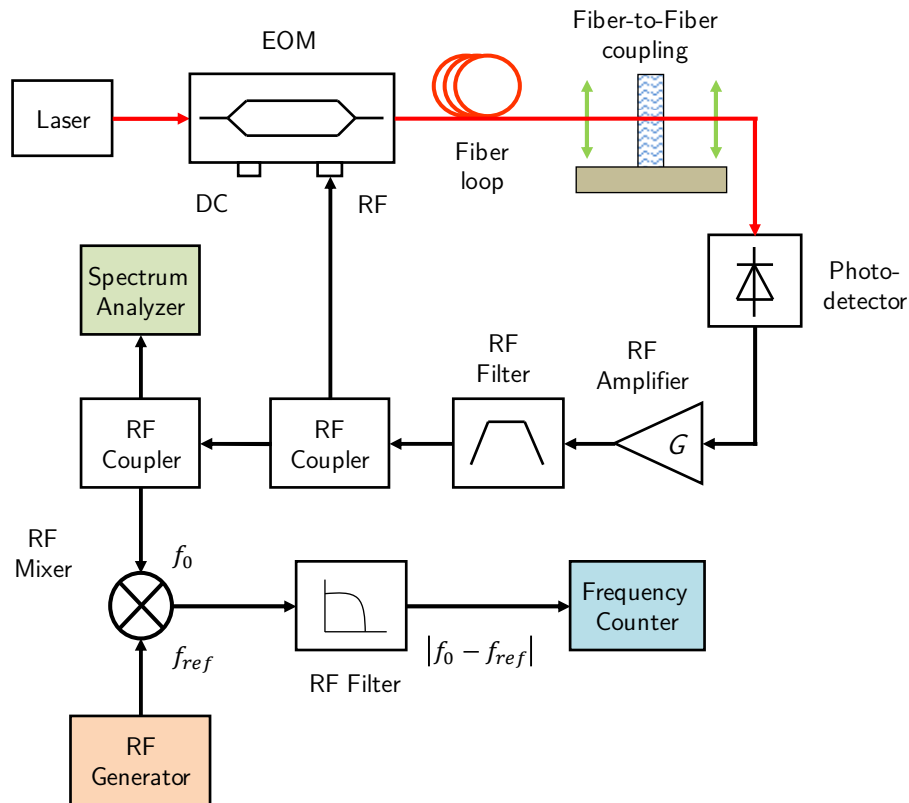


Figure 5.10 Refractive index measurement with an OEO and a generator.

The output of the measurement oscillator is connected to another RF coupler to monitor the oscillation frequency, and at the same time, to transfer the oscillation frequency to the RF port of the RF mixer (Marki double-balanced mixers M1-0212 [93]). The output of the RF generator is applied to the LO input of the mixer.

The mixer produces new frequencies at the sum $f_0 + f_{ref}$, the difference $f_0 - f_{ref}$ and other frequency components as results of different combination of f_0 and f_{ref} . A low pass RF filter is placed at the output of the RF mixer to filter out high frequencies. By using a frequency counter at the output of RF filter, we obtain the difference $|f_0 - f_{ref}|$. The frequency counter is a HP53131A [94].

To perform the refractive index measurement, an empty cuvette is placed into the fiber-to-fiber coupler. The measurement OEO generates the oscillation frequency at f_0 . Then, we tune the RF generator to create the frequency at f_{ref} , and at this step, $f_{ref} = f_0$. When we put the liquid into the cuvette, the measurement OEO has a new frequency f_0 . The quantity $\Delta f = |f_{ref} - f_0|$ reflects the difference between the refractive indexes of the liquid and of the air.

How can we determine the changing direction of f_0 compare to f_{ref} ? As we know that the velocity of light in vacuum is the fastest which corresponding to its refractive index of 1. The light travels in the air with a slower speed than in vacuum because of air's refractive index is greater but very close to 1. Other chemical liquids have refractive index higher than 1, so according to Eq. (5.9) the oscillation frequency will decrease when the cuvette is filled by a chemical solution, it means that $f_0 < f_{ref}$.

Other studies have figured out that, the OEO is very sensitive to the surrounding changes. This drawback can be eliminated by putting the fiber spool and RF filter into a well temperature stabilized box with a stability as low as 0.001 °C over 1 hour and 0.003 °C over 24 hours in a constant ambient temperature [76], [77].

Table 5.6. Measurement results with 4 m fiber, 10 mm cuvette and an external RF generator

Measured solution	Δf_{osc} (kHz)	Refractive index	Standard deviation
Acetone	865.525	1.3607	0.0044
Acetonitrile	823.089	1.3431	0.0037
1,4 – Dioxane	1,014.046	1.4226	0.0013
1,3 – Dioxolane	960.255	1.4002	0.0029

Before taking measurement, we tune the RF generator to create a signal at frequency $f_{ref} = f_0$, the power is set to -10 dBm. When starting new measurement,

we also need to repeat this tuning procedure. This is due to the fact that, the oscillation frequency f_0 is drifted slowly due to the ambient change. When we fill the liquid into the cuvette, f_0 becomes f_1 , and by looking at frequency counter, we can get directly the Δf .

Applying this procedure to the same set of four chemical solutions, we have results as shown in Table 5.6. Here we can observe that the oscillation frequency variations Δf_{osc} in Table 5.6 are systematically smaller than those in Table 5.5. The reason has to be further investigated.

5.3 Real-time and long-term measurement by using an external frequency source

In some situations, it could be necessary to measure the refractive index in real-time and long-term, however, the configuration mentioned in 5.2.4 could not be used. Because the real-time and long-term measurement method based on the variation of two different frequency sources, the first one is the reference frequency and the second one is the measured frequency. To achieve a good result, the reference source must be stable enough. However, as discussed in 3.7, under the temperature change, the OEO has always a slow drift of the oscillation frequency by itself if the system is not well thermal stabilized. In order to get directly the frequency shift due to the change in liquid's refractive index, we propose a new configuration as shown in Figure 5.11.

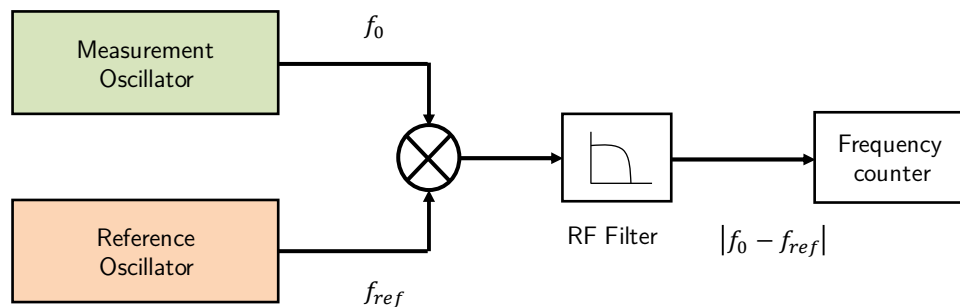


Figure 5.11 Real-time and long-term refractive index measurement with two identical OEOs

Two OEOs are assumed to use the same elements and ideally, they can be considered as identical except in the measurement oscillator, one sensing part is inserted to measure the liquid. The two OEOs can be considered to have the same behavior with respect to ambient environment changes. Any changes not caused by

the sensing part in the measurement OEO is compensated by the same change happened in the reference OEO. These changes at both OEOs will be canceled by the RF mixer. The detail scheme is shown in Figure 5.12.

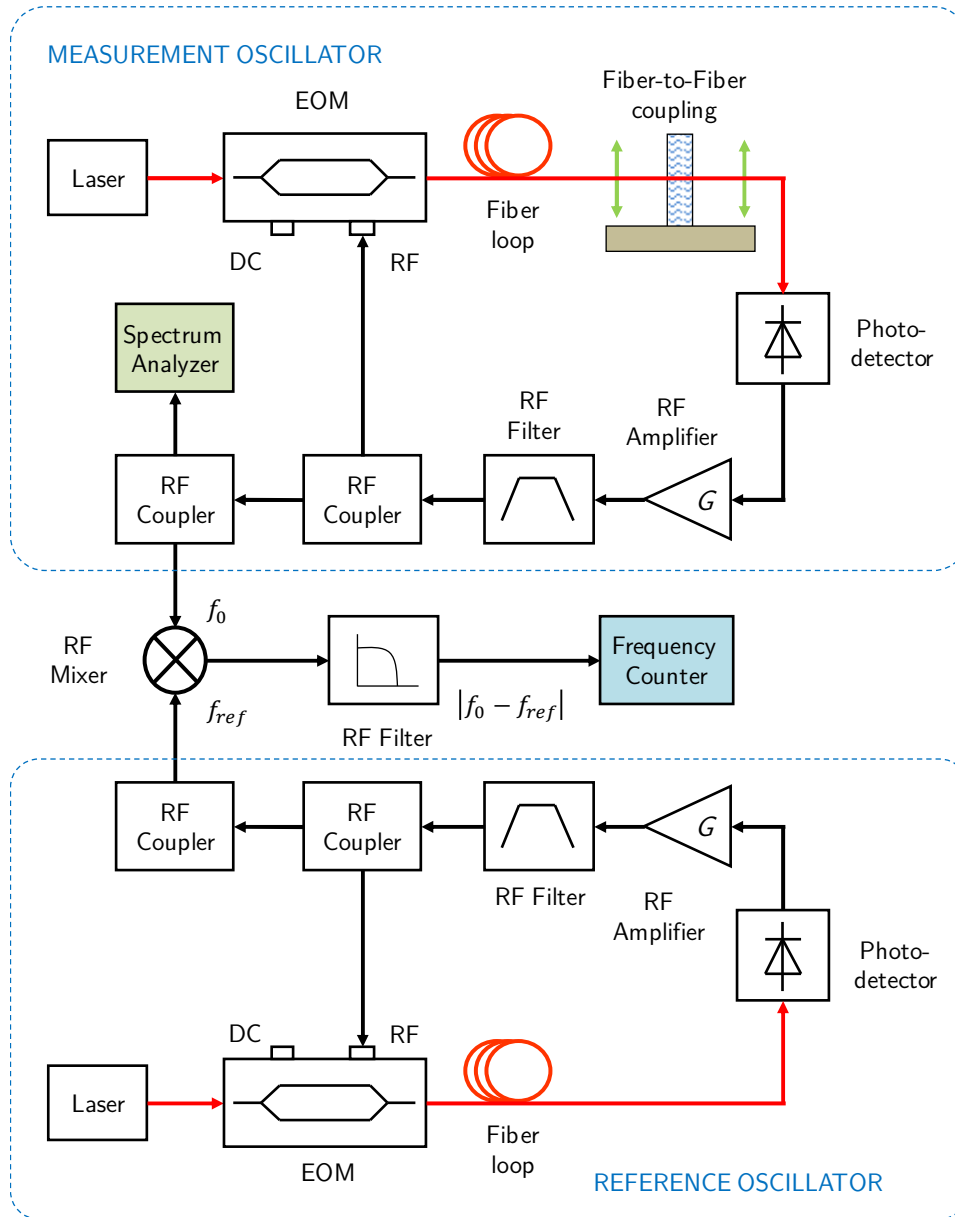


Figure 5.12 Two-OEO-based configuration for real-time and long-term refractive index measurement

The advantage of this configuration is significantly useful when monitoring refractive index variations of a chemical reaction in long-term. This two-OEO-based configuration can overcome the unwanted drift effect caused by ambient fluctuations.

At the beginning, if the oscillation frequencies of two oscillators are not the same, one RF phase shifter could be added to the reference oscillator to tune $f_{ref} = f_0$.

Then the chemical reaction is filled into the cuvette. Similar to section 5.2.4, the value shown on frequency counter indicates the frequency change due to the chemical reaction.

5.4 Conclusions

In this chapter, we have presented the relation between oscillation frequency and loop delay which can be used to apply the OEO in sensing application. We realized different configurations to measure the refractive index for four chemical solutions. In order to compare our results to previous publications, we show below the refractive indexes of the four liquids already published in [10]; they are listed in Table VII. These standard values have been obtained at wavelength $\lambda = 589$ nm (sodium D line) and a temperature of 20 °C. These experimental conditions are different compared to those of our laboratory without air conditioned and a room temperature measured during the experiments is in the range of 22 \leftrightarrow 24 °C.

The refractive indexes values in Table 5.2, Table 5.3, and Table 5.4 are lower than those listed in Table 5.7. This is in agreement with the Cauchy law, because the wavelength used in our experiments is 1550 nm which leads to a decrease in the refractive index results. The measurement results for acetone solution are also suitable by comparison with the value of 1.3540 measured with an Abbe refractometer at the wavelength of 830 nm and 20 °C [95], and the value of 1.345 measured at the wavelength of 1551 nm and 25 °C [96].

Table 5.7. Reference refractive indexes

Measured solution	n_D^{20}
Acetone	1.3588
Acetonitrile	1.3442
1,4 - Dioxane	1.4224
1,3 - Dioxolane	1.3974

The measurements data obtained in Table 5.5 and a part of Table 5.6 are slightly over estimated than those listed in Table 5.7. This irregular result is still under examination. One possibility could be an effect of the RF filter, because with a deviation of 1 MHz for the oscillation frequency the phase-shift could be rather important and it needs to be further characterized.

From the experimental data shown in section III, we can see that with the same fiber loop length, the results measured with the 10 mm cuvette have better standard deviation than those measured with the 2 mm cuvette. That was predictable from Eq. (5.8). However, there is a tradeoff between the stability of the oscillation frequency, the resolution and the fiber loop length. The shorter the fiber loop, the higher the measurement resolution. Unfortunately, for a shorter loop, the oscillation frequency stability tends to decrease. Among our four experiments, the configuration including 504 m fiber loop and 10 mm cuvette is the best combination because it has the lowest standard deviation.

More systematic tests should be implemented in order to find the real optimal combination. However, from Eq. (5.9), mathematically, another method to increase the measurement resolution is to work with higher oscillation frequency.

From the previous results, we can infer some characteristics of this measurement system. For example, with $f_{osc} = 8$ GHz, a free spectral range of 400 kHz (corresponding to a fiber loop of 500 m) and a cuvette of 10 mm width, the sensitivity of the frequency measurement is $\Delta f_{osc} = 103.5$ kHz/RIU (RIU = Refractive Index Unit). Or if frequency measurement accuracy is approximately 1 kHz as Δf_{osc} then it should be possible to detect a variation of the refractive index $\Delta n_x \simeq 10^{-2}$. When measuring oscillation frequency at 8 GHz, our spectrum analyzer Agilent PSA-E4446A can be configured with a span of 100 Hz and a resolution of 1 Hz. With the accuracy of frequency measurement is 1 Hz, theoretically, this leads to a refractive index sensitivity of $\Delta n_x = \frac{1}{103500} \approx 0.966 \cdot 10^{-5}$. Obviously, the stability of the OEO oscillation frequency needs to be more improved to be able to achieve this result.

The advantages of our method lies in the fact that it can be applied in-situ, under the condition that it is possible to access to the material by the way of aligned optical fibers, to track the variation of refractive index in real-time and for a long-term. Otherwise determining a change of frequency presents a much better noise immunity than that of amplitude or intensity.

Chapter 6

Improving long-term refractive index measurement with a vector network analyzer

Beside applications in radar, telecommunication and satellite systems, OEO can also be used in sensor applications such as refractive index or distance measurements. However, the long-term stability of the OEO is easily affected by ambient environment variations. The optical fiber loop effective refractive index varies corresponding to its surrounding temperature changes. Consequently, it makes the optical transmission path inside the fiber loop differ from the initial state, leading to oscillation frequency changes. To stabilize the oscillation frequency of the OEO, it is essential to keep its high Q elements in a well-controlled thermal box as much as possible. Unfortunately, in the real implementation condition, this requirement is difficult to be satisfied.

This chapter presents a technique to estimate the oscillation frequency variation under the room temperature by using a vector network analyzer (VNA) [97]. Experimental results show a good correlation between OEO oscillation frequency drift and the phase measured by the VNA. This technique can be used to stabilize the OEO or can be implemented to apply corrections when using the OEO as a distance variation or a refractive index measurement tool. We also tracked the temperature of high Q element at the same time with the VNA-based experiment to compare the correlation of temperature and phase with OEO oscillation frequency.

6.1 Principle of measurement

As mentioned in section 5.3, in order to have a good measurement result, the

measurement system should be put in a thermally stabilized chamber, or using two identical OEOs. How can we do if we cannot satisfy these criteria?

To solve this problem, we need to answer the question: how can we determine the drift generated by the OEO itself and separate it from the effect of the liquid to be measured? One solution could be the use of a vector network analyzer (VNA).

The VNA is a very powerful instrument and can be used for distance measurement if it is associated to the optical head of a laser rangefinder, including the laser beam emitter and the photodetector [98] or for improving the accuracy in distance measurement [99]. In this section, we describe our experiment to monitor the long-term stability of the OEO with a VNA as depicted in Figure 6.1.

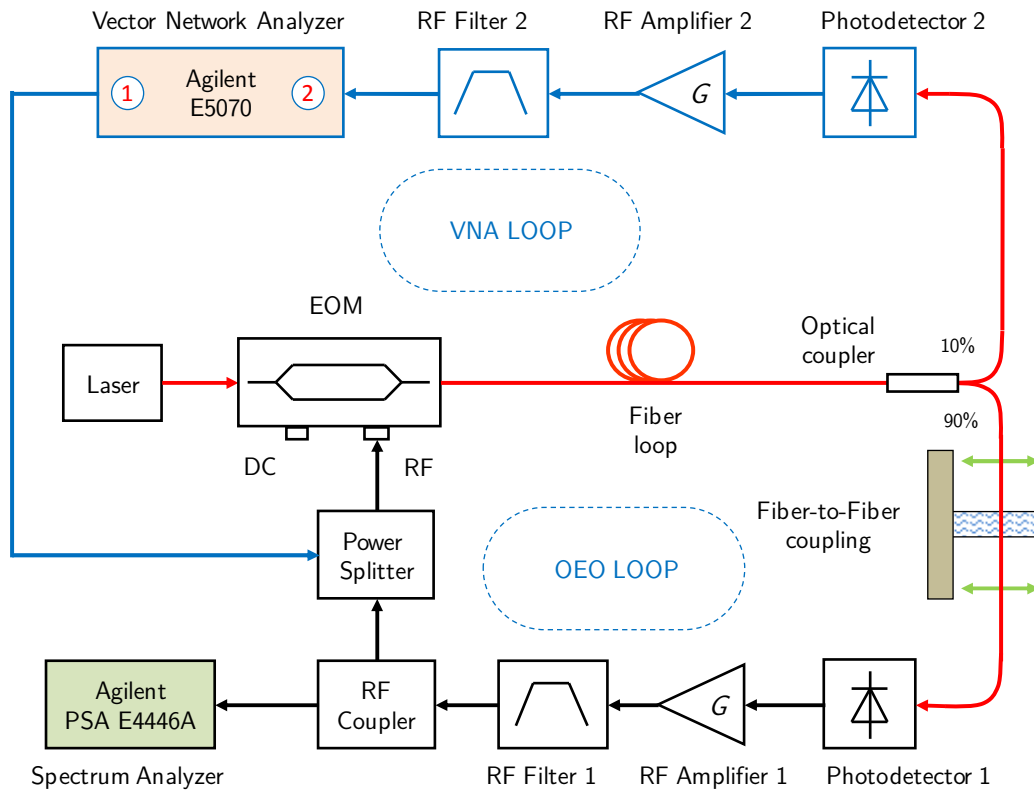


Figure 6.1 System for monitoring and modeling the frequency drift of the OEO. A VNA loop is inserted in order to measure the phase of S_{21} parameter leading to the knowledge of the propagation time across the modulator and the fiber loop.

The VNA is configured to generate a testing signal at 2.1 GHz at the output port 1. This signal is combined with 8 GHz feedback signal of the basic OEO loop and the mixed signal is fed to RF electrode of the MZM. Based on the basic structure of the OEO, we append one more loop by extracting with an optical coupler 10% of optical

beam power at the end of the fiber loop. This extracted light is then detected, amplified, filtered at 2.1 GHz and injected into to the port 2 of the VNA. The VNA used in our experiment is an E5070A model from Agilent Technologies [100].

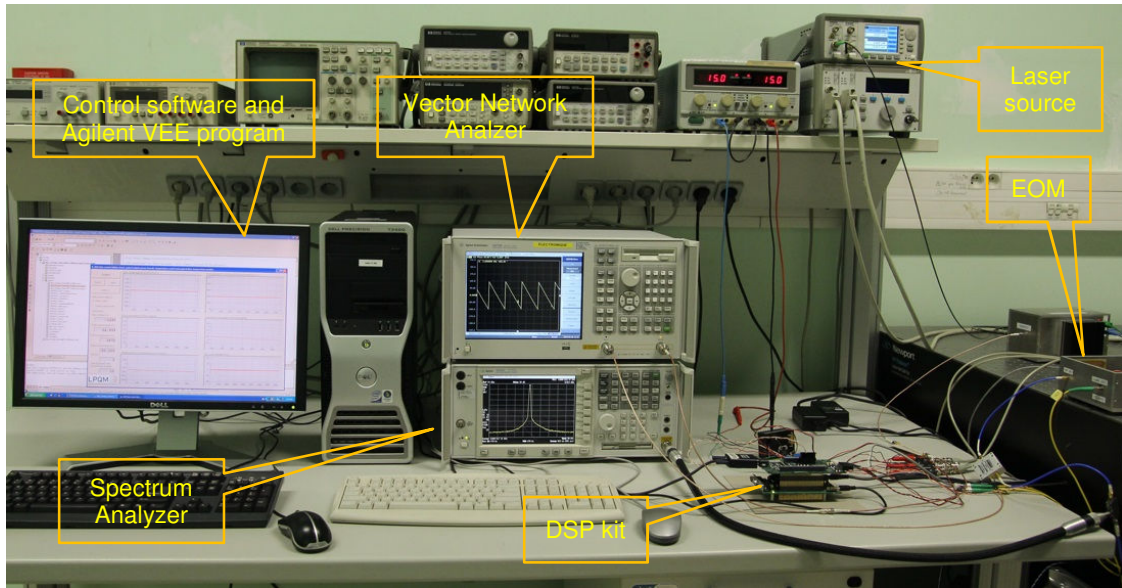


Figure 6.2 Experiment for monitoring and modeling the frequency drift of the OEO (PC, VNA, PSA, DSP and EOM)

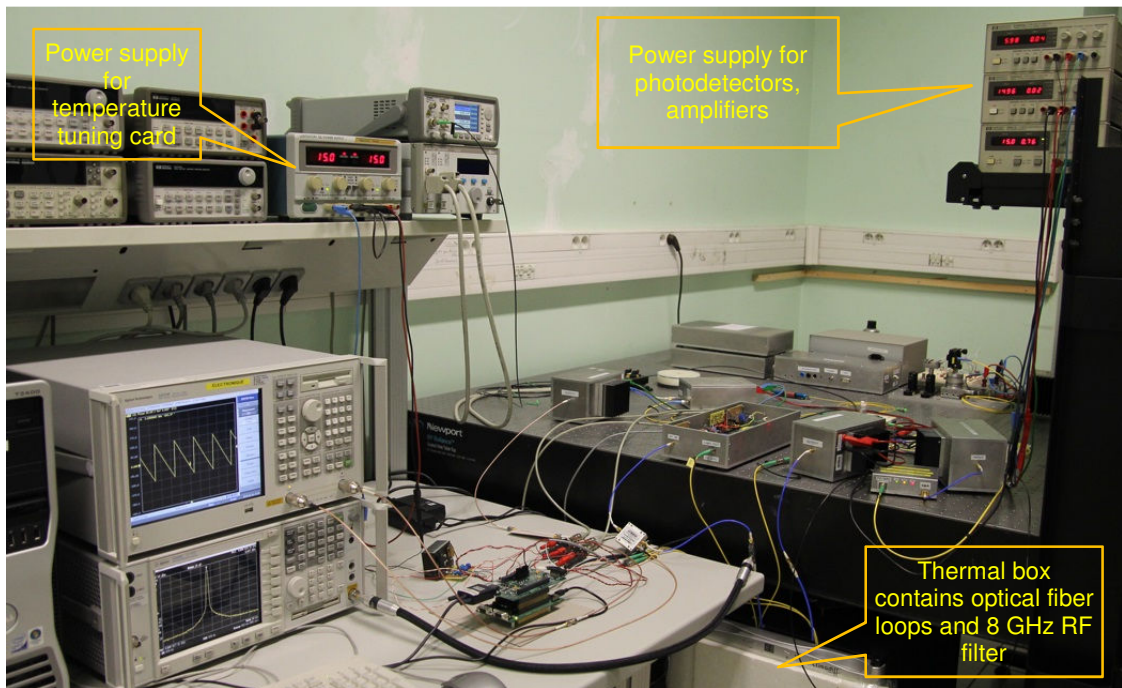


Figure 6.3 Experiment for monitoring and modeling the frequency drift of the OEO (VNA, PSA, DSP and OEO)

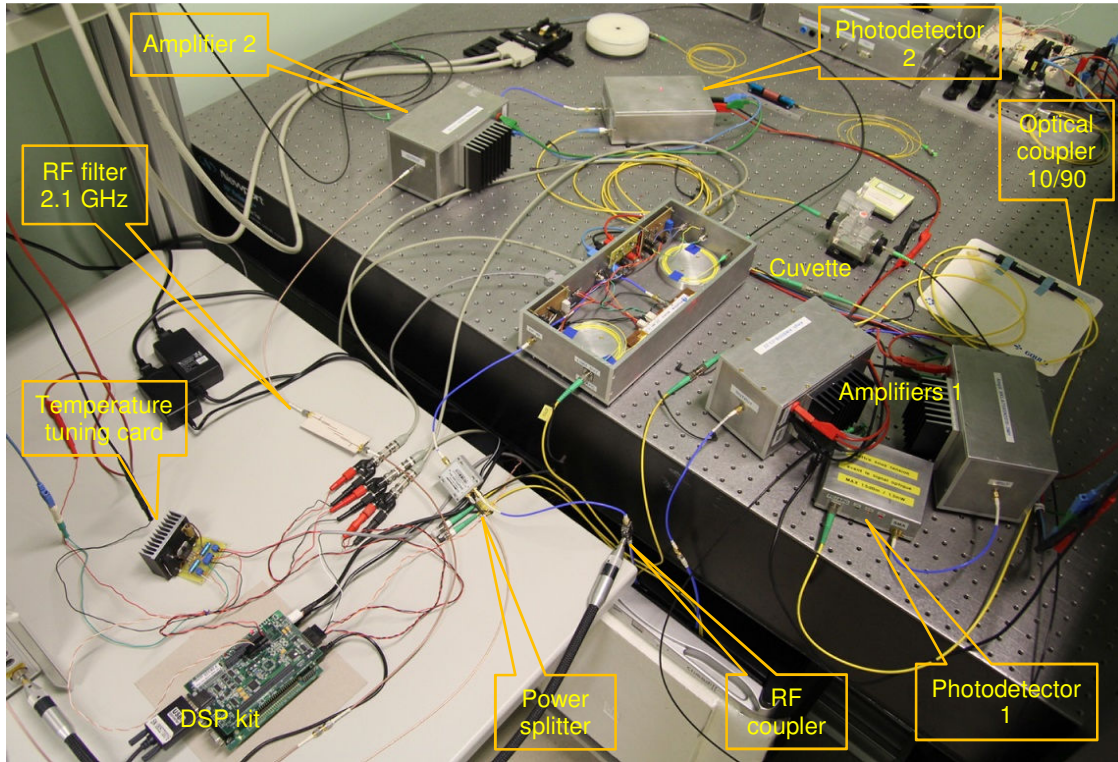


Figure 6.4 Experiment for monitoring and modeling the frequency drift of the OEO (DSP kit, control cards and OEO elements)

The OEO is working at 8 GHz and the VNA operates with a narrow span of 1 MHz centered at 2.1 GHz. These two RF frequencies are chosen far enough in order to be filtered by classical filters. With these frequencies, the testing signal will be filtered by the RF filter 1 already in the main OEO loop and does not disturb the oscillating signal at 8 GHz. On the other hand, the 8 GHz signal will also be filtered by the RF filter 2 in the VNA loop. This filter is a homemade coupled line filter at 2.1 GHz [11] with a bandwidth of 90 MHz, the quality factor is equal to 24 and insertion losses of 1.8 dB; the substrate is made of Duroid 6010. Detailed design of this filter is illustrated in Annex C.2. The 8 GHz filter is the same as in the simple loop already presented in this document. The fiber loop length is 1 km and the free spectral range of the oscillator is approximately 200 kHz. The 8 GHz filter and 2.1 GHz filter were fabricated with different technologies and operates at different frequencies leading to different behaviors under the same temperature fluctuation. However, according to our calibration in section 5.2.2 and other studies [76], [77], [101], the contribution of electrical elements to global delay is very small compared to that of long optical fiber. So, these two filters are assumed to have same behavior under the same temperature change.

The port-1 of the VNA is connected to an input of the power splitter, the other one being connected to the RF coupler of the OEO; the power splitter is used in additive mode the sum of the two RF signals being applied to the same electrode of the modulator. In the VNA loop, an amplification stage and a selective filter at 2.1 GHz have been introduced in order to improve the phase measurement accuracy. The VNA port-2 is connected to the output of the filter. With this structure, it is possible to measure the S_{21} phase leading to the determination of the propagation time in the path including the modulator and the fiber loop.

From the measured phase difference $\Delta\phi_{S_{21}}$, the VNA loop delay variation $\Delta\tau_{g_{VNA}}$ can be derived as:

$$\Delta\tau_{g_{VNA}} = \frac{\Delta\phi_{S_{21}}}{360 \times f_{VNA}} \quad (6.1)$$

where f_{VNA} is the center frequency of the VNA being used to measure the S_{21} parameter.

In an OEO system, in case of ambient temperature changes, the most sensitive component to temperature is the fiber loop and the second one is the RF filter. Other electrical components have negligible sensitivity effect. We assume that the behavior of two filters corresponding to surrounding changes are similar, so that we can consider that $\Delta\tau_g \approx \Delta\tau_{g_{VNA}}$.

From this global loop delay variation $\Delta\tau_g$, at the same oscillation mode k , the oscillation frequency is shifted to a new value that can easily be calculated.

$$f_{osc1} = f_{0k1} = \frac{k}{\tau_g + \Delta\tau_g} \quad (6.2)$$

In the main loop of the OEO, a fiber-to-fiber coupling element is inserted which can be used for distance measurement if the lenses are movable, or for refractive index measurement, for example, a quartz cuvette with a liquid to be analyzed is inserted between the lenses. The experiment has been conducted without any cuvette and without changing the distance between the two lenses: the optical path in the fiber-to-fiber coupler remains constant.

6.2 Improving the phase measurement

Because VNAs are very powerful instruments, they can detect very small signals

and obtain phase information for the S parameters. Nevertheless with a higher power of the signals it should be possible to increase the accuracy of the measurement. Here the modulus of S_{21} parameter is considered. Because of the modulated signal transmitted with the optical carrier, the modulus of S_{21} has no real physical meaning for this experiment, but it can be a good indicator for the quality of the measurement.

For studying this problem, a homemade amplifier has been designed for inserting into the VNA loop. It is based on a pHEMT GaAs FET transistor SPF-2086. The design is achieved in order to get a 50 mA drain current and the gate-source voltage is -0.40 V. Matching cells to 50 ohms, based on transmission lines and short-circuit stubs, have been implemented. When the amplifier is associated to the 2.1 GHz filter, we get a gain of approximately 14 dB (see Figure 6.5). The amplifier has been realized on an available FR4 substrate.

The data from VNA are saved in Touchstone (S2P file) format to be included in ADS software for graphical presentation.

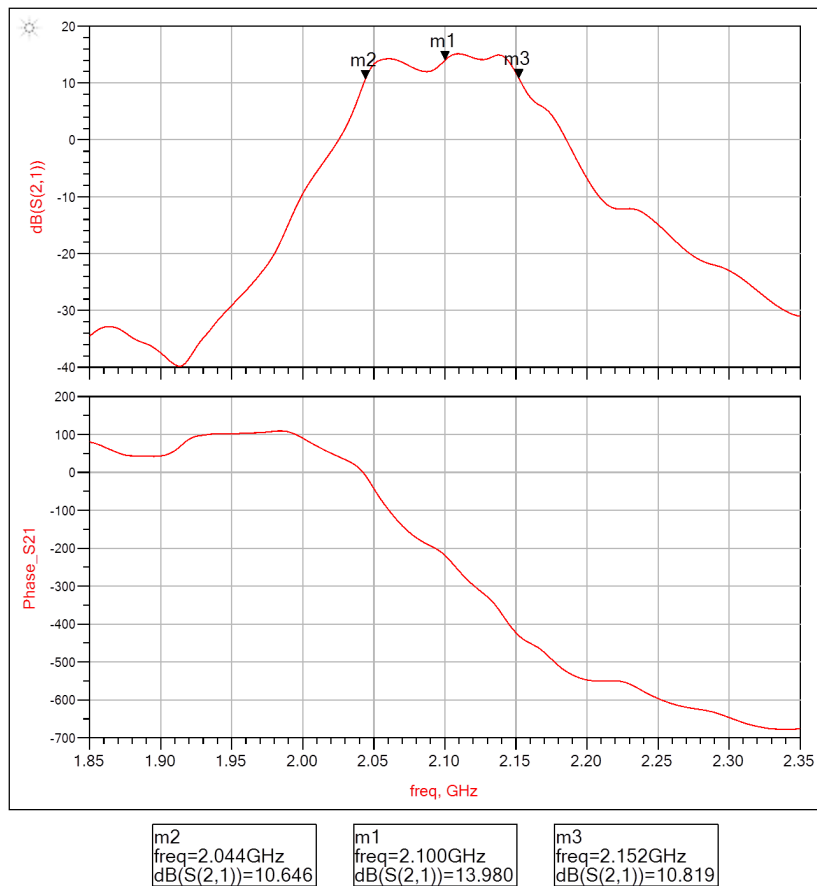


Figure 6.5 Behavior of the homemade filter associated to the amplifier. The bandwidth is equal to 108 MHz. The quality factor is approximately equal to 20.

The homemade amplifier can be also associated to the amplifier which is a Photline DR-GA-10, with a 15 GHz bandwidth and a gain of 27 dB at 2 GHz.

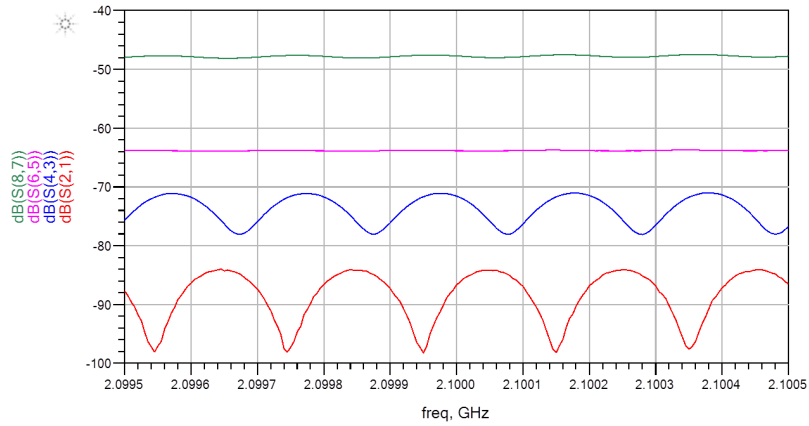


Figure 6.6 Modulus of S_{21} parameter in the VNA loop, showing the improvement in the quality of measurement thanks to the amplifiers placed in the loop.

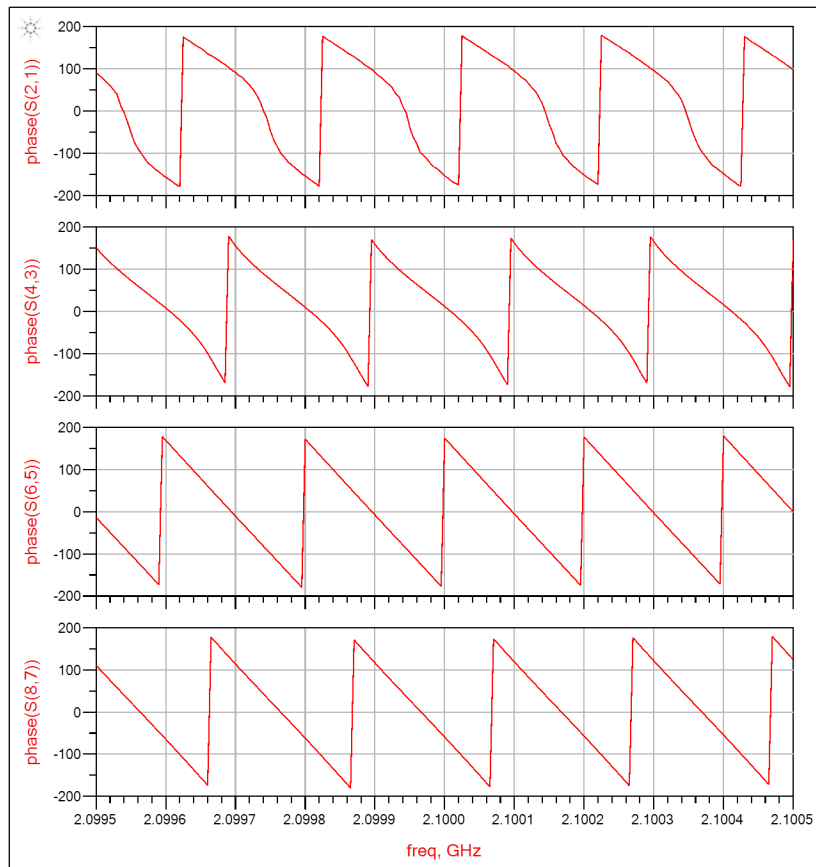


Figure 6.7 S_{21} phase measurement improvement by increasing the amplification in the VNA loop. On top is the case of the filter alone, then with only the homemade amplifier, the Photline one and finally in the bottom with the two amplifiers.

The modulus of S_{21} is shown in Figure 6.6 for different cases. Without any

amplifier in the phase measurement loop ($S(2,1)$ in Figure 6.6) the modulus of S_{21} is approximately -92 dB, with the homemade amplifier alone ($S(4,3)$ in Figure 6.6) it is -74 dB, with the commercial one alone ($S(6,5)$ in Figure 6.6) it is -64 dB and with both commercial and homemade amplifiers ($S(8,7)$ in Figure 6.6) the modulus rises to -48 dB. There is a clear improvement for S_{21} modulus, which means by the way on the power received by the VNA. So the accuracy for phase measurement should also increase.

Then the evolution of phase of S_{21} is shown for the same cases in Figure 6.7. It is also possible to see the improvement in the phase measurement as made by the VNA. Here all the results are obtained with an averaging process of 16 counts.

Better results could be obtained by designing a narrow bandpass amplifier associating, on the same good substrate as duroid, both filter and amplifier.

6.3 Data acquisition program

Similar to Section 3.7.1, this program is created with Agilent VEE Pro 9.3 but in addition to oscillation frequency, power, date and time parameters, it can also register the phase and power of the signal generated by the VNA.

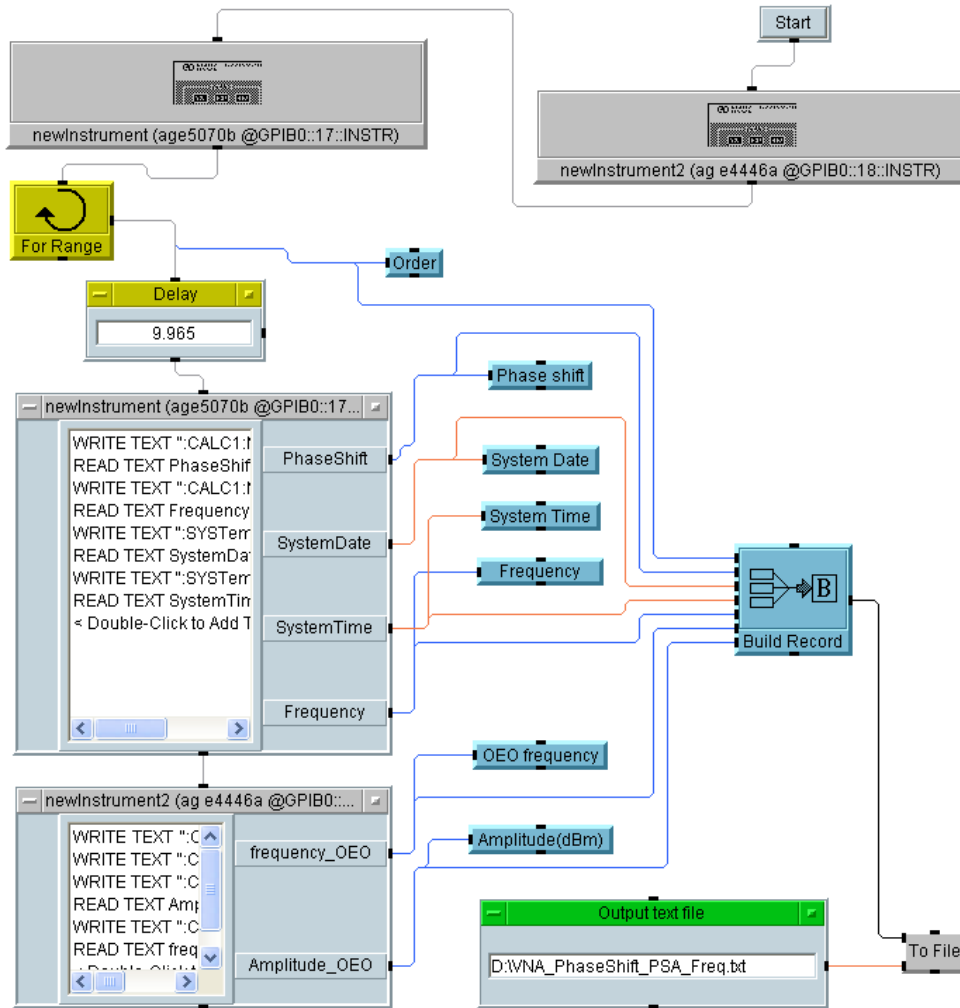


Figure 6.8 Data acquisition program with Agilent VEE Pro 9.3 for recording OEO oscillation frequency and VNA phase shift

6.4 Monitoring OEO frequency drift with a VNA

In order to compare the relation between OEO oscillation frequency and the temperature as well as the relation between OEO oscillation frequency and the phase, we measure simultaneously, as a function of time, three parameters: OEO oscillation frequency, temperature and the phase $\phi_{S_{21}}$.

6.4.1 OEO oscillation frequency vs temperature

This measurement is similar to section 3.5 but with longer duration. After 62 hours, we obtain the following results:

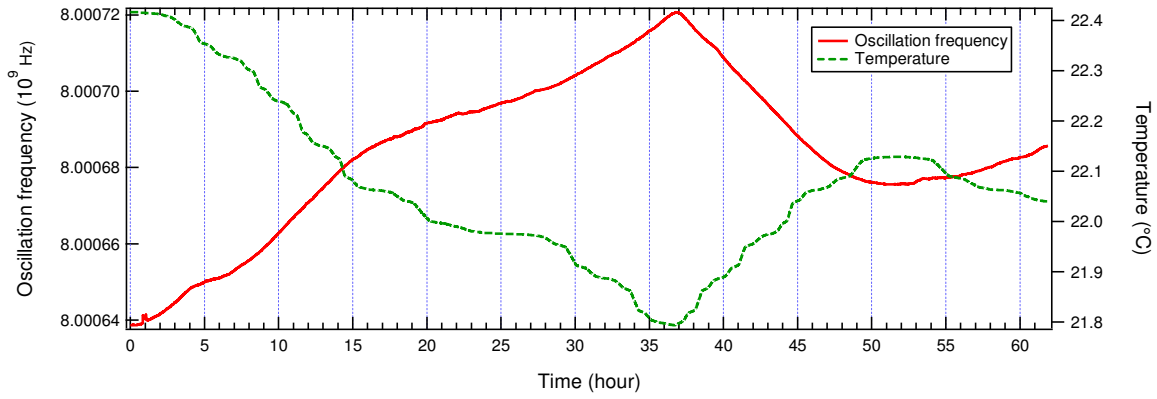


Figure 6.9 Drift of the oscillation frequency and temperature changes versus time

The data acquisition has been carried out for 62 hours and is illustrated in Figure 6.9. Because the OEO oscillation frequency changes in the opposite direction with the change of temperature, for a more clear view, the temperature data is presented in the opposite values in Figure 6.10. The result shows a good correlation between the evolutions of oscillation frequency and those of the opposite temperature.

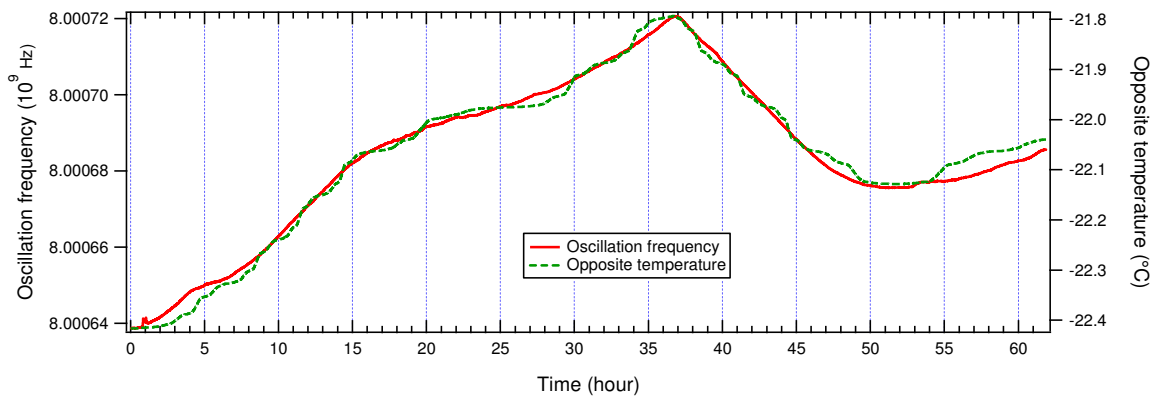


Figure 6.10 Drift of the oscillation frequency and opposite temperature changes versus time

To estimate the correlation between these two curves, the oscillation frequency was plotted as a function of the opposite temperature (see Figure 6.11) and then was fitted by a line by Igor software. The fitting function leads to a line determined by:

$$f_{osc1} = 8.003495 \times 10^9 + 1.2737 \times 10^5 \times (-\theta) \quad (6.3)$$

The oscillation frequency fluctuations defined as the differences between the measured frequency and the value obtained by Eq. (6.3) are presented in Figure 6.12 as a function of time.

In Figure 6.10, the peak-to-peak variation of the oscillation frequency is equal to 82.1 kHz, its standard deviation is 20.31 kHz. For the fluctuations of the OEO

frequency with respect to the modeling of Eq. (6.3), in Figure 6.12, the peak-to-peak variation is 9.80 kHz, and the standard deviation is 2.07 kHz. Taking into account the standard deviation, the improvement corresponds to a factor of 9.8, and for a less flattering comparison, with the peak-to-peak variations, the improvement factor is equal to 8.4.

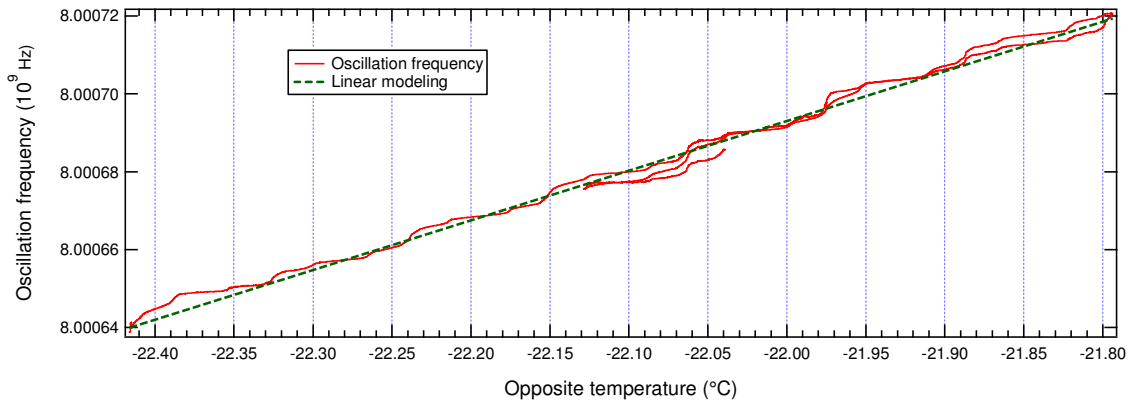


Figure 6.11 Oscillation frequency as a function of the opposite temperature and the fitting curve determining a modeling of the frequency drift behavior

In some parts, the changes in the oscillation frequency are slower than the changes in the temperature. This can be explained by the fact that the heat needs some time for expanding into inner layers of the fiber loop.

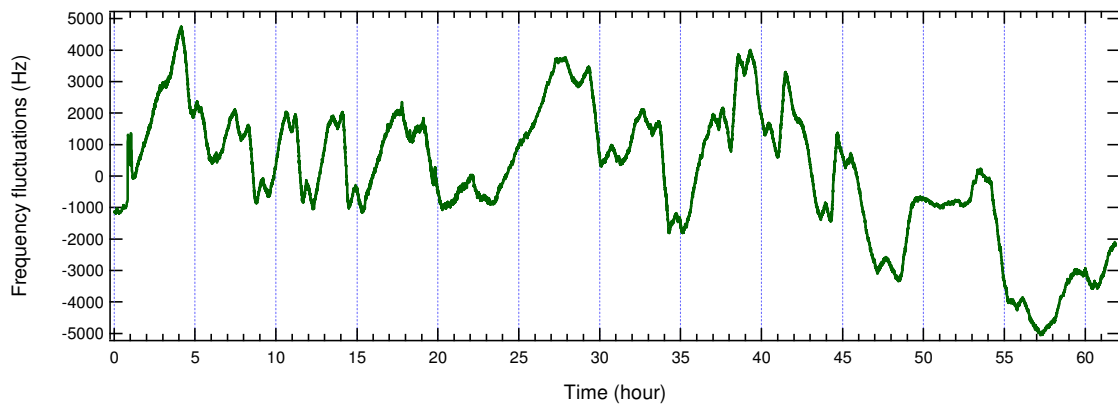


Figure 6.12 Fluctuations of the oscillation frequency compared to the modeling expressed by Eq. (6.3), as a function of time

On this day, the periodicity of the fluctuations still present but less visible than it was on the day corresponding to the results in Figure 3.34

6.4.2 OEO oscillation frequency vs phase

The S21 phase data measured by the VNA are sent every 10 s to the PC via an

IEEE-488 connection (GPIB). This process has been performed simultaneously with the temperature measurement mentioned in previous section. Evolutions of the oscillation frequency and the phase of S21 for duration of 62 hours are illustrated in Figure 6.13.

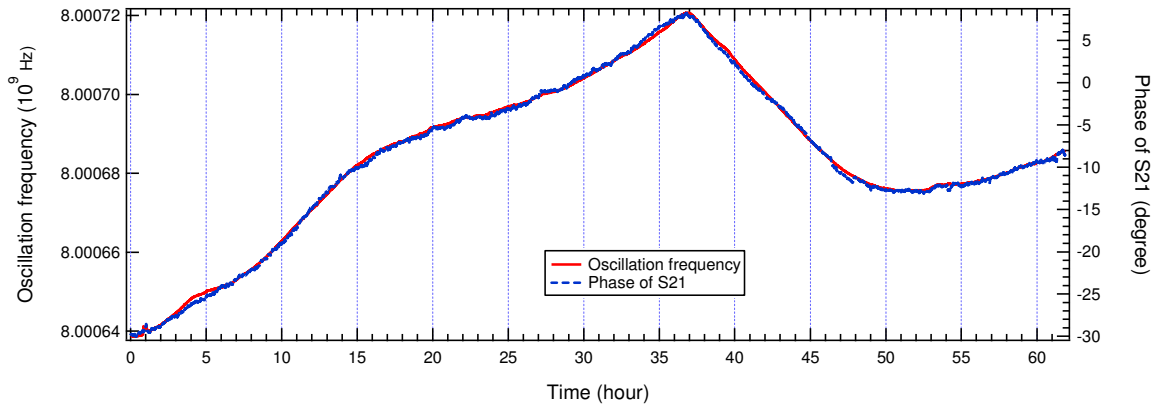


Figure 6.13 Drift of the OEO oscillation frequency and S21 phase parameter versus time.

The variations of the OEO oscillation frequency as a function of the S21 parameter phase are presented in Figure 6.14. From this result we have determined the new experimental modeling given by Eq. (6.4) based on the same mode number. The variations of the frequency are smaller than the FSR so there is clearly no mode hopping effect.

$$f_{osc,m} = 8.000703 \times 10^9 + 2129 \times \phi_{S21} \quad (6.4)$$

From it is possible to determine the fluctuations of the OEO oscillation frequency around the theoretical value obtained from the phase of S21 parameter. These fluctuations are presented in Figure 6.15, with variations from -1.72 kHz up to $+1.74$ kHz.

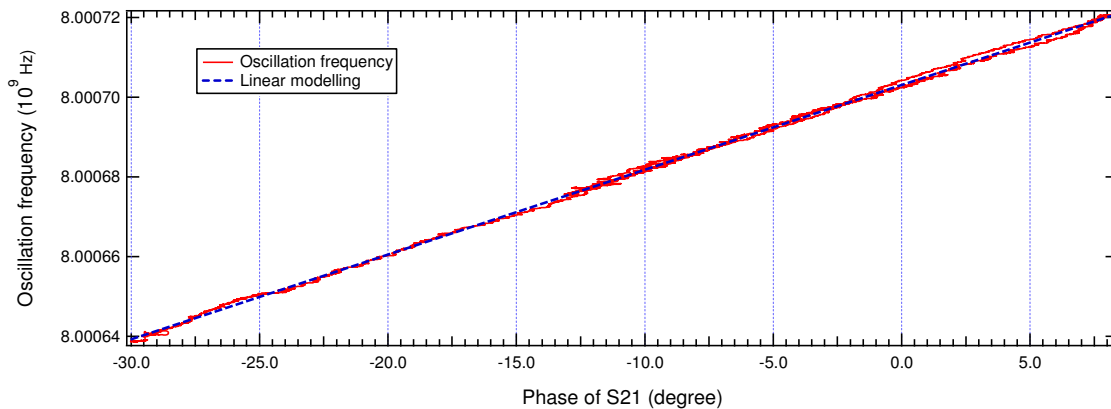


Figure 6.14 Oscillation frequency of the OEO, as a function of the S_{21} phase

In Figure 6.13 as in Figure 6.9, the peak-to-peak variation of the oscillation frequency is 82.1 kHz and its standard deviation is 20.31 kHz. For the fluctuations of the OEO frequency with respect to the modeling in Eq. (6.4) (Figure 6.15), the peak-to-peak variation is 3.47 kHz, and the standard deviation is 0.606 kHz. Considering the standard deviation the improvement corresponds to a factor 33.51, and for the less flattering comparison with the peak-to-peak variations the improvement factor is equal to 23.66.

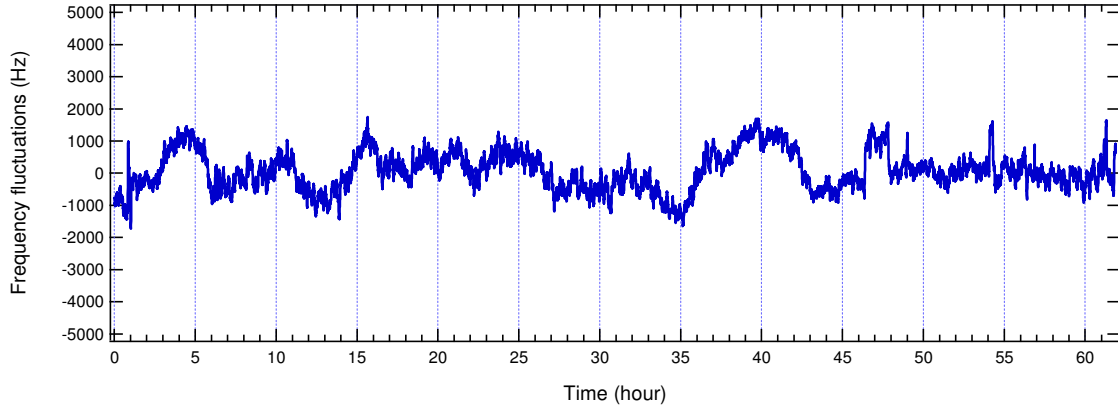


Figure 6.15 Fluctuations of the OEO oscillation frequency with respect to the modeled frequency, calculated from the measured S_{21} phase, as a function of time

From these results, it can be said that this phase-based method leads to a better modeling than the one based on temperature measurement mentioned in Section 3.5.

6.5 Accuracy of this technique when applied for long-term measurement

The technique proposed in section 6.4 can be applied in sensor applications including distance variation and refractive index measurements [92], [102] as indicated in Figure 6.16. The fiber-to-fiber coupling system part can be used in two ways.

In Figure 6.16 (a), lens L2 is movable and will be attached to the object to be measured the distance variation. In Figure 6.16 (b), the two lenses are fixed and a quartz cuvette containing the liquid to be measured is put in the middle of two lenses. The fiber loop is opened and two collimated lenses are inserted. These two lenses are placed in the basic OEO loop but after the optical coupler in order to be self-isolated from the fiber delay variation measurement by the VNA. This arrangement separates the variation of the fiber loop delay itself and the variation induced by the sensing

part.

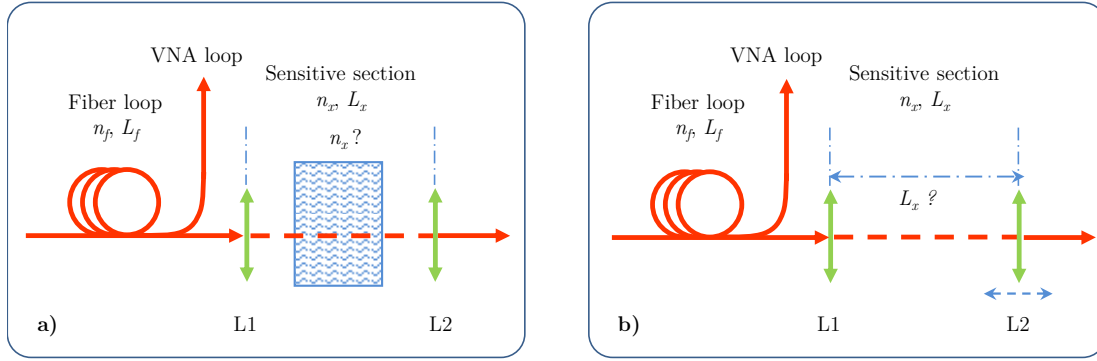


Figure 6.16 Introduction of a sending part in the fiber loop for detecting a refractive index change (a). Another possibility is to detect a small distance modification obtained by moving the lens L2 (b)

The new global delay of the OEO τ'_g is a sum of the optical fiber loop delay τ_f which has a length of L_f , and a refractive index of n_f , the variable delay of the sensing part τ_x , the electronic delay τ_e caused the electrical components and is expressed by Eq. (6.5). The sensing part delay τ_x will be determined by the multiplication of the refractive index n_x and the distance L_x .

$$\tau'_g = \tau_f + \tau_x + \tau_e = \frac{(n_f L_f + n_x L_x)}{c_0} + \tau_e \quad (6.5)$$

Under the temperature fluctuation, the electronic delay τ_e does not change so much and is negligible. The global delay variation of the OEO can be written as:

$$\Delta\tau'_g \approx \Delta\tau_f + \Delta\tau_x \quad (6.6)$$

where the optical fiber delay variation $\Delta\tau_f$ could be calculated from the phase shift measured by the VNA.

At a given time t of the experiment, the oscillation frequency change compared to time 0 is due to the temperature change and the refractive index n_x or distance L_x change. The effect of temperature is known from the phase of S_{21} parameter measurement, leading to the experimental modeling expressed in (4). Our hypothesis for calculating the variations with time of n_x or L_x , is to take at time t the modeled frequency f_{osc2} as a reference. So the considered variations of the oscillation frequency are given by $\Delta f_{osc,m}(t) = f_{osc}(t) - f_{osc2}(t)$ and by this way the variations $\Delta\tau_f$ due to the temperature change, are included in f_{osc2} . This method corresponds to a

calibration of the experimental system.

The variation $\Delta\tau_x$ is easily obtained in Eq. (6.7).

From Eq. (5.8), with a given variation of refractive index, it is easy to calculate the change of oscillation frequency:

$$\Delta(n_x L_x) = c_0 \Delta\tau_x = -c_0 \frac{\Delta f_{osc,m}}{FSR \cdot f_{osc2}} \quad (6.7)$$

For the case of distance variation measurement, n_x is unchanged, so (7) becomes:

$$\Delta L_x = -c_0 \frac{\Delta f_{osc,m}}{FSR \cdot f_{osc2} \cdot n_x} \quad (6.8)$$

For the case of refractive index variation measurement, L_x is a constant, (7) equivalent to:

$$\Delta n_x = -c_0 \frac{\Delta f_{osc,m}}{FSR \cdot f_{osc2} \cdot L_x} \quad (6.9)$$

From Figure 6.14, Figure 6.15 and from Eq. (6.4) we got a standard deviation in the fluctuations of the oscillation frequency with respect to the experimental modeling $\sigma(f_{osc2}) = 0.606$ kHz. This standard deviation effect is actually included in the measured variation of the oscillation frequency $\Delta f_{osc,m}$ leading to a detection limit of n_x or L_x . It is important to remind that these limits correspond to long term variation detection as the modeling has been obtained from 62 hours data acquisition.

$$\left| \Delta L_{x_{min}} \approx c_0 \frac{\sigma(f_{osc2})}{FSR \cdot f_{osc2} \cdot n_x} \right| \quad (6.10)$$

$$\left| \Delta n_{x_{min}} \approx c_0 \frac{\sigma(f_{osc2})}{FSR \cdot f_{osc2} \cdot L_x} \right| \quad (6.11)$$

In our case $f_{osc2} \approx 8$ GHz and with 1 km of fiber loop the FSR is approximately 200 kHz.

For distance variation measurement, we have $n_x = 1$ so $|\Delta L_{x_{min}} \approx 0.113 \text{ mm}|$.

Considering refractive index variation measurement, if the liquid is placed in a quartz cuvette with $L_x = 10$ mm the limit is $|\Delta n_{x_{min}} \approx 0.0113|$.

From Eq. (6.10) and Eq. (6.11), we can see that the measurement accuracy should be improved by increasing both the oscillation frequency and the FSR of the OEO.

But increasing the FSR is obtained by decreasing the fiber loop length the consequence being also decreasing the quality of the oscillator by the phase noise. There is a tradeoff to be analyzed more precisely in a future work.

6.6 Method for implementing the correction to the oscillation frequency drift

6.6.1 Principle

We determine the theoretical expression of the frequency drift as it can be obtained from S_{21} parameter measured by the VNA.

The frequency oscillation is given by $f_{osc} = k/\tau_g$ where the global delay is $\tau_g = \tau_e + \tau_{op}$ and k is the order of the oscillating mode.

The delay of the RF modulating signal across the optical fiber is related to the phase of the transmission parameter S_{21} by $\phi_{S_{21}} = -\omega_{VNA}\tau_{op}$. The RF signal at the output of the fiber (or at Port -2 of the VNA) can be written as $y = A \cdot \cos(\omega t + \phi_0 - \omega_{VNA}\tau_{op})$.

The phase variation during time is then $\Delta\phi_{S_{21}} = \phi_{S_{21}}(t) - \phi_{S_{21}}(0) = -\omega_{VNA}\Delta\tau_{op}$.

If frequency variations are due to temperature change only then they can be written as:

$$\Delta f_0 = f_{osc}(t) - f_{osc}(0) = \frac{k}{\tau_g} - \frac{k}{\tau_{g0}} = \frac{k}{\tau_e + \tau_{op}} - \frac{k}{\tau_e + \tau_{op,0}} \quad (6.12)$$

$$\begin{aligned} \Delta f_0 &\approx \frac{k(-\Delta\tau_{op})}{(\tau_e + \tau_{op})(\tau_e + \tau_{op,0})} = - \left(\frac{k}{\tau_e + \tau_{op}} \right) \left(\frac{1}{\tau_e + \tau_{op,0}} \right) \Delta\tau_{op} \\ &= -f_{osc} \cdot FSR \cdot \Delta\tau_{op} \end{aligned} \quad (6.13)$$

$$\Delta f_0 = f_{osc} \cdot FSR \cdot \frac{\Delta\phi_{S_{21}}}{\omega_{VNA}} \quad (6.14)$$

Finally the frequency variation is given by: $\Delta f_0 = b\Delta\phi_{S_{21}}$ where:

$$b = \frac{f_{osc} \cdot FSR}{2\pi f_{VNA}} \quad (6.15)$$

$$\begin{aligned} \Delta f_0 = f_{osc}(t) - f_{osc}(0) &= b [\phi_{S_{21}}(t) - \phi_{S_{21}}(0)] \\ &= \frac{f_{osc} \cdot FSR}{2\pi f_{VNA}} [\phi_{S_{21}}(t) - \phi_{S_{21}}(0)] \end{aligned} \quad (6.16)$$

And the frequency at time t is given by:

$$f_{osc}(t) = f_{osc}(0) - b\phi_{S_{21}}(0) + b\phi_{S_{21}}(t) = f_a + b\phi_{S_{21}}(t) \quad (6.17)$$

With 1 km of optical fiber, $FSR \approx 199.4$ kHz, $f_{osc} = 8$ GHz and $f_{VNA} = 2.1$ GHz we obtain if the phase is expressed in degree: $b = 2116$ Hz/deg.

This theoretical value of the slope b can be compared with different experimental values. We obtained 4 values corresponding to different dates, different durations and different experimental conditions concerning the use of one or two amplifiers, or the placing or not of the filter at 2.1 GHz in a thermal box. Anyway the results are summarized in Table 6.1.

Table 6.1. Theoretical and experimental results of coefficient b

Case	Theory	Exp-1	Exp-2	Exp-3	Exp-4
Slope (Hz/deg)	2116	2134	2354	2054	2129

where the experimental conditions of 4 cases as below:

- Exp-1: the fiber loop and the 8 GHz filter are placed in the thermal box; the experimental duration is 12 hours; two amplifiers are used in the VNA loop.
- Exp-2: the fiber loop, the 8 GHz filter and the 2.1 GHz filter are placed in the thermal box; the experimental duration is 12 hours; one commercial amplifier is used in the VNA loop.
- Exp-3: the fiber loop and the 8 GHz filter are placed in the thermal box; the experimental duration is 12 hours; one commercial amplifier is used in the VNA loop.
- Exp-4: the fiber loop and the 8 GHz filter are placed in the thermal box; the experimental duration is 62 hours; two amplifiers are used in the VNA loop.

The standard deviation of frequency fluctuation in Exp-1 is 433.3 Hz. There is some

agreement between all these values, but not really satisfying. The reason for the dispersion of these results should be further investigated especially the effect of the RF filters and amplifiers.

6.6.2 Determination of long-term refractive index variations

6.6.2.1 Refractive index of the liquid at time 0

At $t = 0$, the oscillation frequency is $f_{osc,e}(0^-)$. Then the liquid to be studied is placed into the cuvette, the new oscillation frequency is $f_{osc,e}(0^+)$.

The variation of the refractive index, $\Delta(n_x)_0$, at $t = 0$ can be determined from Eq. (5.2), (5.6) and Figure 5.6.

$$\frac{\Delta f}{f_{osc,e}(0^-)} = -\frac{\Delta\tau_g}{\tau_g} = -\frac{\Delta\tau_x}{\tau_{g0}} = -\frac{\Delta\left(\frac{n_x L_x}{c_0}\right)}{\tau_g} = -\frac{L_x \cdot FSR}{c_0} \Delta(n_x)_0 \quad (6.18)$$

Finally the refractive index is:

$$n_x(0) = 1 + \Delta(n_x)_0 = 1 - \frac{c_0}{L_x \cdot FSR} \frac{\Delta f}{f_{osc,e}(0^-)} \quad (6.19)$$

6.6.2.2 Refractive index of the liquid at time t

Here we introduce the variation of refractive index $\Delta_{0t}n_x$ from time 0 to time t . The refractive index at time t is:

$$n_x(t) = n_x(0) + \Delta_{0t}n_x \quad (6.20)$$

where $n_x(0)$ is the refractive index at time $t = 0$, already determined in Eq. (6.19).

6.6.2.2.1 Direct determination of the refractive index variation

At time t we get the experimental value of the oscillation frequency $f_{osc,e}(t)$ that can be compared to the initial one $f_{osc,e}(0^+)$.

We consider $\Delta_1 f_{osc} = f_{osc,e}(t) - f_{osc,e}(0^+)$. This variation is resulting from temperature effects and from the refractive index that we want to determine.

If there is no mode hopping we can write: $\Delta_1 f_{osc} = \frac{k}{\tau_g(t)} - \frac{k}{\tau_g(0^+)}$ with $\tau_g = \tau_e + \tau_x + \tau_{op}$

$$\begin{aligned}\Delta_1 f_{osc} &= \frac{k[(\tau_{x,0} - \tau_x) + (\tau_{op,0} - \tau_{op})]}{\tau_g(t)\tau_g(0^+)} \\ &= f_{osc,e}(t)(-\Delta_1\tau_x - \Delta\tau_{op})FSR\end{aligned}\quad (6.21)$$

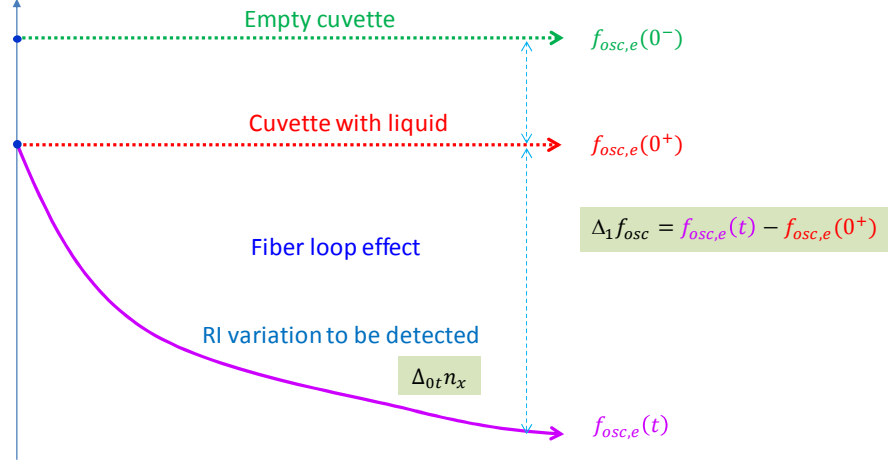


Figure 6.17 Refractive index variation determination without modeling frequency drift generated by fiber loop.

The effect of refractive index variation is $\Delta_1\tau_x = \frac{L_x}{c_0}\Delta_{0t}(n_x)$ where $\Delta_{0t}(n_x) = n_x(t) - n_x(0)$.

As seen previously, the effect of temperature on the propagation time across the optical fiber leads to a variation $\Delta\tau_{op} = -\frac{\Delta\phi_{S_{21}}}{2\pi f_{VNA}}$

$$\Delta_1 f_{osc} = f_{osc,e}(t) \left(-\frac{L_x}{c_0}\Delta_{0t}n_x + \frac{1}{2\pi f_{VNA}}\Delta\phi_{S_{21}} \right) FSR \quad (6.22)$$

The variation of refractive index is so given by:

$$\Delta_{0t}n_x = -\frac{c_0}{L_x} \frac{\Delta_1 f_{osc}}{f_{osc,e}(t) \cdot FSR} + \frac{1}{2\pi f_{VNA}} \frac{c_0}{L_x} \Delta\phi_{S_{21}} \quad (6.23)$$

6.6.2.2.2 Indirect determination of the refractive index variation

At time t , we get two quantities: the experimentally measured frequency $f_{osc,e}(t)$, and $\phi_{S_{21}}(t)$ from the VNA. Based on Eq. (6.17) and on the VNA data a frequency modelling $f_{osc,m}(t)$ is calculated:

$$f_{osc,m}(t) = f_a + b\phi_{S_{21}}(t) = f_{osc,e}(0^+) + b\Delta\phi_{S_{21}}(t) \quad (6.24)$$

The oscillation frequency difference $\Delta_2 f_{osc} = f_{osc,e}(t) - f_{osc,m}(t) = f_{osc,e}(t) -$

$$[f_{osc,e}(0^+) + b\Delta\phi_{S_{21}}].$$

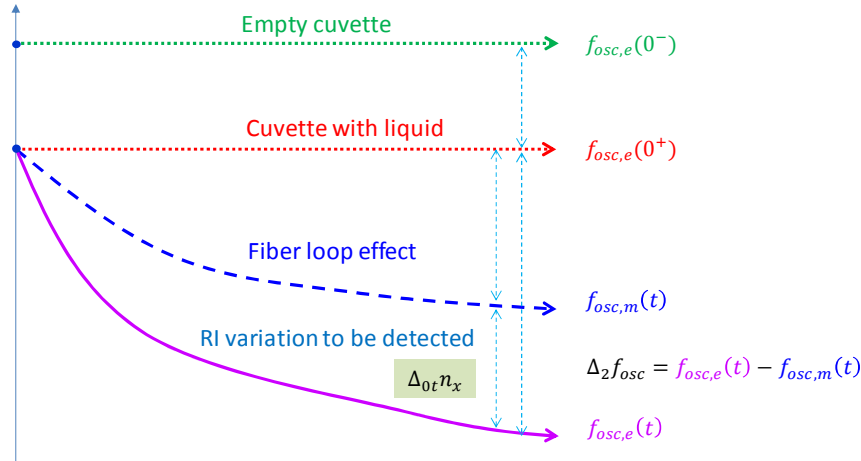


Figure 6.18 Refractive index variation determination with modeling frequency drift generated by fiber loop.

$$\Delta_2 f_{osc} = f_{osc,e}(t) - f_{osc,e}(0^+) - \frac{f_{osc,e}(0^+) \cdot FSR}{2\pi f_{VNA}} \Delta\phi_{S_{21}} \quad (6.25)$$

with b determined in Eq. (6.15). Dividing two sides by $f_{osc,e}(t)$, Eq. (6.25) becomes:

$$\frac{\Delta_2 f_{osc}}{f_{osc,e}(t)} = \frac{f_{osc,e}(t) - f_{osc,e}(0^+)}{f_{osc,e}(t)} - \frac{FSR}{2\pi f_{VNA}} \Delta\phi_{S_{21}} \quad (6.26)$$

Multiplying two sides with $-\frac{c_0}{L_x \cdot FSR}$, Eq. (6.26) becomes:

$$\begin{aligned} & -\frac{c_0}{L_x \cdot FSR} \frac{\Delta_2 f_{osc}}{f_{osc,e}(t)} \\ &= -\frac{c_0}{L_x \cdot FSR} \frac{f_{osc,e}(t) - f_{osc,e}(0^+)}{f_{osc,e}(t)} \\ &+ \frac{c_0}{L_x \cdot 2\pi f_{VNA}} \Delta\phi_{S_{21}} \end{aligned} \quad (6.27)$$

In the left side of the Eq. (6.27), we can recognize $\Delta_{0t} n_x$ as expressed in Eq. (6.9):

$$\begin{aligned} \Delta_{0t} n_x &= -\frac{c_0}{L_x \cdot FSR} \frac{\Delta_2 f_{osc}}{f_{osc,e}(t)} = -\frac{c_0}{L_x \cdot FSR} \frac{f_{osc,e}(t) - f_{osc,m}(t)}{f_{osc,e}(t)} \\ &= -\frac{c_0}{L_x \cdot FSR} \frac{f_{osc,e}(t) - f_{osc}(0)}{f_{osc}} + \frac{c_0}{L_x \cdot 2\pi f_{VNA}} \Delta\phi_{S_{21}} \end{aligned} \quad (6.28)$$

The right side of Eq. (6.28) is the same with that of Eq. (6.23). It means that, two methods give the same result.

The correction method is based on the measurement at time t of $f_{osc,e}(t)$ and

$\phi_{S_{21}}(t)$ and then the determination of the modelling frequency $f_{osc,m}(t)$. The refractive index $n_x(t)$ at time t is determined by replacing $\Delta_{0t}n_x$ to Eq. (6.19) and Eq. (6.20):

$$\begin{aligned} n_x(t) &= 1 + \Delta n_x(0) + \Delta_{0t}n_x \\ &= 1 - \frac{c_0}{L_x \cdot FSR} \frac{\Delta f}{f_{osc,e}(0^-)} - \frac{c_0}{L_x} \frac{\Delta_1 f_{osc}}{f_{osc,e}(t) \cdot FSR} + \frac{1}{2\pi f_{VNA}} \frac{c_0}{L_x} \Delta \phi_{S_{21}} \end{aligned} \quad (6.29)$$

6.7 New software for long-term measurement

In Chapter 3 and Chapter 4, we have presented several programs developed with Microsoft Visual Basic 6.0 (MS Visual Basic 6.0) when controlling the EOM. In Chapter 6, we developed program with Agilent VEE Pro to acquire data from Spectrum Analyzer and Vector Network Analyzer to monitor the drift of oscillation frequency of the OEO and phase variation of S_{21} . The acquired data with MS Basic and Agilent VEE then are combined into a MS Excel file and are synchronized by taking some calculations in MS Excel. Then the final Excel file is loaded by Igor to view the chart.

For long-term measurement or tracking based on our OEO system, it is necessary to develop a software package that can monitor the OEO oscillation frequency, VNA S_{21} phase and control the EOM. We could continue to work with our software packages developed in MS Visual Basic 6.0. However, for OEO applications in long-term measurement, we found that Matlab is more powerful programming environment than MS Basic 6.0 due to following advantages:

- Communicating easier with measurement instruments through GPIB interface such as Agilent Spectrum Analyzer and Agilent Vector Network Analyzer.
- Working easier and faster with big MS Excel file, especially when saving a long-term data.
- Suitable for future digital signal processing tasks which can be used in combination with the DSP kit.

Finally, we have completed new software with Matlab as shown in Figure 6.19. It can acquire data from Spectrum Analyzer, Vector Network Analyzer and DSP kit. The current frequency and phase values are compared in the real-time with their values and these variations are shown automatically by the software. Other

information related to EOM control process is also retrieved and displayed.

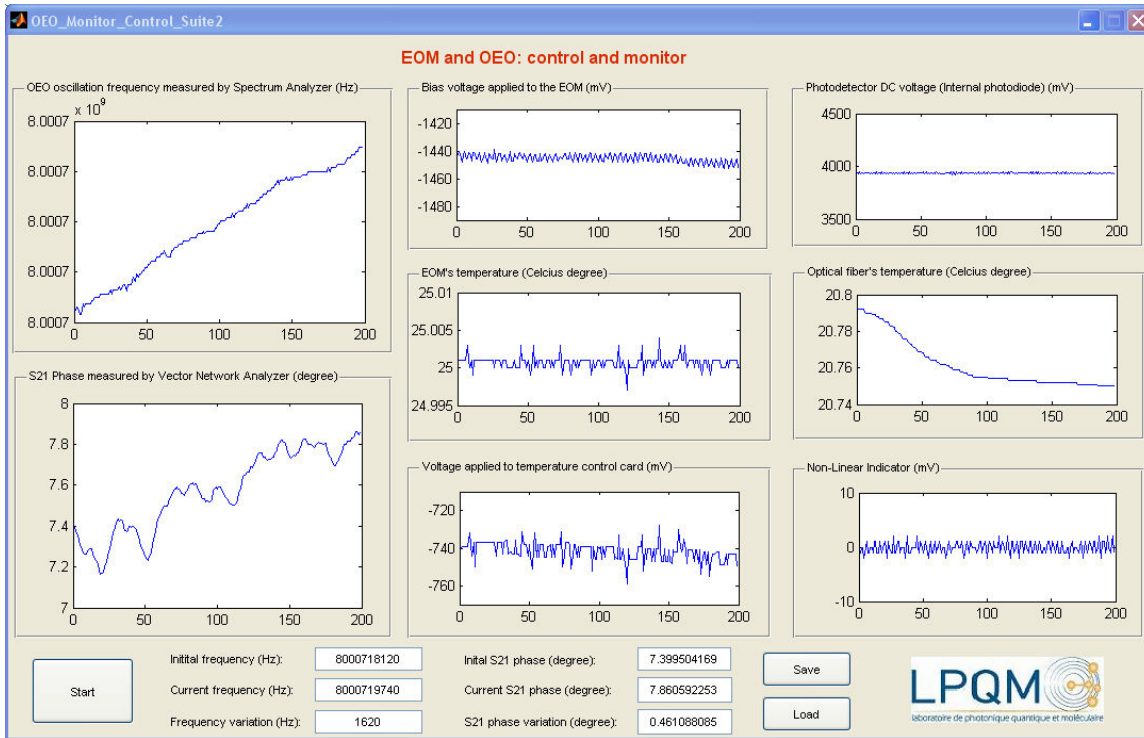


Figure 6.19 Interface of new software for all controls and long-term measurement

The combination of new software suite, electronic cards, VNA and DSP kit improves that the implementation of this technique is feasible. The long-term measurement and real-time tracking could be done automatically with this combination of software and hardware.

6.8 Conclusions

In this chapter, we presented a technique for enhancing the long-term refractive index measurement based on the OEO. This technique is very essential because the ideal stable working condition of an OEO could not be satisfied in many cases. To deal with this situation, we have performed an experiment to analyze the relation between the global delay and the OEO oscillation frequency under the room temperature conditions. We have proposed a new technique to monitor the OEO stability in a long-term by using a VNA to track the change of the S_{21} phase caused by the temperature variation.

The correlation between oscillation frequency and the S_{21} phase has been compared with the correlation between oscillation frequency and the temperature. The results obtained from S_{21} phase measurements are much better than those from direct

temperature measurement. With this technique, in the applications for distance and refractive index measurements, the tolerance induced by the fiber under temperature change can be separated from the sensing part and can be easily estimated. We also presented two methods for implementing the correction to the oscillation frequency from measured S_{21} phase.

Finally, in order to make this technique become more applicable, we have developed new software with Matlab which can acquire data from measurement instruments as well as communicate with the DSP kit for the EOM control process. When equipped with the new software, our technique become more applicable because the real-time detection or in-situ measurements such as tracking chemical reaction could be automatically implemented by only one software package.

General conclusions and perspectives

In this manuscript, we have presented a study of the optoelectronic oscillator (OEO) system focused on a possible development of optical path variations sensing application, especially refractive index variations measurement. The work is a contribution in defining a measurement tool and features some multidisciplinary aspects. Furthermore, this work is also a contribution to the knowledge baseline of the optoelectronic oscillator for an application oriented study at the laboratory level: different aspects, mainly DSP based instrumentation, could be used for other OEO structures or other systems.

A simulation study of the OEO has been conducted in order to have a good theoretical base to optimize the system, by which we could introduce the sensing part and to study the effect of various parameters of the system. This modelling is based on loop calculations developed in MatLab® software. For a good modelling, comparing to experimental results, we have determined the required number of iterations.

Then we have developed a measurement and control system based on a DSP kit. That is useful in the prospect of other applications like radars or telecommunications. Thanks to this kit, it is possible to monitor different parameters of the OEO like temperature of the electrooptic modulator (EOM), temperature of the fiber loop, but we could also get that of the RF filters. The DSP kit allowed us also to control the bias point of the EOM. Several software packages have been developed for data acquisition, and control with MatLab-Simulink®, Code Composer Studio, then been converted for application to the DSP board. With high data processing rate, it is possible to perform simultaneously optical bias point control, temperature control as well as other data acquisition. Other software like displaying, in real time, simultaneous acquired data in graphical format or monitoring of measurement instruments have been also implemented. For the global instrumentation, we have also developed all the analog interface circuits to get the data (photodetectors, temperature measurement) or for acting on the system (temperature tuning by the way of Peltier

effect based module). And of course, the designs of different boxes for mounting the elements have also been done.

Controlling the bias point of the EOM during operation is essential to maintain the working condition of the OEO. In case of an EOM made of Lithium Niobate, the transfer function drifts faster at the beginning of the operating time, then it becomes more stable after some working hours. For other technology such as polymer material, the drift phenomenon is bigger than that in Lithium Niobate EOM. Two techniques for controlling the bias point at the quadrature position have been developed: the first one is based on a dither signal at 500 Hz and the second technique is based on the optical average output power.

The measurement of different solutions refractive index shows the feasibility of this method, for which the main advantages rely in the frequency based technique less sensitive to noise, in the fundamentally communicant tool, and in the real time and in-situ aspects. With a configuration using 500 m fiber loop and 10 mm wide cuvette containing the liquid to be analyzed, the standard deviation for refractive index measurement is approximately three per thousand. The results are in rather good agreement with what can be found in the literature [10] but they should be improved in the future.

In order to monitor long-time chemical reactions a special attention during our work has been attached to long-term measurement possibilities. Because of the long fiber loop used in the system, there is an important sensitivity of the oscillation frequency to temperature variations. Thanks to the simultaneous registration of both oscillation frequency and optical fiber temperature the supposed correlation between them has been demonstrated. A solution based on determining the propagation time through the optical fiber loop has been introduced, based on the use of a vector network analyzer. Without taking into account temperature changes in the fiber loop the resulting oscillation frequency can be affected by some tens of kilohertz fluctuations. These fluctuations are accumulated with specific variations to be detected such, for example, as small refractive index variations due to the chemical reaction under process. Consequently this makes long-term measurement becomes no really accurate. With the corrections obtained from the VNA, fluctuations of the oscillation frequency can be estimated and eliminated making the sensing part effect more visible. Finally the fluctuations of the oscillation frequency are reduced to approximately 500 Hz even for rather long-term (compared to the initial tens of thousands ones): we

should obtain an improvement of the measurement signal to noise ratio. This is a significant result especially if compared also to the 8 GHz of the oscillation frequency for getting an idea of the order of magnitude.

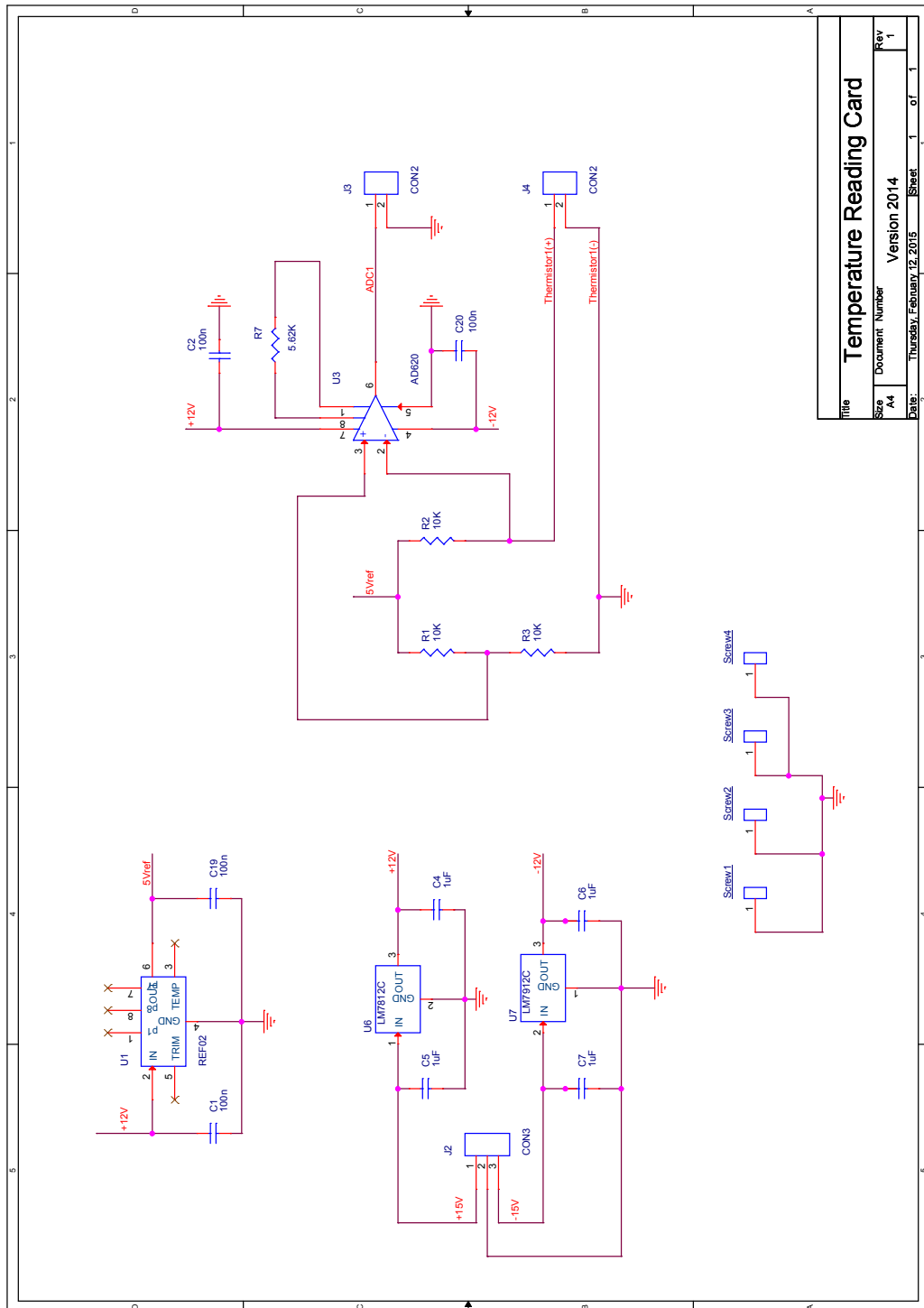
Future work will concern increasing the oscillation frequency and one possibility is up to 18 GHz. As seen in chapter 5, by increasing the oscillation frequency we can increase the frequency variation corresponding to a refractive index change, so it will be possible to increase the sensitivity of the system. Then, refractive index measurements of a chemical reaction in the real experimental conditions could be developed. Concerning to long-term measurement, to reduce the cost and minimize the size of the system, the VNA should be replaced by a dedicated system with ability to modulate and demodulate the 2.1 GHz signal. The parameters of the OEO like FSR and oscillation frequency should also be improved for a better accuracy taking into account their effects on the oscillator phase noise and stability.

Mode hopping possibility is an intrinsic characteristic of the oscillator based on delay line. Reducing the phase noise is obtained by increasing the length of the optical fiber. However, the consequence is to reduce the distance between the peaks of the frequency comb. In this case, the mode hopping can happen more easily. There is a trade-off to solve, but it should also be possible to study a better selective RF filter to be placed in the microwave part of the loop. The first solution could be to introduce a multiloop configuration where one loop determines the oscillation frequency and a second one enables to reduce the phase noise [22]. Another solution, looking only to the principle of the OEO, is to replace the fiber loop by an optical resonator: the oscillator is no more a delay line oscillator but a classical oscillator with a filter, the resonator which acts as an optical filter. The oscillation frequency is equal to the free spectral range of the resonator. Measurement can be conducted based on a change of the FSR change but like this it is not possible to make direct measurement of the refractive index change as previously. Such solution is one of research and development directions concerning the OEO in our laboratory.

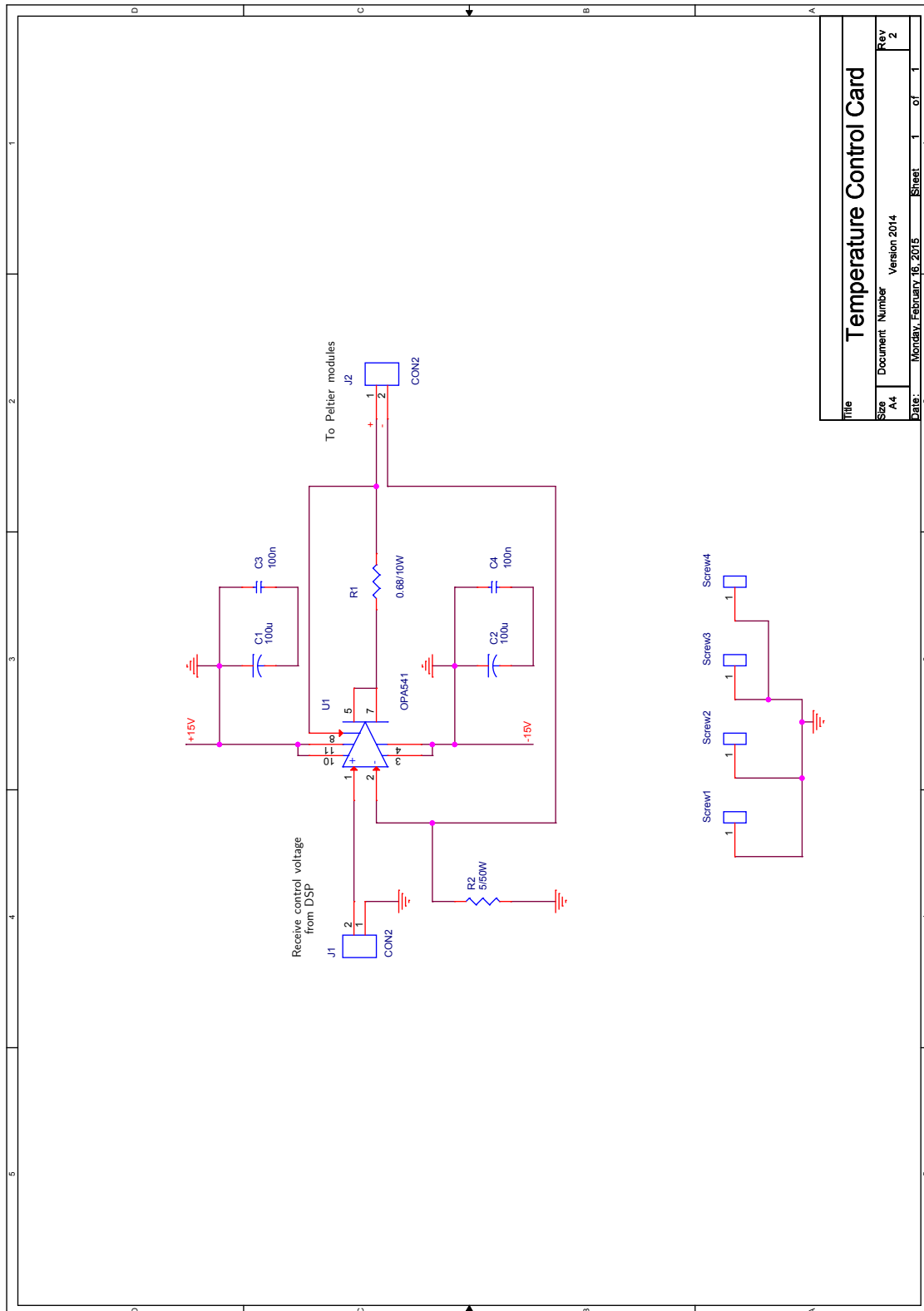
Annex A

Schematic diagrams of electronics cards

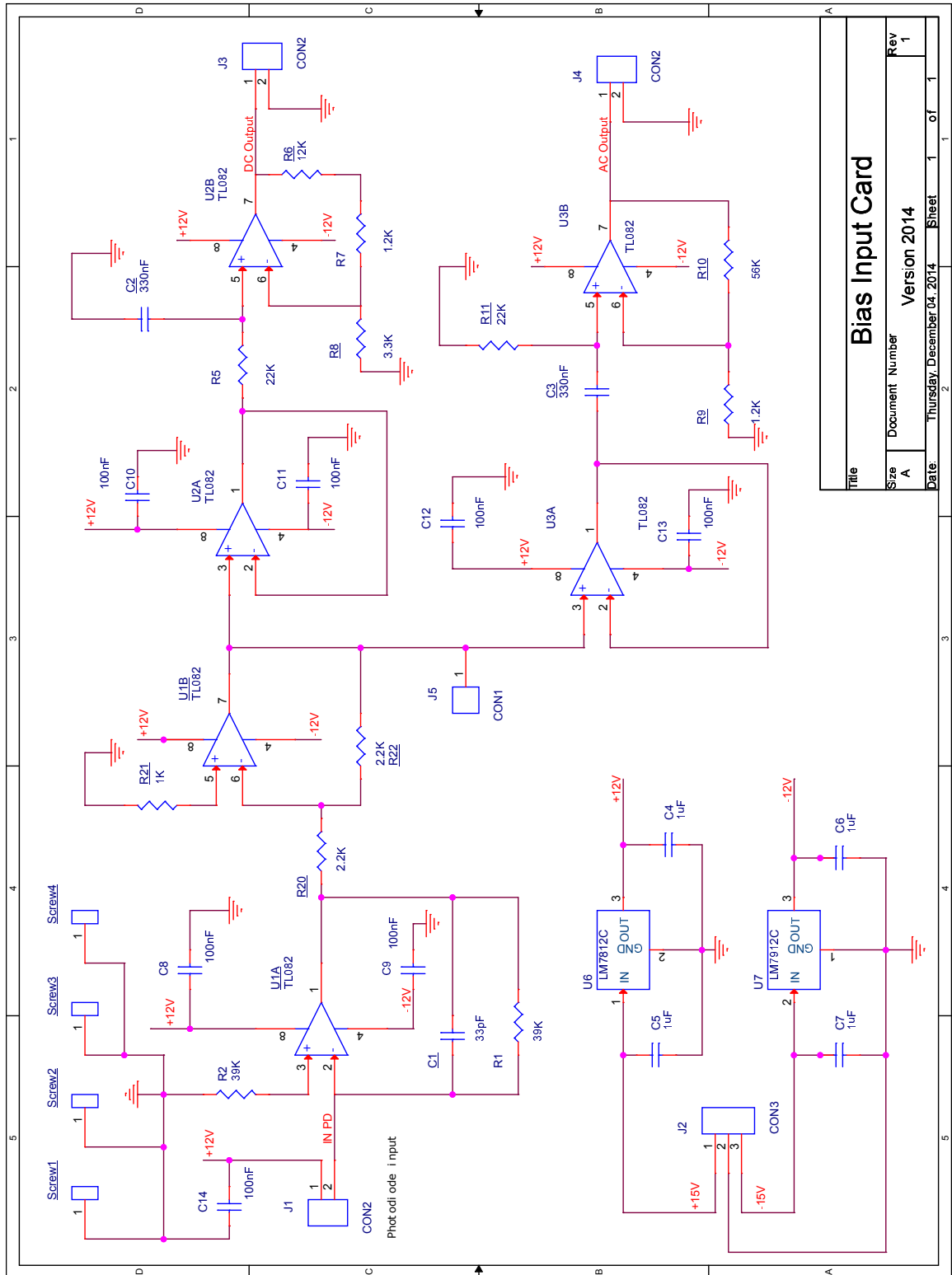
A.1 Schematic of temperature measuring card



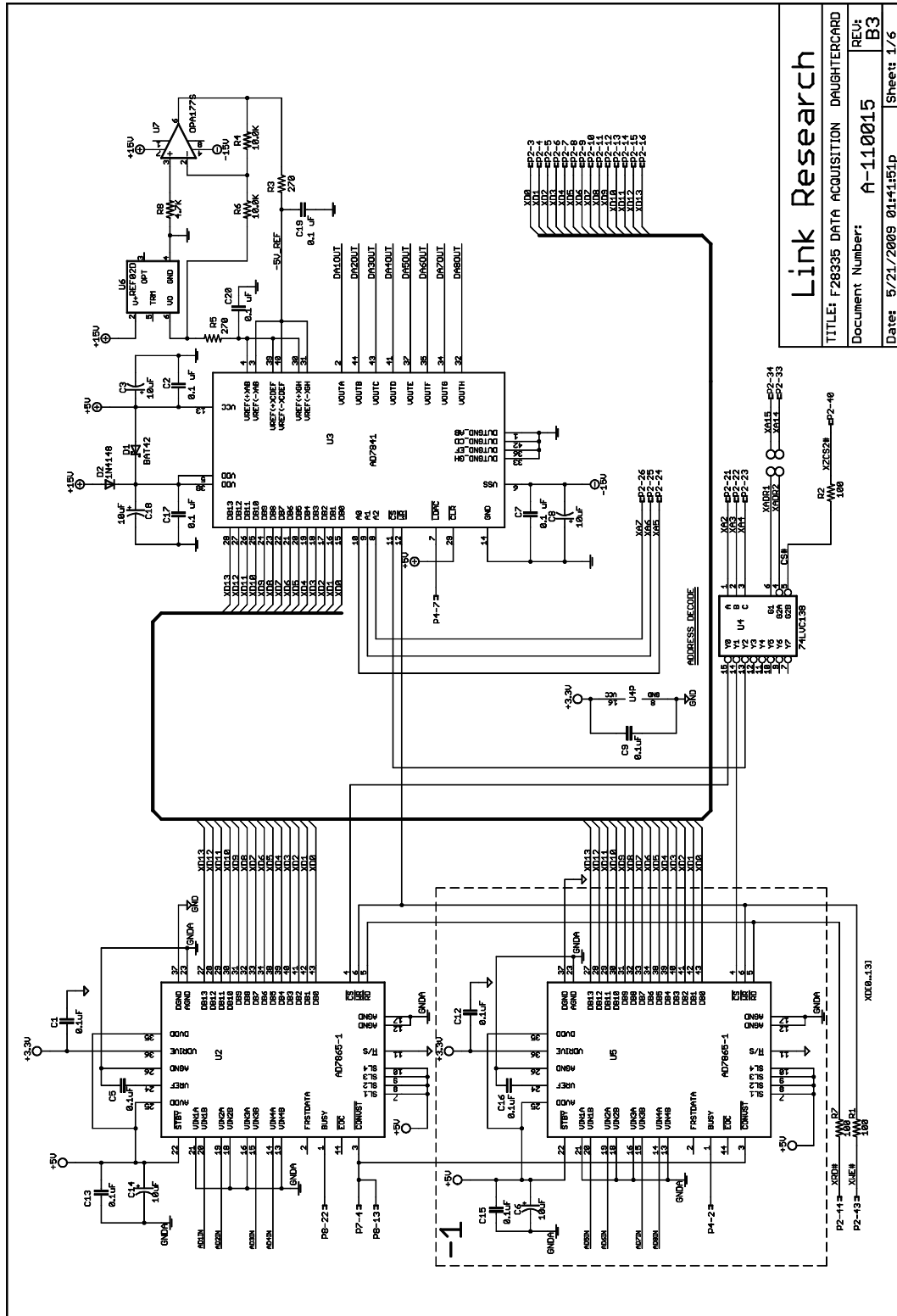
A.2 Schematic of temperature tuning card



A.3 Schematic of bias input card



B.2 Link Research F28335 daughter card



Annex C

RF filters specifications

C.1 8 GHz RF filter

Type: BL Microwave filter 8GHz BP8000-20/T-5TE01

1. Electrical Specifications

No	Item	Specification
1-1	Description	TE01 Model Filters
1-2	Part Number	BP8000-20/T-5TE01
1-3	Center Freq	8000MHz
1-4	-3dB BW	≤20MHz
1-5	IL@8GHz	≤4.2dB
1-6	Attenuation	40dB(min)@F0±70MHz
1-7	VSWR	1.5
1-8	Input Connector	SMA- F
1-9	Output Connector	SMA- F

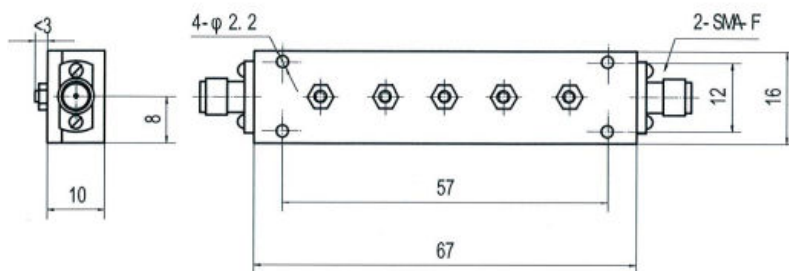
2. Environmental Specifications

No	Item	Specification
2-1	Temperature range	-30 to +70 deg C

3. Mechanical Specifications

No	Item	Specification
3-1	Dimensions	See Figure 3-1

Figure 3-1 Unit : mm



List of publications

1. **Toan Thang Pham**, Isabelle Ledoux-Rak, Bernard Journet, Van Yem Vu, “Calibration of the optical propagation time of an optoelectronic oscillator for sensing applications”, *Proceedings of the IEEE International Topical Meeting on Microwave Photonics*, MWP2014, Sapporo, Japan, Oct. 20-23, 2014.
DOI: 10.1109/MWP.2014.6994525
2. **Toan Thang Pham**, Duong Bach Gia, Van Yem Vu, Isabelle Ledoux-Rak, Bernard Journet, “Monitoring the oscillation frequency drift of an optoelectronic oscillator with a vector network analyzer”, *Proceedings of the IEEE International Conference on Advanced Technologies for Communication*, ATC 2014, Ha Noi, Việt Nam, Oct. 15-17, 2014.
DOI: 10.1109/ATC.2014.7043422
3. **Pham Toan Thang**, Isabelle Ledoux-Rak, Bernard Journet, “A new technique to monitor the long term stability of an optoelectronic oscillator”, *Proceedings of the SPIE Photonics Prague 2014*, Praha, Aug. 27-29, 2014.
DOI: 10.1117/12.2070357
4. **Toan Thang Pham**, Isabelle Ledoux-Rak, Bernard Journet, Van Yem Vu, “A study on measuring refractive index by using an optoelectronic oscillator”, *Proceedings of the IEEE International Conference on Communications and Electronics*, ICCE 2014, pp. 17-22, Da Nang, Viet Nam, July 30 – Aug. 1, 2014.
DOI: 10.1109/CCE.2014.6916673
5. **Pham Toan Thang**, Bernard Journet, “Opto-Electronic Oscillator Applications to Sensors”, *Journée de l'Institut d'Alembert*, ENS Cachan, France (May 12, 2014).
6. **Pham Toan Thang**, Pham Van Chi, Pham Tien Thông, Vu Van Yem, Isabelle Ledoux-Rak, Bernard Journet, “Simulation and experimental study of single-loop opto-electronic oscillator”, *Proceedings of the IEEE International*

- Conference on Advanced Technologies for Communication*, ATC 2013, pp. 680-685, Ho Chi Minh City, Viet Nam, Oct. 16-18, 2013.
DOI: 10.1109/ATC.2013.6698201
7. **Pham Toan Thang**, Vu Van Yem, Bach Gia Duong, Bernard Journet, “Electro-optic modulator drift compensation based on DSP system”, *Proceedings of the IEEE International Conference on Advanced Technologies for Communication*, ATC 2012, pp. 367-370, Ha Noi, Viet Nam, Oct. 10-12, 2012.
DOI: 10.1109/ATC.2012.6404295
8. Dang Thanh Bui, **Toan Thang Pham**, Vu Van Yem, Bernard Journet, “Improving opto-electronic oscillator stability by controlling the electro-optic modulator”, *Proceedings of the IEEE International Conference on Communications and Electronics*, ICCE 2012, pp. 63-68, Hue, Viet Nam, Aug. 02-04, 2012.
DOI: 10.1109/CCE.2012.6315872
9. Nguyen Tuan Minh, **Pham Toan Thang** and Bernard Journet, “Controlling the electro-optic modulator bias point by using a DSP system”, *International Symposium on Electrical-Electronics Engineering*, ISEE-2011, Ho Chi Minh City, Viet Nam, Nov. 08-09, 2011.

Bibliography

- [1] X. S. Yao and L. Maleki, "High frequency optical subcarrier generator," *Electronics Letters*, vol. 30, no. 18. p. 1525, 1994.
- [2] X. S. Yao and L. Maleki, "A Light-Induced Microwave Oscillator," *TDA Prog. Rep. 42-123*, pp. 47–68, 1995.
- [3] X. S. Yao and L. Maleki, "Optoelectronic oscillator for photonic systems," *IEEE J. Quantum Electron.*, vol. 32, pp. 1141–1149, 1996.
- [4] X. S. Yao and L. Maleki, "Optoelectronic microwave oscillator," *Vol. 13, No. 8/August 1996/J. Opt. Soc. Am. B*, vol. 13, no. 8, pp. 1725–1735, 1996.
- [5] J. R. Vig, "Military applications of high accuracy frequency standards and clocks," *IEEE Trans. Ultrason. Ferro- Electr. Freq.*, vol. 40, no. 5, pp. 522–527, 1993.
- [6] P. Salzenstein, *Optoelectronic Devices and Properties*. 2011, p. 674.
- [7] O. Sergiyenko, Ed., "Optoelectronic Devices and Properties," 19-Apr-2011. [Online]. Available: <http://www.intechopen.com/books/optoelectronic-devices-and-properties>. [Accessed: 04-Dec-2014].
- [8] P. Devgan, "A Review of Optoelectronic Oscillators for High Speed Signal," vol. 2013, 2013.
- [9] E. C. Levy, M. Horowitz, and C. R. Menyuk, "Modeling optoelectronic oscillators," *J. Opt. Soc. Am. B*, vol. 26, no. 1, p. 148, Dec. 2008.
- [10] D. R. Lide, *CRC Handbook of Chemistry and Physics*, 90th ed. CRC Press/Taylor and Francis, Boca Raton, FL., 2010.
- [11] N. L. Duy, "Contribution à l'étude d'un oscillateur opto-électronique micro-ondes Applications fondées sur une variation de sa fréquence," Thèse de Doctorat, ENS Cachan, soutenance le 17 juin 2010.
- [12] B. D. Thanh, "Étude et réalisation d'un système instrumental de stabilisation d'un modulateur électrooptique. Application à l'amélioration du comportement d'un oscillateur optoélectronique." Thèse de Doctorat, ENS Cachan, soutenance le 09 juin 2011.
- [13] David M. Pozar, *Microwave engineering*, 4th ed. John Wiley & Sons, 2011.

- [14] E. Lindberg, "The Barkhausen Criterion (Observation ?)," in *18th IEEE Workshop on Nonlinear Dynamics of Electronic Systems (NDES2010)*, 2010, no. May, pp. 26–29.
- [15] V. Singh, "Discussion on Barkhausen and Nyquist criteria," *Analog Integr. Circuits Signal Process.*, vol. 62, pp. 327–332, 2010.
- [16] V. Singh, "Failure of Barkhausen oscillation building up criterion: Further evidence," *Analog Integr. Circuits Signal Process.*, vol. 50, pp. 127–132, 2007.
- [17] V. Singh, "A note on determination of oscillation startup condition," *Analog Integr. Circuits Signal Process.*, vol. 48, pp. 251–255, 2006.
- [18] H. Wang, C. Huang, and Y. Liu, "Comment: A note on determination of oscillation startup condition," *Analog Integr. Circuits Signal Process.*, vol. 51, pp. 57–58, 2007.
- [19] F. He, R. Ribas, C. Lahuec, and M. Jézéquel, "Discussion on the general oscillation startup condition and the Barkhausen criterion.," *Analog Integr. Circuits Signal Process.*, vol. 59, pp. 215–221, 2008.
- [20] L. Von Wangenheim, "On the Barkhausen and Nyquist stability criteria," *Analog Integr. Circuits Signal Process.*, vol. 66, pp. 139–141, 2011.
- [21] A. Neyer and E. Voges, "High-frequency electro-optic oscillator using an integrated interferometer," *Appl. Phys. Lett.*, vol. 40, no. 1, pp. 6–8, 1982.
- [22] X. S. Yao, L. Maleki, and G. Lutes, "Dual-loop opto-electronic oscillator," *Proc. 1998 IEEE Int. Freq. Control Symp. (Cat. No.98CH36165)*, pp. 545–549, 1998.
- [23] E. Salik, N. Yu, and L. Maleki, "An Ultralow Phase Noise Coupled Optoelectronic Oscillator," *IEEE Photonics Technol. Lett.*, vol. 19, no. 6, pp. 444–446, 2007.
- [24] D. Eliyahu, D. Seidel, and L. Maleki, "RF Amplitude and Phase-Noise Reduction of an Optical Link and an Opto-Electronic Oscillator," *IEEE Trans. Microw. Theory Tech.*, vol. 56, no. 2, pp. 449–456, 2008.
- [25] P. Lecoy, *Fibre-Optic Communications*. 2010.
- [26] G. P. Agrawal, *Fiber-Optic Communication Systems*, 4th ed. Wiley, 2010, p. 626.
- [27] G. L. Li and P. K. L. Yu, "Optical Intensity Modulators for Digital and Analog Applications," *J. Light. Technol.*, vol. 21, no. 9, pp. 2010–2030, Sep. 2003.
- [28] B. E. A. Saleh and M. C. Teich, *Fundamental of photonics*, 2nd ed. Wiley-Interscience, 2007, p. 1200.
- [29] J. P. Salvestrini, L. Guilbert, M. Fontana, M. Abarkan, and S. Gille, "Analysis and Control of the DC Drift in LiNbO₃-Based Mach – Zehnder Modulators," *J. Light. Technol.* 2011;29(10)1522-1534, vol. 29, no. 10, pp. 1522–1534, 2011.

- [30] M. Aillerie, N. Théofanous, and H. L. Saadon, "Thermo-optic effect in an electro-optic modulation system," in *Proceedings of the New Achievements in Materials and Environmental Sciences (NAMES), 3rd France-Russia Seminar*, 2007, pp. 87–91.
- [31] W. Mo and N. Chen, "Source stabilization for high quality time-domain diffuse optical tomography," in *Proceeding of SPIE, Design and Quality for Biomedical Technologies II*, 2009, p. 71700N–9.
- [32] J. Snoddy, Y. Li, F. Ravet, and X. Bao, "Stabilization of electro-optic modulator bias voltage drift using a lock-in amplifier and a proportional-integral-derivative controller in a distributed Brillouin sensor system," *Appl. Opt.*, vol. 46, no. 9, pp. 1482–1485, Mar. 2007.
- [33] G. L. Li, R. B. Welstand, W. X. Chen, J. T. Zhu, S. A. Pappert, C. K. Sun, Y. Z. Liu, and P. K. L. Yu, "Novel bias control of electroabsorption waveguide modulator," *IEEE Photonics Technol. Lett.*, vol. 10, no. 5, pp. 672–674, May 1998.
- [34] S. Park, J. J. Ju, J. Y. Do, S. K. Park, and M.-H. Lee, "Thermal Stability Enhancement of Electrooptic Polymer Modulator," *IEEE Photonics Technol. Lett.*, vol. 16, no. 1, pp. 93–95, Jan. 2004.
- [35] P. Heuk, H. Wol-Yon, and Kim Jang-Joo, "Origin of direct current drift in electro-optic polymer modulator," *Appl. Phys. Lett.*, vol. 70, no. 21, pp. 2796–2798, 1997.
- [36] E. Photonics GmbH, *APPLICATION NOTE: Relative Intensity Noise of Distributed Feedback Laser Rev. 1.5*. 2013.
- [37] K. Volyanskiy, Y. K. Chembo, L. Larger, and E. Rubiola, "Contribution of Laser Frequency and Power Fluctuations to the Microwave Phase Noise of Optoelectronic Oscillators," *J. Light. Technol.*, vol. 28, no. 18, pp. 2730–2735, Sep. 2010.
- [38] R. Paschotta, *Encyclopedia of Laser Physics and Technology*. Wiley, 2008.
- [39] H. Brahim, "Etude en bruit de systèmes optiques hyperfréquences: Modélisation, caractérisation et application à la métrologie en bruit de phase et à la génération de fréquence," *Thèse présentée à l'Université Toulouse*, 2010.
- [40] L. D. Turner, K. P. Weber, C. J. Hawthorn, and R. E. Scholten, "Frequency noise characterisation of narrow linewidth diode lasers," *Opt. Commun.*, vol. 201, no. 4–6, pp. 391–397, Jan. 2002.
- [41] L. Jacubowicz, J. Roch, J. Poizat, and P. Grangier, "Teaching photodetection noise sources in laboratory," pp. 1–13.
- [42] E. Rubiola, "Flicker noise in high-speed p-i-n photodiodes," *IEEE Trans. Microw. Theory Tech.*, vol. 54, no. 2, pp. 816–820, 2006.
- [43] E. Rubiola, E. Salik, N. Yu, and L. Maleki, "Flicker noise in high-speed photodetectors," in *Proceedings of the IEEE International Frequency Control Symposium and Exposition*, 2005,

- vol. 2005, pp. 861–864.
- [44] A. Chenakin, “Phase Noise Reduction in Microwave Oscillators,” *Microw. J.*, vol. 52, no. 10, p. p124, 2009.
- [45] P. Kartaschoff, *Frequency and Time*. New York: Academic Press, 1978.
- [46] H. H. (Chairman), “(IEEE Standard 1139-1988) IEEE Standard Definitions of Physical Quantities for Fundamental Frequency and Time Metrology - Random Instabilities.” IEEE, 1988.
- [47] E. Rubiola, *Phase noise and frequency stability in oscillators*. The Cambridge RF and Microwave Engineering Series, 2009.
- [48] J. R. V. (Chairman), *(IEEE Standard 1139-1999) IEEE Standard Definitions of Physical Quantities for Fundamental Frequency and Time Metrology - Random Instabilities*. IEEE, 1999, p. 36.
- [49] D. Leeson, “A simple model of feedback oscillator noise spectrum,” *Proc. IEEE*, vol. 54, no. 2, pp. 329–330, 1966.
- [50] Photline, “MX-LN-10 Modulator,” *Photline Technologies*,. [Online]. Available: [Http://www.photline.com/product/view/33/](http://www.photline.com/product/view/33/).
- [51] Y. Kouomou Chembo, L. Larger, H. Tavernier, R. Bendoula, E. Rubiola, and P. Colet, “Dynamic instabilities of microwaves generated with optoelectronic oscillators,” *Opt. Lett.*, vol. 32, no. 17, p. 2571, 2007.
- [52] E. C. Levy, Z. Toroker, M. Horowitz, and C. Menyuk, “SINGLE-LOOP OEO SIMULATION SOFTWARE,” *Computational Photonics Laboratory*. [Online]. Available: http://www.photonics.umbc.edu/software/Single-Loop-OEO_Simulation-Software/index.html.
- [53] J. Hong and C. Yang, “Modeling for opto-electronic oscillator considering the nonlinearity of microwave amplifier,” *Microw. Opt. Technol. Lett.*, vol. 55, no. 4, pp. 715–719, 2013.
- [54] H. Brahimi, P. Merrer, and O. Llopis, “CAD of microwave optical systems for time&frequency applications,” *Proc. EFTF*, 2008.
- [55] H. Brahimi, H. L. Martinez-Reyes, P. H. Merrer, a. Bouchier, and O. Llopis, “A CAD approach of microwave optical systems including noise performance,” *Eur. Microw. Week 2009, EuMW 2009 Sci. Prog. Qual. Radiofreq. Conf. Proc. - 39th Eur. Microw. Conf. EuMC 2009*, pp. 1642–1645, 2009.
- [56] K. (Doctorat) SALEH, “High spectral purity microwave sources based on optical resonators,” L’université de Toulouse, 2012.
- [57] IPSIS, *Manuel d’utilisation du logiciel COMSIS*. .

- [58] *Télécommunications optiques (MASTER IST - UE 435)*. Falcuté des Sciences d'ORSAY/E.N.S. de CACHAN, 2004.
- [59] E. Cassan, "Une introduction aux télécommunications optiques par la simulation de systèmes simples," *J3eA*, vol. 2, 2003.
- [60] L. Michalski, K. Eckersdorf, J. Kucharski, and J. McGhee, *Temperature Measurement*, 2nd ed. Wiley, 2001, p. 478.
- [61] G. K. McMillan, *Advanced Temperature Measurement and Control*. The Instrument, Systems and Automation Society, 2010, p. 250.
- [62] Analog Devices, *Low Cost, Low Power AD620 Instrumentation amplifier*. 1999.
- [63] "Thermoelectric effect." [Online]. Available: http://en.wikipedia.org/wiki/Thermoelectric_effect.
- [64] H. Julian Goldsmid, *Introduction to Thermoelectricity*. Springer, 2009, p. 242.
- [65] Texas Instruments, "OPA541," no. September 2000, 2006.
- [66] C. T. Nguyễn, A. Clouqueur, R. Hierle, B. Journet, P. Labbé, and J. Zyss, "Stabilization of the bias point of an electro-optic modulator based on polymer material," in *Proceeding of SPIE on Integrated Optoelectronic Devices*, pp. vol. 6117–47, February 23, 2006.
- [67] D. T. Bui, C. T. Nguyen, I. Ledoux-Rak, J. Zyss, and B. Journet, "Instrumentation system for determination and compensation of electro-optic modulator transfer function drift," *Meas. Sci. Technol.*, vol. 22, no. 12, p. 125105, Dec. 2011.
- [68] *eZdsp TM F28335 Technical Reference - DSP Development Systems*. Spectrum Digital Incorporated, 2007.
- [69] *Models LR-F28335DAQ & LR-F28335DAQ8x8 - Technical Reference Manual, Document Number : 9-403-60*. Link Research, 2008.
- [70] K. J. Astrom and H. Tore, *PID Controllers: Theory, Design, and Tuning*, 2nd ed. ISA: The Instrumentation, Systems, and Automation Society, 1995, p. 343.
- [71] V. a. Oliveira, L. V. Cossi, M. C. M. Teixeira, and a. M. F. Silva, "Synthesis of PID controllers for a class of time delay systems," *Automatica*, vol. 45, no. 7, pp. 1778–1782, 2009.
- [72] A. Datta, M.-T. Ho, and S. P. Bhattacharyya, *Structure and Synthesis of PID Controllers*. Springer, London, England, 2000, p. 235.
- [73] R. Isermann, *Digital Control Systems*, 2nd ed. Springer - Verlag Berlin Heidelberg, 1991.
- [74] V. Bobál, J. Böhm, J. Fessl, and J. Macháček, *Digital Self-tuning Controllers*. Springer,

- 2005, p. 318.
- [75] G. F. Franklin, J. D. Powell, and L. W. Michael, *Digital Control of Dynamic Systems*, 2nd ed. Addison-Wesley Publishing Company, 1997, pp. 222–229.
- [76] D. Eliyahu, K. Sariri, J. Taylor, and L. Maleki, “Opto-Electronic Oscillator with Improved Phase Noise and Frequency Stability,” *SPIE Photonics West*, vol. 4998, pp. 139–147, 2003.
- [77] D. Eliyahu, K. Sariri, A. Kamran, and M. Tokhmakhian, “Improving short and long term frequency stability of the opto-electronic oscillator,” in *Proceedings of the 2002 IEEE International Frequency Control Symposium and PDA Exhibition (Cat. No.02CH37234)*, 2002, pp. 580–583.
- [78] R. Helsel, *Visual Programming with HP VEE*, 3rd ed. Prentice Hall PTR, 1998, p. 432.
- [79] M. T. Abuelma’atti, “Large signal analysis of the Mach-Zehnder modulator with variable bias,” in *Proceedings of the National Science Council*, 2001, pp. 254–258.
- [80] J. P. Farina and G. J. McBrien, “Ditherless optical modulator control,” US. Patent 8184991. 22 May, 2012.2012.
- [81] C. M. Gee, G. D. Thurmond, H. Blauvelt, and H. W. Yen, “Minimizing dc drift in LiNbO₃ waveguide devices,” *Appl. Phys. Lett.*, vol. 47, no. 3, p. 211, 1985.
- [82] Shi Y, WangW, Lin W, Olson D J, and Bechtel J H, “Long term stable direct current bias operation in electro-optic polymer modulators with an electrically compatible multilayer structure polymer,” *Appl. Phys. Lett.*, vol. 71, no. 16, pp. 2236–2238, 1997.
- [83] Y. Takahashi, M. J. Rabins, and D. M. Auslander, *Control and Dynamic Systems*. Addison-Wesley Reading, Massachusetts, 1972.
- [84] F. W. Isen, “DSP for MATLAB™ and LabVIEW™ III: Digital Filter Design,” *Synthesis Lectures on Signal Processing*, vol. 3. morgan, pp. 1–239, 2008.
- [85] B. A. Shenoi, *Introduction to Digital Signal Processing and Filter Design*. Wiley-Interscience, 2005.
- [86] A. Report, *Handbook of operational amplifier applications*, no. October. Texas Instruments, 2001.
- [87] E. I. Ackerman and I. Cox, C.H., “Effect of pilot tone-based modulator bias control on external modulation link performance,” *Int. Top. Meet. Microw. Photonics MWP 2000 (Cat. No.00EX430)*, pp. 121–124, 2000.
- [88] A. DePalma, “Refractometer Uses in Industry and Selection.” [Online]. Available: <http://rudolphresearch.com/refractometers-use-selection/>.
- [89] R. A. Auras, L.-T. Lim, S. E. M. Selke, and H. Tsuji, *Poly(lactic acid): Synthesis*,

- Structures, Properties, Processing, and Application*. Wiley, 2010, p. 528.
- [90] Thuet, “Cuves standard pour fluorescence 441/2mm,” *Thuet France*. [Online]. Available: <http://www.thuet-france.com/index2.htm>.
- [91] Hellma, “Fluorescence cells 111-QS,” *Hellma GmbH & Co. KG*. [Online]. Available: http://www.hellma-analytics.com/kuevetten/136/en/pg_id,41/fluorescence-cells.html.
- [92] L. D. Nguyen, K. Nakatani, and B. Journet, “Refractive index measurement by using an optoelectronic oscillator,” *IEEE Photonics Technol. Lett.*, vol. 22, no. 12, pp. 857–859, 2010.
- [93] Microwave Marki. and Inc, “Marki double-balanced mixers M1-0212 datasheets,” pp. 10–12.
- [94] Agilent Technologies, *Agilent 53131A/132A 225 MHz Universal Counter Operating Guide*. Agilent Technologies, 2006, p. 194.
- [95] J. Rheims, J. Köser, and T. Wriedt, “Refractive-index measurements in the near-IR using an Abbe refractometer,” *Meas. Sci. Technol.*, vol. 8, no. 6, pp. 601–605, Jun. 1997.
- [96] C.-B. Kim and C. B. Su, “Measurement of the refractive index of liquids at 1.3 and 1.5 micron using a fibre optic Fresnel ratio meter,” *Meas. Sci. Technol.*, vol. 15, no. 9, pp. 1683–1686, Sep. 2004.
- [97] Agilent, *Agilent Network Analyzer Basics*. Agilent Technologies, Inc, 2004, pp. 1–94.
- [98] G. Bazin, B. Journet, and D. Placko, “General characterization of laser range-finder optical heads,” in *Conference Proceedings LEOS’96 9th Annual Meeting IEEE Lasers and Electro-Optics Society*, 1996, vol. 1, pp. 232–233.
- [99] T. Zhang, J. Zhu, T. Guo, J. Wang, and S. Ye, “Improving accuracy of distance measurements based on an optoelectronic oscillator by measuring variation of fiber delay.,” *Appl. Opt.*, vol. 52, no. 15, pp. 3495–9, May 2013.
- [100] A. Technologies, *E5070B/E5071B ENA Series RF Network Analyzers*, no. June. Agilent Technologies, Inc, 2007.
- [101] W.-H. Tseng and K.-M. Feng, “Enhancing long-term stability of the optoelectronic oscillator with a probe-injected fiber delay monitoring mechanism.,” *Opt. Express*, vol. 20, no. 2, pp. 1597–607, Jan. 2012.
- [102] N. L. Duy, B. Journet, I. Ledoux-Rak, J. Zyss, L. V. H. Nam, and V. Van Luc, “Opto-electronic oscillator: Applications to sensors,” in *2008 International Topical Meeting on Microwave Photonics jointly held with the 2008 Asia-Pacific Microwave Photonics Conference*, 2008, pp. 131–134.

Résumé

L'oscillateur optoélectronique (OEO) a été introduit pour la première fois en 1996 par S. Yao et L. Maleki, en tant qu'oscillateur microondes à très faible bruit de phase et obtenu par synthèse directe. Les développements de l'OEO concernent les applications en photonique microondes, télécommunications optiques, radar et traitement du signal. Mais l'OEO devrait aussi pouvoir être utilisé dans le domaine des capteurs. Dans cette thèse nous étudions plusieurs aspects de l'OEO pour son application à la mesure d'indice de réfraction d'un liquide.

Compte tenu de sa structure l'OEO dépend fortement des conditions ambiantes d'utilisation. S'il n'est pas bien optimisé ni contrôlé, il ne peut pas fonctionner correctement sur une longue durée. Nous avons étudié les influences de la température sur le modulateur électrooptique (EOM) et sur le comportement global de l'OEO. Un contrôle de température réduit de façon significative le phénomène de dérive de l'EOM. Afin de la supprimer complètement, nous avons mis au point une instrumentation construite autour d'une carte DSP, permettant de détecter et compenser la dérive du point de fonctionnement optique de l'EOM tout en contrôlant simultanément sa température. Une première technique est basée sur un signal de test, basse fréquence, appliqué à l'électrode DC du modulateur. Une deuxième solution consiste à travailler sur la puissance optique en sortie du modulateur. En combinant les deux on peut profiter des avantages de ces deux méthodes.

Utilisant ainsi l'OEO nous avons testé plusieurs configurations pour mesurer l'indice de réfraction de quatre solutions chimiques bien connues, nous avons obtenu une variance de 3 pour mille. Les résultats sont en assez bon accord avec les publications correspondantes. Enfin nous avons aussi introduit une nouvelle méthode pour améliorer les mesures d'indice de réfraction faites à long terme en suivant, grâce à un analyseur vectoriel de réseau, les évolutions au cours du temps du temps de propagation dans la fibre optique. En introduisant à partir de cette mesure une correction aux mesures de la fréquence d'oscillation il est possible de réduire les fluctuations de cette fréquence à seulement 606 Hz, sur une durée de 62 h, ce que l'on peut comparer aux 8 GHz de l'oscillateur. Ainsi le rapport signal à bruit, peut être grandement amélioré lors de la mesure d'indice de réfraction et il doit être possible de diminuer la limite de détection des variations de l'indice de réfraction au cours du temps.

Abstract

The optoelectronic oscillator (OEO) was first introduced in 1996 by S. Yao and L. Maleki as a very low phase noise microwave oscillator working in direct synthesis. The OEO developments concern applications in microwave photonics, optical telecommunication, radar and high speed signal processing systems but it should also be used in the sensing domain. In this thesis, we study several aspects to apply the OEO to liquid refractive index measurement.

Because of its structure the OEO is very dependent on the ambient conditions. If the OEO is not optimized and controlled, it cannot operate well for long duration. We have analyzed the influences of temperature on the electrooptic modulator (EOM) and the global OEO behavior. Temperature control can significantly reduce the drift phenomena of the EOM. In order to totally remove this drift, we have developed a complete digital system, based on a DSP kit, to detect and compensate automatically the EOM optical bias point drift and to control simultaneously its temperature. The first technique is based on a dither signal at low frequency, injected to DC electrode of the EOM. The second one is based on the average optical output power of the EOM. A combination of these two techniques can take advantages from both of them.

Using like that the OEO, we have tested several configurations to measure the refractive index of four classical chemical solutions leading to a standard deviation of 3 per thousand. The results are in rather good agreement with previous publications. Finally, we have introduced a new method to improve the long-term refractive index measurement by monitoring, with a vector network analyzer, the variations of the optical delay in the fiber loop of the OEO. Introducing by this way a correction to the long-term frequency measurement it is possible to reduce the oscillation frequency fluctuations to only 606 Hz, compared to the 8 GHz of the oscillator, for a duration of 62 hours. Therefore the signal-to-noise ratio in the refractive index measurement can be enhanced and so the detection resolution of the refractive index variations during time.